

ENERGY DISSIPATING CONNECTOR FOR PRECAST SHEAR WALLS IN
HIGH-SEISMIC AREAS

by

Mohammed Aljuboori

A Dissertation Submitted in
Partial Fulfillment of the
Requirements for the Degree of
Doctor of Philosophy
in Engineering

at

The University of Wisconsin-Milwaukee

August 2019

ABSTRACT

ENERGY DISSIPATING CONNECTOR FOR PRECAST SHEAR WALLS IN HIGH-SEISMIC AREAS

by

Mohammed Aljuboori

The University of Wisconsin – Milwaukee, 2019

Under the Supervision of Dr. Habib Tabatabai

Precast concrete systems are widely used in a variety of structures such as parking garages, residential units, shopping centers, and transportation stations. In some cases, precast structures are preferred over conventional cast-in-place (CIP) concrete conventional structures because of ease of construction, rapid implementation, and lower levels of energy consumption. One area where precast systems have traditionally been at a disadvantage is high seismic applications. In seismic regions, precast concrete structures must have enhanced connection systems to address the inherent discontinuity between various components. The lateral load resisting systems may consist of shear wall systems, moment frames, or a combination of the two.

The objective of this research was to develop a new seismic connector device for precast shear walls that could significantly enhance energy dissipation and improve the performance of the building under seismic load by reducing drift and base shear forces. Several devices were previously developed and tested by the PRESS program. The U-bar system that was studied in the PRESS program is currently the most commonly-used connector device for precast shear wall applications. This study was aimed at developing a device that could offer improved seismic performance with compared to the U-bar system.

Several geometries and shapes were considered as potential new devices based on trials and optimization studies. Subsequently, two shapes were chosen for scaled laboratory testing. Based on the analytical and experimental results, one shape (designated NS-5) is proposed because of its improved performance in relation to the U-bar system. The response of a shear wall building system utilizing either the new NS-5 connector or the current U-bar system was then evaluated using a frame model proposed in the PRESS study. This simplified frame model was used to simulate the response of the building under a seismic excitation used in the PRESS study. In addition to the two connector systems, the structure response was also examined under free (no connection between walls) and rigid (rigid point connections) conditions to understand the limiting structural response values. The proposed NS-5 connector performed better than the U-bar system both in terms of energy dissipation in the device and with respect to improved structure response (30% lower drift and 70% higher dissipated energy). The NS-5 connector offers resistance and energy dissipations when relative movement occurs in both horizontal and vertical directions, whereas the U-bar system only offers substantial resistance under vertical deformation. Therefore, the proposed connector is a feasible alternative to the U-bar system in seismic precast wall applications. The NS-5 can also be an alternative in other energy dissipation applications in building and bridge structures.

© Copyright by Mohammed Aljuboory, 2019
All Rights Reserved

TABLE OF CONTENTS

CHAPTER 1: INTRODUCTION	1
1.1 Background	1
1.2 Objectives.....	8
1.3 Scope.....	9
CHAPTER 2: Literature Review	11
2.1 Introduction	11
2.2 Types of horizontal and vertical connections	12
2.2.1 Vertical connections:.....	13
2.2.2 Horizontal connections	19
2.3 Previous Studies.....	24
2.3.1 Stanton, J. F., and Nakaki, S. D [10].....	24
2.3.2 E. I., Saqan and R. A Haweeleh [11]	30
2.3.3 C. Bora, M. G. Oliva, S. D. Nakaki, R Pecker [12].....	37
2.3.4 Sritharan S., Aaleti S. [15].....	41
2.3.5 Perez, F. J., Pessiki, S., and Sause R. [17] [18]	41
2.3.6 Ajrab J. J., Pekcan G., and Mander J. B. [20]	44
2.3.7 Seymore D. and Laflamme S. [22]	48
2.3.8 Sun J., Qiu H., Yang Y. and Lu B. [24] & [25].....	48
2.4 Summary of previous studies.....	50
CHAPTER 3: Computational Modeling	52
3.1 Overview and preliminary modeling.....	52
3.2 Basic seismic connectors.....	57
3.2.1 U-shaped test results by PRESSS [5]	57
3.2.2 U-shape shear connector – partial thickness.....	60
3.2.3 U-shaped connector (full width) with constant displacement	65
3.2.4 U-shaped connector with cyclic displacement	67
3.2.5 Simple plate models.....	69
3.2.6 Truss mechanism models.....	76
3.2.7 Beehive-shaped (Hexagonal) model	82
3.2.8 Model OS-2D.....	86
3.3 Topology optimization and Model development	90
3.3.1 Introduction to topology optimization	90

3.3.2	ABAQUS topology optimization	93
3.3.3	ANSYS topology Optimization	100
3.3.4	Altair (SolidThinking) topology Optimization.....	100
3.3.5	Results of the topology optimization of different FEM software	101
3.4	Behavior of connectors	104
3.4.1	Vertical response (Equivalent vertical springs).....	104
3.4.2	Horizontal response (Equivalent horizontal spring)	104
3.5	Shape selection (Trial shapes).....	106
3.5.1	TSI-1 shape	106
3.5.2	TSI-2 shape	108
3.5.3	TSI-3 shape	110
3.5.4	TSI-3 with bracing.....	112
3.5.5	Shape (TS).....	114
3.6	NS shape.....	121
3.6.1	Shape NS1	124
3.6.2	Shape NS2	130
3.6.3	Shape NS3	134
3.6.4	Shape NS4	137
3.6.5	Shape NS5	141
3.7	Localized resistance of concrete	149
3.7.1	Verification model.....	152
3.7.2	Modeling of TS connector with precast wall.	159
3.7.3	Cyclic response.....	164
3.8	Full building analytical model	167
3.8.1	Description of building model.....	167
3.8.2	Analysis with vertical springs only	173
3.8.3	Analysis with vertical and horizontal springs.....	189
CHAPTER 4:	Experimental work	195
4.1	Background	195
4.2	Test Setup and protocol	195
4.3	TS Specimens – Results and Discussion	201
4.3.1	First set of specimens of TS shape – TS1.....	202
4.3.2	Second set of specimens of TS shape – TS2.....	204

4.3.3	Third set of specimens of TS shape – TS3	206
4.4	Summary of TS shape testing.....	210
4.5	Testing, Results, and Discussion of NS5	211
4.5.1	Test NS5-1	214
4.5.2	Test NS5-2	218
4.5.3	Test NS5-3	221
4.6	Summary of NS-5 shape testing.....	224
4.7	Comparison between various models	224
4.7.1	Background	224
4.8	Comparison of tested shapes.....	224
CHAPTER 5:	Summary and Conclusion.....	227
5.1	Summary and conclusions	227
CHAPTER 6:	REFERENCES	234
APPENDIX A.	EXPERIEMENT PHOTOS	238
APPENDIX B.	TEST SETUP DRAWINGS	260
CURRICULUM VITAE	276

LIST OF FIGURES

Figure 1-1: Elevation of Special Unbonded Hybrid Posttensioned Split Precast Shearwall [3]	5
Figure 1-2: Elevation of deflected shearwall [3]	6
Figure 1-3: Typical U-Shaped flexural plate [5]	7
Figure 2-1: Detail of NSP Connector [5]	13
Figure 2-2: Details of SFP Connector [5]	14
Figure 2-3: Details of IFP Connector [5]	15
Figure 2-4: Details of XAP Connector [5]	16
Figure 2-5: Details of PTS Connectors [5]	17
Figure 2-6: Details of VJF Connectors [5]	18
Figure 2-7: Details of UFP Connectors [5]	19
Figure 2-8: Details of GSS Connectors [5]	20
Figure 2-9: Details of PTT Connectors [5]	21
Figure 2-10: Details of PVJ Connector [5]	22
Figure 2-11: Details of DSB Connection [5]	23
Figure 2-12: layout of PRESSS phase III test building [10]	25
Figure 2-13: Drift versus strength of resisting members [10]	26
Figure 2-14: UFP connector Free body diagram [10]	29
Figure 2-15: Critical stress and strain in UFP material [10]	30
Figure 2-16: Shearwall consists of four panels under design drift [11]	31
Figure 2-17: Shearwall panels subjected to seismic force [11]	31
Figure 2-18: Tension and compression forces at the wall toes [12]	38
Figure 2-19: Ideal Elastic-Plastic response [12]	39
Figure 2-20: Slotted-Bolted connection [12]	40
Figure 2-21: Wall Prototype [17] & [18]	42
Figure 2-22: Base shear versus Roof drift [17] & [18]	43
Figure 2-23: Rocking wall system on rigid foundation [20]	46
Figure 2-24: (a) Draped tendons configurations and (b) Vertical tendons configurations [20]	47
Figure 2-25: I-Shaped Shear wall [24]	49
Figure 3-1: Preliminary model	53
Figure 3-2: Deformed shape of Preliminary model	54
Figure 3-3: Relative difference of horizontal displacement between nodes on opposite sides of shear wall	54
Figure 3-4: Relative difference of vertical displacement between nodes on opposite sides of shear wall	55
Figure 3-5: Vector displacement at each level	56
Figure 3-6: U-shaped plate configuration [5]	58
Figure 3-7: U-shaped plate dimensions [5]	58
Figure 3-8: Test set-up of U-shaped Connection by PRESSS [5]	59
Figure 3-9: Displacement amplitude used by PRESSS to test UFP [5]	59
Figure 3-10: Force versus Displacement of UFP by PRESSS [5]	60
Figure 3-11: U-shaped generated model	61
Figure 3-12: Equivalent stress contour map for U-shaped model	62
Figure 3-13: Strain energy contour map for U-shaped model	63

Figure 3-14: Reaction versus Time relationship for U-shaped model	63
Figure 3-15: Force versus Deformation relationship for U-shaped model	64
Figure 3-16: Strain energy versus time relationship for U-shaped model.....	64
Figure 3-17: U-shaped connector	65
Figure 3-18:U-shaped boundary condition	66
Figure 3-19: Equivalent stress contour map	66
Figure 3-20: Energy dissipation of U-shaped connector.....	67
Figure 3-21: Finite elements model in ANSYS workbench: (a) meshed shape, (b) Boundary condition	68
Figure 3-22: Finite elements results of U-shaped connector.	69
Figure 3-23: Simple plate model SP-1: (a) 3D view, (b) elevation view	70
Figure 3-24: Equivalent stress contour map for SP-1	71
Figure 3-25: Strain energy contour map for SP-1	71
Figure 3-26: Reaction versus Time relationship for SPM-1.....	72
Figure 3-27: Force versus Deformation relationship for SPM-1	72
Figure 3-28: Strain energy for SPM-1.....	73
Figure 3-29: Simple plate model SP-2: (a) 3D view, (b) elevation view	73
Figure 3-30: Equivalent stress and strain contour map for SP-2: (a) stress contours, (b) strain contours.	75
Figure 3-31: Reaction versus Time relationship for SP-2	75
Figure 3-32: Force versus Deformation relationship for SP-2	76
Figure 3-33: Strain energy for SP-2	76
Figure 3-34: Illustration of TM-1	77
Figure 3-35: TM-1 response: (a) stress contours, (b) strain contours	78
Figure 3-36: TM-1 Response: (a) Reaction force, (b) Force vs Displacement.....	78
Figure 3-37: Strain energy for TM-1.....	79
Figure 3-38: Illustration of TM-2	80
Figure 3-39: TM-2 response: (a) stress contours, (b) strain contours	81
Figure 3-40: Reaction versus Time relationship for TM-2	81
Figure 3-41: Force versus Deformation relationship for TM-2	82
Figure 3-42: Strain energy for TM-2.....	82
Figure 3-43: Beehive-shaped model	84
Figure 3-44: SPM-1 response; (a) stress contours, (b) strain contours	84
Figure 3-45: Reaction versus Time relationship for SPM-1.....	85
Figure 3-46: Force versus Deformation relationship for SPM-1	85
Figure 3-47: Strain energy for SPM-1.....	86
Figure 3-48: Model OS-2D.....	87
Figure 3-49: Model OS-2d - Side view.....	87
Figure 3-50: OS-2D - Top view	88
Figure 3-51: OS-2D boundary conditions.....	89
Figure 3-52: Stress contour map of model OS-2D	89
Figure 3-53: Dissipated energy of model OS-2D	90
Figure 3-54: Force vs Displacement results of OS-2D	90
Figure 3-55: Optimization process [27].....	92
Figure 3-56: Starting (initial) block model prior to topology optimization.....	94
Figure 3-57: Boundary conditions and locations of imposed displacement.....	95
Figure 3-58: Various of strain energy and volume during the optimization cycles.	96

Figure 3-59: Optimization steps.....	97
Figure 3-60: Top view of optimized shape.....	98
Figure 3-61: Stress contour map of initial shape	98
Figure 3-62: Stress map contour for the final optimized shape	99
Figure 3-63: Plan view of stressed optimized shape.....	99
Figure 3-64: General shape and boundary condition	101
Figure 3-65: Optimized shape.....	102
Figure 3-66: Altai (SolidThinking) optimization output.....	102
Figure 3-67: ANSYS optimization results.....	103
Figure 3-68: U-shape plate boundary condition	105
Figure 3-69: Displacement amplitude.....	105
Figure 3-70: Force vs Displacement for U-shaped plate under horizontal displacement	106
Figure 3-71: Model TSI-1; plates with holes	107
Figure 3-72: force versus displacement for TSI-1	108
Figure 3-73: TSI-2 Geometry: (a) Elevation, (b) 3D view.....	108
Figure 3-74: Dimensions of TSI-2	109
Figure 3-75: Force versus displacement of TSI-2	110
Figure 3-76: TSI-3 geometry: (a) elevation, (b) 3D view	111
Figure 3-77: TSI-3 dimensions.....	111
Figure 3-78: Force vs Displacement for TSI-3	112
Figure 3-79: TSI-4 geometry: (a) 3D view, (b) elevation	113
Figure 3-80: TSI-4 dimensions.....	113
Figure 3-81: Force versus displacement for TSI-4.....	114
Figure 3-82: ANSYS model of TS shape - Front view: (a) elevation, (b) 3D view	115
Figure 3-83: TS shape – Dimensions	115
Figure 3-84: Displacement amplitude used by PRESSS to test UFP [5].....	116
Figure 3-85: Force versus displacement of the TS shape.....	117
Figure 3-86: Abaqus model of TS shape: (a) 3D view. (b) elevation	118
Figure 3-87: C3D20R element [38].....	118
Figure 3-88: Stress - strain relationship of A36 steel.....	119
Figure 3-89: ABAQUS force versus displacement graph.....	120
Figure 3-90: Shapes NS1 & NS2	122
Figure 3-91: Shapes NS3 & NS4	123
Figure 3-92: Final shape NS5.....	124
Figure 3-93: Shape NS1: (a) Meshed shape, (b) boundary conditions	125
Figure 3-94: Analysis amplitude.....	126
Figure 3-95: Plastic strain at 1" & -1" (left to right) NS1.....	126
Figure 3-96: Plastic strain at 1.5" & -1.5" (left to right) NS1.....	127
Figure 3-97: Plastic strain at 2" & -2" (left to right) NS1.....	127
Figure 3-98: Plastic strain at 2.5" & -2.5" (left to right) NS1.....	128
Figure 3-99: Force vs Displacement of shape NS1.....	128
Figure 3-100: Plastic strain path of the model.....	129
Figure 3-101: Shape NS2: (a) meshed shape, (b) boundary conditions.....	130
Figure 3-102: Plastic strain at 1 & -1 Displacement (left to right) NS2	131
Figure 3-103: Plastic strain at 1.5 & -1.5 Displacement (left to right) NS2	132

Figure 3-104: Plastic strain at 2 & -2 Displacement (left to right) NS2	132
Figure 3-105: Plastic strain at 2.5 & -2.5 Displacement (left to right) NS2	133
Figure 3-106: Force vs Displacement of Shape NS2.....	133
Figure 3-107: Shape NS3: (a) meshed shape, (b) boundary conditions.....	135
Figure 3-108: Plastic Strain at 1 & -1 Displacement (left to Right) NS3	135
Figure 3-109: Plastic Strain at 1.5 & -1.5 Displacement (left to Right) NS3	136
Figure 3-110: Plastic Strain at 2 & -2 Displacement (left to Right) NS3	136
Figure 3-111: Plastic Strain at 2.5 & -2.5 Displacement (left to Right) NS3	137
Figure 3-112: Force vs Displacement of Shape NS3.....	137
Figure 3-113: Shape NS4: (a) mesh shape, (b) boundary condition	138
Figure 3-114: Plastic Strain at 1 & -1 Displacement (left to Right) NS4	139
Figure 3-115: Plastic Strain at 1.5 & -1.5 Displacement (left to Right) NS4	139
Figure 3-116: Plastic Strain at 2 & -2 Displacement (left to Right) NS4	140
Figure 3-117: Plastic Strain at 2.5 & -2.5 Displacement (left to Right) NS4	140
Figure 3-118: Force vs Displacement of shape NS4	141
Figure 3-119: Sketch of Shape NS5	142
Figure 3-120: Shape NS5; (a) meshed shape, (b) boundary condition	143
Figure 3-121: Plastic stains at -1 & 1 displacement (left to right) NS5	144
Figure 3-122: Plastic stains at -1.5 & 1.5 displacement (left to right) NS5	144
Figure 3-123: Plastic stains at -2 & 2 displacement (left to right) NS5	145
Figure 3-124: Plastic stains at -2.5 & 2.5 displacement (left to right) NS5	145
Figure 3-125: Force vs Displacement for shape NS5	146
Figure 3-126: NS5 boundary condition	147
Figure 3-127: Displacement amplitude.....	148
Figure 3-128: Force vs Displacement for NS5 shape	148
Figure 3-129: ANSYS model illustration: (a) wall with the device, (b) the device with embed plate	150
Figure 3-130: Stress contours for the wall model.....	151
Figure 3-131: Gross et. al model; plate with two anchors [40]	153
Figure 3-132: Concrete Block [39].....	153
Figure 3-133: Concrete block with anchors and plate [39].....	154
Figure 3-134: Concrete block with reinforcement [39]	154
Figure 3-135: Reinforcement layout with respect to anchors [39].....	155
Figure 3-136: Test results of all specimens.....	156
Figure 3-137: Boundary condition of the model.....	157
Figure 3-138: Meshed model.....	158
Figure 3-139: Wireframe view of the model.....	158
Figure 3-140: Simulation results	159
Figure 3-141: Model parts; (a) Embed plate, (b) TS shape	160
Figure 3-142: Assembled parts: (a) solid view, (wireframe)	160
Figure 3-143: Boundary conditions of the model	161
Figure 3-144: Meshed parts; (a) concrete block, (b) embed plate	162
Figure 3-145: Force vs Displacement of the model	162
Figure 3-146: Damage effect on the concrete block	163
Figure 3-147: Damaged concrete around the anchors.	163
Figure 3-148: Displacement amplitude.....	164

Figure 3-149: Force vs reinforcement of the cyclic model	165
Figure 3-150: Damaged model.....	165
Figure 3-151: Damaged area around the anchors	166
Figure 3-152: Relative vertical movement between panels [44].....	167
Figure 3-153: Analytical model of the PRESSS Building [44].....	168
Figure 3-154: Force vs Displacement of full building model.....	172
Figure 3-155: Ground excitation [44].....	173
Figure 3-156: Base shear [44]	173
Figure 3-157: ANSYS building model; (a) concept model, (b) Ansys presentation	174
Figure 3-158: Foundation and PT springs	175
Figure 3-159: Ground Acceleration [44]	175
Figure 3-160: Typical spring connector.....	176
Figure 3-161: Bilinear data of U-shape connector	177
Figure 3-162: Force vs displacement of the full building model with U-shape connector	177
Figure 3-163: Story drift of the full building model with U-shape connector	178
Figure 3-164: Base shear of the full building model with U-shape connector	178
Figure 3-165: Accumulated dissipated energy of the full building model with U-shape connector	179
Figure 3-166: Bilinear data of NS5 shape.....	180
Figure 3-167: Force vs Displacement for shape NS5	180
Figure 3-168: Story drift of the full building model with U-shape connector	181
Figure 3-169: Base shear of the full building model with NS5 connector	181
Figure 3-170: Accumulative dissipated of the full building model with NS5 connector	182
Figure 3-171: Story drift of the full building model with Rigid connector	183
Figure 3-172: Base shear of the full building model with Rigid connector.....	183
Figure 3-173: Story drift of the full building model with no connector (free).....	184
Figure 3-174: Base shear of the full building model with no connector (free).....	184
Figure 3-175: Force vs Displacement for UFP and NS5.....	185
Figure 3-176: Story drift of all models	186
Figure 3-177: Top of building drift for all models	186
Figure 3-178: Base shear for all models.....	187
Figure 3-179: Base shear for U-shaped and NS5	187
Figure 3-180: Incremental energy dissipation of shear connectors for U-shape and NS5	188
Figure 3-181: Cumulative dissipated energy	188
Figure 3-182: Bilinear data of NS5 connector in the horizontal direction.....	190
Figure 3-183: Bilinear data of UFP connector in the horizontal direction.....	190
Figure 3-184: Force vs displacement responses for single r U-shaped and NS-5 connectors located in the building model with horizontal and vertical springs.....	191
Figure 3-185: Story drift for U-shaped and NS-5	191
Figure 3-186: Top of building drift with U-shaped and NS-5 springs in the horizontal and vertical directions.	192
Figure 3-187: Base shear for all models.....	192
Figure 3-188: Base shear for NS-5 and U-shaped connectors in building models with horizontal and vertical springs	193
Figure 3-189: Incremental energy in building with U-shaped and NS-5 springs in the horizontal and vertical directions.....	193

Figure 3-190: Cumulative dissipated energy for U-shaped and NS-5.....	194
Figure 4-1:TS shape test setup layout.....	196
Figure 4-2: Section details of test setup; (a) section A-A, (b) section B-B, (c) section C-C	197
Figure 4-3: Elevation view of TS shape: (a) full-scale dimensions, (b) half-scale dimensions	199
Figure 4-4: Imposed vertical displacements (scaled).....	200
Figure 4-5: Test setup in the MTS Test machine.....	201
Figure 4-6: TSI fractures sequence.....	202
Figure 4-7: Experimental force vs displacement results for first set of specimens	203
Figure 4-8: Experiment vs FEM results of TS1.....	203
Figure 4-9: Test setup TS2.....	204
Figure 4-10: TS2 fractures sequence.....	205
Figure 4-11: Force vs Displacement of TS2	206
Figure 4-12: Experiment vs FEM results of TS2.....	206
Figure 4-13: Test setup TS3.....	207
Figure 4-14: TS3 fractures sequence.....	208
Figure 4-15: Force vs Displacement of TS3	209
Figure 4-16: Experiment vs FEM results of TS3.....	209
Figure 4-17: NS-5 shape test setup layout.....	212
Figure 4-18: Test setup in the MTC machine	212
Figure 4-19: Half-scaled test specimen.....	213
Figure 4-20: Test protocol of shape NS5.....	214
Figure 4-21: Failure mode of NS-1	215
Figure 4-22: Failure model of NS-1	216
Figure 4-23: Force vs displacement of shape NS5-1	217
Figure 4-24: Experiment vs FEM results of NS5-1.....	217
Figure 4-25: Failure mode of NS5-2	218
Figure 4-26: Failure mode of NS5-2	219
Figure 4-27: Force vs Displacement for shape NS5-2	220
Figure 4-28: Experiment vs FEM results of NS5-2.....	220
Figure 4-29: Failure mode of NS5-3	221
Figure 4-30: Failure mode of NS5-3	222
Figure 4-31: Force vs Displacement of test NS5-3	222
Figure 4-32: Experiment vs FEM results of NS5-3.....	223
Figure 4-33: Force vs Displacement for first tested shape	225
Figure 4-34: Force vs Displacement for Shape NS5	226
Figure 4-35: Force vs Displacement for all tests	226
Figure 5-1: Shape NS-5.....	229
Figure 5-2: Vertical force vs Displacement for NS-5 and U-shaped plate.....	230
Figure 5-3: Two NS-5 shapes parallelly connected	231
Figure 5-4: Horizontal force vs Displacement for NS-5 and U-shape plate under horizontal displacement	231
Figure 5-5: Story drift for U-shape plate and NS-5 (With or without horizontal springs)	232
Figure 5-6: Base shear for U-shape plate and NS-5	232

LIST OF TABLES

Table 3-1: Displacement in X-Direction and Y-Direction	61
Table 3-2: Material properties - ABAQUS	119
Table 3-3: Concrete damage plasticity parameters [39].....	152
Table 3-4: Concrete modeling properties	156
Table 3-5: Steel modeling properties.....	156
Table 3-7: Equivalent Wall member section properties [44].....	169
Table 3-8: Equivalent Column member section properties [44].....	169
Table 3-9: Rigid link member properties [44]	169
Table 3-10: Properties of Compression-Only base spring [44]	170
Table 3-11: Walls and Columns PT spring properties [44].....	170
Table 3-12: Scaled properties of the bi-linear spring representing the U-shaped connector [44]	171
Table 4-1: Test protocol for TS specimens (scaled)	200
Table 4-2: Test protocol of shape NS5	214

ACKNOWLEDGMENTS

I would like to thank Professor Habib Tabatabai for his great efforts, guidance and support in this research. This study could not have been accomplished without his never-ending assistance, brilliant thoughts, and encouragement. I would like to also thank Professor Tabatabai for his advice and counseling throughout the course of this research. I am also grateful for the guidance and help from my committee; Professor Hani Titi, Professor Adeeab Rahman, Professor Konstantin Sobolev, Professor Rami Haweeleh.

I would like to thank my family, especially my father who was the first source of inspiration for me to accomplish this study and the one always believed in me. Also, I am extremely grateful to my mother who never stopped motivating me.

The experimental tests were conducted in in the Structural Engineering laboratory at the University of Wisconsin-Milwaukee (UWM). I am also thankful to Professor Ghorbanpoor who allowed me to use the structural laboratory and the help provided by Mr. Rahim Rashadi. Thanks are also due to all my friends for their unlimited support and encouragement.

I'm also thankful to my supervisors and coworkers who helped me throughout my research and were there whenever I needed them.

Finally, I am grateful for the help that the Department and its faculty offered to me throughout my graduate education.

CHAPTER 1: INTRODUCTION

1.1 Background

Precast concrete systems are used widely in a variety of structures such as parking garages, residential units, shopping centers, transportation stations, etc., when large spans with high clearance are desired. In some cases, precast structures are preferred over conventional Cast-In-Place (CIP) concrete conventional structures due to ease of construction, rapid implementation, and lower levels of energy consumption [1]. Serviceability factors such as reduced shrinkage, deflection, and cracking are additional advantages of such systems. Precast structures also need less finishing work in the field, making them a preferred option by many architects.

One area where precast systems have traditionally been at a disadvantage is high seismic applications. In seismic regions, Precast concrete structures must have enhanced connection systems to address the inherent discontinuity between various components. Designers are increasingly using precast concrete structures in low and mid-rise buildings. Therefore, addressing seismic issues are an important consideration. In a precast building, the lateral load resisting systems consist of shear wall systems, moment frames, or a combination of the two.

There are three main types of walls in precast buildings [1]:

- Solid walls with a typical thickness ranging between 6 and 12-in and typical heights of 10 to 50 ft. [1]
- Sandwich walls with a typical 1.5- to 3-in Wythe thickness and a maximum height of 50ft [1].

- Thin-Shell and Glass Fiber Reinforced Concrete (GFRC) walls. These types of walls have relatively smaller sections [1].

The solid walls are the only practical shear wall systems in lateral load resisting systems of precast buildings, especially in high seismic areas. This is due to the fact that sections with large cross-sectional areas and larger moments of inertia are more desirable in such applications. Also, slenderness requirements should be met for components used in resisting significant seismic or wind loads.

Shearwalls systems are preferred in precast systems in comparison to moment frames when lateral loads are significant. Precast moment frames may require large beam and column sections to achieve sufficient resistance to large lateral loads due to earthquake or wind.

Seismic design approaches are based on resisting lateral loads through a combination of strength and ductility [2]. The desired level of safety during earthquakes are hard to quantify due to the uncertainty related to the earthquake forces [2]. As a result, large member sections may be needed in seismic design when moment frames are used. Therefore, shear walls could be advantageous for use as lateral load resisting system since walls are already present in precast buildings in stairwells, elevator shafts, or ramp walls.

One type of precast shear wall that is widely used in seismic zones is the unbonded post-tensioned split precast shear walls. This type of precast wall is also referred to as “hybrid” because it utilizes mild steel reinforcement for energy dissipation, and high-strength unbonded post-tensioning (PT) tendons. PT reinforcement is used both for lateral load resistance and for

restoring the displaced shear walls after earthquakes [3]. Figure 1-1 shows typical unbonded post-tensioned split precast shear wall.

Over the last couple of decades, researchers have focused on studying and analyzing the behavior of precast structures under severe lateral loads. Numerous works have been done on precast systems and buildings under severe seismic loads. The most prominent of these studies have been conducted under the Precast Seismic Structural Systems (PRESSS) program [4, 7].

Two types of wall construction were studied: emulative and non-emulative. Precast emulative systems are known to behave in the same manner as monolithic conventional concrete structures under lateral loads. On the other hand, the response of non-emulative structures are normally governed by the behavior of joints between precast members that form the lateral load resistance system [3]. Under lateral loads, the gaps developed at joints between lateral resisting members are studied to predict the behavior of non-emulative systems [3]. The unbonded hybrid post-tensioned split precast shear walls are examples of non-emulative lateral load resisting systems.

Special unbonded hybrid posttensioned split precast shear walls have many advantages such as ease of constructability and significant seismic and lateral resistance characteristics [4]. This is due mainly to a self-centering ability where the shearwall could be restored to its original undisplaced position after the high seismic event as well as controlling lateral drift and displacement during seismic events [3].

The Unbonded Hybrid Posttensioned Split Precast shear walls are constructed by stacking rectangular precast panels vertically above the foundation. Fiber reinforced non-shrink dry-

pack grout is used in the horizontal joints between panels for alignment and bearing strength reasons. Post-tensioning tendons are embedded inside ungrouted ducts to avoid any bonding mechanism between concrete and steel strands/tendons. Unbonded tendons are used to reduce the maximum strain in strands below yield and to minimize localized high tensile stresses in concrete under severe lateral loads. As a result, potential for cracks within concrete is reduced and yielding of strands is delayed [3]. Post-tensioning forces and the gravity loads are the main mechanisms for the self-centering of the wall [3].

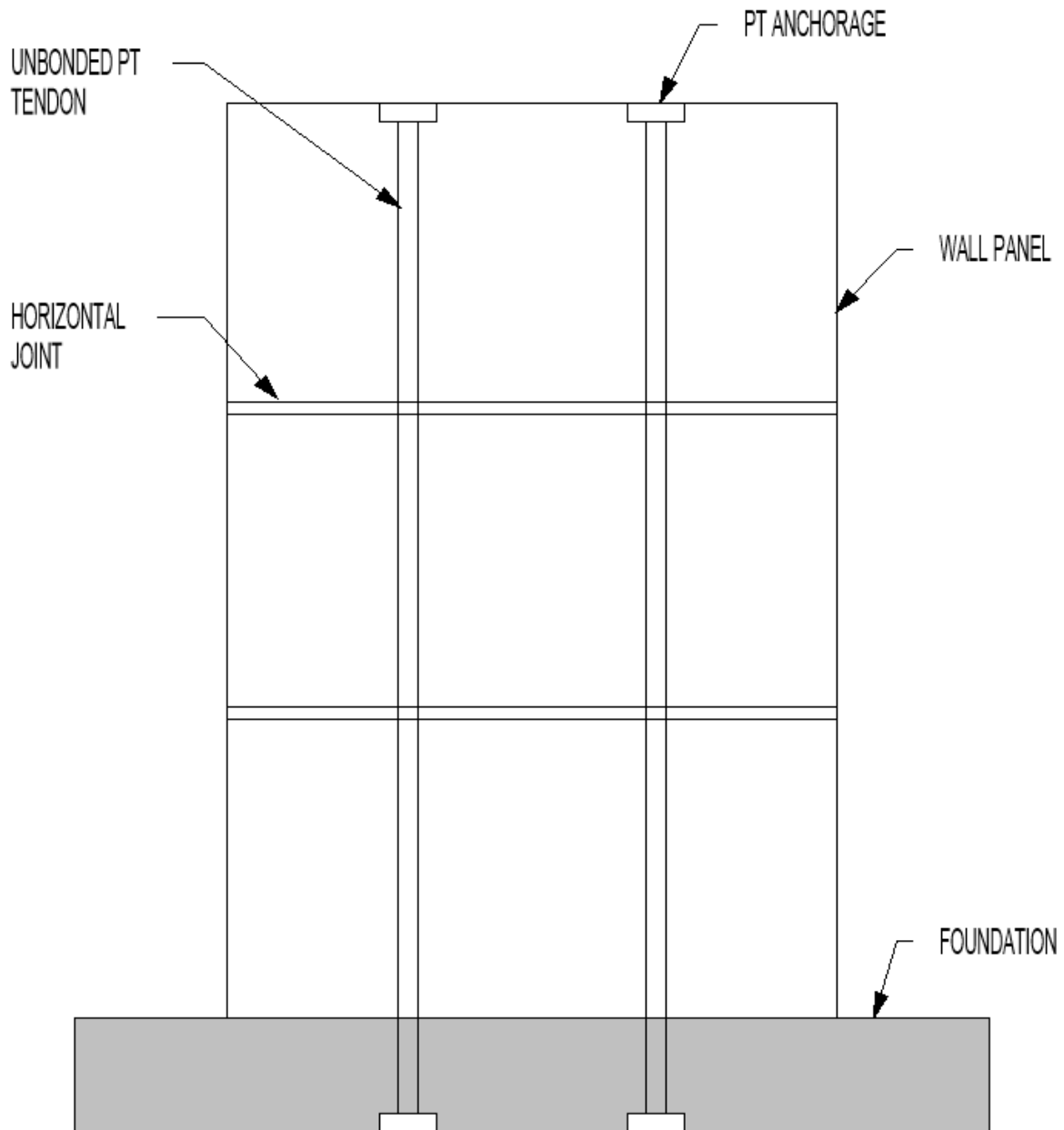


Figure 1-1: Elevation of Special Unbonded Hybrid Posttensioned Split Precast Shearwall [3]

Mild steel that crosses the interface between bottom panel and the foundation plays an important role in dissipating energy by repetitive yielding [3]. Mild reinforcing bars also contain short, unbonded zones along their lengths. This is done to avoid wide cracks or large gap

opening at the bottom of the wall as shown in Figure 1-2. Displacement of this types of walls under lateral loads usually occurs at the bottom of the wall. Thus, the wall has relatively high rigidity, allowing it to tilt over its base or foundation.

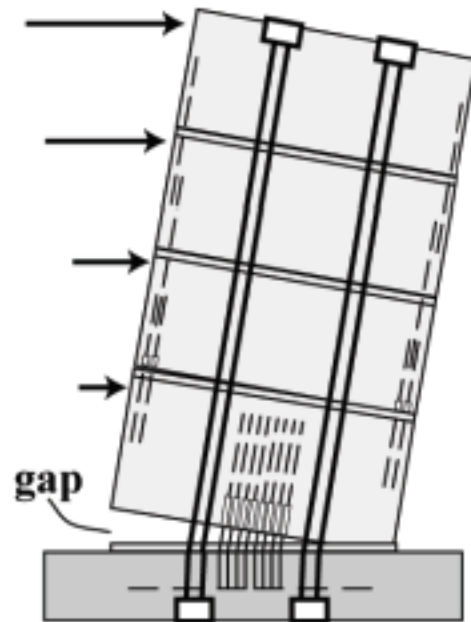


Figure 1-2: Elevation of deflected shearwall [3]

As a result, cracks are expected to appear at the joint between the wall and the foundation. However, cracks are considered narrower than those occurring in a monolithic conventional concrete shear wall [3]. Tendons are usually placed around the center of the wall, to reduce strands elongation and keep tendons outside the wall's critical tension/compression zones at the bottom end corners [3].

Mild steel bars are placed across the joint between the shear wall and foundation (in the center area) with main functions of these bars to improve energy dissipation and low-cycle fatigue.

Precast shear walls could also consist of several panels placed side-by-side when wide shear walls are utilized. In such cases, joints are located vertically along the height between individual shear wall panels. One of most commonly used mechanisms for dissipating energy in vertical joints is U-shaped flexure plate (UFP). Figure 1-3 shows a typical U-shaped flexure plate. This type of connection was first introduced by Kelly et. al [6]. It is basically an energy dissipating connection where the rolling action of the wall segments yields the device and transfer forces between panels. This type of connection along with many other types of energy-dissipating vertical and horizontal joints and mechanisms will be discussed in the next chapter.

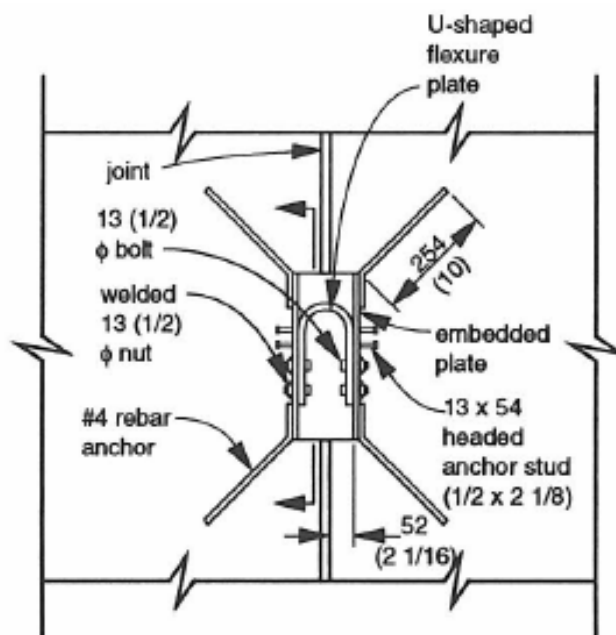


Figure 1-3: Typical U-Shaped flexural plate [5]

There has been increasing interest recently in low-damage seismic resistance systems where the inelastic behavior is concentrated at energy dissipating devices. Those connector devices are preferred to be easy to replace and maintain and low overall cost. Most current connection

devices are not easy to fabricate or to place and are relatively costly. A new connection with high energy-dissipation capability and ease would be needed to meet the ever-increasing seismic design requirements. The key would be to develop an effective shape to maximize energy-dissipation. This thesis is focused on finding optimized energy-dissipating devices for side-by-side wall panels, and other similar structural systems where energy dissipation is needed. In the following chapters, examples of various vertical and horizontal connection systems will be discussed in detail, and a proposed new connection system will be developed.

Energy dissipating devices are required for connecting precast shear walls that are subjected to lateral loads in major seismic events. This type of connection must be designed to develop the required strength under the imposed movements between precast segments. Such devices are essentially designed to yield as a result of relative moment between adjacent wall panels. Therefore, overall deformation of such devices must be studied in detail. Such devices should ideally be low-cost, easy to fabricate, and easy to install during construction of the shear wall panels, and during assembly of the panels. Ultimately, the most efficient devices are those that can dissipate the most energy without excessive transfer of force that could cause damage to the concrete near the connection. They should also be low-maintenance and be able to withstand the loads and deformations associated with major earthquakes. They should serve to improve the structural response with increased energy dissipation, and be replaceable, as needed, after major earthquakes to restore the shear wall to its full capacity.

1.2 Objectives

The primary objective of this research is to develop a new type of energy-dissipating steel connection for use between adjacent shear wall panels in precast buildings (and other similar applications) to maximize energy dissipation through optimized geometry of the device. The new device should fit

within the general physical dimensions of the commonly-used U-shaped flexural plate connectors, adequately transfer forces to the walls without major damage to the reinforced concrete in the vicinity of the connection, and substantially improve energy-dissipation properties when compared to UFP systems. The new device should ideally be relatively low-cost, easy to fabricate and easy to install in the field.

1.3 Scope

In this study, a new type of seismic connection-device for precast shear wall panels is developed. The geometry of the device is optimized by maximizing the dissipated energy through yielding. A topology optimization module within the ABAQUS finite element program was used to develop the geometry and estimate energy dissipation in response of imposed relative displacement cycles between the two sides of the device. The developed device was tested experimentally and evaluated analytically to verify its intended performance. A finite element model of a typical shear wall panel system under later load is generated and analyzed. In addition, a comparison between the proposed suggested device and the commonly-used UFP device is presented to assess the relative effectiveness of the proposed device.

Chapter two of this research will include a literature to discuss previous studies that were conducted in this topic. It will also shed light on the different types of connections that are going to be categorized based on their location such as vertical and horizontal. Third chapter is to discuss the finite element models work done in this study. Moreover, it will show all the shapes that were tried and reasons why were eliminated based and the elimination criteria. Chapter four is a brief of the work plan and guidelines of overall work needs to be done to complete this research. In the fifth chapter of this research, a progress and development of the final shape that is going to be presented. Starting with the methods of optimization that is going to be used as a helpful resource and going through the different

shapes ideas till the final shape is reached and proposed. Lastly chapter six will be about the test of the proposed shape and the analysis and discussion of the results.

CHAPTER 2: Literature Review

2.1 Introduction

Precast structures are being designed and used increasingly over the years for its constructability and rapid erection, characteristic load capacities as well as durability and serviceability features. Many research agencies and organizations around the globe have launched programs to focus on studies that improve precast characteristics pertaining to loads in general and lateral loads in specifics. One of the major programs in the United States is Precast Seismic Structural System (PRESSS). PRESSS is a research program began as a part of the protocol between the United States and Japan. It is one of other three programs under that protocol and the other programs were focusing on steel, concrete and masonry type of structures [7]. Several reasons lead to such program in the United States upon those days such as, the lack of confidence in precast structures to withstand high seismic loads, hesitation to use precast systems due to the lack in tests despite its potential benefits such as rapid erection, lower cost and the aspect of high technology to low labor. Other reasons such as poor knowledge of precast technology, lack of descriptive requirements in design codes, and lastly the poor performance of precast buildings in Eastern Europe under seismic events like 1988 Armenian earthquake [7]. All aforementioned reasons lead to launch PRESSS program to increase the use of precast structures. The main objective of PRESSS program is to develop comprehensive and rational design recommendations and develop new materials, concepts, and technologies for precast construction in different seismic zones [7]. Finally, PRESSS had has three phases; phase I included developing a design concept, classification, and modeling of connections, development of the analytical platform, design recommendations and coordination. Phase II provided detailed experimental and analytical data, that was expelled from phase I, in order to form design recommendations. That basically includes all types of precast lateral resisting systems. Phase III tested five different precast structural systems [4]. Precast shear wall systems were referred to as

Unbonded post-tensioned (PT) wall (Hybrid wall) in PRESS III report (Stanton and Nakaki 2002). This type of walls has an effective damping shear connector along the vertical joint of wall's panels.

According to PRESS final report, this type of shear walls has shown good performance under seismic loads [4], [7].

Precast shear walls have significance lateral resisting characteristics because of their high stiffness and load capacity. In addition to the high inelastic deformation of their connections and energy dissipation [5]. It should be noted that the seismic force and deformation depends on the use of the structure in some applications. For instance, deformation and seismic forces in residential buildings are relatively lower than those in office buildings. The main reason of that is because of architectural restraints in office buildings where walls are less and spans are bigger. Thus walls tend to be slender and wall's aspect ratio, wall height to wall length, larger than two [5].

2.2 Types of horizontal and vertical connections

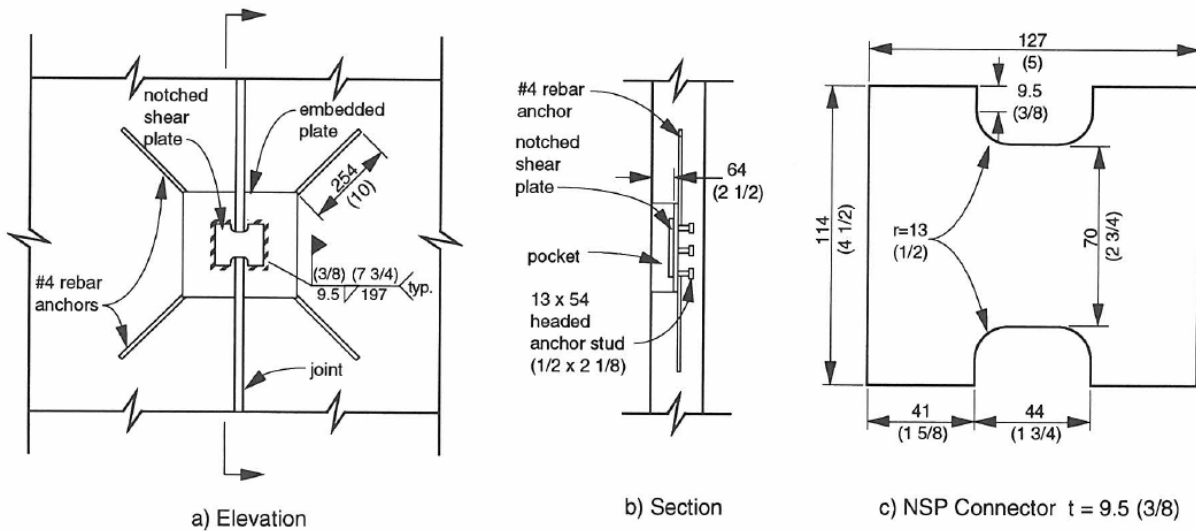
In the University of Nebraska and under PRESS program a study of six-story precast building with slender shearwalls was conducted to test both horizontal and vertical joints between shear wall panels. Rocking type of loading was assumed and also since it is a jointed construction, relative displacement between panels was inevitable. Furthermore, total drift was compared to the relative displacement along vertical joints between panels [5]. Energy dissipation mechanisms were used within the vertical joints between panels to increase wall's toughness and since vertical joints have less impact on walls stability than horizontal joints. Ductility was the main purpose of horizontal joints in order to deform same time as maintaining peak load capacity. Finally, as the second priority of this study is to reduce the damage that could occur on concrete and anchorages. Nevertheless, horizontal connections are used in the precast panel because some code do not allow prestress reinforcement across horizontal joints [13] & [14]. Herein a list and brief description of main horizontal and vertical connections that were tested in aforementioned study [5]:

2.2.1 Vertical connections:

A list of vertical connections is presented as follow:

2.2.1.1 Notched Shear Plate (NSP)

This connection is considered the simplest and most economical connection in this study. Figure 2-1 shows NSP connection details. The notches reduce the connections cross section to assure that it yields in shear rather flexure. Weld was designed to be stronger than the connector. it offered steady force-deformation hysteresis with sufficient energy dissipation similar to those of beams.

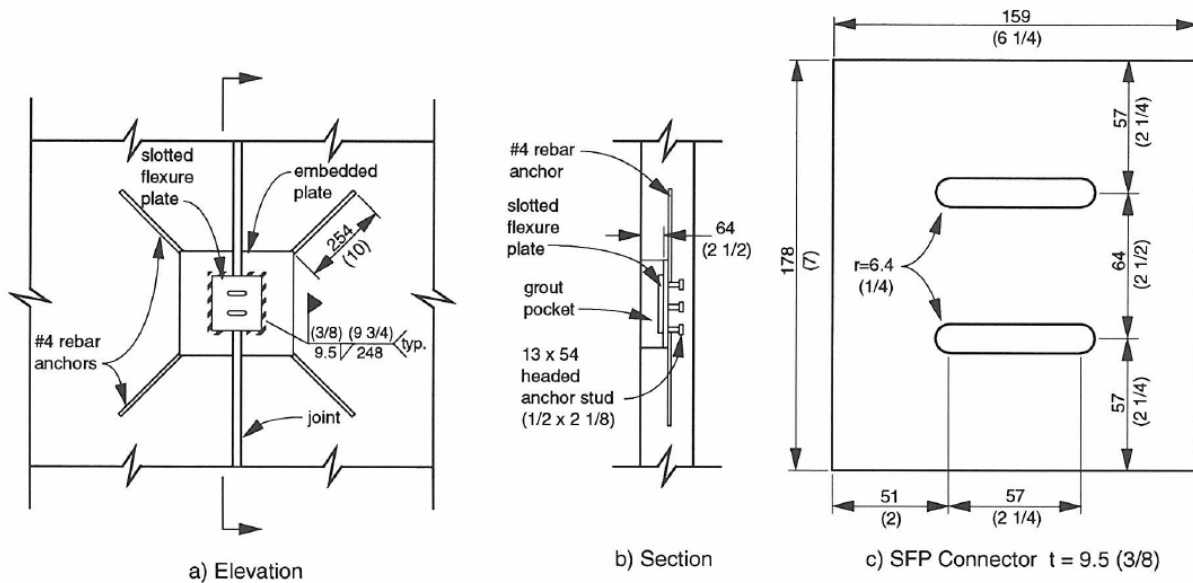


All dimensions are in mm (in.)

Figure 2-1: Detail of NSP Connector [5]

2.2.1.2 Slotted Flexure Plate (SFP)

It is similar to NSP connection but slots are used instead of notches which create three struts that have a slenderer profile than that in the NSP connection. This aspect makes the connector responds to the shear interface mainly in flexure. As a result, it offers higher deformation capacity than NSP. Figure 2-2 shows detail of SFP. it offered steady force-deformation hysteresis with sufficient energy dissipation.



All dimensions are in mm (in.)

Figure 2-2: Details of SFP Connector [5]

2.2.1.3 Inclined Flat Plate (IFP)

Figure 2-3 shows IFP connectors. This type of connectors could be fabricated by welding a flat narrow plate with an angle to the vertical joint axis. It utilizes material efficiently and offers good force/deformation capacity. It was first presented by Stanton et al [8], who suggested that the buckling could be the dominating aspect of this type of connectors. In addition, that the out-of-plane buckling caused strength decreasing and large stress concentration than failure due to low cycle fatigue. It offered moderately steady force-deformation hysteresis with sufficient energy dissipation.

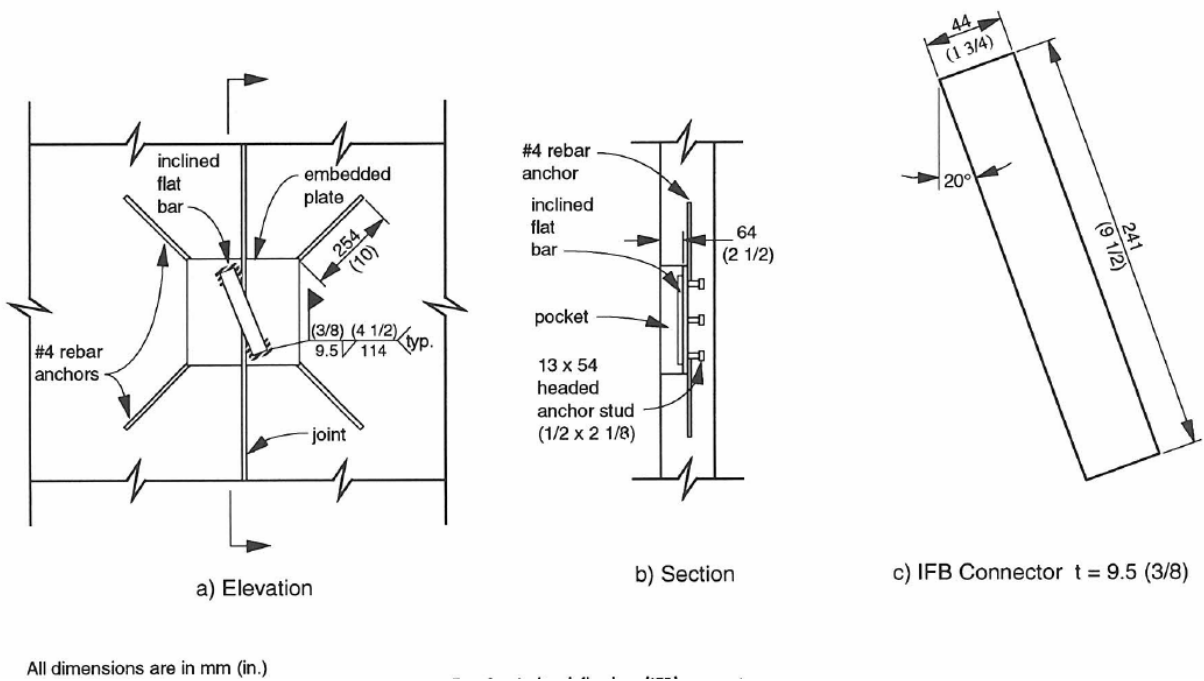
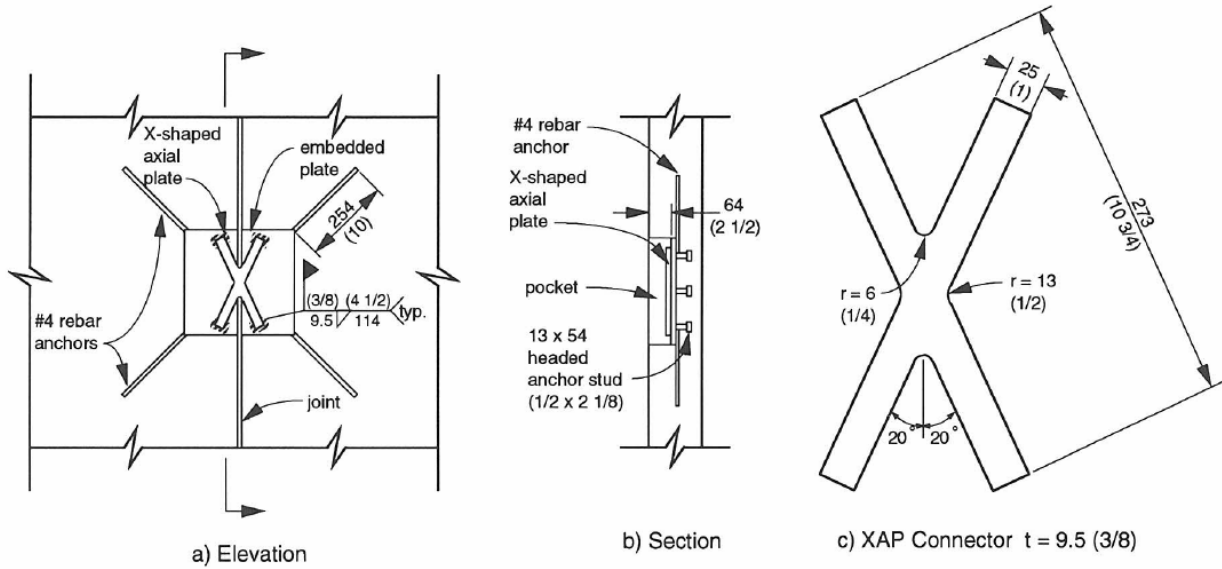


Figure 2-3: Details of IFP Connector [5]

2.2.1.4 X-Shaped Axial Plate (XAP)

It could be considered a modification if aforementioned IFP connector, where across leg was added to enhance the capacity of out-of-plane compression. Figure 2-4 shows details of XAP connector. It should be noted that the intersection region between leg experience uniaxial tension/compression. Also, it should be mentioned that those connectors were installed same panels were used to test the IFP connectors to mimic the case of replacing damaged connectors. In general, XAP connectors presented steady response to the simulated seismic hysteresis and sufficient energy dissipation and no “pinching that affected IFP’s. it should be mentioned that the out-of-plane bending was controlled for most of the test. However, their failure was similar to IFP’s failure pertains to low-cycle fatigue failure.

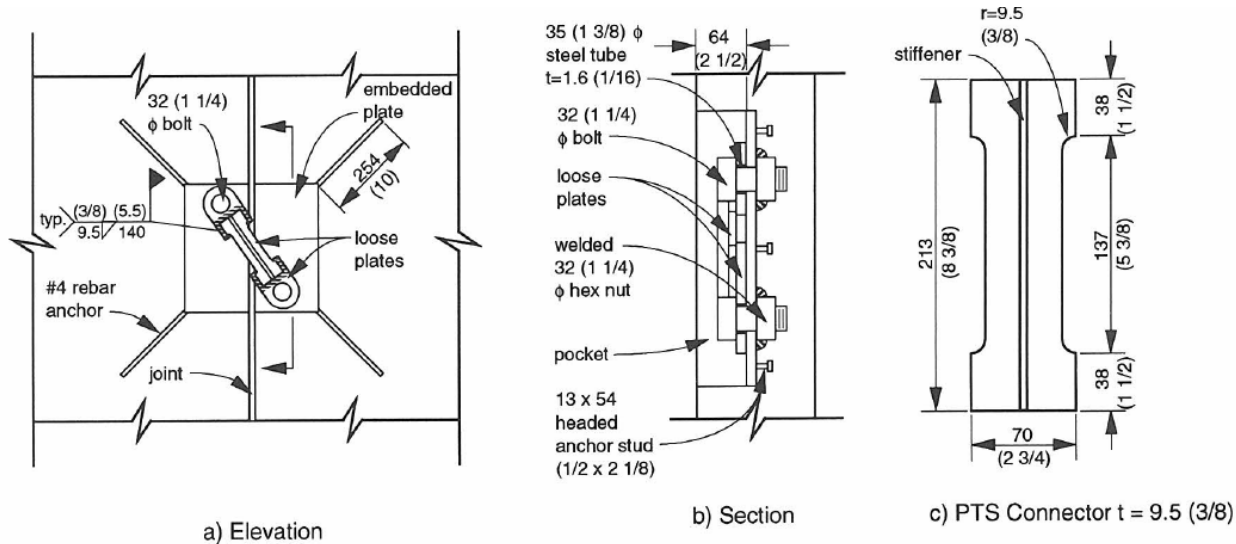


All dimensions are in mm (in.)

Figure 2-4: Details of XAP Connector [5]

2.2.1.5 Pinned Tension Strut (PTS)

PTS connectors could be considered as another model that was intended to improve characteristics of IFP connectors. That was achieved by enhancing the tendency of out-of-plane bending/buckling and the flexural demands. Furthermore, the bolts in PTS were used as the primary field connection and welds were added just ensure sufficient tolerance which makes this type of connection feasible to replace after an earthquake event. The results confirmed the improvement over IFP connectors. It exhibited higher compression strength and lower tension stiffness than IFP's due to the flexibility in the bolted connection. The model failure was premature and due to failure of one of the rebar caused by rotation of one of the anchor plates. However, it was noted that the connector yielded same time as the rebar anchor failed. Ultimately, the pinching in PTS connectors have significantly limited its energy dissipation capacity. Figure 2-5 shows PTS connectors.

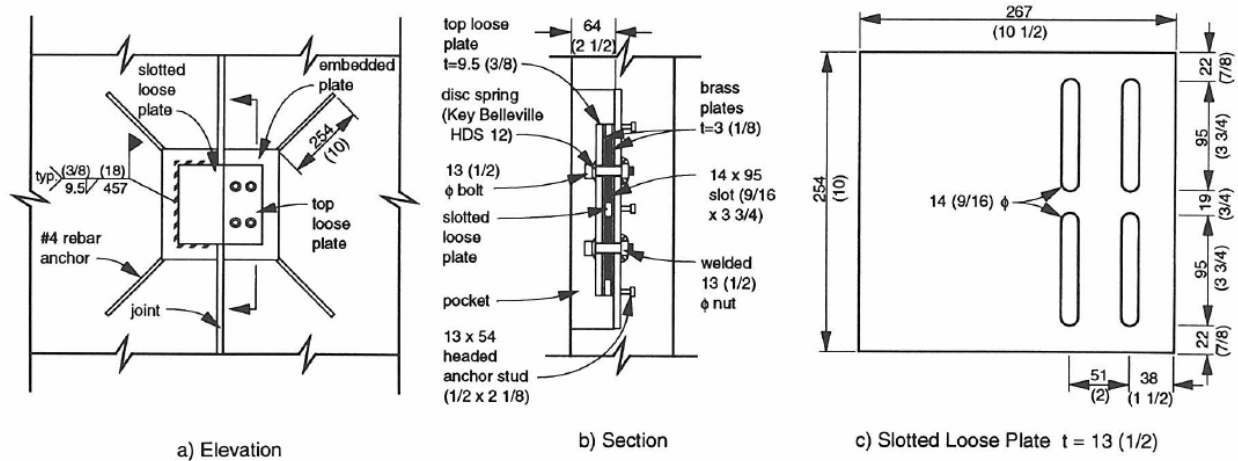


All dimensions are in mm (in.)

Figure 2-5: Details of PTS Connectors [5]

2.2.1.6 Vertical Joint Friction (VJF)

This type of connectors is proposed for cases when the large displacement is expected and as a result, a large capacity is required. It utilizes field bolting and it is a version of slotted, bolted friction connection proposed by Grigorian et al. [9]. In this instance, the connection was designed to transfer shear rather than axial and there was eccentricity between shear planes. Figure 2-6 shows details of VJF connectors. It exhibited elastoplastic behavior nearly steady capacity over the entire range of displacement in addition to unmatched energy dissipation. Nevertheless, towards the end of the test, one of the bolts hit its slot which caused premature failure in one of the rebar anchors. As a result, the test was terminated while the connector was far from a failure. Ultimately, VJF exhibited energy dissipation almost three times of that for SFP and XAP connectors due to the large deformation capacity and the elastoplastic behavior.

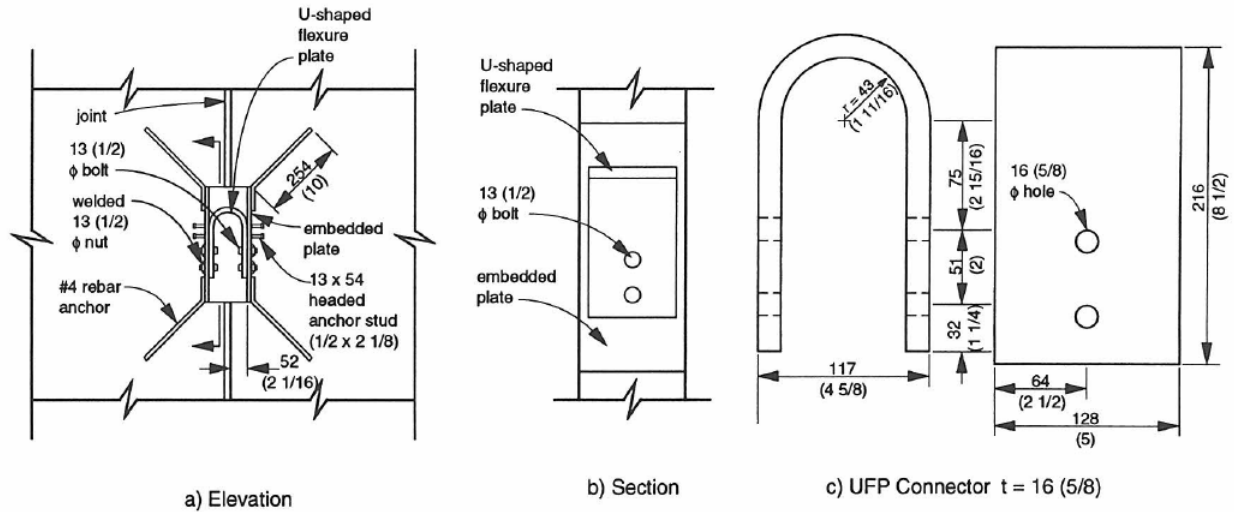


All dimensions are in mm (in.)

Figure 2-6: Details of VJF Connectors [5]

2.2.1.7 U-Shaped Flexure Plate (UFP)

UFP connector details is shown in Figure 2-7. It is a bolted type connection that is proposed for high deformation cases. It was first proposed by Kelly et al. [6]. The idea of this type of connectors are basically rely on resisting the vertical shear force by rolling bending action in the connector due to the energy dissipation. UFP has minimal resistance to in-plane movement which makes it suitable for locations where control points are required. Also, its deformation capacity, similar to VJF connectors, is governed by strain capacity and that makes its geometry the main constraint on vertical displacement. It exhibited high steady response to lateral loads with sufficient energy dissipation capacity. Force-displacement loops showed hysteresis over the entire range of proposed drift and that because of nature of rolling, bending action and localized yielding. However, UFP did not show signs of global yielding. It should be mentioned that this type of connectors exhibited energy dissipation as much as two times of that for SFP and XAP details.



All dimensions are in mm (in.)

Figure 2-7: Details of UFP Connectors [5]

2.2.2 Horizontal connections

Tested horizontal connections are listed below:

2.2.2.1 Grouted Splice Sleeve (GSS)

It is a simple detail that is used widely in precast industry. It basically includes vertical rebars spliced in proprietary sleeves and grout. By doing so, rebars are crossing the horizontal joints and allowing rebars to yield and form a plastic hinge under lateral loads. It should be noted, that rebar should be debonded for a certain length of rebar below the joint to increase the part of rebars that could be yielded and plastically deformed which increase the energy dissipation. Also, debonding helps to prevent cracks in the precast panels at the location of GSS rebars. Figure 2-8 shows details of GSS type of connection.

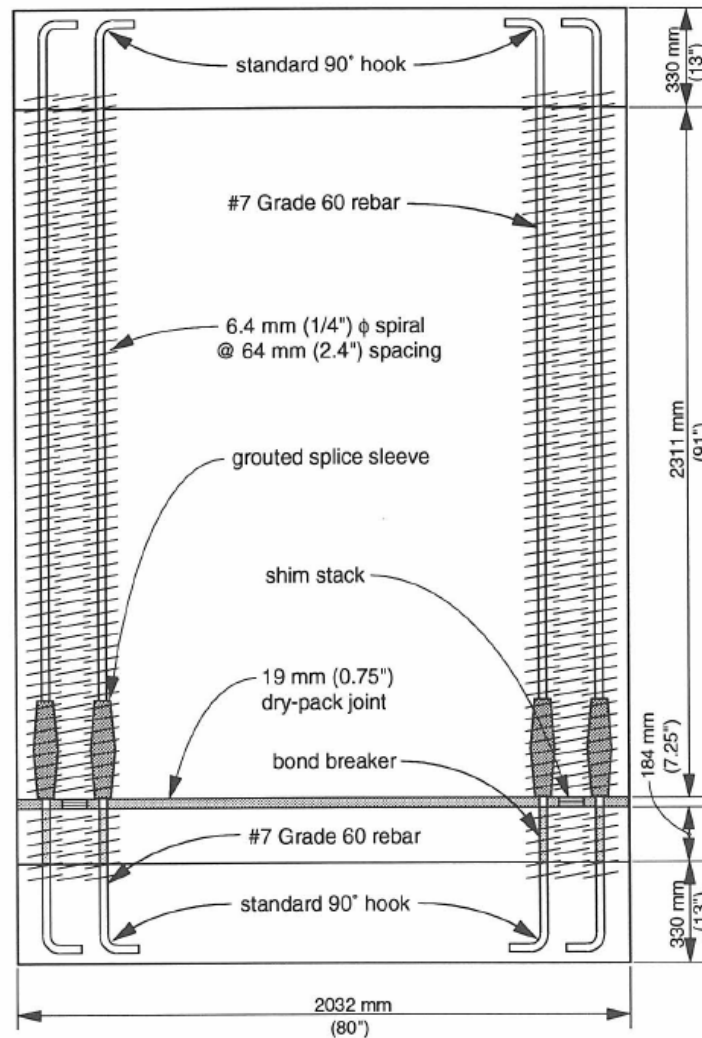


Figure 2-8: Details of GSS Connectors [5]

2.2.2.2 Post-Tensioned Tendon (PTT)

Figure 2-9 shows details of PTT type of connections. There is no grout in the pocket of PTT connections to keep the tendons unbonded so this help protecting the tendons from inelastic strains which could reduce the prestress in the panel. Such connections are used when the panel gravity stress is low where tendons play a role of vertical reinforcement and spliced using standard couplers. Energy dissipation is not high but debonding of the tendons allow panel to undergo high inelastic displacement. Lateral loads

are transferred by flexure across horizontal joints. Prestressing strands could be used and it allows higher linear strain capacity than that of bars, yet bars are used due to the simplicity of placement. Uniformly spaced tendons are a dual functioning of performance-based strategy that needed to protect tendons from large straining due to rocking and the construction-based demand that's required to provide vertical reinforcement for placement of the panel and also to minimize out-of-plane sliding as the panel shakes.

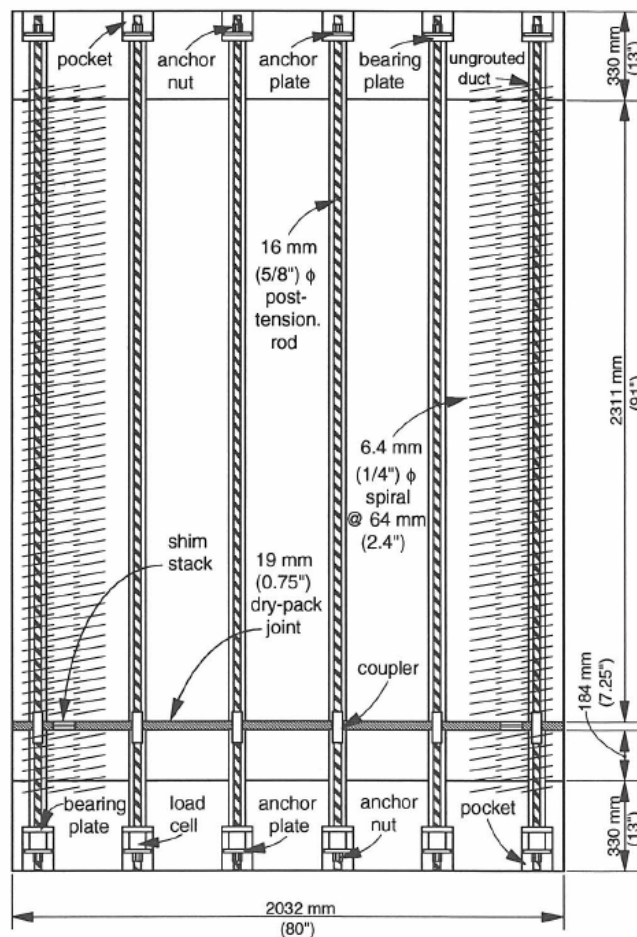


Figure 2-9: Details of PTT Connectors [5]

2.2.2.3 Precast Vertical Joint (PVJ)

Figure 2-10 shows the PVJ connection. It utilizes two horizontal joints that are attached by grouted splices sleeves similar to those in GSS connection. However, the unique aspect of this connection is the clever mechanism that is used to utilize the energy dissipation in a panel at certain vertical control points. PVJ connection could be constructed by forming a v-shaped groove in the panel and precast it. The effective thickness of the panel at the groove location depends on the expected peak shear force (design force). When cracks propagate, the shear reinforcement along the horizontal joint prevents the separation of the wall. In addition to, sliding of the panels helps energy dissipation and create vertical shear resistance.

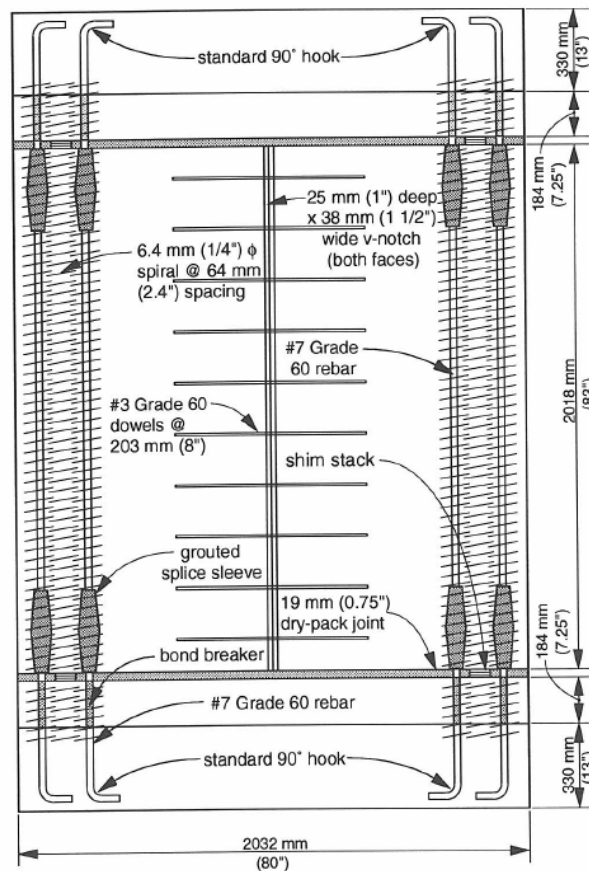


Figure 2-10: Details of PVJ Connector [5]

2.2.2.4 Debonded Smooth Bar (DSB)

In this type of connections, a smooth hot-rolled bar created from mild structural steel (grade 50) is used as vertical reinforcement, as shown in Figure 2-11. Those bars, in fact, are debonded from the panel for a portion of their length. The reason in that is to maximize the amount of yielded steel during lateral load application. In its turn, the latter helps to maximize the amount of energy that could be dissipated. Also, a proprietary coupling system is used to splice the smooth bars to the deformed reinforcement bars. Ultimately, high-strength and high flow grout are used to fill the ducts and plastic sheathing is applied to ensure debonding of the lower part of the smooth bars.

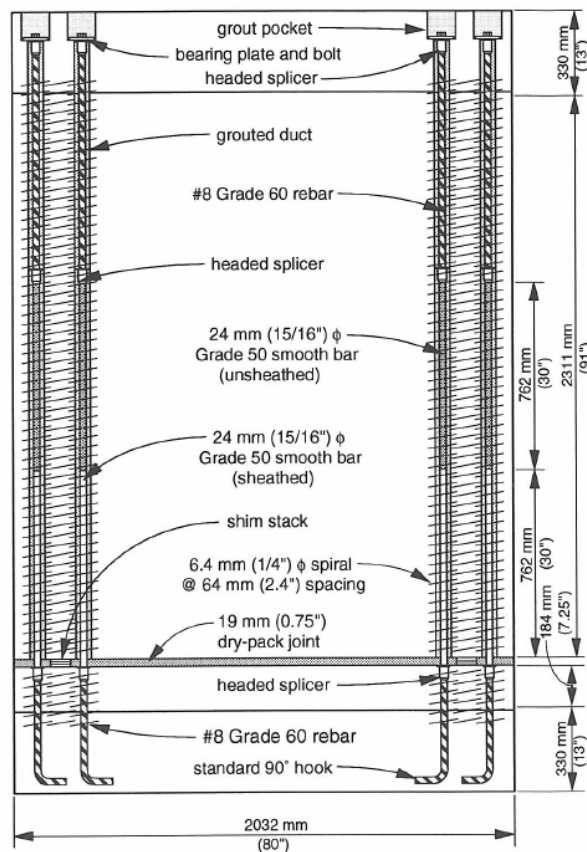


Figure 2-11: Details of DSB Connection [5]

Shultz and Magna [5] summarizes their study that it's possible to design yielding plates in different layout and configurations using the current design methodologies. Also, VJF and UFP have exhibited significant capability to resist lateral loads over large displacement range. VJF connectors hold almost elastoplastic behavior. Therefore, VJF and UPF are the best choices for high-seismic regions. No results were presented for horizontal joints. All four horizontal joints are suitable to be used and the main factor in choosing the type of horizontal connections is the structural performance for seismic resistance and materials availability.

2.3 Previous Studies

Several types of research have conducted extensive studies on precast shear walls under lateral loads. PRESSS have issued in their report [10] a procedure to design Unbonded Posttensioned Split Precast Shear Walls, along with recommendations and analytical data. A description and discussion of some studies that focused on Unbonded Posttensioned Split Precast Shear Walls will be presented next:

2.3.1 Stanton, J. F., and Nakaki, S. D [10]

This report is part of phase III of PRESSS test. As mentioned in the previous chapter, PRESSS research included three phases while in phase I consisted of developing conceptual basics. Phase II included design connections and conduct laboratory tests on those connections. Finally, phase III included a real-life test on a building that was designed and tested using the findings of phase I and phase II. The test was conducted on a building that is 60% of a full-scale building. It was a five-story building and two bay wide and two bay long. Figure 2-12 shows a layout of the building that was used in this study [10]. The building was designed to include some original aspects such as, deformation was designed to be in the connections similar to most precast concrete buildings, which means minimizing the overall damage. Also, the building was designed in a way that after the earthquake, the building experience zero residual

drift. Ultimately, no new materials nor new technologies were used, which increased their level of acceptance.

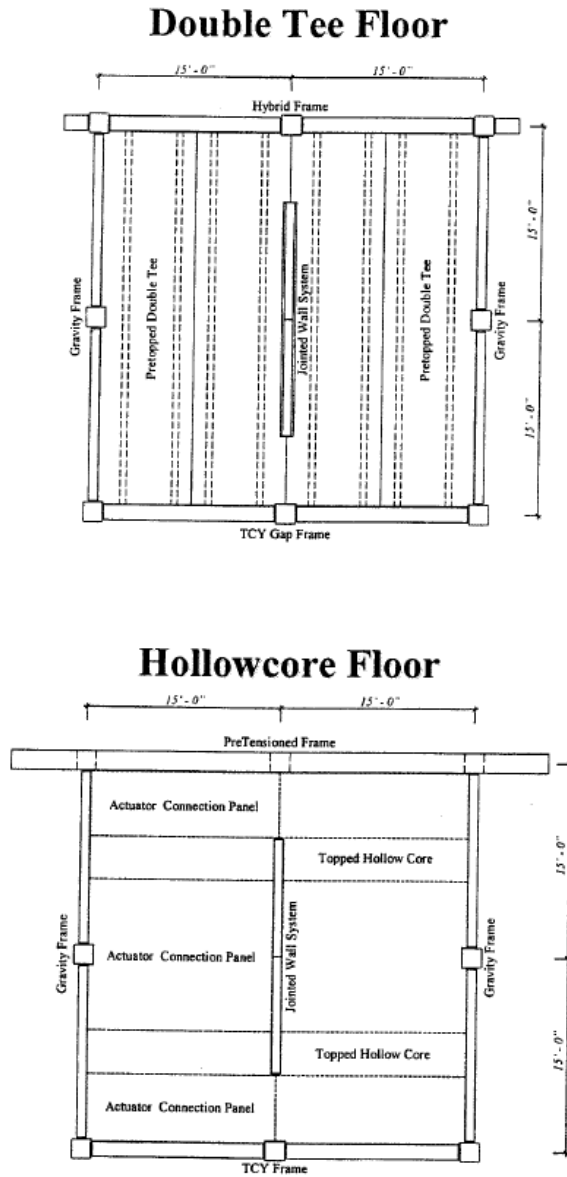


Figure 2-12: layout of PRESSS phase III test building [10]

It noteworthy that the procedure that was used to design the tested building for later load is Displacement-Based Design method. In which, a targeted displacement is set, then required stiffness is calculated and subsequently lateral load resistant system is designed. Figure 2-13 shows the relationship between the drift and the ratio of yielding reinforcement to total moment. The main design philosophy

that was used in designed the Unbonded post-tensioned split wall is to keep the residual drift equal zero. to do so, the strength due to yielding reinforcement have to be limited to approximately half of total moment resistance and the dashed line in Figure 2-13 refers to that method. The larger the ratio of yielding reinforcement to total moment reinforcement the more possible to have residual drift.

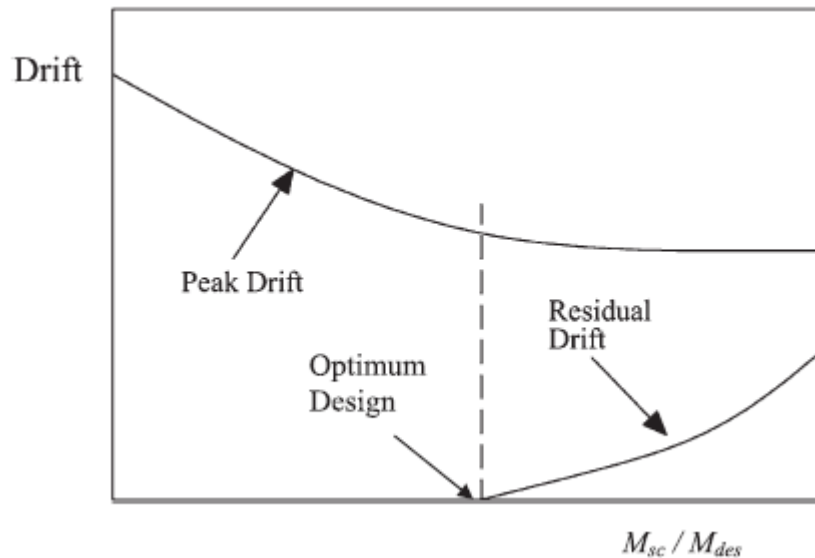


Figure 2-13: Drift versus strength of resisting members [10]

Unbonded post-tensioned split shear wall was designed and tested in this study. U-shaped flexure plates were provided as vertical connectors and unbonded post-tensioning tendons were provided as horizontal connectors. As mentioned previously, post-tension strand should stay elastic while the shear connectors deform inelastically. This system has unique characteristic features that make it different from cast-in-place concrete walls:

- 1- This system of shear panels undergoes a displacement that resulted from rocking the panels, which means less displacement due to shear or moment and less damage at the base comparing to fixed-end walls.

- 2- Panel dimensions (aspect ratio) are chosen in a way that makes them rock instead of sliding which increases the drift capacity.
- 3- Two different types of systems where one of them resist providing damping (shear connectors) and the other provide elastic restoring (post-tension tendons).

During earthquake event, some parts of the shear connector plate (UFP) responds inelastically as they bend and that is how this plate dissipate energy. Also, the geometry of the system governs the shear displacement. In addition, it should be noted that the rocking cause cracks at the base of the panel and might also lead to reinforcement buckling.

PRESSS report also had listed assumptions that were made to develop the design equations:

- 1- Design drift and forces are known where they could be calculated using Force Based Design procedure or Displacement Based design procedure.
- 2- Wall dimensions are known, which they could be suggested by designers or architectures.
- 3- Panels have same exact dimensions.
- 4- Shear connectors must be considered rigid-plastic for sake of simplicity. They would need more complicated procedure if they were to assume elastoplastic.
- 5- At the design drift, post-tensioning tendons should be at the primary stage of yielding. However, a lower value of tension could be used in the equation that follows that stage.
- 6- Materials' properties and strengths must be known.

The design procedure included ten lengthy step which leads researchers [4] to develop shorter procedures satisfy the assumption listed above. The final procedure was iterative and included the following steps [10]:

- 1- Establish material properties
- 2- Obtain design loads and drifts.

- 3- Select the number of panels.
- 4- Establish constants such as panel length, panel self-weight, design moment, the total dead load on the wall, wall's compression capacity, the net shear force on the panel and the increase in tension force in tendons between zero and design drift.
- 5- Select reinforcement like Prestressing area, tendons force, and total yield force of shear connectors.
- 6- Establish conditions at base of panels immediately as they experience displacement (after lift-off at the base).
- 7- Establish conditions at design load and drift.
- 8- Calculate design moment of wall panels.
- 9- Calculate resisting moment.
- 10- Check acceptance criteria.

Most importantly here for this research is the design procedure of UFP shear connectors. According to PRESS report and phase III recommendation, any connectors that provide enough ductility, strength and displacement capacity could be used to connect shear wall panels. As mentioned earlier, UFP is one good example of such connectors. Figure 2-14 shows UFP connector. This connector includes a flat plate mounted to each panel and one bent plate that is connected to those plates. Usually, the design of UFP depends on number of connectors, plate dimensions, size of plates, radius of bend and finally material properties which make the design procedure more like trial and error design procedure. If the moment from free body diagram shown in Figure 2-14 was to be calculated, then:

$$V_{sc} D_{sc} = 2M_{sc} \dots \dots \dots (1)$$

M_{sc} is the plastic moment capacity of the plate which could be calculated as follow:

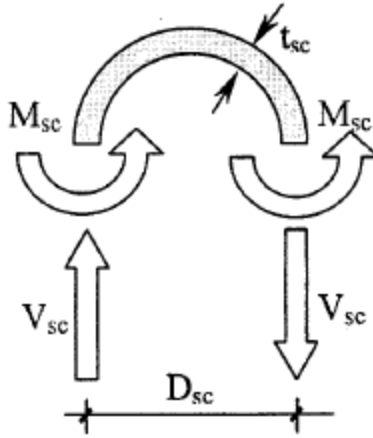


Figure 2-14: UFP connector Free body diagram [10]

$$M_{sc} = \left(\frac{b_{sc} t_{sc}^2}{4} \right) f_{sc,des} \dots \dots \dots (2)$$

Where $f_{sc,des}$ = plastic stress of plate including strain-hardening. Strain due to bending of plate could be calculated using:

$$\epsilon_{sc,des} = \frac{t_{sc}}{D_{sc}} \dots \dots \dots (3)$$

Using equations (1) and (3) to solve for (Versus) yields:

$$V_{sc} = \left(\frac{b_{sc} t_{sc}^2}{4} \right) (f_{sc,des} \epsilon_{sc,des}) \dots \dots \dots (4)$$

Number of required shear connectors then could be calculated from:

$$n_{sc} = \frac{F_{sc}}{V_{sc}} \dots \dots \dots (5)$$

A limit for $(\epsilon_{sc,des})$ could be setup based on number of bending cycles without damaging the plate which also relies on ground motion. Due to lack in certainty when it comes to ground motion, $(\epsilon_{sc,des})$ is taken with respect to the strain in materials corresponding to maximum stress and as follow:

$$\varepsilon_{sc,max} = \frac{\varepsilon_{sc,u}}{3} \dots \dots \dots (6)$$

In order to stretch the plate from no strain condition to maximum strain ($\varepsilon_{sc,max}$), the value of (Versus_c) in equation (4) becomes about one-half the work done to do that. As a result, the shear capacity depends on material toughness more than strength.

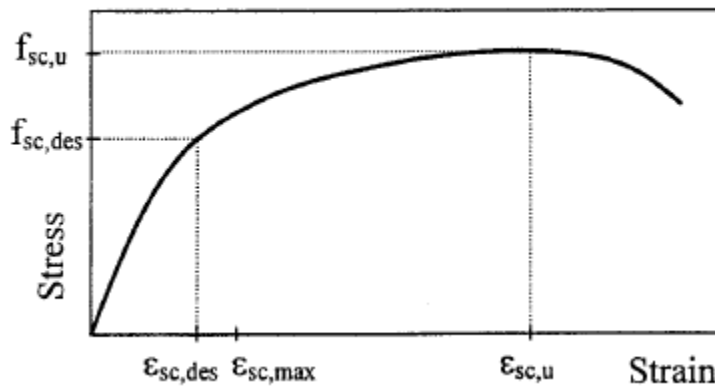


Figure 2-15: Critical stress and strain in UFP material [10]

Ultimately, according to Magna and Schultz [5], ASTM 36 was found to be cracked under a stress corresponding to 15% strain. Therefore, ASTM 240 type 304 stainless steel was used in Magna and Shultz study and in PRESSS phase III for UFP where no crack reported for the stainless steel.

2.3.2 E. I., Saqan and R. A Haweeleh [11]

Saqan and Haweeleh used same concepts that were used in PRESSS phase III study to come up with non-dimensional design charts to replace the lengthy iterative procedure that was proposed in PRESSS Report No. 01/03-09 and Report No. SM02-02. Main objective as mentioned previously is to develop non-dimensional parameters and charts to ease the design process and replace PRESSS trial and error procedure, minimizing overall drift and maintaining zero drift by conducting parametric studies on non-dimensional formulation of PRESSS design procedure, creating non-dimensional design charts and perform a comparison between PRESSS design procedure and the new design procedure. Shearwalls in

buildings could consist a number of panels that are stacked horizontally and vertically. Saqan and Haweeleh stated that only first panel, last panel, and middle panel matter in the design, so if a wall, for example, and as shown in Figure 2-16, includes four panels, the middle two panels are going similar to each other. Also, it should be noted that, similar to PRESSS requirements, all panels should be of same dimensions. Figure 2-17 presents a free body diagram of panels subjected to seismic forces under design drift.

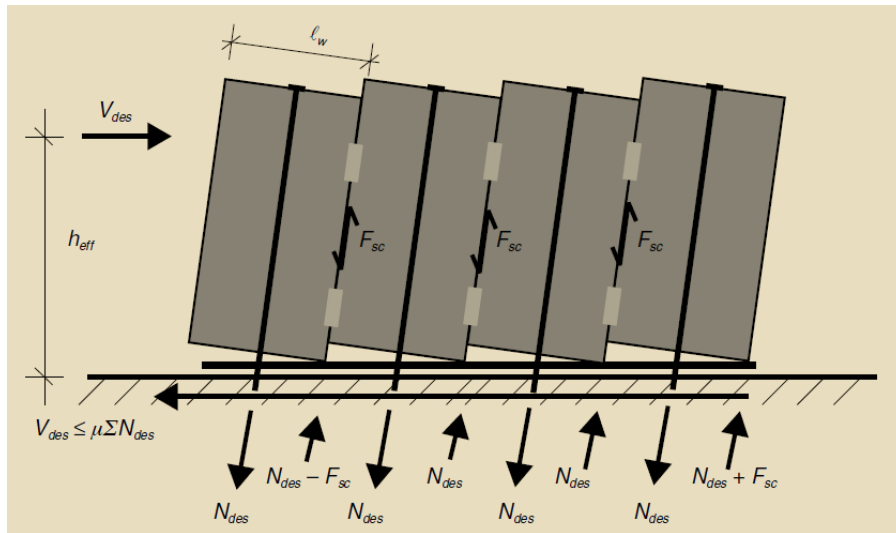


Figure 2-16: Shearwall consists of four panels under design drift [11]

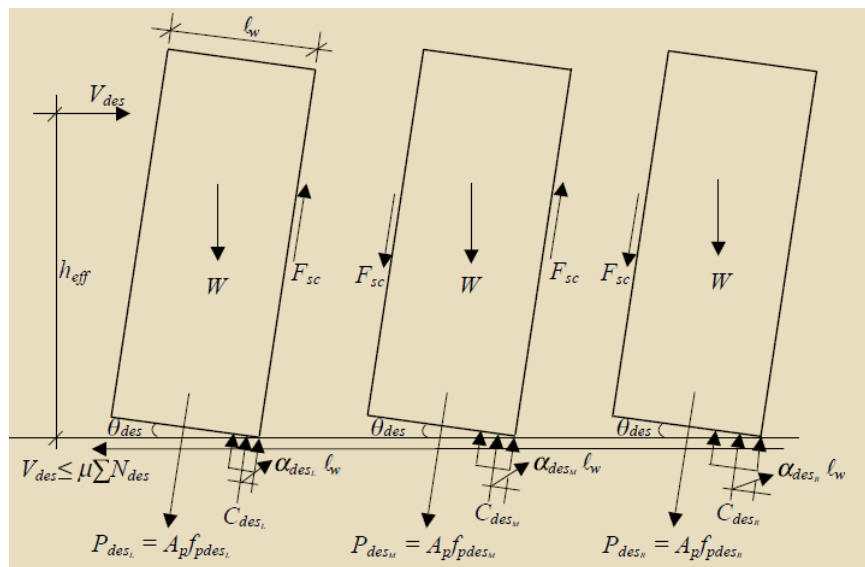


Figure 2-17: Shearwall panels subjected to seismic force [11]

As shown in Figure 2-17, first step in the design procedure is to calculate the compression reaction at the base of wall panel:

$$C_{des} = P_{des} + W + F_{SCL} - F_{SCR} \dots \dots \dots (7)$$

Due to an assumption that shear forces at the sides of panels are equals:

$$F_{SCL} - F_{SCR} = 0$$

However, different shear connector capacities could be used. Using equilibrium of forces yields to:

$$C_{des} = k_1 f'_g (2\alpha_{des} \ell_w) t_w \dots \dots \dots (8)$$

Where k_1 is uniform stress in Whitney stress block divided by the smaller of compressive strength of grout or wall concrete (f'_g), (α_{des}) is the distance between the center of compressive reaction to wall edge, (ℓ_w) and (t_w) are length and thickness of wall panel respectively.

Also,

$$\alpha_{des} = \frac{0.5C_{des}}{k_1 f'_g \ell_w t_w} = \frac{0.5(P_{des} + W + F_{SCL} - F_{SCR})}{k_1 f'_g \ell_w t_w} \dots \dots \dots (9)$$

Hence, moment capacity of each panel could be calculated using:

$$M_{Cap,Panel} = \ell_w (C_{des} (0.5 - \alpha_{des}) + 0.5(F_{SCL} + F_{SCR})) \dots \dots \dots (10)$$

Finally, the total moment capacity resisted by all panels is:

$$M_{Cap,Wall} = M_{Cap,Panel} \dots \dots \dots (11)$$

As described previously, middle wall panels have similar parameters (C_{des} and α_{des}), therefore three sets of design equations were presented in Saqan and Haweeleh research; one of leading (right) panel, one for rear (left) panel and one represents middle panel (s). Derivation of left panel equations is as follow:

First, non-dimensional parameter is the ratio of wall panel's height to length [11]:

$$\phi 1 = \frac{h_w}{\ell_w} \dots \dots \dots (12)$$

The effective height of wall panel could be calculated by dividing the design moment by shear [11]:

$$h_{eff} = \frac{M_{des}}{V_{des}} \dots \dots \dots (13)$$

Then, the ratio of effective Height to shear wall length could be calculated as follow [11]:

$$\phi_2 = \frac{h_{eff}}{\ell_w} \dots \dots \dots (14)$$

Subsequently the following parameters could be found using wall panel's parameters and force of shear connectors [11]:

$$\rho_1 = \frac{A_p}{\ell_w t_w} \dots \dots \dots (15)$$

$$\rho_2 = \frac{F_{sc}}{\ell_w t_w f'_g} \dots \dots \dots (16)$$

$$\Omega = \frac{h_w (\gamma_c + \gamma_L)}{f'_g} \dots \dots \dots (17)$$

Where (γ_L) is calculated by dividing the distributed vertical weight of the floor by the multiplication product of wall panel's height and thickness as shown in Eq. 18 [11] below, and (γ_c) is concrete unit weight.

$$\gamma_L = \frac{W_{floor}}{h_w t_w} \dots \dots \dots (18)$$

The ratio of the stress post-tensioning reinforcement after zero losses to the smaller of compressive strength of grout or wall concrete and ratio of stress in post-tensioning reinforcement in left panel to the smaller of compressive strength of grout or wall concrete are calculated as follow [11]:

$$\psi_o = \frac{f_{po}}{f'_g} \dots \dots \dots (19)$$

$$\psi_L = \frac{f_{p,desL}}{f'_g} \dots \dots \dots (20)$$

From Eq. (9):

$$\alpha_{des} = 0.5 \frac{(A_p f_{p,desL} + t_w \ell_w h_w (\gamma_c + \gamma_L) - F_{SC})}{k_1 f'_g \ell_w t_w} \dots \dots \dots (21)$$

Substituting parameters calculated in equations 15-20 in Eq. 21 [11]:

$$\alpha_{desL} = \frac{0.5}{k_1} (\rho_1 \psi_L + \Omega - \rho_2) \dots \dots \dots (22)$$

The distance between panel's compression face and its neutral axis at the required design drift is [11]:

$$\eta_{desL} = 2 \frac{\alpha_{desL}}{\beta_1} = \frac{0.5}{k_1 \beta_1} (\rho_1 \psi_L + \Omega - \rho_2) \dots \dots \dots (23)$$

Where (β_1) is the depth of equivalent compressive stress block divided by the neutral axis depth.

Post-tensioning tendons elongation (Δ_{PL}) at the design drift is [11]:

$$\Delta_{PL} = \theta_{des} \ell_w (0.5 - \eta_{desL}) \dots \dots \dots (24)$$

Where (θ_{des}) is the rotation of panel as limit state.

Based on that, the increase or change in stress in post-tensioning reinforcement is [11]:

$$\Delta f_{PL} = E_p \frac{\Delta_{PL}}{h_w} = E_p \left(\frac{\theta_{des} \ell_w}{h_w} \right) (0.5 - \eta_{desL}) \dots \dots \dots (25)$$

Where (E_p) is modulus of elasticity of post-tensioning strands. Substituting the non-dimensional parameters that already been calculated in Eq.23 yields [11]:

$$\Delta f_{PL} = E_p \frac{\theta_{des}}{\theta_1} \left[0.5 - \left(\frac{\rho_1 \psi_L + \Omega - \rho_2}{k_1 \beta_1} \right) \right] \dots \dots \dots (26)$$

Total stress in post-tensioning tendons is shown in Eq.27, and it should be less than (f_{py}) [11]:

$$f_{p,desL} = (f_o + \Delta f_{pL}) \dots \dots \dots (27)$$

Substituting the non-dimensional parameters found before in Eq.25 [11]:

$$\begin{aligned} \Delta f_{pL} &= f_{p,desL} - f_o = \Psi_L f'_g - f_o \\ &= E_p \frac{\theta_{des}}{\theta_1} \left[0.5 - \left(\frac{\rho_1 \Psi_L + \Omega - \rho_2}{k_1 \beta_1} \right) \right] \dots \dots \dots (28) \end{aligned}$$

Solving for (Ψ_L) [11]:

$$\psi_L = \frac{f_{po} + \frac{E_p \theta_{des}}{k_1 \beta_1 \theta_1} (0.5 k_1 \beta_1 - \Omega + \rho_2)}{f'_g + \left(\frac{E_p \theta_{des}}{k_1 \beta_1 \theta_1} \right) \rho_1} \dots \dots \dots (29)$$

To calculate the compressive reaction in a form of non-dimensional parameters, substitute Eq.22 into Eq.8 [11]:

$$C_{desL} = \ell_w t_w f'_g (\rho_1 \Psi_L + \Omega - \rho_2) \dots \dots \dots (30)$$

Lastly, moment capacity could be calculated using non-dimensional parameters [11]:

$$M_{capL} = \frac{\ell_w^2 t_w f'_g}{2} \left[\rho_1 \Psi_L + \Omega - \frac{1}{k_1} (\rho_1 \Psi_L + \Omega - \rho_2)^2 \right] \dots \dots \dots (31)$$

Seemingly, non-dimensional parameters were derived for interior and leading panels. The following equations are for the leading (right) panel [11]:

$$\alpha_{desR} = \frac{0.5}{k_1} (\rho_1 \Psi_R + \Omega + \rho_2) \dots \dots \dots (32)$$

$$\psi_R = \frac{f_{po} + \frac{E_p \theta_{des}}{k_1 \beta_1 \theta_1} (0.5 k_1 \beta_1 - \Omega - \rho_2)}{f'_g + \left(\frac{E_p \theta_{des}}{k_1 \beta_1 \theta_1} \right) \rho_1} \dots \dots \dots (33)$$

$$C_{desR} = \ell_w t_w f'_g (\rho_1 \Psi_L + \Omega + \rho_2) \dots \dots \dots (34)$$

$$M_{CapR} = \frac{\ell_w^2 t_w f'_g}{2} \left[\rho_1 \psi_R + \Omega + 2\rho_2 - \frac{1}{k_1} (\rho_1 \psi_R + \Omega + \rho_2)^2 \right] \dots \dots \dots (35)$$

Ultimately, middle panel(s) equations are [11]:

$$\alpha_{desM} = \frac{0.5}{k_1} (\rho_1 \psi_M + \Omega) \dots \dots \dots (36)$$

$$\psi_M = \frac{f_{po} + \frac{E_p \theta_{des}}{k_1 \beta_1 \theta_1} (0.5 k_1 \beta_1 - \Omega)}{f'_g + \left(\frac{E_p \theta_{des}}{k_1 \beta_1 \theta_1} \right) \rho_1} \dots \dots \dots (37)$$

$$C_{desM} = \ell_w t_w f'_g (\rho_1 \psi_M + \Omega) \dots \dots \dots (38)$$

$$M_{CapM} = \frac{\ell_w^2 t_w f'_g}{2} \left[\rho_1 \psi_M + \Omega + 2\rho_2 - \frac{1}{k_1} (\rho_1 \psi_M + \Omega)^2 \right] \dots \dots \dots (39)$$

The wall's total moment then could be calculated using [11]:

$$M_{CapWall} = M_{CapL} + (n - 2)M_{CapM} + M_{CapR} \dots \dots \dots (40)$$

Where (n) is number of wall's panels. Moment capacity of the wall must be equal to the design moment.

The portion of moment that's resisted by shear connectors is referred to as (M_{sc}). The parameter (ω) is the ratio of moment capacity of shear connectors to design moment [11]:

$$M_{CapWall} = M_{des} = \frac{M_{sc}}{\omega} \dots \dots \dots (41)$$

Total moment that is resisted by shear connectors is as shown below [11]:

$$\begin{aligned} M_{sc} &= (n - 1)F_{sc} \ell_w \\ &= (n - 1)\rho_2 \ell_w t_w f'_g \ell_w \\ &= (n - 1)\rho_2 \ell_w^2 t_w f'_g \dots \dots \dots (42) \end{aligned}$$

Substituting equations 40 and 42 into 41:

$$M_{sc} = \frac{2(n-1)}{\omega} \rho_2 \dots \dots \dots (43)$$

PRESSS report has referred to acceptance criteria that have to be checked and those criteria are:

1. Post-tensioning reinforcement should not yield
2. No uplift at end panel.
3. Minimizing residual drift.
4. Panels should slide rather than rocking.

Saqan and Haweeleh also have recommended ranges or minimum to maximum values for some parameters as a startup. They were able to reduce the number of variables to only five ($f_g, f_{po}, \theta_{des}, \Omega$ and n) and then charts were provided to find the suitable values of those variables and finish the design process. Overall procedure of designing Unbonded split shear wall became shorter and more importantly is that no iteration calculation cycles are required. It must be noted that Haweeleh have conducted several other studies in this field [45], [46], [47] & [48].

2.3.3 C. Bora, M. G. Oliva, S. D. Nakaki, R Pecker [12]

This study aimed to utilize narrow and thin cross section precast panels in lateral load resistance system as shearwalls like hollow-core panels and meeting the existing code criteria. Also, developing new mechanism to attach panels to each other and to the foundation because these walls are not thick enough to accommodate unbonded tendons or reinforcement splice. Another objective was added later on, which is identifying the yielding components of this system versus component that needs to be kept below yielding. The main challenge in such walls is that the moment arm of lateral force (height of the wall) is greater than wall width which lead to higher compression and tension forces at the wall toes as shown is Figure 2-18. Concrete tensile capacity is not great and this type of walls where the section is

hollow, the overall tension capacity is limited. Using yielding connectors at walls toes could help solving that problem.

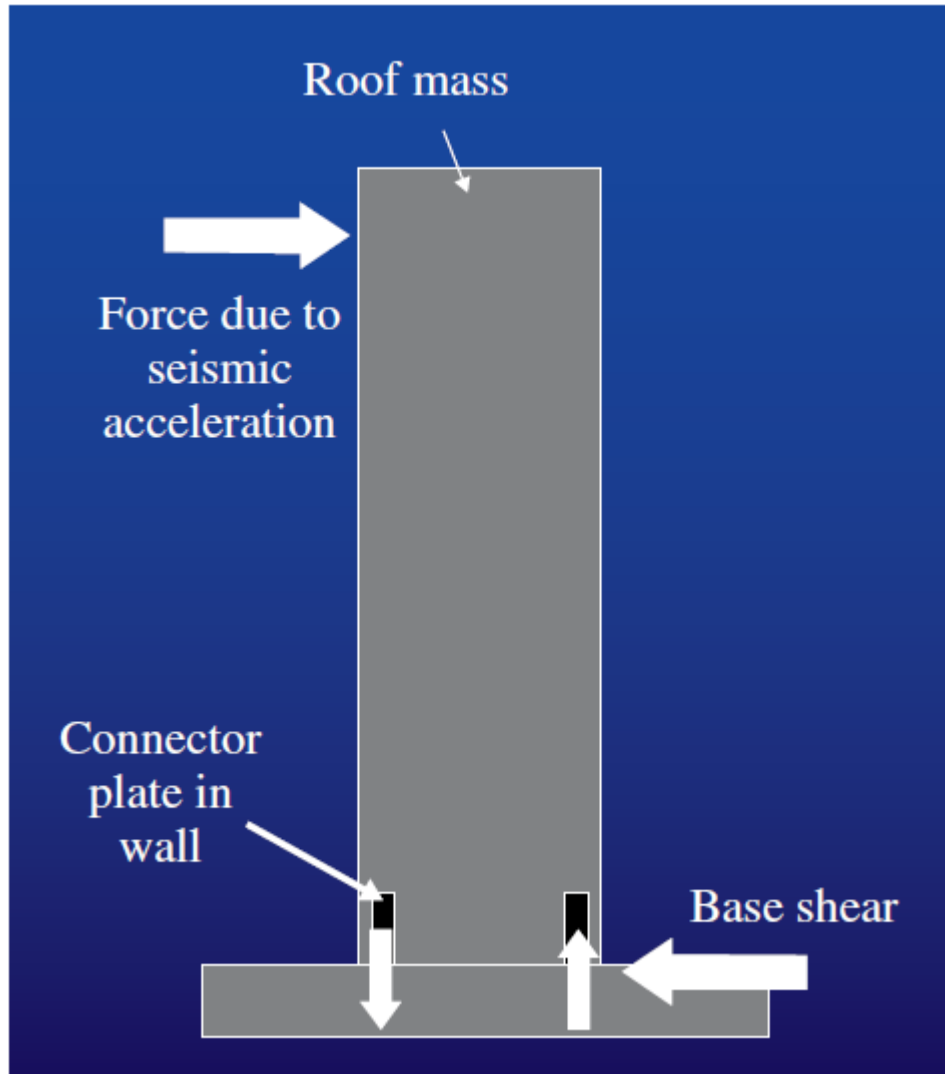


Figure 2-18: Tension and compression forces at the wall toes [12]

It should be noted that failure mode of these walls is brittle and using yielding connectors helps improving the failure mode and wall behavior. However, using yielding connectors is limited by either cracking the wall panel or the pull out mode failure of the anchorage. That leads to limit the force that could be resisted by one panel. Nonetheless, the shear force that is applied on wall system and its

connections could be limited by using slotted-bolted type of connections. This type of connectors allows the wall to slip as their stiffness decreases. That also leads to lengthening the building period significantly which causes reduction in seismic force magnitudes. The intention of using such connections is to maintain elastic-plastic response as shown in Figure 2-19. However, as mentioned previously, a goal was added is that to identify the yielding components in this system. As a result, the connection was designed to be elastic which makes the design procedure simpler since the design could be controlled by the connection elastic capacity.

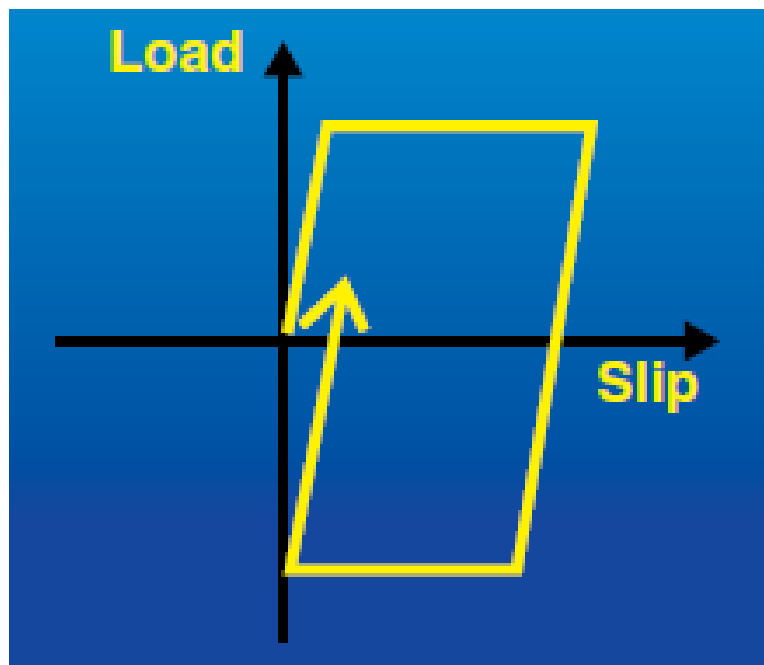


Figure 2-19: Ideal Elastic-Plastic response [12]

A special Slotted-Bolted connection was used in this study to meet the main objectives. The connection consists a center slotted plate that is embedded into the concrete foundation, wall embed plate that is welded to steel bars, steel cover plate to provide friction and cover, and two brass plates to provide firmer friction than friction between steel plates. Figure 2-20 shows illustration of the used Slotted-Bolted connection.

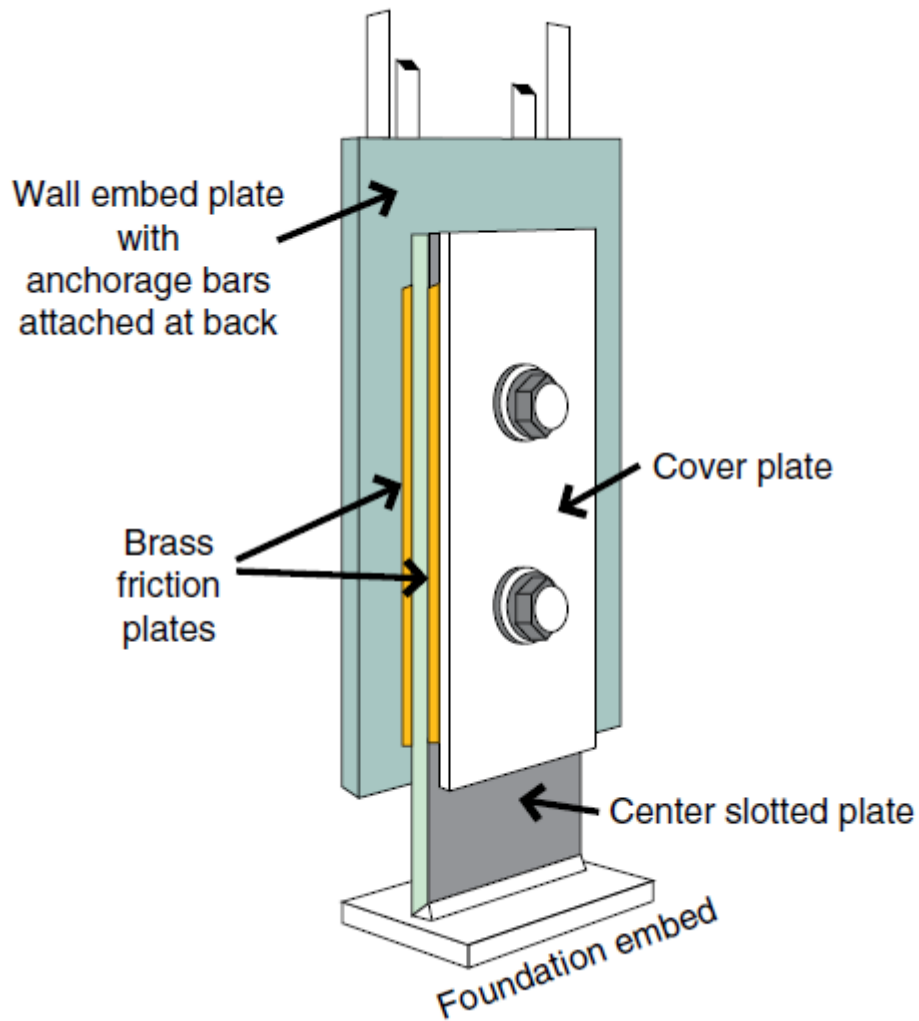


Figure 2-20: Slotted-Bolted connection [12]

The different components of this system, such as base embed plate and slotted-bolted connection, were first tested separately. Subsequently, a full size hollow-core wall was tested and non-linear analysis was conducted as well. The wall tested under possible service level earthquake motion, then a ground motion taken from 1940 El Centro earthquake was applied. In addition to, three cycles of reversed cyclic load also were applied to the top of the wall. As a summary of this study, a full height shear wall of hollow-core panel was tested and the slotted-bolted connection was found to be acceptable after it was designed as the only yielding connection in this system.

2.3.4 Sritharan S., Aaleti S. [15]

Sritharan and Aaleti et al. have followed PRESSS phase III study guideline in general and Stanton and Nakaki [10] report in particular. Thomas and Sritharan et al [16] have addressed some inadequacies in PRESSS report proposed by Stanton and Nakaki [10]. Sritharan and Aaleti objective of this research was to address those inadequacies. The design moment distribution between wall panels was not addressed in the design guideline of PRESSS phase III report neither in Thomas and Sritharan evaluation. Sritharan and Aaleti have proposed that a simplified method could be used which is by designing the most critical panel and the rest of the panels could be detailed similarly to the critical panel. Eventually, all assumptions of Stanton and Nakaki have been followed in this research. Sritharan and Aaleti concluded that if the jointed wall consists of only two panels, the leading panel endure $2/3^{\text{rd}}$ the applied lateral load. While in the case of more than two panels, middle panels undergo the largest portion of applied later load and the leading and rear panels undergo less lateral load. Also, the post-tensioning of the rear panel yields first, therefore it governs the design. Nonetheless, the post-tensioned area should be determined by the panel that undergoes the largest moment. Three examples were presented in this paper using a modified procedure that was derived from PRESSS procedure. Calculations showed that minimum code requirement reinforcement at compression toe is sufficient. Ultimately, they found that post-tensioning tendons could be distributed symmetrically along wall length and this case, the design force for post-tensioning tendons should be taken from the furthest post-tensioning steel in the rear wall, that is to make sure that post-tensioning tendons do not yield at the design drift.

2.3.5 Perez, F. J., Pessiki, S., and Sause R. [17] [18]

Research objectives of this study were to find closed-form relationship between the base shear to roof or top of wall displacement, and propose design procedure to relate wall capacities with code design requirements. They used split precast wall with unbonded post-tensioning tendons as horizontal connectors between wall panels and yielding vertical joint connectors. Figure 2-21 shows the wall

prototype that was used in this study. The wall is consisted of three panels, two-story and full height each. Researchers have used spiral confining concrete at wall's toes to improve panels compression at panel's base.

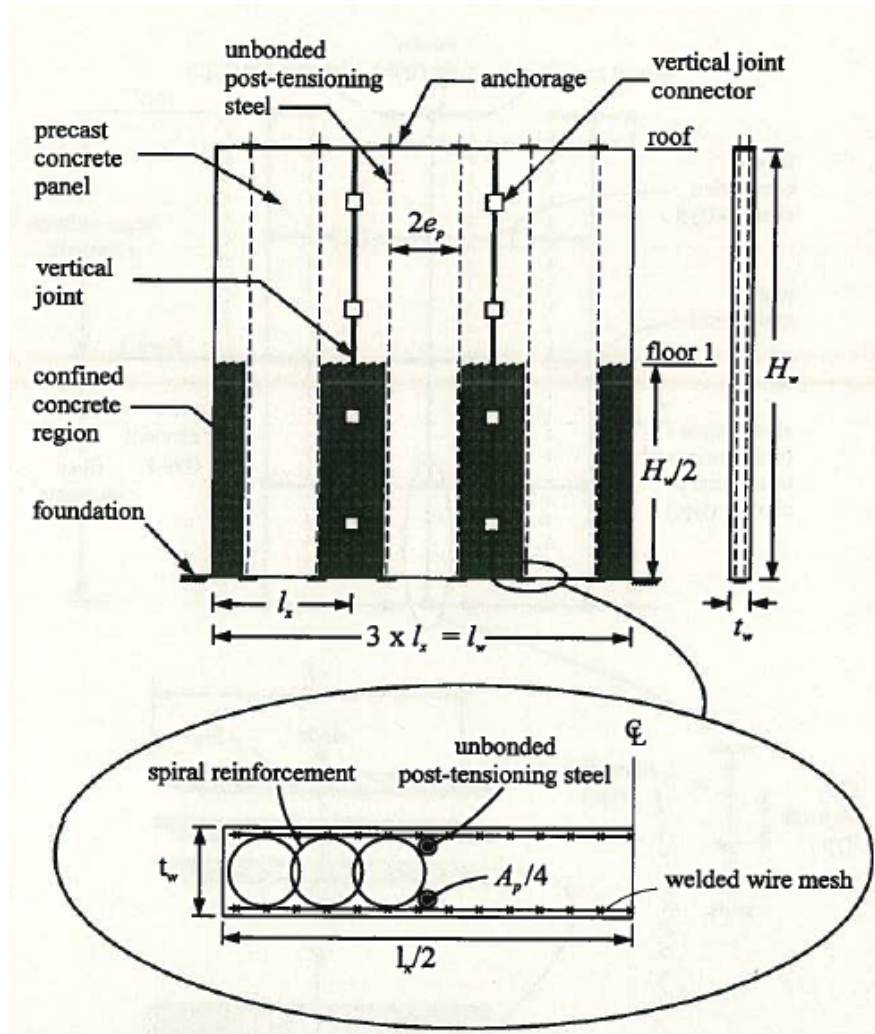


Figure 2-21: Wall Prototype [17] & [18]

Analytical model was generated to compare its results with the test of the prototype wall results. First story was modeled as fiber elements because the first story portion of the wall undergoes an axial-flexural behavior and according to Kurama et al [19] it is the best fit for this application. Second story,

however, was modeled as beam-column element because the developed strain in the upper part of the wall is expected to be in linear elastic range.

It was intended that the wall undergoes high non-linear lateral displacement due to the usage of vertical shear connectors that helps to dissipate the energy to avoid yield of post-tensioning reinforcement, compression failure at the base, or significant drift in the wall. One prototype and total number of seventeen walls were modeled and analyzed [18]. The scale test was 60% of real-life building size. 150% of the design motion was applied on the system before the wall witnessed spalling failure at the base. Figure 2-22 shows the relationship of base shear and roof or top of wall drift. It could be noticed that the wall response is linear elastic until the softening. Due to progression of gap opening along the horizontal joint, the wall stiffness dropped and that caused a “softening” response. Researchers have referred to the point of “softening” as Effective Linear Limit (ELL). Figure 2-22 shows the relationship of base shear and roof or top of wall drift. It could be noticed that the wall response is linear elastic until the softening. Due to progression of gap opening along the horizontal joint, the wall stiffness dropped and that caused a “softening” response. Researchers have referred to the point of “softening” as Effective Linear Limit (ELL).

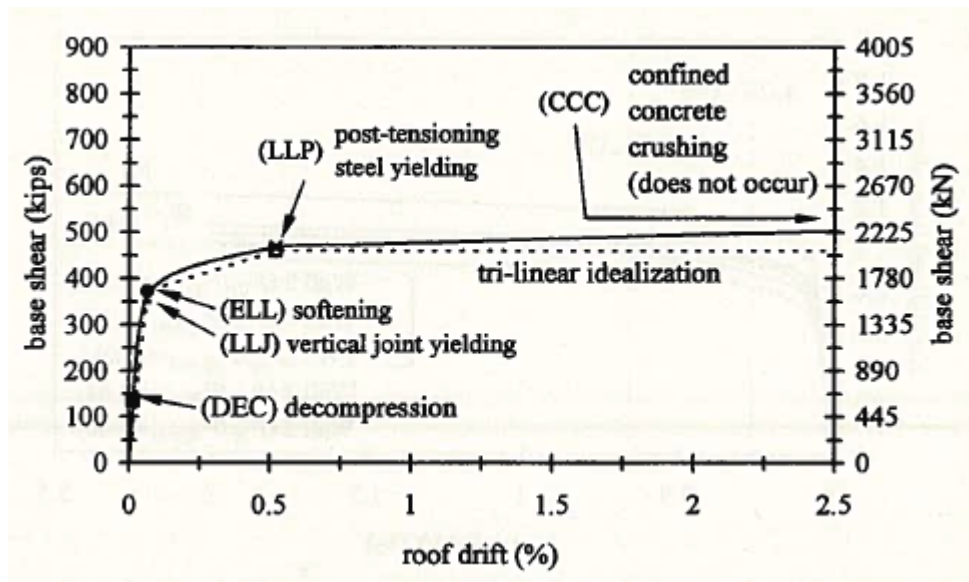


Figure 2-22: Base shear versus Roof drift [17] & [18]

Figure 2-22 shows that there three control points in the overall behavior, firstly, is the point when shear connectors yield in shear. Secondly, is the post-tensioning yield point, and finally is the confined concrete crush point. Thus, the idealization of the plot was called by the researchers as a “trilinear” Wall did not undergo high lateral load after softening then the failure occurs when confined concrete crushes. The researchers proposed a seismic design approach that is in a way Performance-Based design procedure. This approach requires that building performance must be determined which means in the level of damage that should occur. Also, seismic demand and structure limit state and capacity and structure demands. In addition to that, the design objectives of this study were to not exceed the immediate occupancy level under the ground motion design level, and to no exceed the collapse prevention performance level under maximum ground motion level. Results of the analytical results were successfully compared with the conducted tests on the prototype wall. Overall behavior of split wall with unbonded post-tensioning tendons could be controlled by changing area of unbonded post-tensioning tendons, initial prestress and number of shear connectors along the vertical joint.

2.3.6 Ajrab J. J., Pekcan G., and Mander J. B. [20]

In this study, the researchers have proposed a system includes rocking wall along with a supplementary energy dissipation system and Prestressing tendons to improve wall’s vibration. This system called rocking wall frame structure. They usually are designed to be free to rotate at the base in order to reduce damages due to seismic effects. This concept was presented first by Housner et al (1963) when he studied the free vibration of rocking blocks. A combination of lateral loads and the post-tensioning force in tendons are the main resources of the lateral resisting system of this type of structures [21]. The behavior of rocking wall before rocking (earthquake event) similar to that of fixed-based elastic structure and mainly controlled by its flexibility. After rocking, the behavior changes and it becomes controlled by rigid body kinematics behavior. The design objective of this study for capacity-demand spectrum was to satisfy the following criteria [20]:

$$(SA)_c \geq (SA)_d \dots \dots \dots (44)$$

Where (SA) stands for spectral acceleration and the subscript (c) and (d) are for capacity and demand, respectively. This design objective was set to types of ground motion which are the maximum assumed earthquake and maximum considered earthquake. Also, researchers have followed the design philosophy that was presented by Mander and Cheng et al [21] which is the Damage-Avoidance Design philosophy. According to that philosophy and in order to satisfy Eq. 44, the required performance for the maximum assumed earthquake requires the structure to remain elastic during ground motion. That means the wall rotation with respect to the base is less than 1%. While, for the maximum considered earthquake, it is acceptable that the structure might yield with a limited damage where the rotation is <0.5%. Figure 2-23 illustrate the proposed system which consists of rocking shear wall and supplementary post-tensioning tendons that work as damping system. the Researchers also examined the level of Prestressing at 0%, 33% and 67% of the yield strength. in addition to, examining different type of tendons configurations and wall widths as shown in Figure 2-24. Two types of extreme ground motion were applied, El Centro and Pacoima Dam ground motions. Results revealed that the behavior of the structure did not differ when draped and vertical tendons were used under same ground motion. Also, base width did not improve the overall performance of the structure. Post-tensioning tendons in this study were used as a damping mechanism. Also, Damping-Fuser-Tendon system was used.

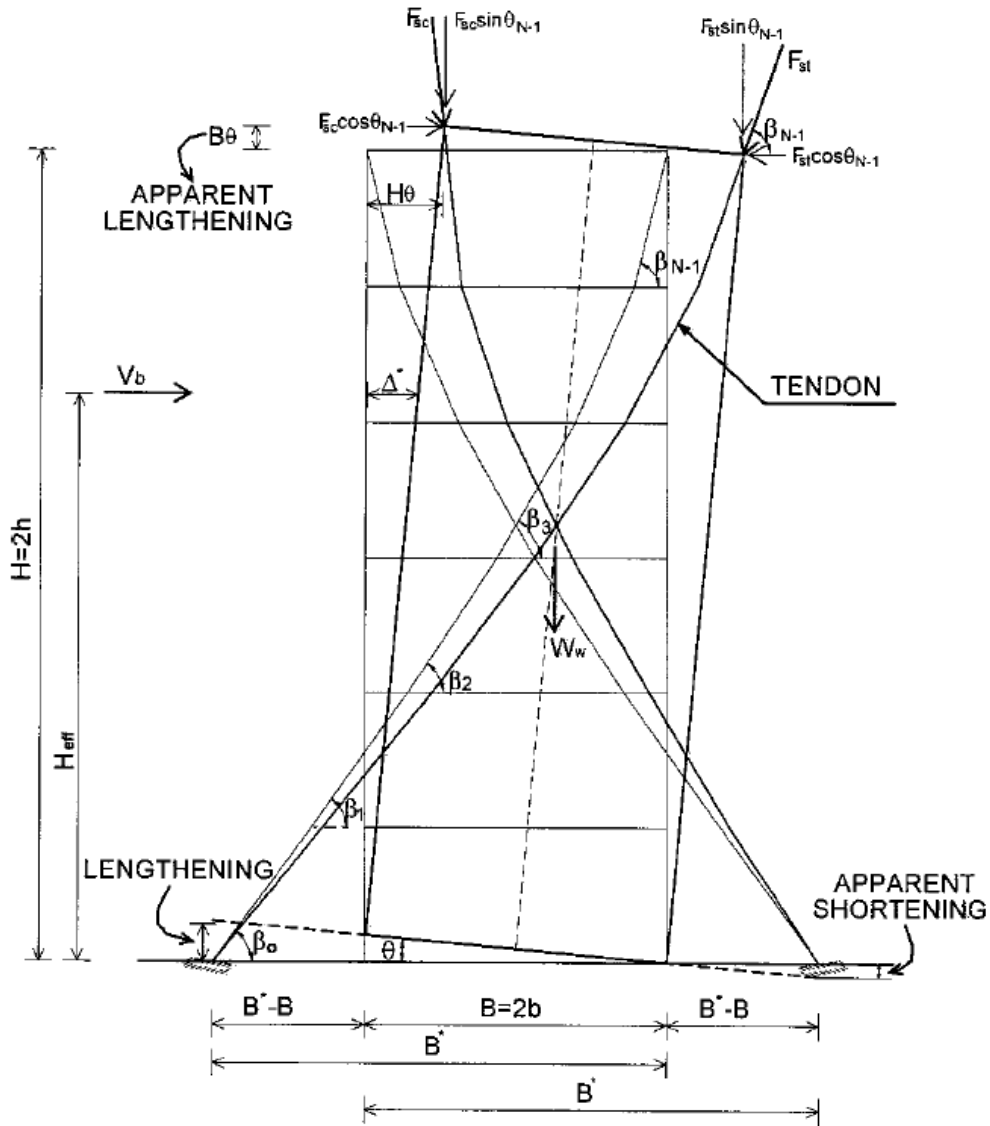
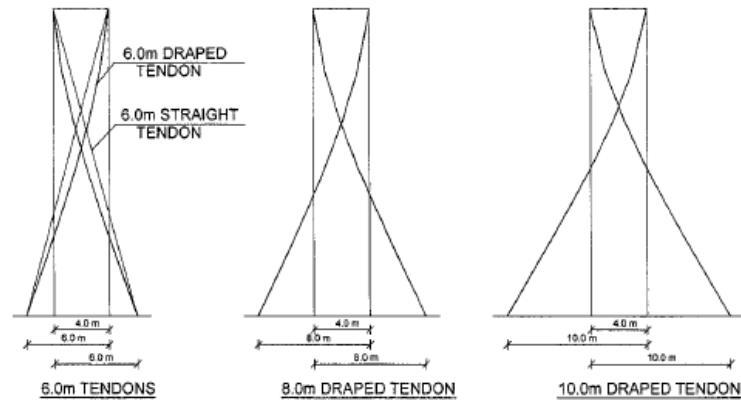
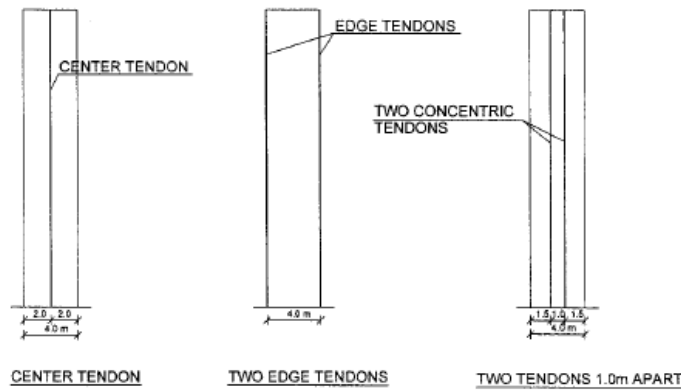


Figure 2-23: Rocking wall system on rigid foundation [20]



(a)



(b)

Figure 2-24: (a) Draped tendons configurations and (b) Vertical tendons configurations [20]

Ultimately, in this study tendons were used as a damping system that could be designed based on the required damping level that could be derived from the desired ground motion. Those damping tendons could be supplied in many different configurations and layout. Results have shown that a damping percentage of almost 20% could be achieved by using the tendon-fuser damper system comparing to 2-5% of those conventional systems. Prestress level was found to have no effect on the drift or structure's performance, so they could be designed for minimum requirements. Vertical concentric tendons, Figure 2-24 (b), was found beneficial to be used in construction applications where using draped tendons not applicable like masonry walls. Finally, the capacity-demand method that followed in this study is based

on first mode of vibration and does not take into account the higher modes. Although higher modes effects were found to be not tremendous when nonlinear time-history analysis was applied.

2.3.7 Seymore D. and Laflamme S. [22]

This research addresses the lengthy design procedure of rocking walls and their extensive analytical and experimental determination of wall dimensions. Researchers have concentrated on finding a relationship between maximum story drift and wall's size. An analytical quasi-static model was generated and studied for rocking wall system. Also, it includes a case study on a building that utilize this system in Japan.

A set of equations were derived in this paper. A stiffness matrix of an arbitrary building that has (N) number of stories was created. Those equations were intended to find wall's dimension and also design the link members between the lateral resisting system (rocking wall) and the building mass.

Subsequently, software program was generated based on the derived equations. Relationships between wall width and maximum drift were generated so the optimized (maximum and minimum) values could be calculated.

It must be mentioned, that this paper focused on quasi-static state of lateral load application, therefore it did not include any discussion of the usage of damping systems or energy dissipation mechanisms.

2.3.8 Sun J., Qiu H., Yang Y. and Lu B. [24] & [25]

Researchers in this study created an I-shaped shear wall that is consisted of on main precast panel that serves as web of the shear wall and four small panels to form the flanges. They connected those panels by steel plates to create a frame at the connections and provide the required ductility at the joints. A High-strength bolts were used to connect those panels to the steel frame. Figure 2-25 shows the prototype of this study.

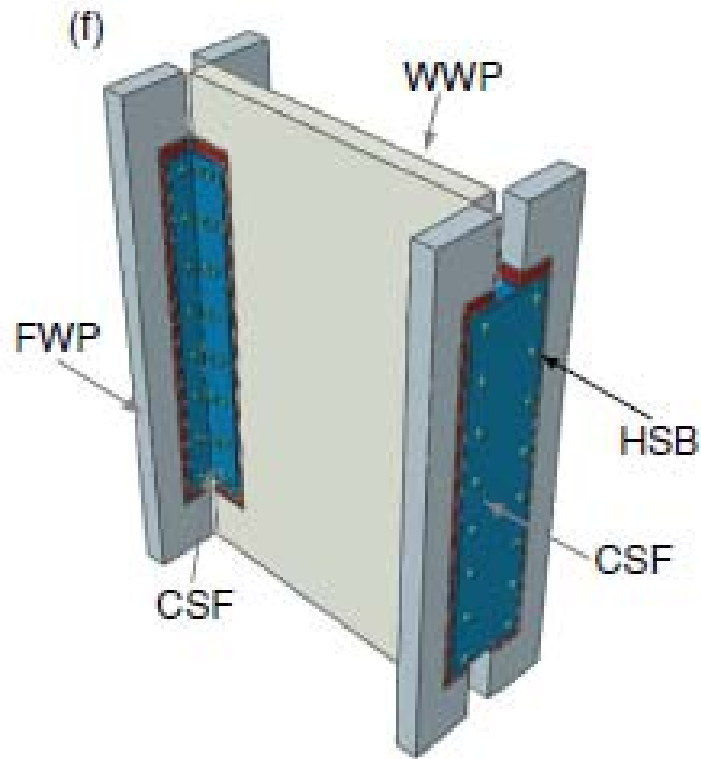


Figure 2-25: I-Shaped Shear wall [24]

For the horizontal joints between panels and foundation, a similar type of steel plates and high-strength bolts were used. Test was conducted by applying monotonic and reversed cyclic loading on the top of the wall to create similar effects of an earthquake.

During testing the vertical connection, Failure occurred in diagonal fashion in the web wall panel and bottom of flanges wall panels. Steel plates did not fail and no reported slippage of anchors. Energy dissipation was determined and found to increase as the lateral load increases. It changed drastically after the yield of the connection plates until it reached the peak with the failure load.

For horizontal connection test, cracks occurred horizontally at the tension face and continued to be in horizontal fashion until failure. Subsequently, steel plates of the connection frame between wall panel and the foundation started slipping. Top of wall displacement was measured throughout the test. It

found to be caused by the elastic deformation of the wall panel, slippage between foundation and connection steel plates, shear and flexural deformation in the wall panel and deformation of the steel plates.

Ultimately, I-shaped precast shearwall are not used widely. Using connection frames that is made of steel plates might not be the best choice from architecture standpoint. Finally, the aftermath restoration of shearwalls was not discussed in this study which is one of the main points that all previous researchers have concentrated on.

2.4 Summary of previous studies

Split unbonded post-tensioning precast shear walls are the point of interest to numerous researchers for the last three decades. PRESS program led the way in the United States to investigate this type of walls due to the fact that is an advantageous application for precast buildings in high seismic zones. PRESS report included types of connections that could be used horizontally and vertically to connect precast panels. Nonetheless, PRESS recommended a procedure to design split Unbonded post-tensioning precast shear walls. That led researchers to conduct several studies to examine this type of walls and understand their behavior under high lateral loads. Some researchers have studied the behavior of this type of walls under reversed cyclic loads to mimic the effect of high lateral loads due to seismic effects. On the other hand, some researchers have studied the connections and types of connections between shear wall panels. In addition, some researchers derived easier procedure to design this type of walls.

For horizontal connections, it was evident that most researchers have found that using post-tensioning tendons between precast panel and foundation and between the precast panels themselves is preferable. The main reason is that due to the fact that post-tensioning tendons help restoring the shear wall panels after earthquake effect. Also, using post-tensioning helps to control the drift other shearwall and minimize it which in its turn lead to minimize the overall drift of the structure. Some other reasons

to use post-tensioning tendons are due to easiness in placing them in vertical members [5]. Location of post-tensioning tendons was recommended to be in the middle of the panel and kept far enough from shearwall toes due to the fact that shearwall toes are the regions of high tension and compression zones since those tendons should be protected from large strains.

For vertical joints, researchers have revealed that vertical connections have to offer high energy dissipation characteristics and should yield in shear. Also, shear connectors should be ductile, deformation flexibility and its deformation is preferred to not be limited by strain capacity [5]. In general, elastic-plastic type of behavior is highly preferred in vertical connectors for split shearwalls.

Two types of vertical connections were recommended by Shultz and Magana et al. [5]; U-shaped Flexure Plate (UFP) and Vertical Joint Friction (VJF). However, Shultz and Magana et al [5] have concluded that the anchorage of these joints should probably be designed in a more conservative manner than it was in that study due to the numerous times of anchorages failure in that study. Number of shear connectors should be determined based on the applied lateral load and wall panel's height and width. Most researchers have indicated that those shear connectors could be distributed evenly along the height of shear wall panels.

Some researchers have developed different types of connections along the vertical face of shearwall panels. Some these connections did not match the function of the need to shear connectors vertically between shear wall panels. Also, some studies did not discuss the drift after earthquake effect and the ability to restore the drift of shear walls. Ultimately, shear wall connections in some of these studies did not follow same requirements and objectives of PRESS.

CHAPTER 3: Computational Modeling

3.1 Overview and preliminary modeling

A major focus of this research is on generating finite element models of the seismic shear wall connectors using the ABAQUS software. ABAQUS is a comprehensive finite element analysis program that is widely used in engineering applications. Early computer models, used in the PRESS study, were conducted using the DRAIN-2DX [19] software. The main assumptions used in the PRESS analyses were that the seismic forces were applied along the strong axis of the wall cross-section and no out-of-plane bending was generated. The torsional, shear or out-of-plane displacement and instability were not modeled. The PRESS study focused on rocking shear walls under seismic loads. Applied shear force was resisted by the shear wall alone and rigid diaphragms were assumed. In addition, all walls were assumed to have the same displacement due to the assumption of rigid diaphragm. Furthermore, any contribution of foundation or supporting base was neglected. Anchorages of post-tensioning tendons were assumed to be fully intact during the seismic event [19]. The main reason for modeling such walls as rigid wall is to study the effect of axial and flexural forces due to the lateral loads

A preliminary FE model was generated that consisted of a precast concrete wall with a height of 45 ft, width of 8 ft and 12" thick [3]. The idea of the model was taken from a research that was conducted by Brian J. S. et. al. In that research a design example of a 4-story parking garage structure with the total height of 45 ft was presented [3]. The height of the first story was 12 ft while other stories had an 11 ft height. The purpose of running this model was to check the horizontal and vertical local displacement of certain points of interest along the wall height. Seismic load was calculated and determined for each level and applied as a concentrated point load at each level [3]. In addition, an assumed uniform dead load was added on top of the wall. Figure 3-1 shows the wall model. The concrete compressive strength was 6000 psi. The wall was modeled as 2D model (plain strain). The foundation was assumed fixed.

The main purpose of the preliminary model was to understand the behavior of the modeled wall and check its lateral drift. The wall was had a 1 ft x 1 ft quad mesh. A comparison between the displacement of points on one side of wall faces with points of the opposite face of the wall needs to be done to figure out the relative local displacement between adjacent shear wall panels to determine the required resistance to that displacement and the dissipated energy. Four points along the height of the wall were examined. Those points are shown as yellow small circles in Figure 3-1. Also, those points represent the height of each level of the building. Figure 3-2 shows the deformed shape the model after applying the lateral load.

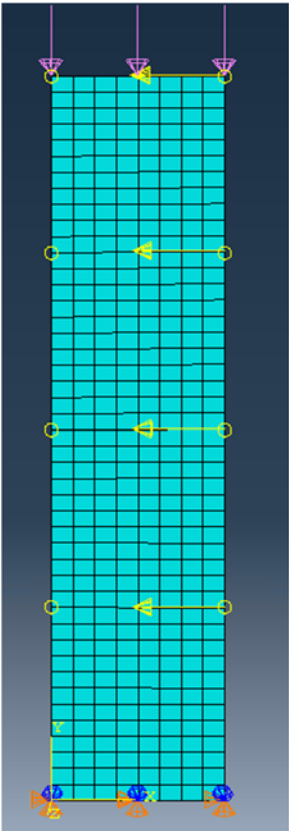


Figure 3-1: Preliminary model

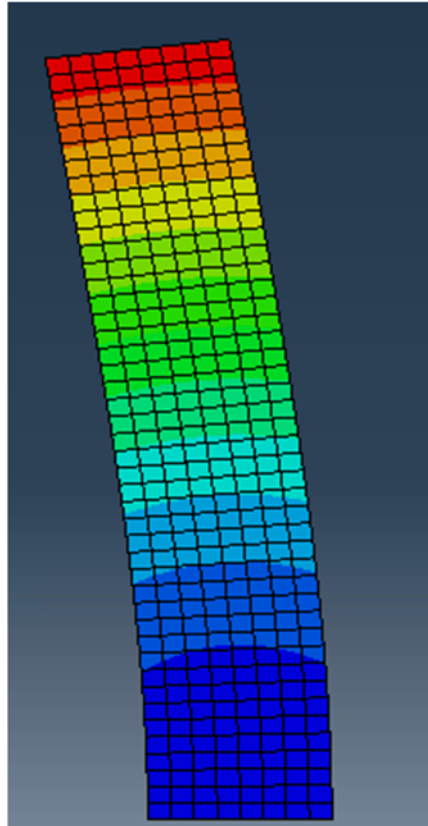


Figure 3-2: Deformed shape of Preliminary model

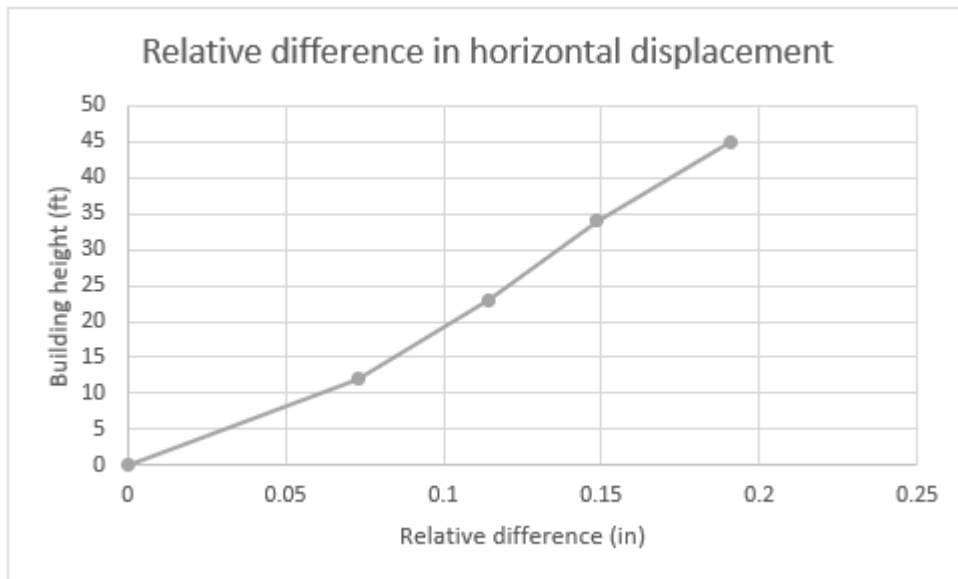


Figure 3-3: Relative difference of horizontal displacement between nodes on opposite sides of shear wall

Figure 3-3 and Figure 3-4 show the relative difference of horizontal and vertical displacement between points along the height of the wall, respectively. The vertical displacement at the points of interest on the two sides of the wall do not differ much. Analysis of data indicate that the difference between vertical displacements of the two sides were 0.073-inch, 0.114-inch, 0.149-inch, and 0.191-inch for the first through fourth level, respectively. The absolute displacement along the height of the shear wall, Figure 3-3, is linear and increasing with height. In general, the displacement of points of interest along the side where lateral loads are applied are larger than those on the opposite side.

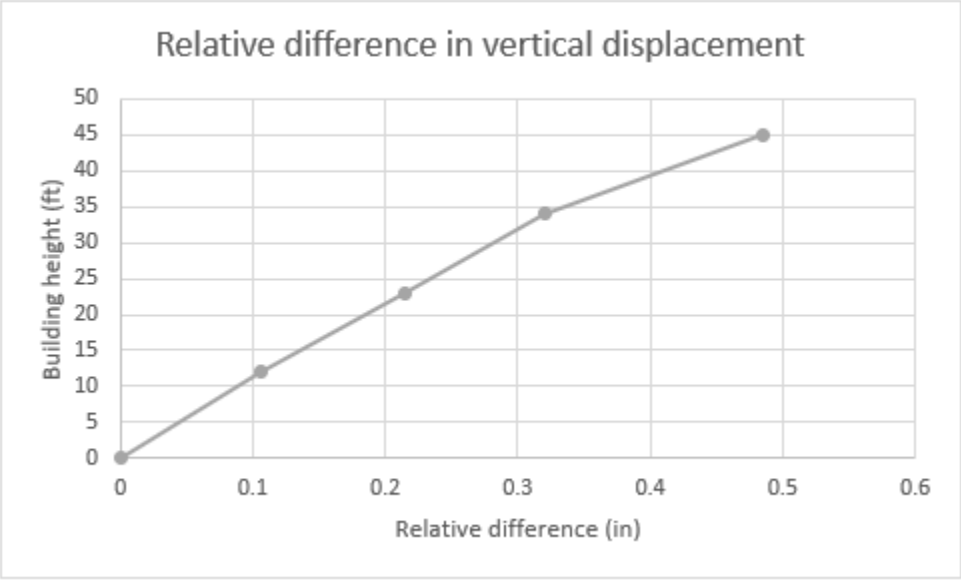


Figure 3-4: Relative difference of vertical displacement between nodes on opposite sides of shear wall

The difference between vertical displacement of points of interest along the shear wall height, ranged between 0.423-inch at first level to 2.28-inch at fourth level. Figure 3-4 shows the relative difference in vertical displacement between nodes on opposite sides of the shear wall.

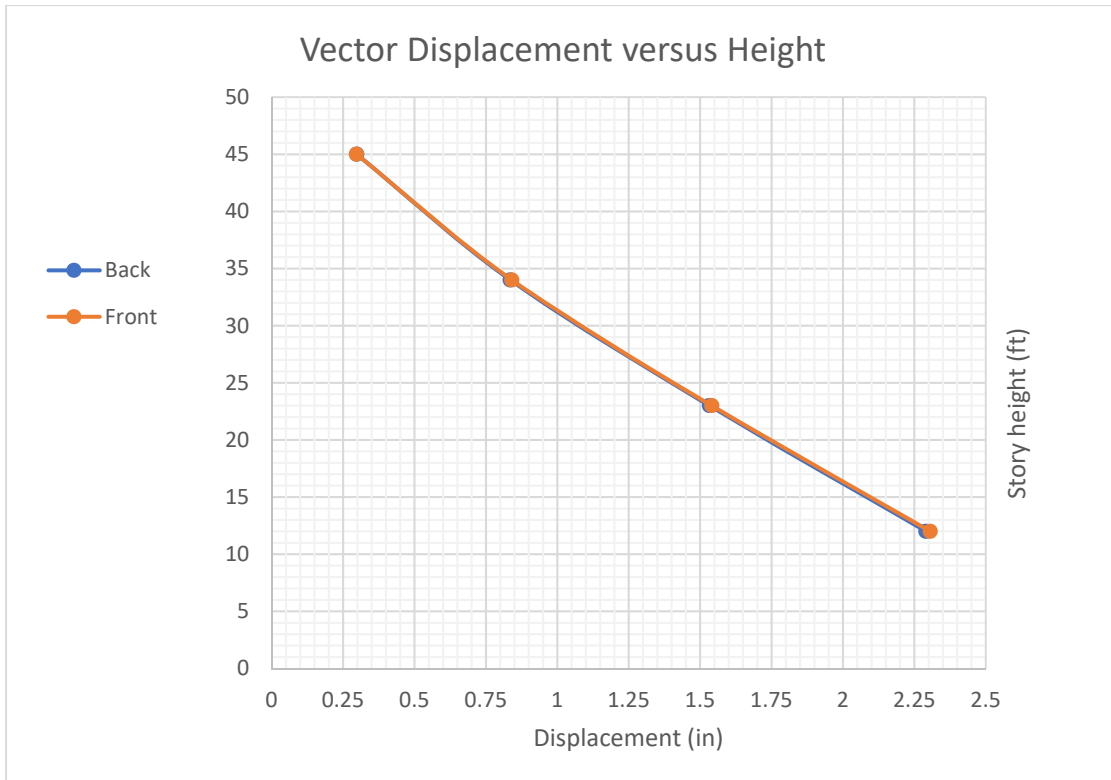


Figure 3-5: Vector displacement at each level

The overall displacement (magnitude of the vector representing both horizontal and vertical displacement) is calculated at each point of interest along the height of the shear wall and as shown in Figure 3-5. In summary, the relative displacement between the sides of the modeled shear wall represents the relative displacement between adjacent shear wall under the application of lateral floor loads.

3.2 Basic seismic connectors

In the following sections, descriptions of models of several existing and new types (shapes) of seismic connectors are discussed. Those analyses were performed to assess the potential performance of proposed new shapes under lateral displacement when compared to a commonly-used connection device. A primary goal was to come up with a new and efficient shear connector between precast shear wall panels. For the sake of simplicity, some shapes were assumed to have a thickness of 0.5-inch. The commonly-used U-shaped model was evaluated first. Each new shape was compared with the results of U-shaped model. The best performing new shapes were then subjected to physical scaled-model testing for verification.

3.2.1 U-shaped test results by PRESSS [5]

Under the PRESSS program, a study of a six-story precast building with shear walls was conducted to test both horizontal and vertical joints between shear wall panels. Total drift was compared to the relative displacement along vertical joints between panels [5]. Several horizontal and vertical type of connectors were tested with the U-shaped connector being one of them. Figure 3-6 shows a typical U-shape connector configuration and attachment to shear wall. Figure 3-7 shows dimensions of typical U-shape connector. Figure 3-8 shows the test setup used by PRESSS to test the U-shaped connection.

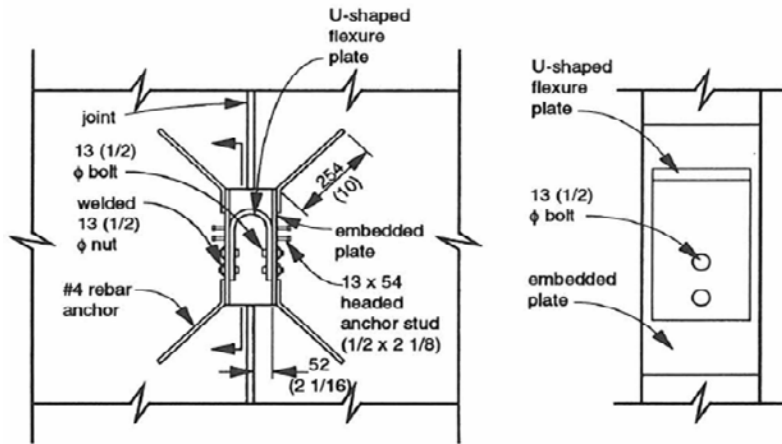


Figure 3-6: U-shaped plate configuration [5]

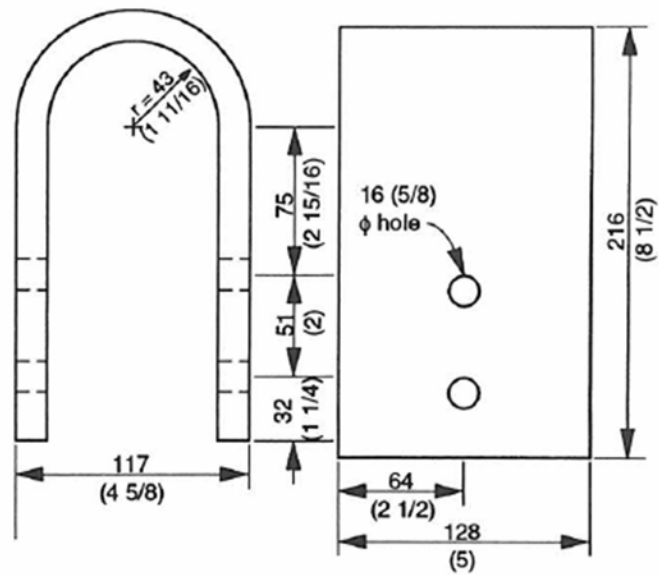


Figure 3-7: U-shaped plate dimensions [5]

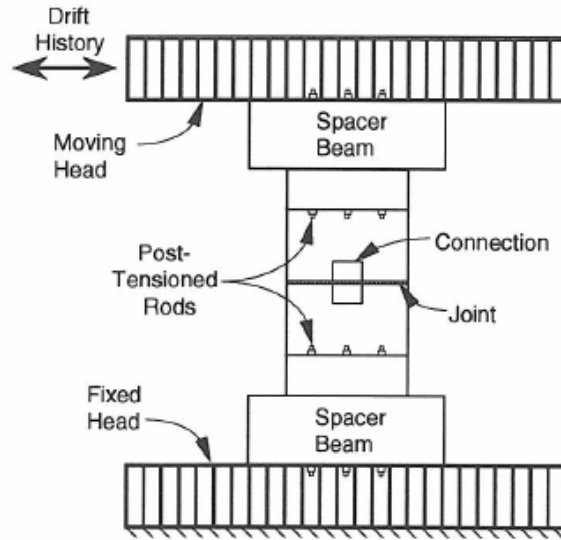


Figure 3-8: Test set-up of U-shaped Connection by PRESS [5]

The test involved applying a 2-in drift, which resulted in a 1.574" displacement at the U-shaped connector. The displacement profile shown in Figure 3-9 was applied. Figure 3-10 shows the force versus displacement graph for the U-shaped connector.

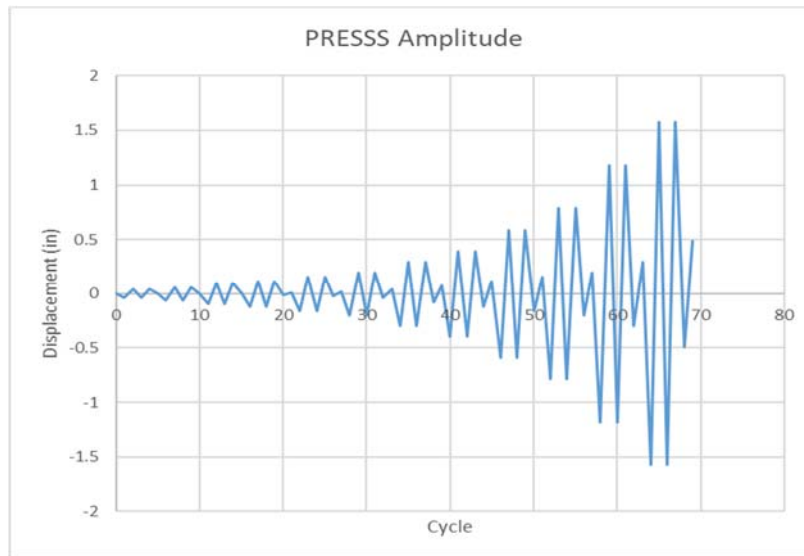


Figure 3-9: Displacement amplitude used by PRESSS to test UFP [5]

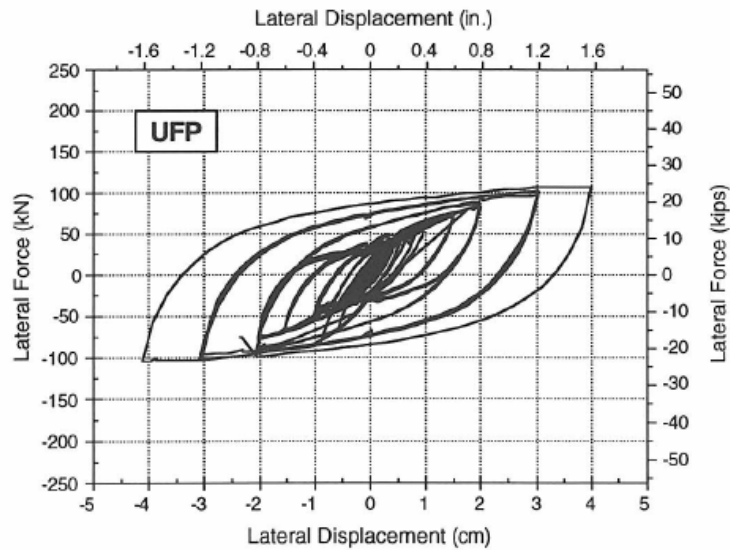


Figure 3-10: Force versus Displacement of UFP by PRESS [5]

3.2.2 U-shape shear connector – partial thickness

A U-shaped model as shown in Figure 3-11. It is 8.5-inch high, 4.625-inch wide and the thickness of the system was assumed to be 0.5-in for simplicity but later adjusted for the larger thickness. The test was based on a given displacement which was taken from earlier test conducted on shear walls in this study.

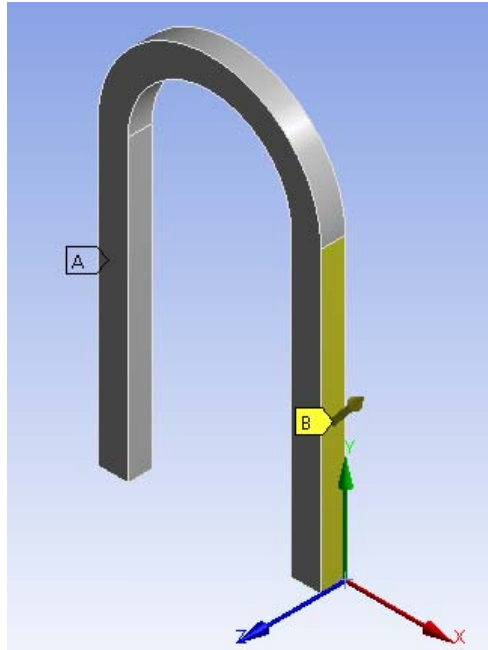


Figure 3-11: U-shaped generated model

The left side face of the U-shaped connector model (labeled A) is fixed and the displacement is applied to right side face of the model (labeled B). A total displacement in X-Direction of 0.328-inch and in Y-Direction of 0.402-inch are used in this analysis. The displacement in each direction is assumed to be applied cyclically and is divided into ten steps as shown in **Error! Reference source not found..** For instance, at first step displacements of 0.0656-inch and 0.0804-inch will be applied on the model in the X and Y direction, respectively. Subsequently, displacements that have similar magnitude but opposite in direction will be applied to simulate the cyclic effect on the model.

Table 3-1: Displacement in X-Direction and Y-Direction

Time (step)	δ -x (in)	δ -y (in)
1	0.0656	0.0804
2	-0.0656	-0.0804
3	0.1312	0.1608
4	-0.1312	-0.1608
5	0.1968	0.2412
6	-0.1968	-0.2412
7	0.2624	0.3216
8	-0.2624	-0.3216
9	0.328	0.402
10	-0.328	-0.402

Figure 3-12 and Figure 3-13 show the equivalent (von-Mises) stress and strain energy contour maps, respectively. Figure 3-12 indicates that most of the high stresses occur at the arched part of the device. In addition, Figure 3-12 indicates that the top portion of the arch and the end of the moving leg of the U-shaped model sustain the highest strains energy. Figure 3-14 shows the relationship between the reaction developed at the fixed leg of the U-shaped model with the time step. It is obvious that the maximum reaction increases as the imposed displacement increases. The highest reaction developed is 2714lbf while the highest stress is 56075 psi. Figure 3-15 shows the relationships between force resulted from applied displacement and deformation endured by the model. Figure 3-16 shows the relationship between the accumulative strain energy and time step.

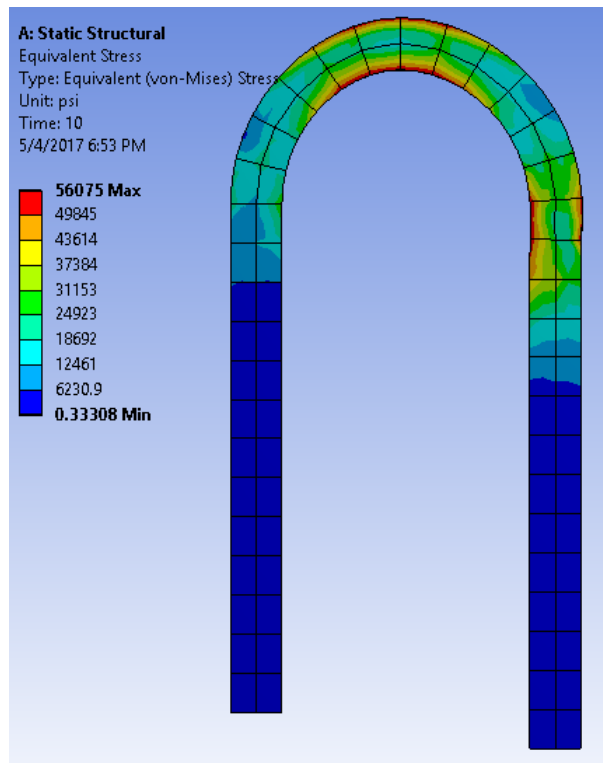


Figure 3-12: Equivalent stress contour map for U-shaped model

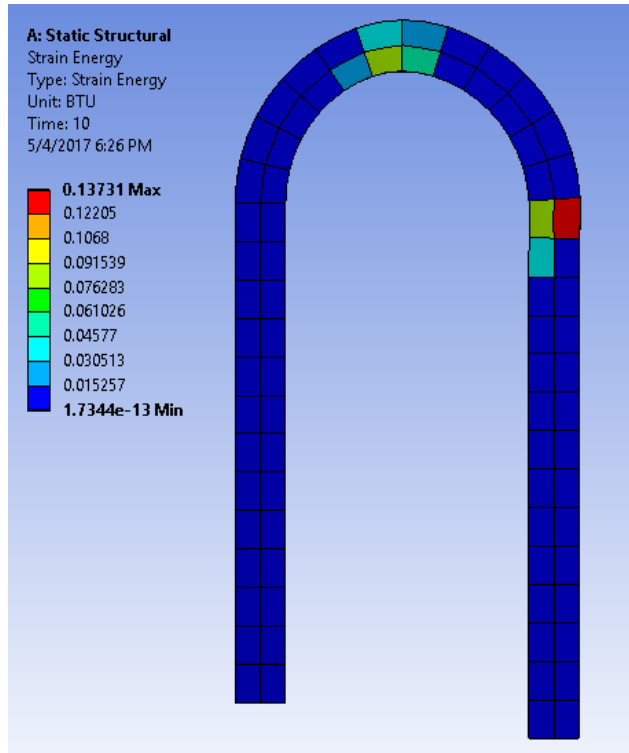


Figure 3-13: Strain energy contour map for U-shaped model

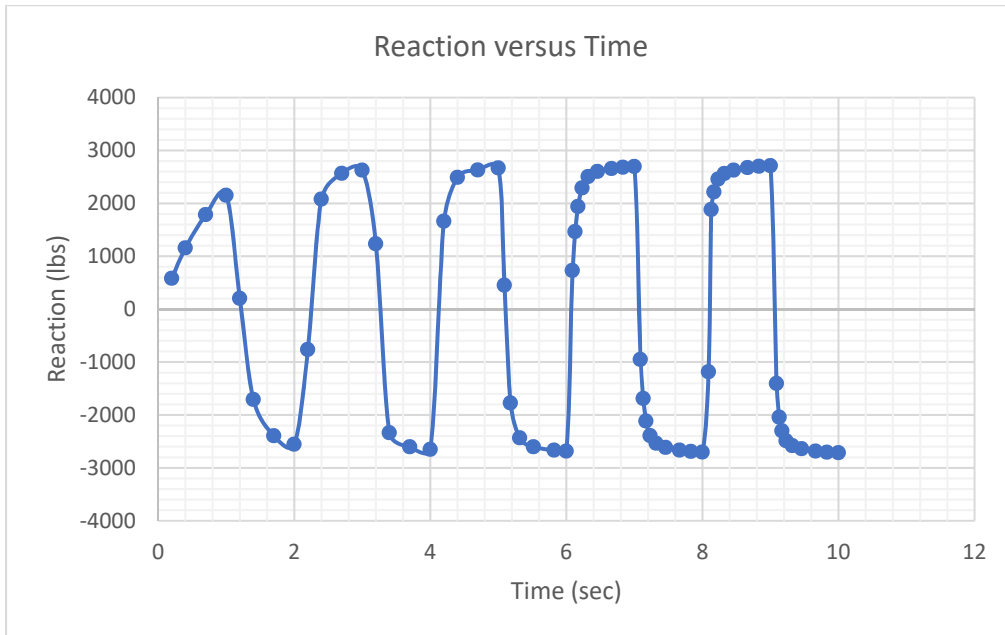


Figure 3-14: Reaction versus Time relationship for U-shaped model

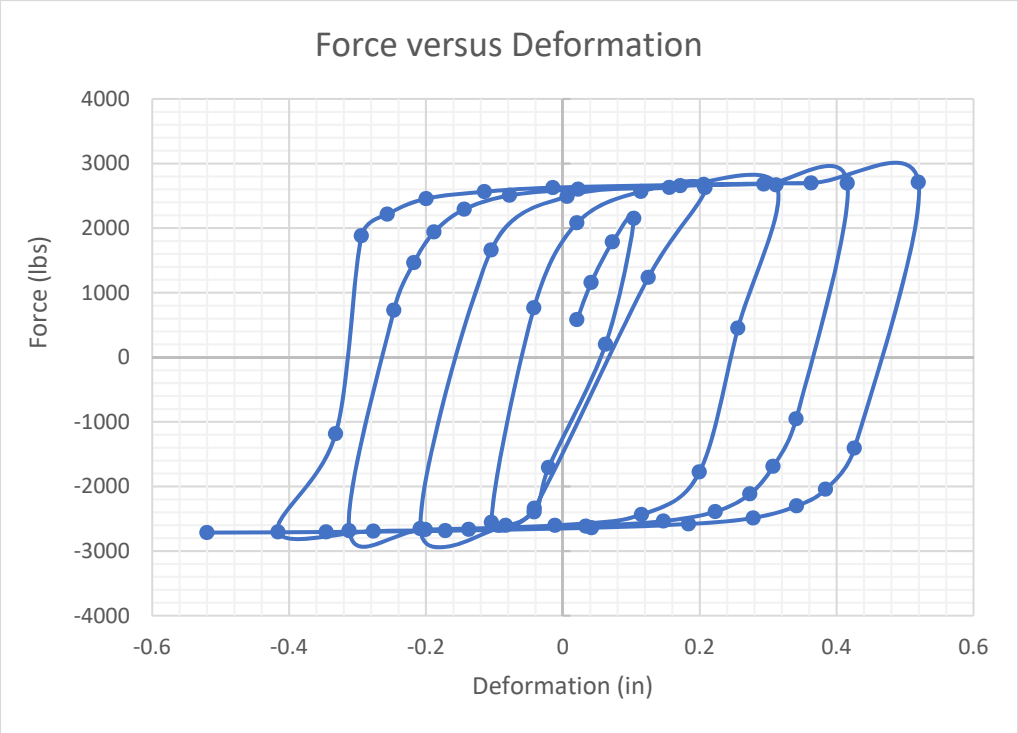


Figure 3-15: Force versus Deformation relationship for U-shaped model

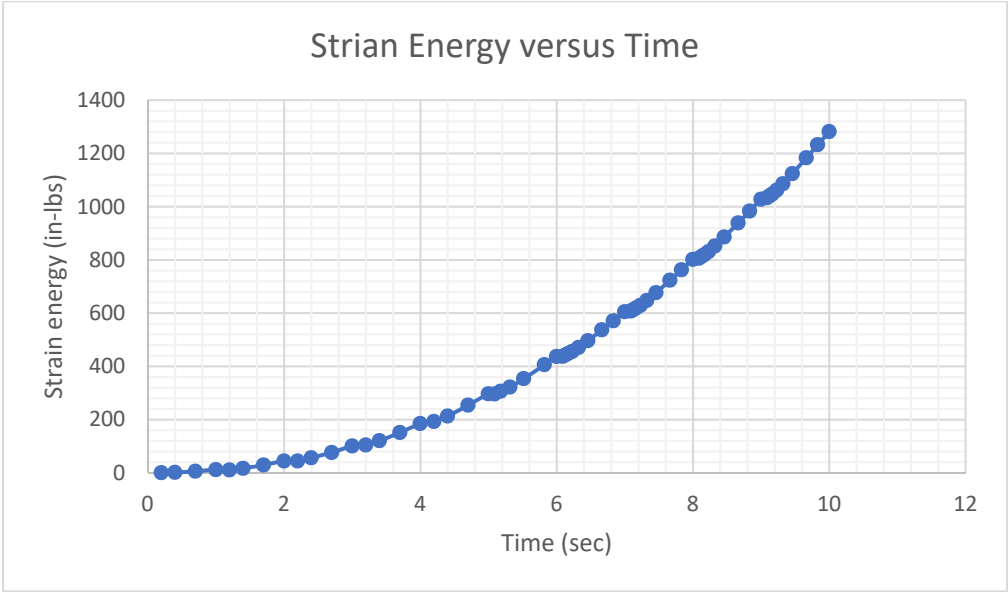


Figure 3-16: Strain energy versus time relationship for U-shaped model

3.2.3 U-shaped connector (full width) with constant displacement

The U-shaped plate's geometry shown in Figure 3-17. A model of the U-shaped plate (Figure 3-17) was generated in ANSYS. One side face was assumed to be fixed and a displacement was imposed on the opposite face (0.402-inch in Y-direction and 0.328-inch in X-direction). Figure 3-18 shows the boundary condition of the U-shaped model. Figure 3-19 shows the stress contour map obtained from the analysis. Figure 3-20 shows the dissipated energy at each step of the analysis.

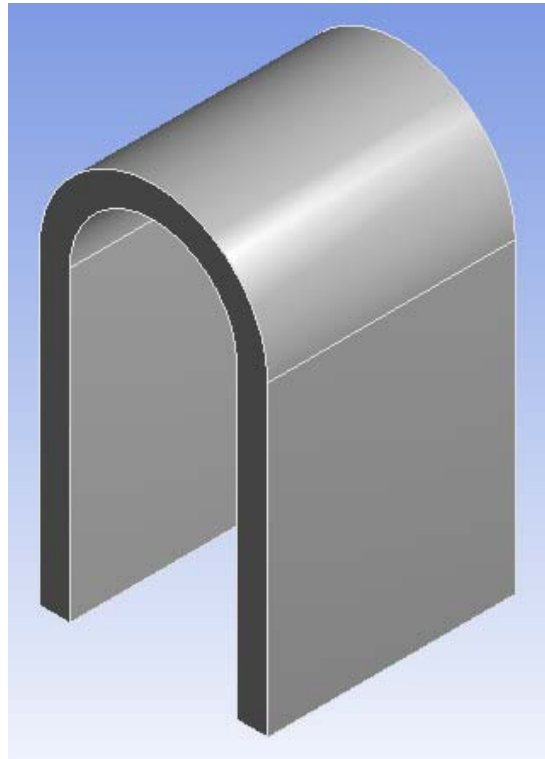


Figure 3-17: U-shaped connector

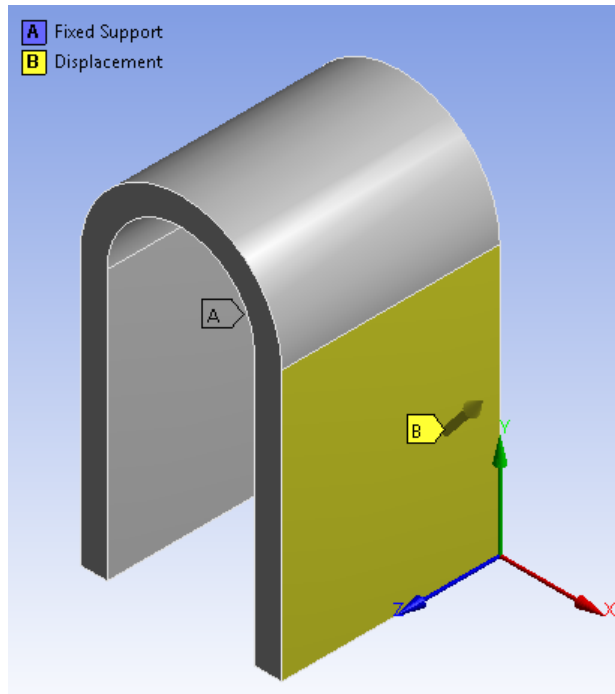


Figure 3-18: U-shaped boundary condition

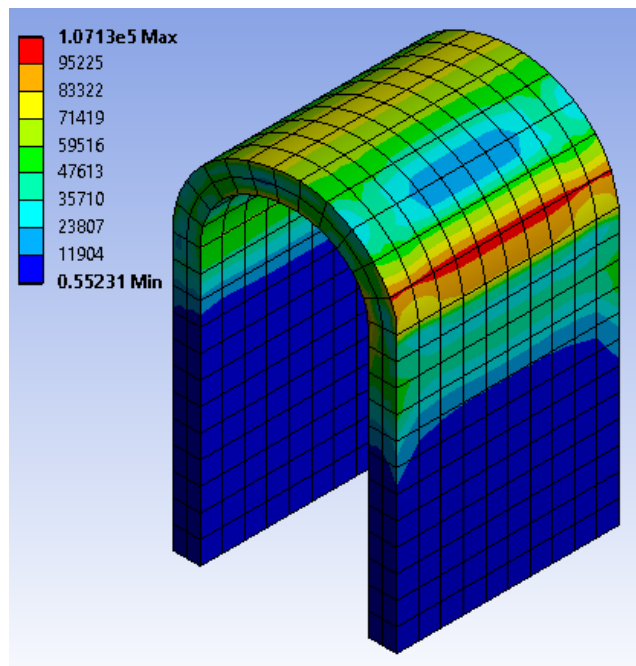


Figure 3-19: Equivalent stress contour map

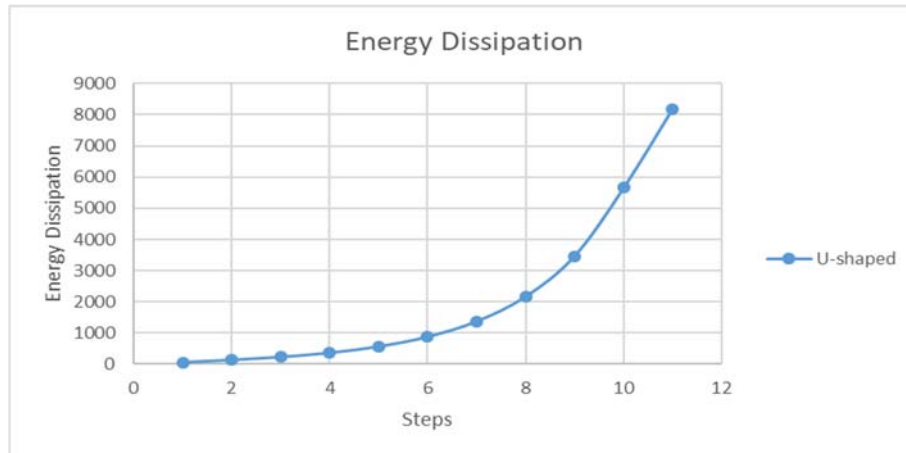


Figure 3-20: Energy dissipation of U-shaped connector

3.2.4 U-shaped connector with cyclic displacement

The ANSYS software was used to represent the PRESS test of the U-bar connector using the displacement profile shown in Figure 3-9. Figure 3-22 shows the results of the finite element modeling of U-shaped connector. The model was generated using same properties of U-shaped connector mentioned in the PRESS report [5]. Figure 3-21 (a) show the meshed model that was generated in ANSYS workbench.

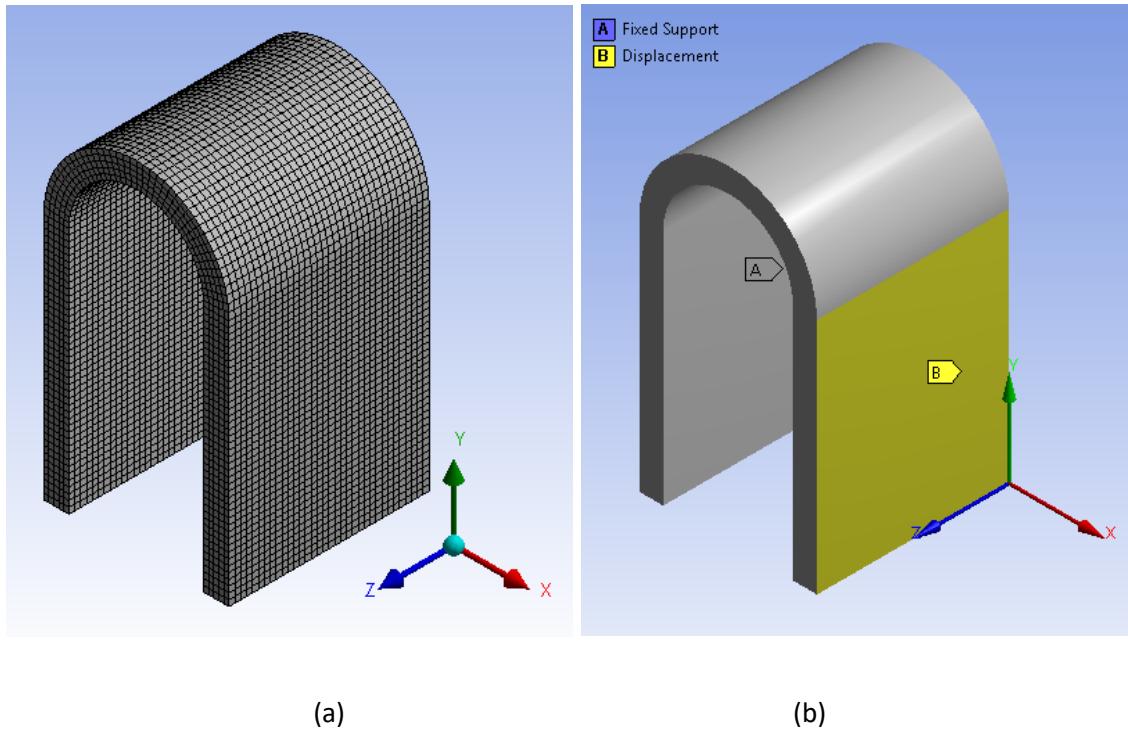


Figure 3-21: Finite elements model in ANSYS workbench: (a) meshed shape, (b) Boundary condition

The ANSYS element type that was used was Solid 186, which is a 3-dimensional solid element with 20-nodes type of elements [26]. The boundary condition is shown in Figure 3-21 (b) where a fixed support was modeled at face “A” and Displacement applied at face “B”. The model was subjected to the displacement profile shown in Figure 3-9 up to a maximum displacement of 1.574-in. The steel material was assumed to be elastoplastic nonlinear 304 stainless steel ($f_y = 31.2$ ksi).

Figure 3-22 shows the force versus displacement diagram. The Maximum reaction force was on the order of 25000 lbf, which was close to the results reported by PRESSS. However, the force versus displacement results for the analytical model (Figure 3-22) and the PRESSS test (Figure 3-10) are not in total agreement. The transition between negative and positive forces at the point where the displacement is reversed is steeper in the PRESSS results. It could be noticed that the initial stiffness of the PRESSS test data (Figure 3-10) is different than that of the FE model. It is believed that due to various elements reaches yield as the displacement increases.



Figure 3-22: Finite elements results of U-shaped connector.

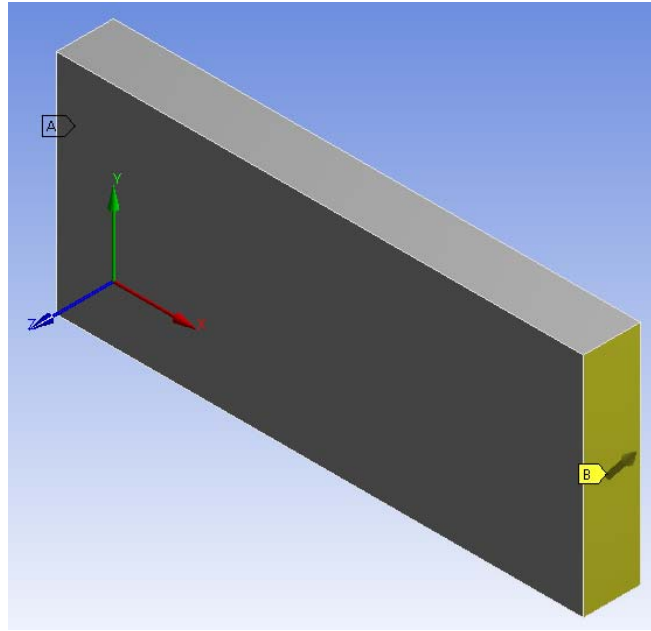
In summary, it was evident that the model has adequately predicted the test of PRESSS and its results were close to real life testing done by PRESSS. Overall exerted force of 25,000lbf reaction was close to that obtained by PRESSS results. Also, the overall dissipated energy resulted from this test was 439,923 lbf-in (49,689J). Ultimately, this could be used as a verification model to be used in the later analytical models of this research.

3.2.5 Simple plate models

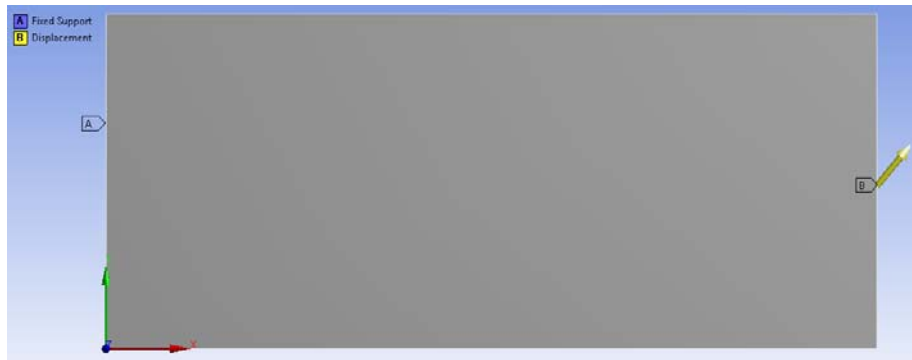
A simple plate model was chosen to explore and compare the behavior of other shapes with the U-shaped device. As indicated earlier, one of the potential beneficial attributes is a connector that would yield primarily in shear rather than in flexural. Thus, two connectors were modeled as simple plate connectors with the difference between the two being the geometric aspect ratio.

3.2.5.1 Simple plate model SP-1

The aspect ratio (width to height ratio) of this device was larger than two. The width was kept same to the overall width of U-shaped device (4.625 in.), and the height was 2-inch. The thickness was maintained at 0.5-inch. The boundary conditions were similar to the U-shaped device (Figure 3-23).



(a)



(b)

Figure 3-23: Simple plate model SP-1: (a) 3D view, (b) elevation view

The test is based on applying displacement to the free end of the simple plate and measure the reaction at the fixed end and then measure stress and strain energy. Displacement is applied in steps and in cyclical manner. **Error! Reference source not found.** shows the change in applied displacement with time. Figure 3-24 shows the equivalent (von Mises) stress in the plate. It could be noticed that almost the entire plate developed high stresses that exceeded the yield strength of the plate material which was 36 ksi. The maximum stress recorded in SP-1 was 56200 psi which is slightly more than the

maximum stress in the U-shaped device (56075 psi). However, the stress in U-shaped plate was concentrated at a few locations only, while for SP-1, the high stress covered the entire plate.

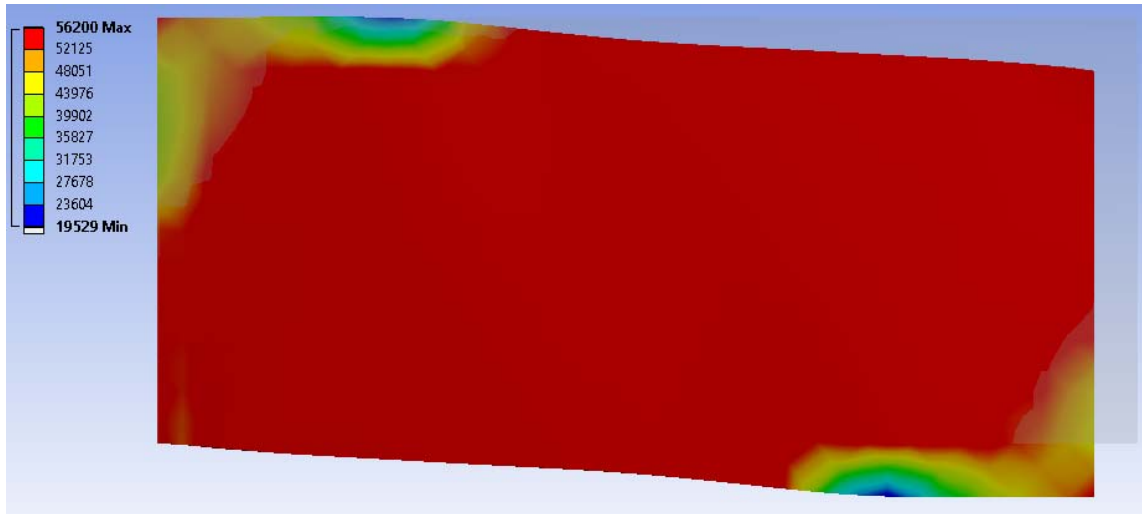


Figure 3-24: Equivalent stress contour map for SP-1

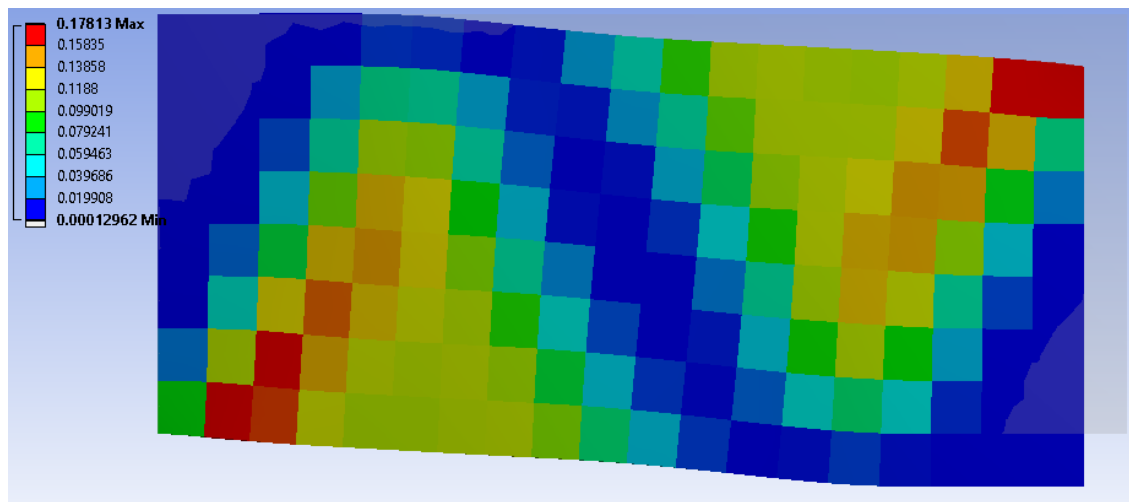


Figure 3-25: Strain energy contour map for SP-1

Figure 3-25 shows a contour of the overall strain energy in SP-1. It could be noticed that the strain energy (dissipated energy) in case SP-1 is higher than that for the U-shaped model. That result is reasonable since the stresses was higher. Figure 3-26 shows the relationship between the developed reaction force and the time step. The resulting maximum reaction is nearly twenty times higher than the maximum reaction for the U-shape model. Figure 3-27 shows the force - deformation relationship for SP-1. It represents a behavior similar to the behavior of U-shaped plate. However, the area under the

graph (energy dissipated) is significantly higher for SP-1. Figure 3-28 illustrates the relationship between dissipated energy and time. It could be observed that the overall dissipated energy in SP-1 is higher than that for U-shaped model results and as shown previously.



Figure 3-26: Reaction versus Time relationship for SPM-1

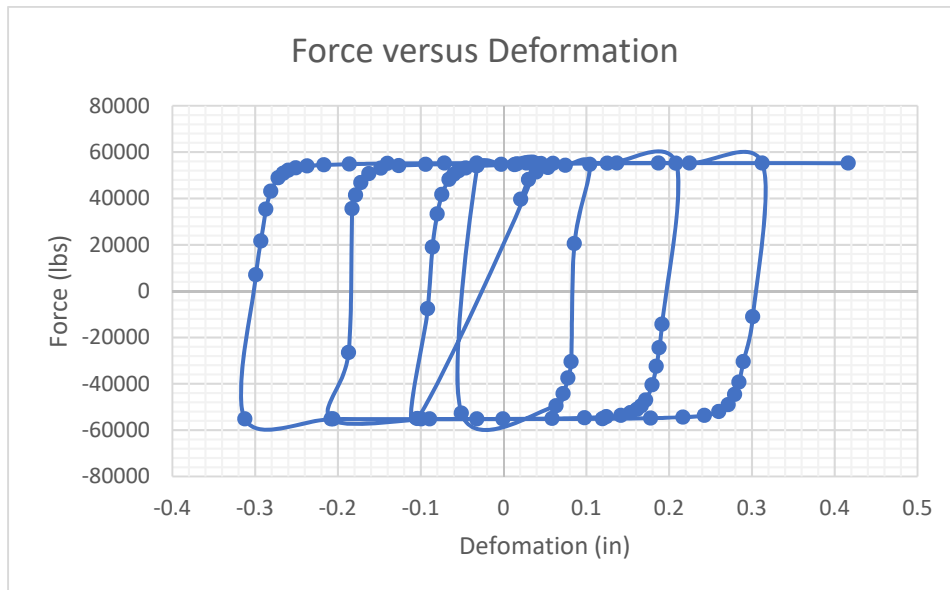


Figure 3-27: Force versus Deformation relationship for SPM-1

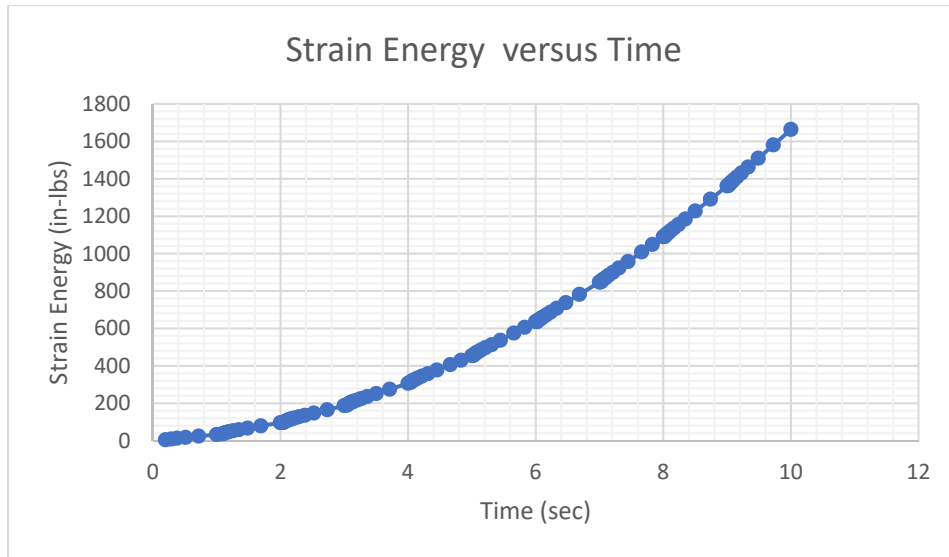


Figure 3-28: Strain energy for SPM-1

3.2.5.2 Simple plate model SP-2

The SPM-2 plate model had an aspect ratio of two with a width of 4.625in. and a height of 9.25 in. The width and thickness were kept the same as in previous models. The boundary conditions were also the same as U-shaped and SP-1 models (Figure 3-29).

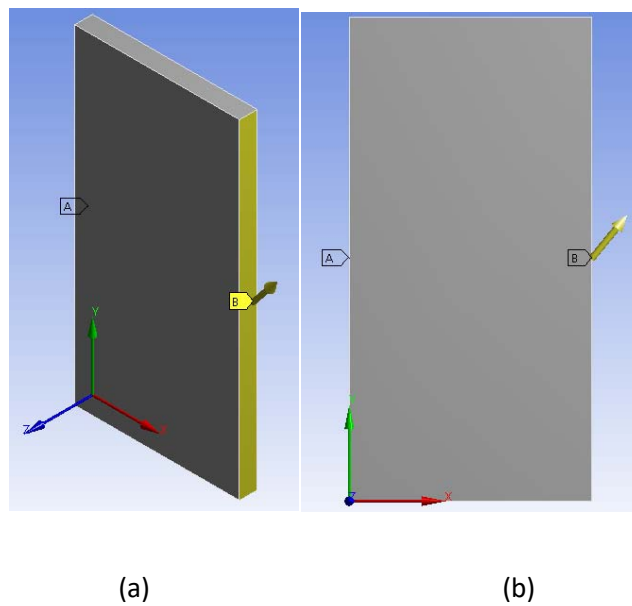


Figure 3-29: Simple plate model SP-2: (a) 3D view, (b) elevation view

The overall displacement is divided to 10 steps and as shown in **Error! Reference source not found.**. The test is a displacement-based test that is conducted by applying displacement to the free end over ten steps. Subsequently, the reaction at the fixed end, stress and strain energy. Displacement is applied in steps and in cyclical manner. Figure 3-30 (a) shows the results of equivalent stress in the plate after the test is done. The stress was spread all over the plate and almost the entire plate has yielded. Maximum stress in SP-2 is 56200 psi which is similar to SP-2 but slightly over the U-shaped stress (56075 psi). however, the stress in U-shaped plate was concentrated at few spots, while in the case of SPM-2 included the entire plate in a similar behavior of SP-1. Figure 3-30 (b) shows the contour map of the overall strain energy in SP-2. It could be noticed that the strain energy (dissipated energy) in case SP-2 is considerably higher than that of SP-1 and the U-shaped model. Figure 3-31 shows the developed reaction forces during the time steps. The resulting reaction was significantly higher than the reactions developed from the SP-1 model. This would require transfer of tremendous load to the fixed end (concrete shear wall) which could result in local failure of the wall. Figure 3-32 shows the force versus deformation relationship for SP-2. It represents a behavior similar to the behavior of both previous models. However, the area under the graph is appreciably higher than both previous models. The reason is due to the very high developed reaction. Figure 3-33 represents the relationship between dissipated energy and time. It could be noticed that the overall energy in SP-2 is substantially higher than any of the both previous models. It could be concluded that the simple plate model SP-2 with an aspect ratio of two is capable of dissipate very high energy. However, to the plate would also develop a very high force to the support, which could lead to local failure in the concrete at low displacements. Despite the fact that substantial energy is dissipated, the development of excessive reaction forces would make this model un desirable.

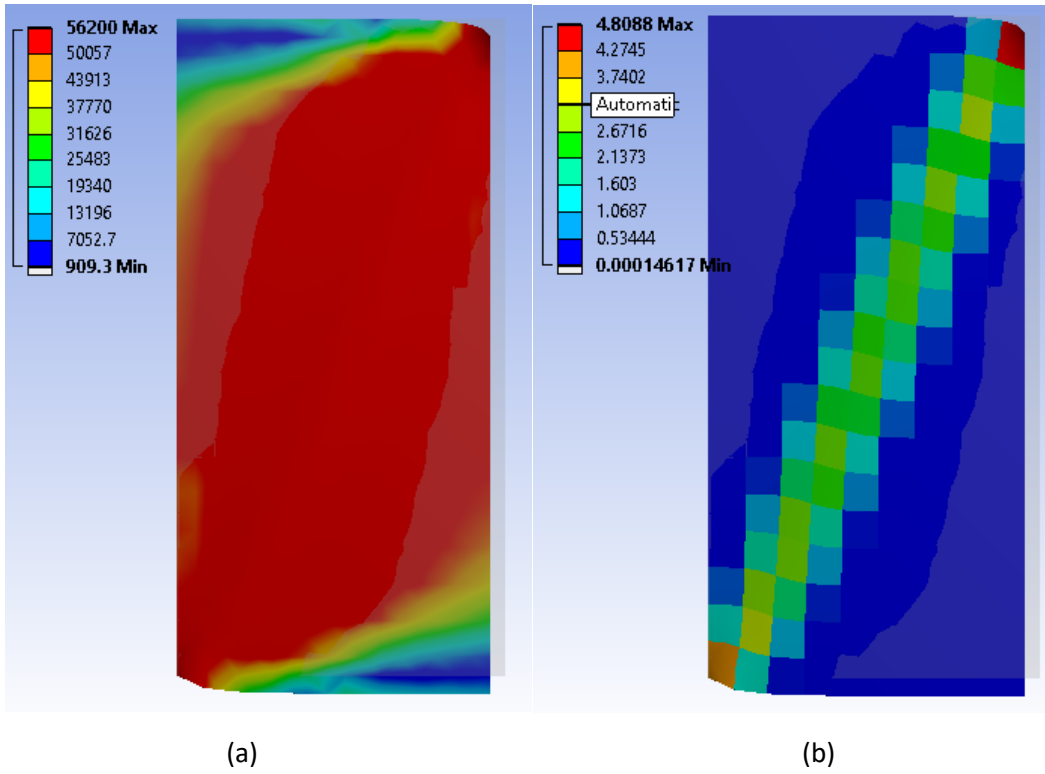


Figure 3-30: Equivalent stress and strain contour map for SP-2: (a) stress contours, (b) strain contours

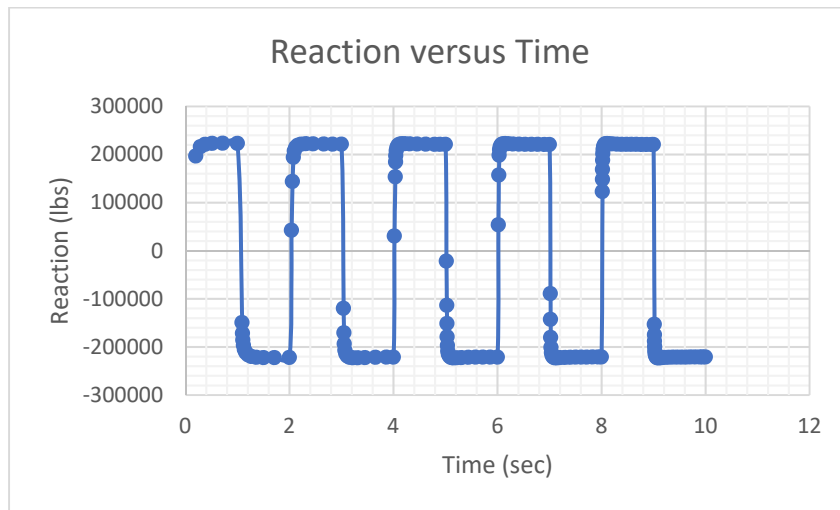


Figure 3-31: Reaction versus Time relationship for SP-2

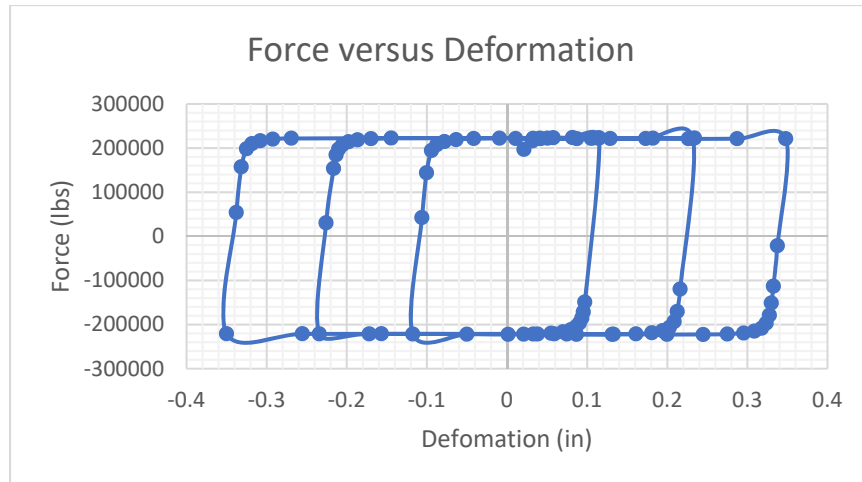


Figure 3-32: Force versus Deformation relationship for SP-2

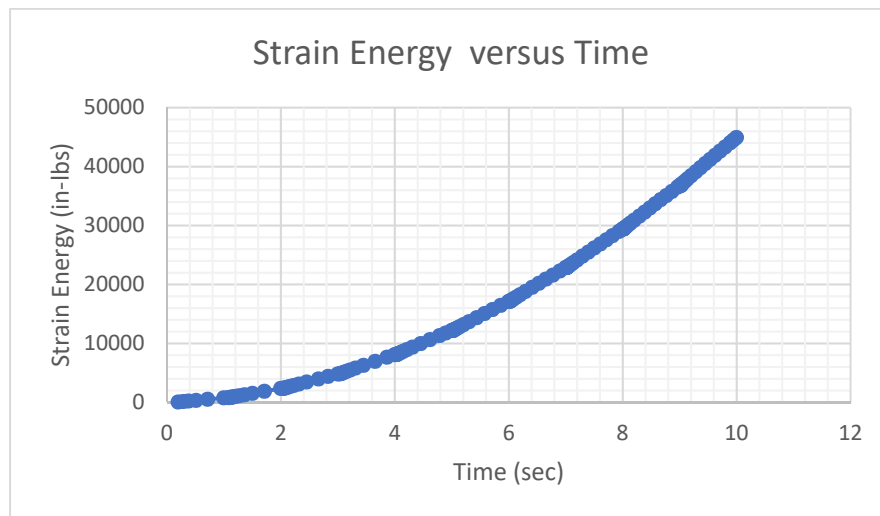


Figure 3-33: Strain energy for SP-2

3.2.6 Truss mechanism models

In this section, a trial was made to explore a shape with less volume than those of the simple plate models. Keeping in mind that the model should offer the same desired aspects of dissipating energy and transferring moderate loads to the support

3.2.6.1 Truss model TM-1

The TM-1 shape (Figure 3-34) had a width of 4.625 in., a height of 4 in, and a thickness of 0.5 in. (similar to earlier shapes). The left side (marked A) is fixed while displacement is applied to the free side

(marked B). The overall displacement is applied in 10 steps as shown in **Error! Reference source not found.** Subsequently, the reaction at the fixed end, stress, and strain energy are assessed. Figure 3-35 (a) shows a stress contour map for TM-1. In general, the top and bottom chords of the truss exhibit the highest levels of stress (maximum stress of 56200 psi). Figure 3-35 (b) shows the contour map of the strain energy of TM-1. It reflects yielding of both the top and bottom chords. Figure 3-36 (a) shows the developed reaction force with time. The maximum reaction is approximately 21000lbs, which is higher than that for the U-shaped model. Figure 3-36 (b) represents the relationship between deformation and reaction force. The area under the graph is significantly larger than that for the U-shaped connector due to higher force and deformation. Figure 3-37 shows the energy dissipated is slightly over double that dissipated from the U-shaped model. The TM-1 shape dissipated higher energy (than the U-shaped) but developed higher reaction force. The top and bottom chords yielded primarily in flexure and not shear.

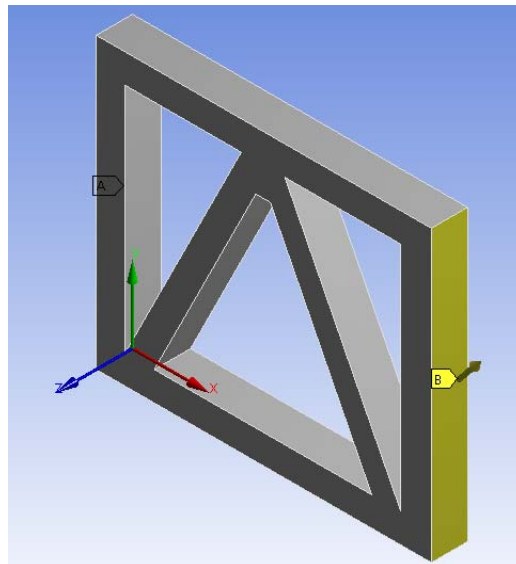
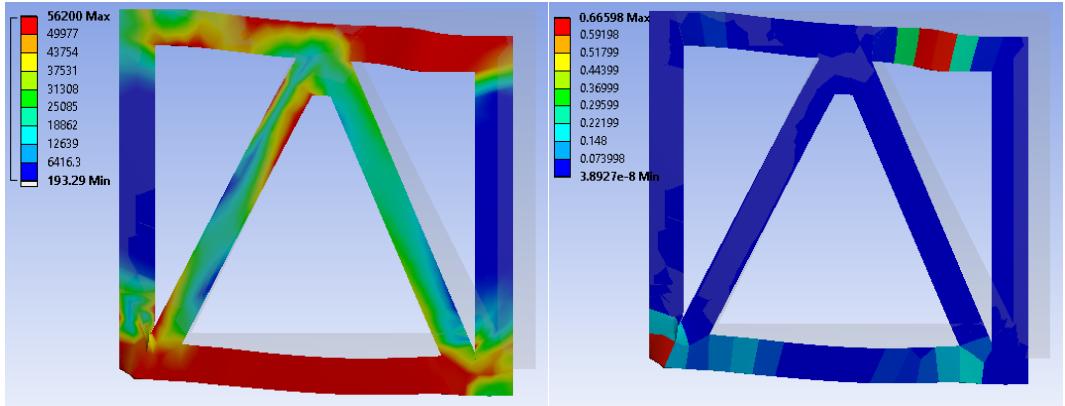


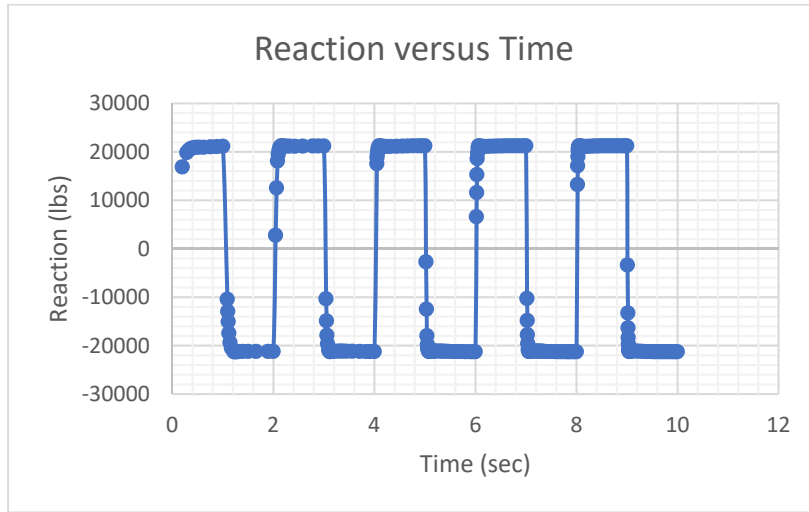
Figure 3-34: Illustration of TM-1



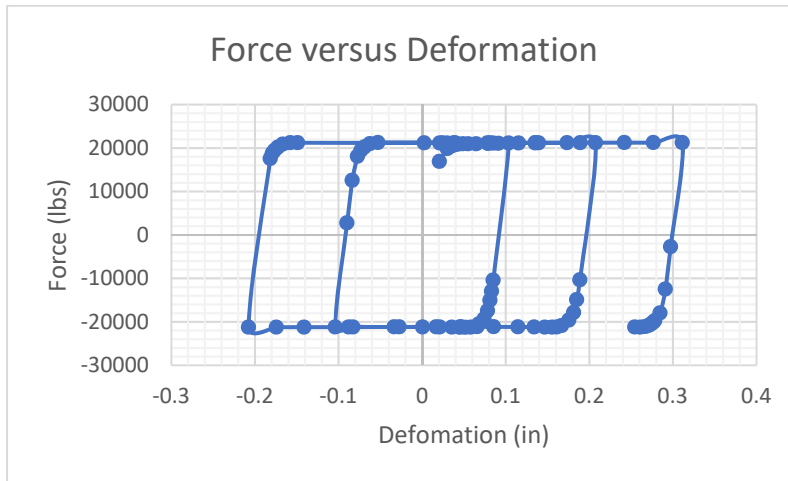
(a)

(b)

Figure 3-35: TM-1 response: (a) stress contours, (b) strain contours



(a)



(b)

Figure 3-36: TM-1 Response: (a) Reaction force, (b) Force vs Displacement

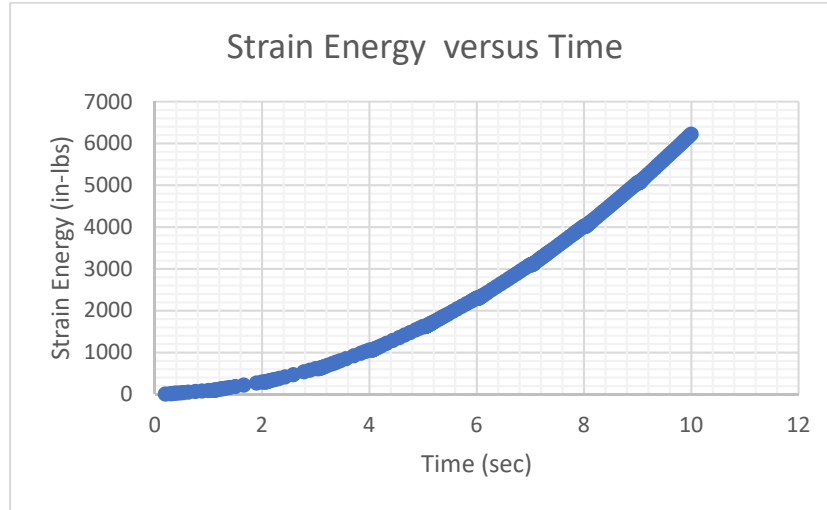


Figure 3-37: Strain energy for TM-1

3.2.6.2 Truss model TM-2

TM-2 has a width of 4.625-inch and a height of 9.25inches to maintain an aspect ratio of two. Figure 3-38 show TM-2. The thickness of this model is used as 0.5-inch which is similar to all previous models. One side is assumed to be fixed which is the side labeled “A” in Figure 3-38, while displacement is applied to the free side labeled “B”. The overall displacement is applied in same manner that have been use in all other tests where it is divided into 10 steps and as shown in **Error! Reference source not found.** The test is a displacement-based test that is conducted by applying displacement to the free end over ten steps. Subsequently, the reaction at the fixed end, stress and strain energy. Displacement is applied in steps and in cyclical manner. Figure 3-39 (a) shows the overall contour map of the equivalent stress (Von Mises) for TM-2. It could be noticed that the horizontal chords have experienced highest levels of stress. The maximum stress resulted in the model is 56198 psi which is close to stress resulted in other tests. Furthermore, it could be seen from Figure 3-39 (a) that the horizontal chords yielded in bending and that could be due to slenderness effect. Figure 3-39 (b) shows the contour map of the strain energy of TM-2. It shows that only few spots have dissipated energy higher than the average of the entire model. The spots of higher energy dissipation are the spots of stress concentration and spots

in top and bottom chords. Figure 3-40 shows the relationship between the resulted reaction with time. The maximum reaction is approximately 43000lbs which is appreciably higher than that for U-shaped model. Also, it's almost doubles the reaction resulted in TM-2. In general, that reaction is very high and could cause local failure in the fixed support. Figure 3-41 represents the relationship between deformation and resulted reaction. It shows an expected behavior and shape of this relationship. Figure 3-42 shows the relationship between strain energy and time. The maximum energy dissipated is less than those of U-shaped and TM-1. TM-2 has shown that the overall behavior is poor comparing to U-shaped model. It dissipated less energy and allowed higher load to be transferred to the support. Ultimately, TM-2 is not efficient since it does not support the main two aspects of this test.

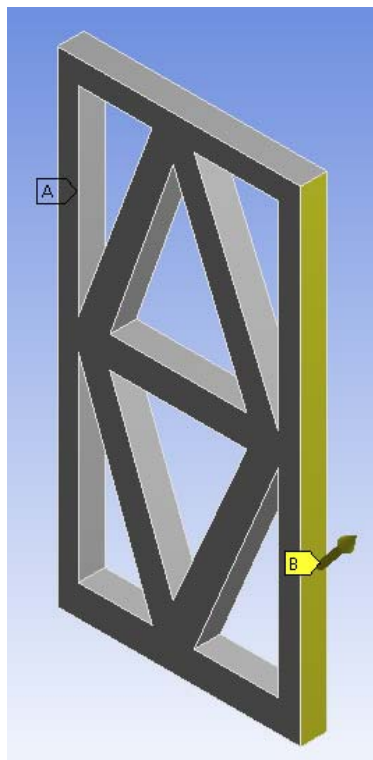
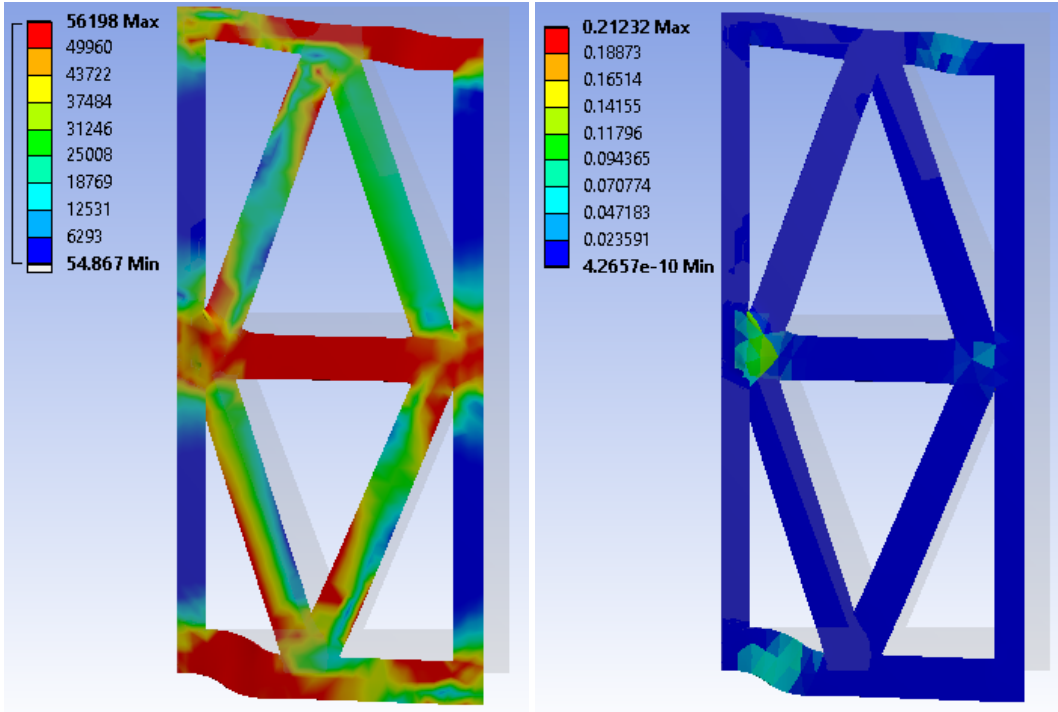


Figure 3-38: Illustration of TM-2



(a)

(b)

Figure 3-39: TM-2 response: (a) stress contours, (b) strain contours

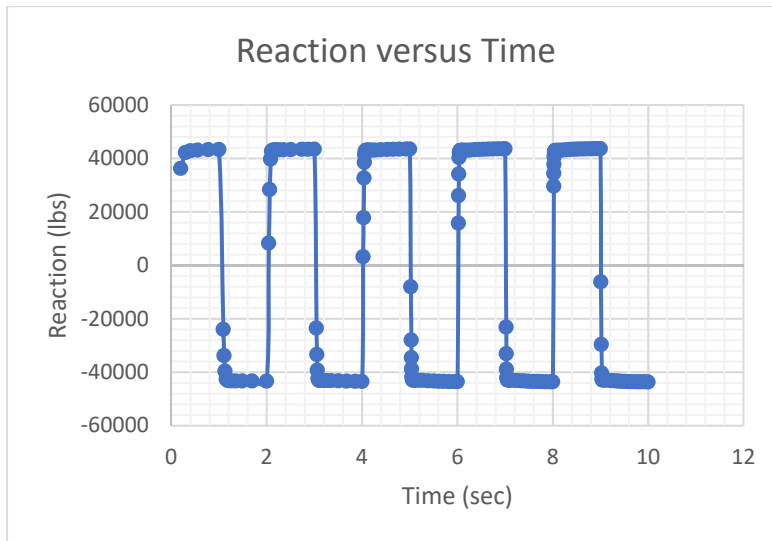


Figure 3-40: Reaction versus Time relationship for TM-2

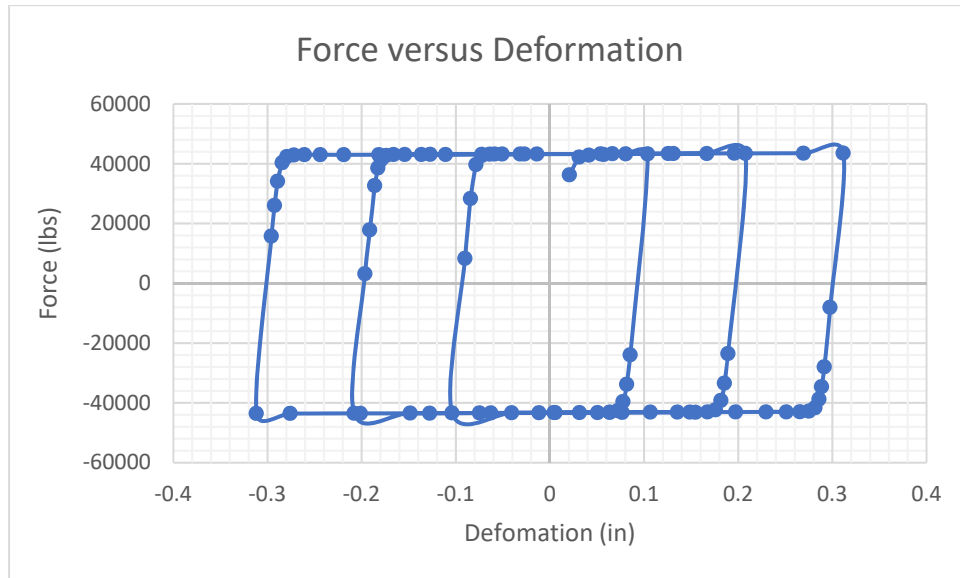


Figure 3-41: Force versus Deformation relationship for TM-2

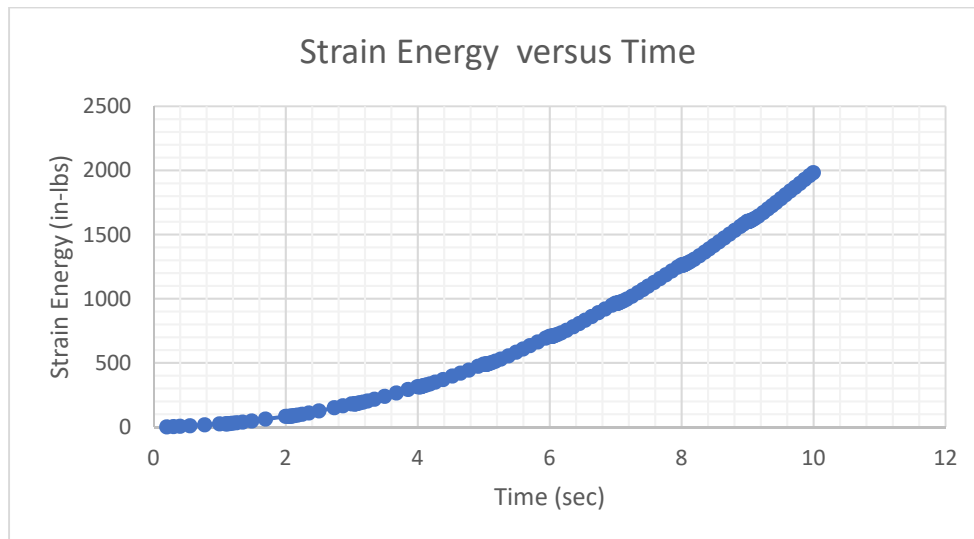


Figure 3-42: Strain energy for TM-2

3.2.7 Beehive-shaped (Hexagonal) model

This shape (Figure 3-43) is designed to have the same overall material volume as the U-shaped model.

The thickness of the beehive-model is set at 0.5 in and the six legs are approximately 3.10 in length.

Also, the width of model is set to be 4.625-inches. The boundary conditions were the same as those

described earlier. The “A” and “B” sides and the imposition of displacements are as described earlier (for other shapes). Figure 3-44 (a) shows the stress contours in the beehive-model. It could be noticed that most of the reached the yield stress of the plate material. Maximum stress in SPM-1 is 56200 psi which is slightly over the U-shaped stress (56075 psi). However, the stress in U-shaped plate was concentrated at few spots, while in case of beehive-model the edges of top and bottom legs have reached yield stress limit. Figure 3-44 (b) shows the contour map of the overall strain energy in beehive-model. It could be noticed that the strain energy (dissipated energy) in beehive-model is slightly higher than that for the U-shaped model in comparison to other models. In addition, only few spots have extreme dissipated energy, which indicate to good behavior under applied loads. Figure 3-45 shows the relationship between the resulted reaction and the time. The resulted reaction is higher than that for the U-shaped model. However, comparing to other models, the reaction is acceptable. Figure 3-46 shows the force versus deformation relationship for beehive-model. It represents a behavior similar to the behavior of U-shaped plate. However, the area under the graph is definitely higher for than that for U-shaped model, since the reaction is almost three time that for the U-shaped mode. Figure 3-47 represents the relationship between dissipated energy and time. It could be noticed that the overall energy in beehive-model is higher than that for U-shaped test. It could be concluded that the beehive-model is capable to dissipate energy higher than that of U-shaped model. However, the resulted reaction from testing this model is relatively high at the fixed end (support). However, this model is promising and could be improved. Ultimately, this model could provide the desired ultimate goals of this study by reducing/increasing the overall volume or change the geometry slightly.

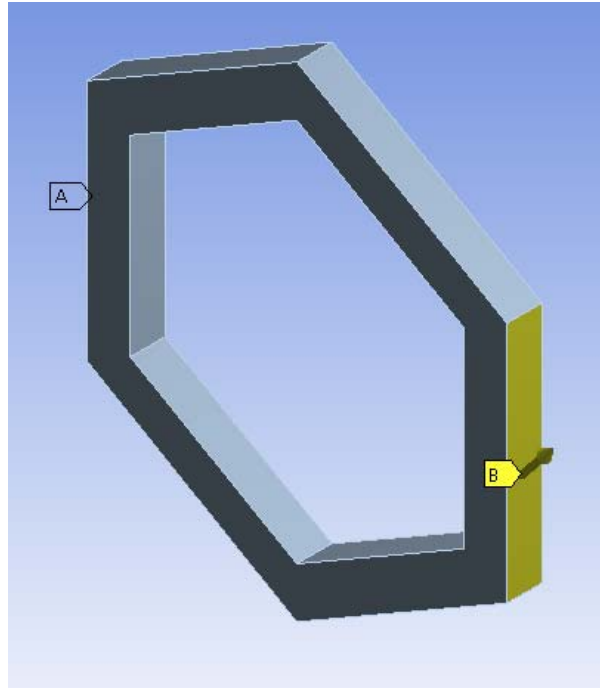


Figure 3-43: Beehive-shaped model

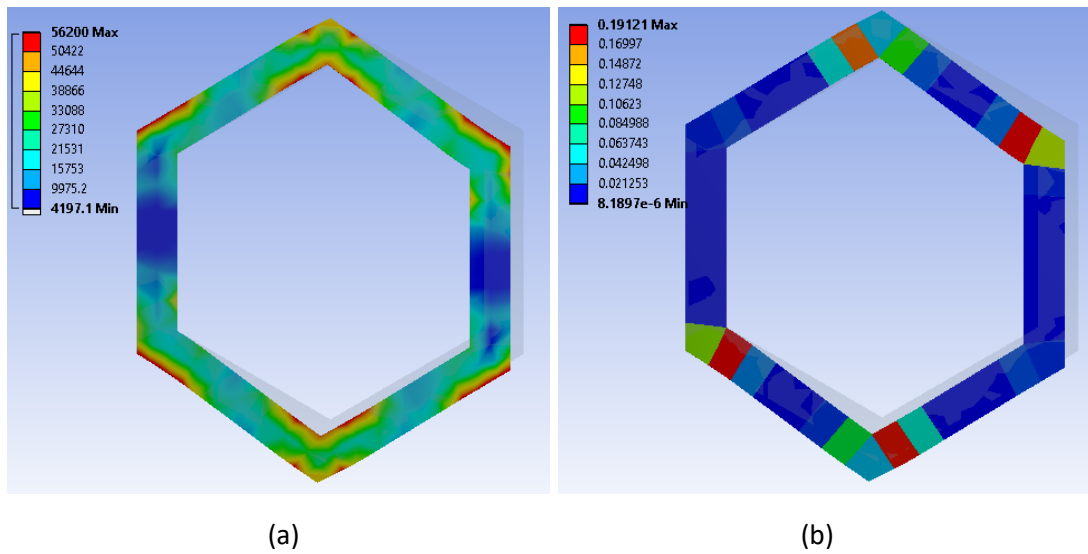


Figure 3-44: SPM-1 response; (a) stress contours, (b) strain contours



Figure 3-45: Reaction versus Time relationship for SPM-1

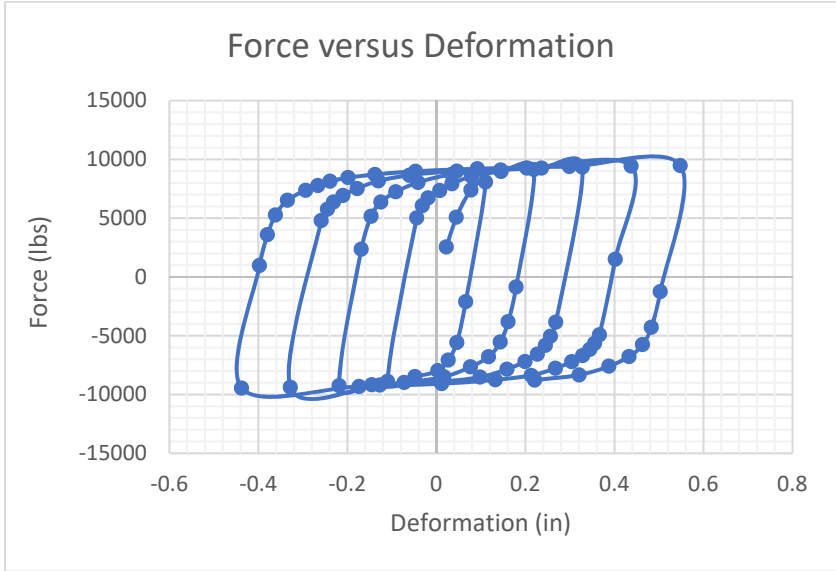


Figure 3-46: Force versus Deformation relationship for SPM-1

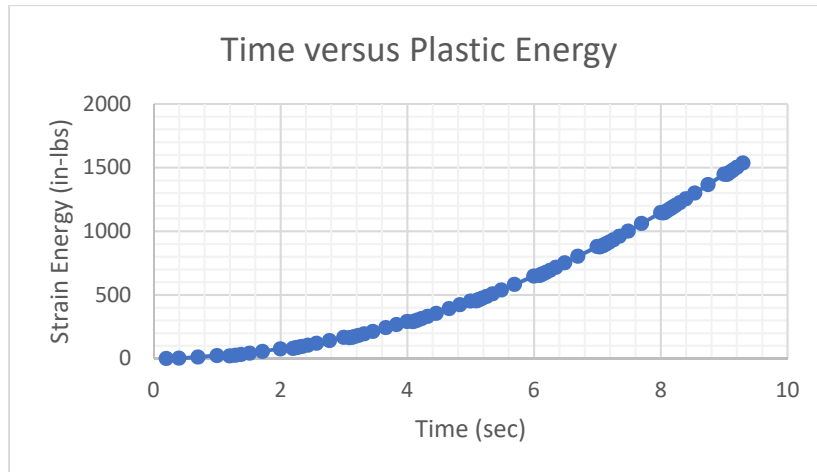


Figure 3-47: Strain energy for SPM-1

3.2.8 Model OS-2D

First model is taken based on the results of the topology optimization conducted on a block of material that is subjected to displacement on one side while fixing the opposite side as shown in Figure 3-48 through Figure 3-50. The height of the model is 6.5", width is 4.625" and depth is 5" to mimic the overall dimensions of standard U-shape connector. The thickness of sides plates is 0.5". It has two diagonal legs that have depth of 3.5" and width of 1.5".

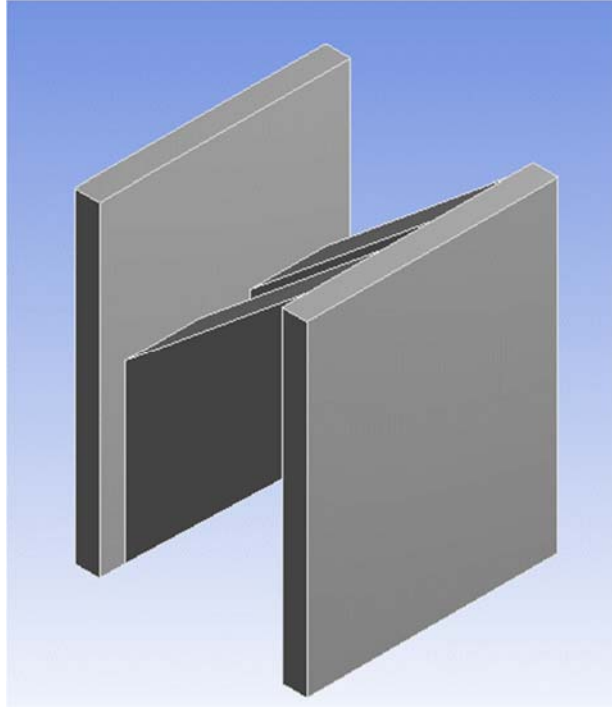


Figure 3-48: Model OS-2D

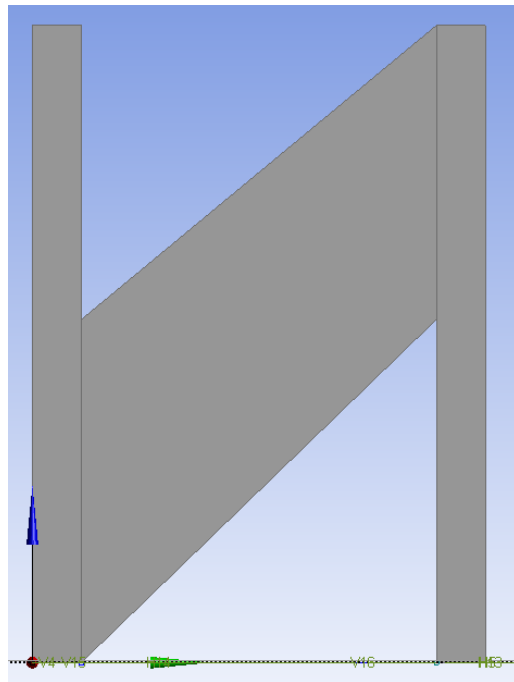


Figure 3-49: Model OS-2d - Side view

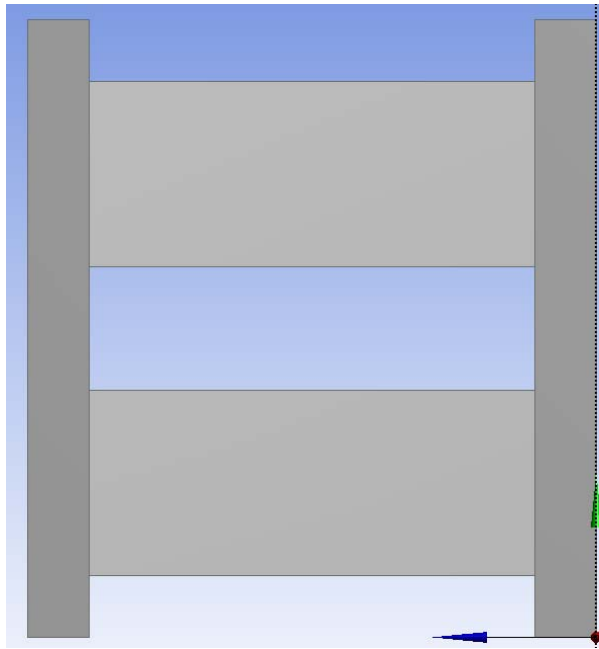


Figure 3-50: OS-2D - Top view

The model was tested under same test configuration that's used to test U-shaped plate connector. One side fixed and the opposite side was under 0.328" displacement in X-direction and 0.402" displacement in Y-direction. Figure 3-51 shows model OS-2d and testing boundary conditions. Figure 3-52 shows the contour map of equivalent stress of model OS-2D. The resulted dissipated energy was higher than that of U-shaped connector. Also, the resulted reaction force was significantly higher, which is not preferred due to the damage could be caused to supporting elements. The summation of C-Index of OS-2D model at all steps is 303 comparing to 107 of the U-shaped connectors. Figure 3-53 shows the dissipation energy graph throughout the test. Figure 3-54 shows the developed reaction force at each step of the analysis. The OS-2D model developed a very high reaction force that is not preferred since excessive reaction force can damage the concrete in the shear wall in the vicinity of the connection.

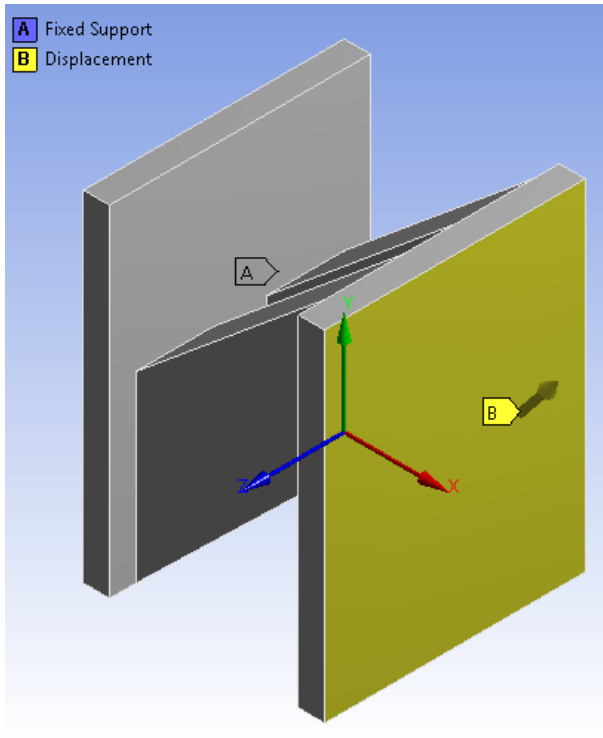


Figure 3-51: OS-2D boundary conditions

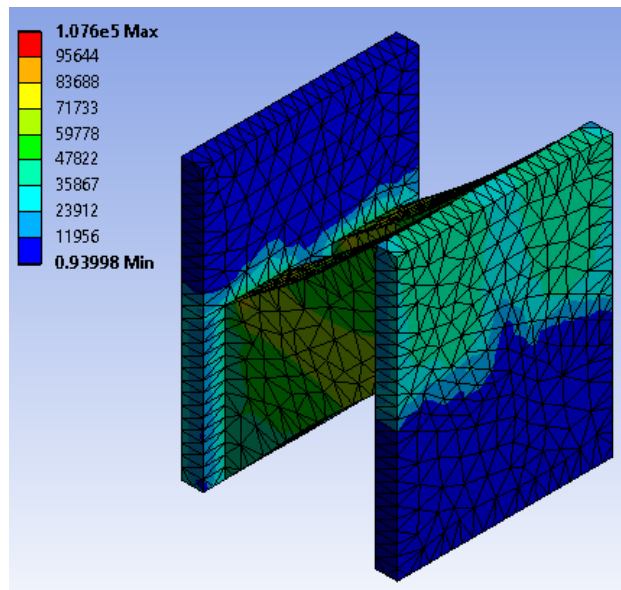


Figure 3-52: Stress contour map of model OS-2D

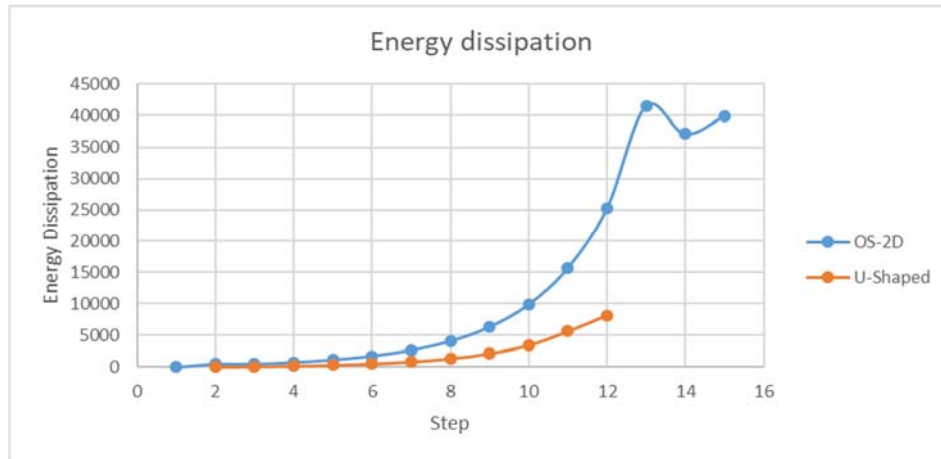


Figure 3-53: Dissipated energy of model OS-2D

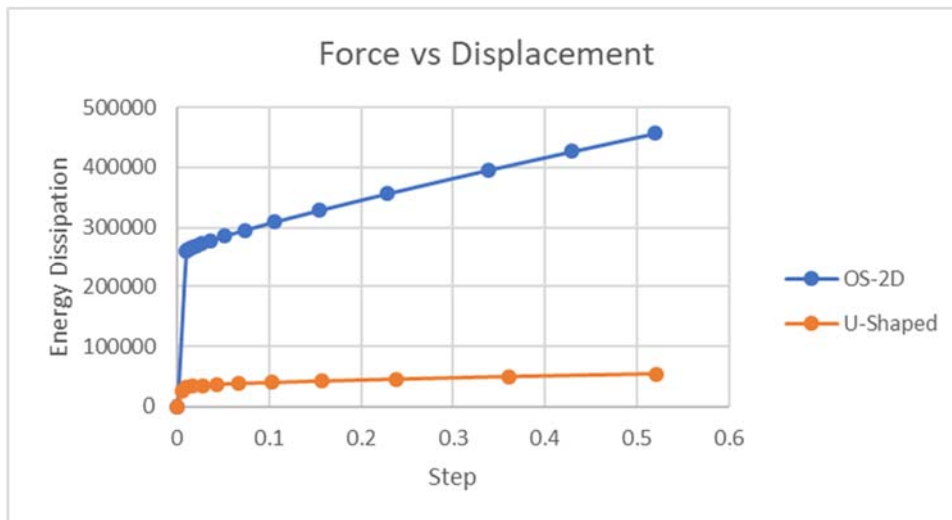


Figure 3-54: Force vs Displacement results of OS-2D

3.3 Topology optimization and Model development

3.3.1 Introduction to topology optimization

Topology optimization is a mathematical approach that enable engineers and designers to come up with the most efficient and economic shapes for their design under certain loadings, boundary conditions, and other constraints [27] & [28]. This approach could be used for small-size applications such as

connections and automobile parts, or large-size applications such that buildings, dams, and bridges. This optimization approach is a useful and time-saving tool when all that is known about a physical model is limited to boundary objective functions, size, and constraints.

Topology optimization has been incorporated into several finite element software packages to optimize geometry using a number of methods including the optimality criteria algorithm, the method of moving asymptotes, or various genetic algorithms [28]. A method used to optimize the geometry and shape of a structure is the Deformable Simplicial Complex (DSC) method, which uses a special type of meshing to provide adaptive resolution and determine the optimum shape with fine details [27]. In the Discrete Topology Optimization, each element is represented by either zero or one. Zero means that the element does not contribute to the response. Thus, the removal of that element would not affect the overall response of the structure. On the other hand, one means that the presence of that element is required and thus it should be kept [28] & [29].

Nowadays, finite element software such as ANSYS and ABAQUS have built-in topology optimization modules that make the design process accessible and easier.

While using topology optimization, a designer would model the overall size (dimensions) of an object and assign boundary conditions. Subsequently, the optimization constraints are assigned such as volume constraint (ratio of final to initial volumes). Lastly, the objective function is defined. Examples include maximizing stress, minimizing weight, minimizing reactions, or maximizing strain energy.

Asger et. al. [27] used topology optimization to determine the geometry of a bridge using the Deformable Simplicial Complex (DSC) method. The author used a tube-like shape and assigned a non-design part (bridge deck). The rest of the structure was assigned to be subject to the topology optimization. The load was applied on the deck. Figure 3-55 (a) through (g) show the progression of the analyses. The volume of the designed part at each stage was considered as a constraint to be further

reduced. Stress was used as objective function to be maximized within the allowable limits. The optimization process was performed over seventy steps in which the elements with lower stresses were removed. The final step shows the non-design and optimized parts of the model.

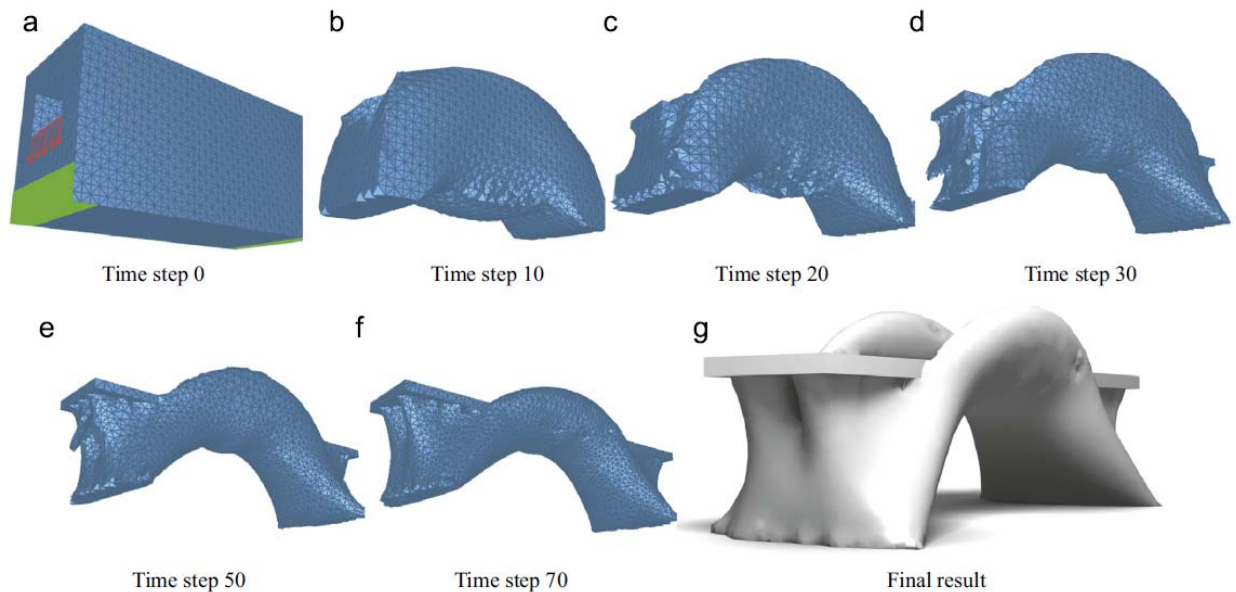


Figure 3-55: Optimization process [27]

The topology optimization was utilized to obtain the best shape that could fulfill have high energy-dissipation capability while limiting the developed reaction force to a level acceptable for resistance by the wall. This must be done while avoiding premature failure of the connector in the form of low-cycle fatigue. The high energy-dissipation capability for a given displacement requires high reaction forces, but those forces should not be too high resulting in localized concrete failure at the connections. The Topology optimization studies were done using three different software programs (ABAQUS, ANSYS and Solid Thinking) to compare and obtain the final shape that could fulfill all aforementioned requirements. In the next section, a brief discussion of each of the three software programs is presented.

3.3.2 ABAQUS topology optimization

Topology optimization is an iterative process that helps develop and refine designs after providing all required inputs. Normally, input parameters include the type of material, boundary conditions, loads, geometry restrictions or constraints, and a definition of parts of the structure that need to be left unchanged [33]. Topology optimization supports two types of algorithms. The general topology optimization uses an algorithm that adjusts the density and stiffness of the design elements while trying to satisfy the objective function under the constraints. The condition-based topology optimization uses the strain energy and stresses at the nodes as input data and does not calculate the local stiffness of the design elements.

In this section, a shape with similar overall dimensions to the U-shaped plate was modeled. A block of steel with a height of 6 ¼-inch, width of 4 5/8-inch, and depth of 5-inch was run through the topology optimization module in the ABAQUS software. Figure 3-56 shows the initial (starting) shape prior to optimization.

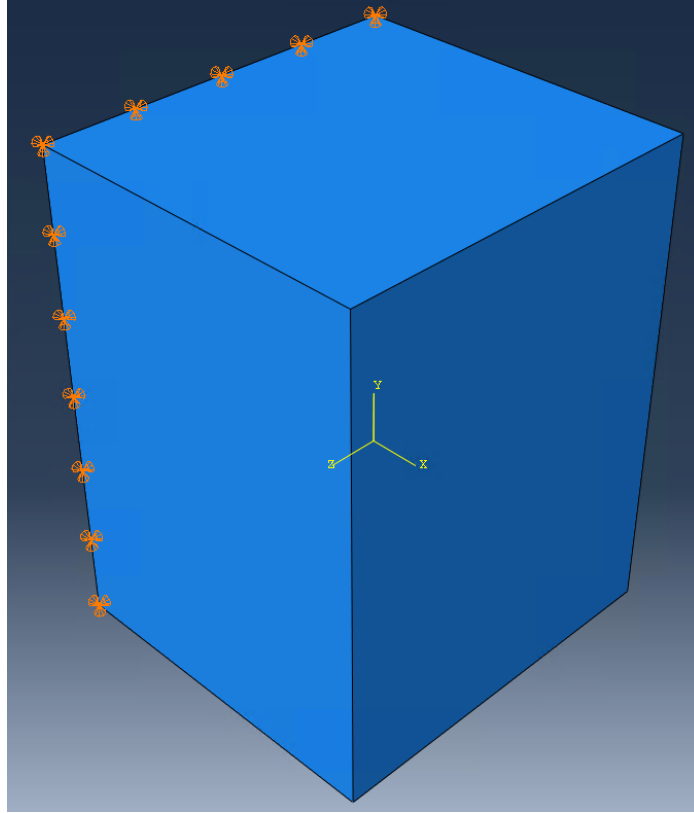


Figure 3-56: Starting (initial) block model prior to topology optimization

The boundary condition applied are as shown in Figure 3-57. One face of the block was assumed to be fixed in X, Y, and Z directions, while all the nodes on the opposite face a were subjected to a displacement of 0.402-inch in the vertical (Y) direction, and 0.328-inch in the X-direction in increments.

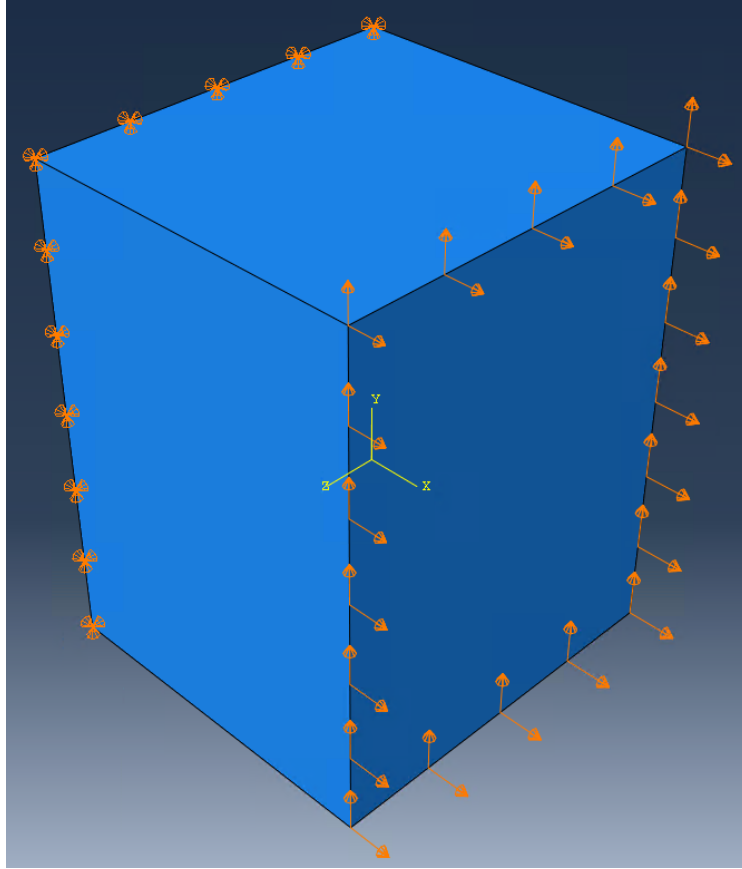


Figure 3-57: Boundary conditions and locations of imposed displacement

This imposed displacement was chosen to mimic the finite element analysis that was done previously on U-shaped connector. For the topology optimization analysis, the maximum volume of block was constrained to 40% of the initial volume. The objective was to maximize the strain energy. In addition, both the loading and boundary conditions were fixed during the optimization process. Figure 3-58 shows the optimization process over thirty steps. The red curve represents the strain energy and the blue curve represents the remaining volume.

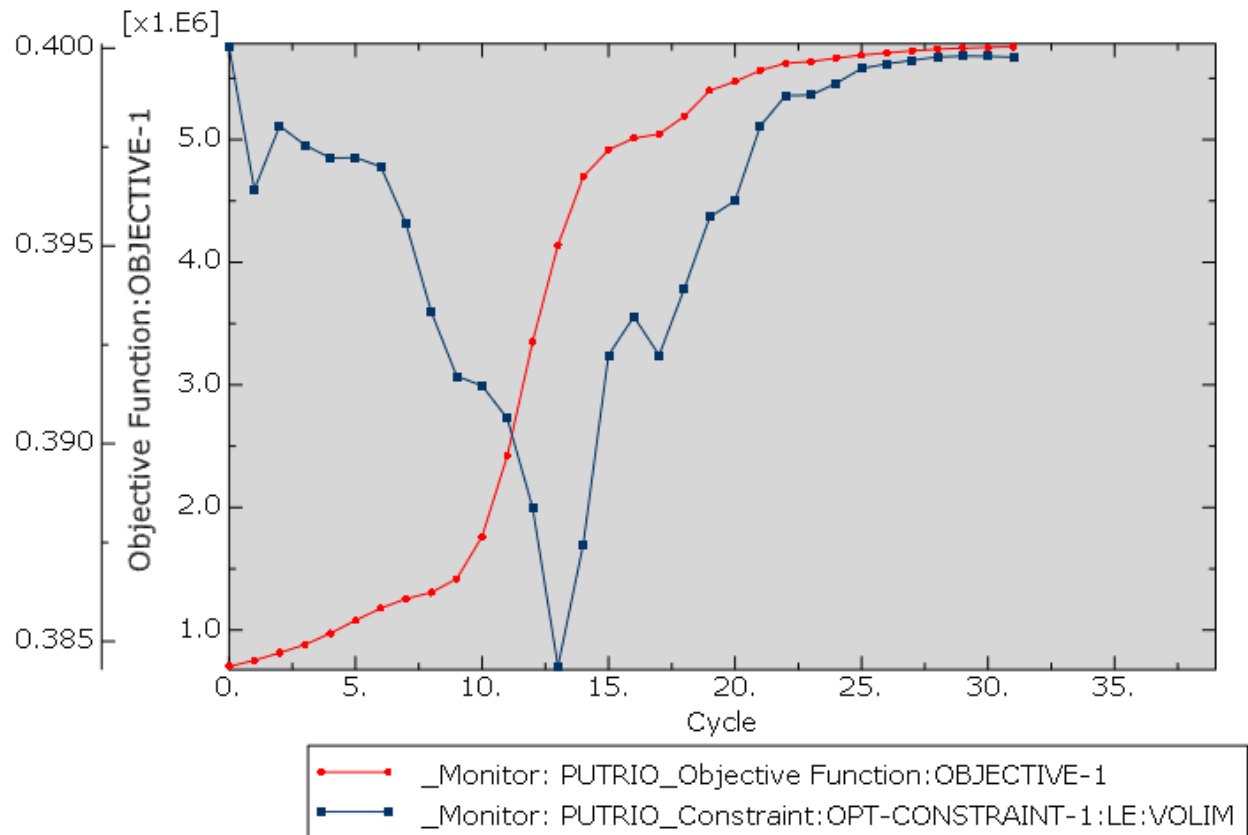
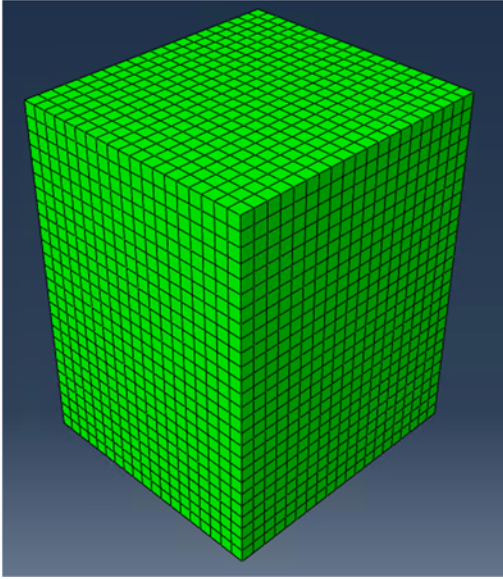
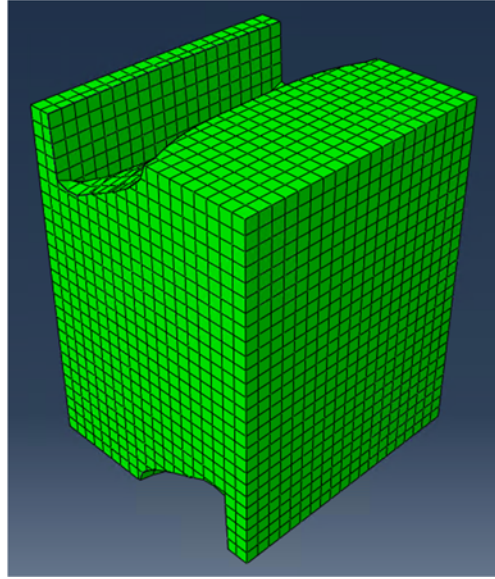


Figure 3-58: Various of strain energy and volume during the optimization cycles.

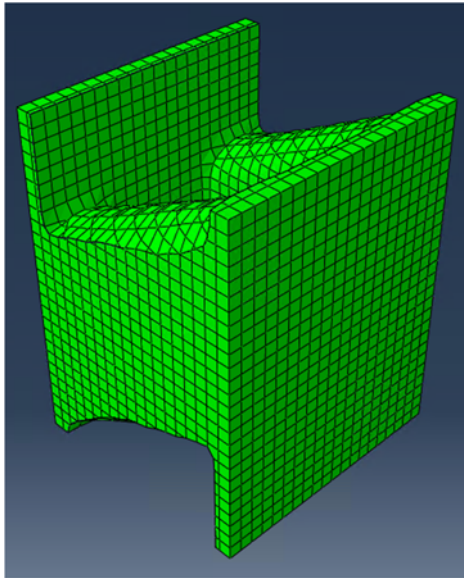
Figure 3-59 (a) through (d) show the optimization steps with the initial shape shown in Figure 3-59 (a). It could be predicted that blue colored materials will be removed during the optimization process. The unstressed elements were removed with more analysis steps. However, at some stages, some of the removed elements were added back to the shape to meet the objective and constraints of the optimization. Figure 3-60 shows the stress contour map of analyzed shape. Figure 3-61 (a and b) show stress contour maps for the initial, middle and final shapes, respectively. Blue-colored elements are removed from the shape.



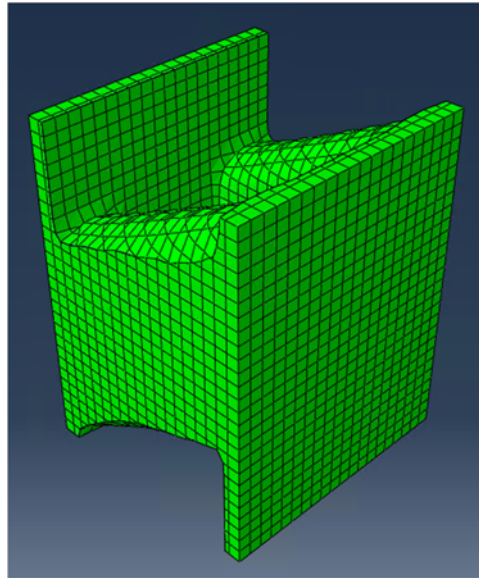
(a)



(b)



(c)



(d)

Figure 3-59: Optimization steps

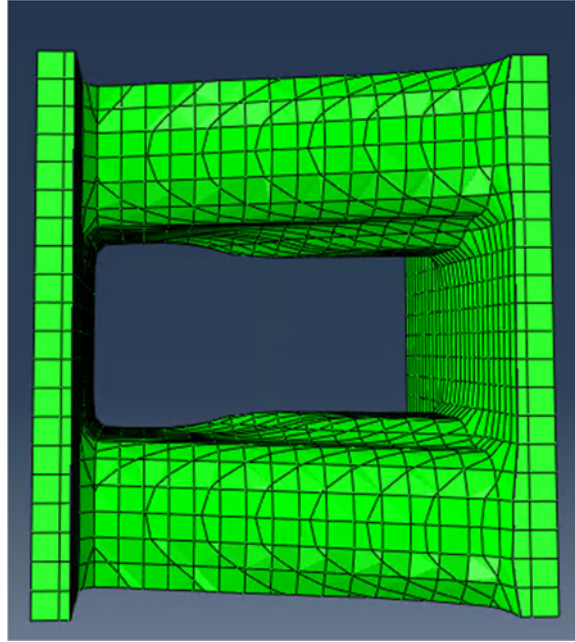
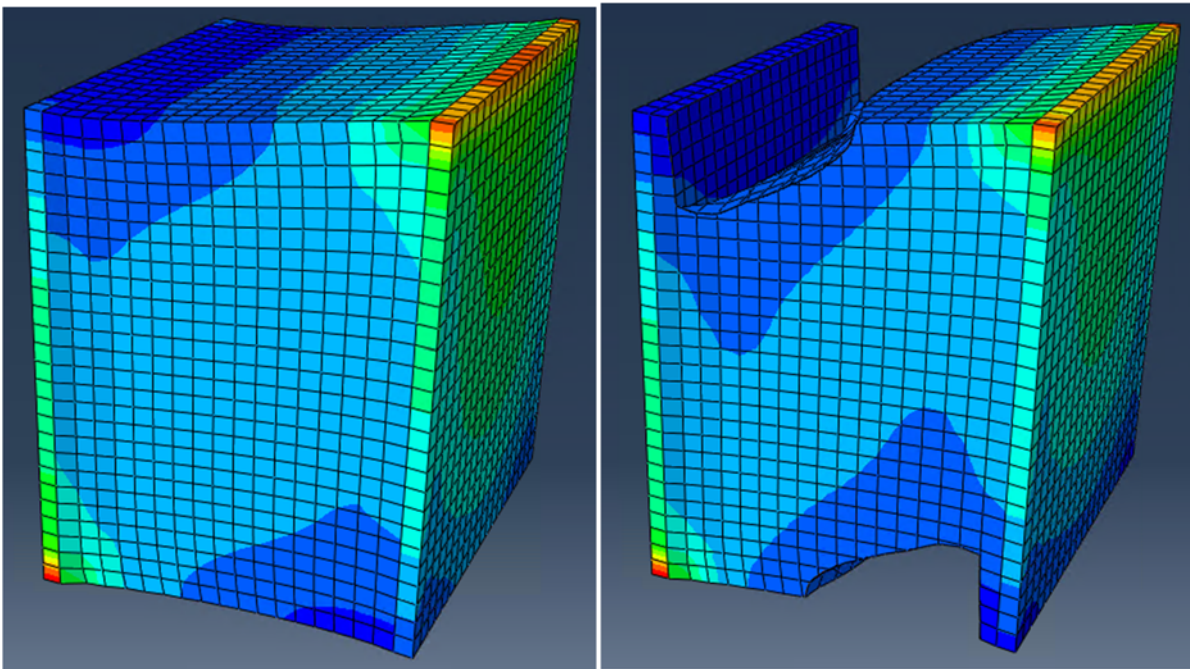


Figure 3-60: Top view of optimized shape



(a)

(b)

Figure 3-61: Stress contour map of initial shape

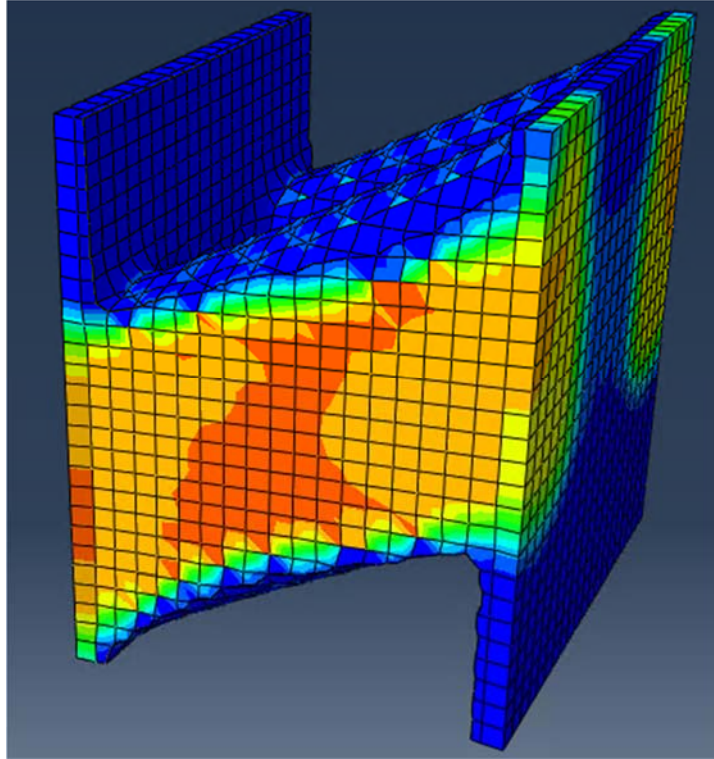


Figure 3-62: Stress map contour for the final optimized shape

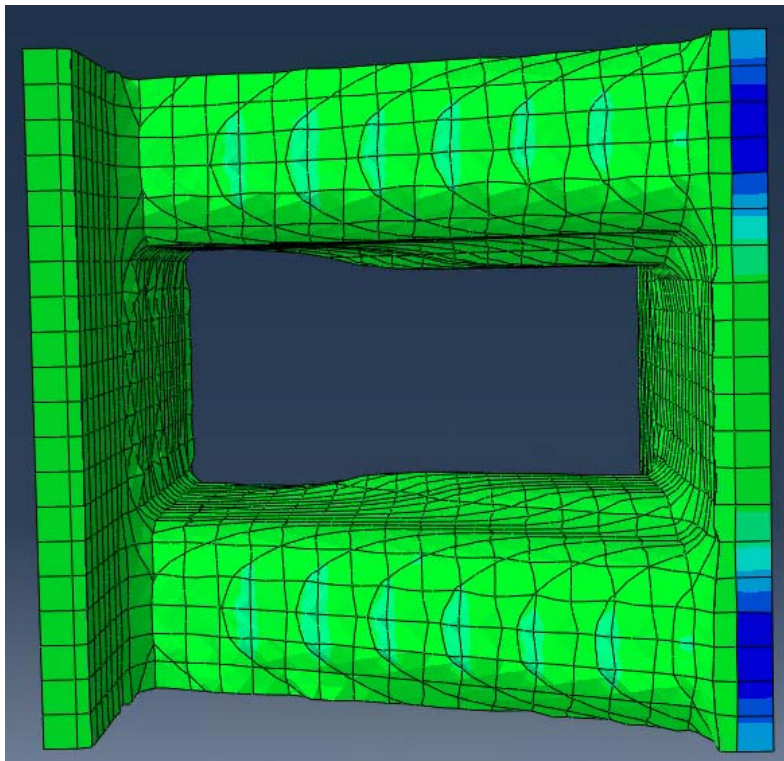


Figure 3-63: Plan view of stressed optimized shape

In summary, it is evident that the topology optimization approach can be used to develop shapes for the seismic connector. The Main requirements for choosing the connector are high levels of dissipated energy and reaction force that is limited to what can be resisted by the concrete at the connection with the shear wall. The cumulative dissipated energy for an elastoplastic system can be estimated by multiplying the imposed deformation by the reaction force.

Based on the topology optimization model discussed above, the best shape may have two inclined legs that connect the fixed side to the moving side of the connector.

3.3.3 ANSYS topology Optimization

The ANSYS software uses the Sequential Convex Programming method, which is an extension of the Method of Moving Asymptotes (MMA). The MMA works with a series of simpler subproblems and the solution of the subproblem is then used as the next design in the iterative process [34]. The test for acceptance is through a merit function [26]. The merit function measures the progress and properly combines the objective function and the constraints.

3.3.4 Altair (SolidThinking) topology Optimization

The Solid Thinking software alters the material distribution to optimize the user-defined objective under given constraints [35]. The software uses an iterative procedure known as the local approximation method to determine the solution of the optimization problem [35].

Two convergence tests are used by Solid Thinking and satisfaction of one of these tests is required. The Solid Thinking software utilizes gradient-based optimization algorithms to solve the optimization problem. The default optimization algorithm is known as the Method of Feasible Directions (MFD) [35].

3.3.5 Results of the topology optimization of different FEM software

Topology optimization was used to develop shapes with different geometries in order to get the objective of this study. As a start, analytical model of a steel block was optimized using ABAQUS. A cyclic displacement was applied in the vertical direction (as assumed in the PRESSS study). Figure 3-64 shows a typical model configuration and boundary conditions. The objective was to maximize the strain energy while setting a maximum volume constraint. The optimized shape is shown in Figure 3-65.

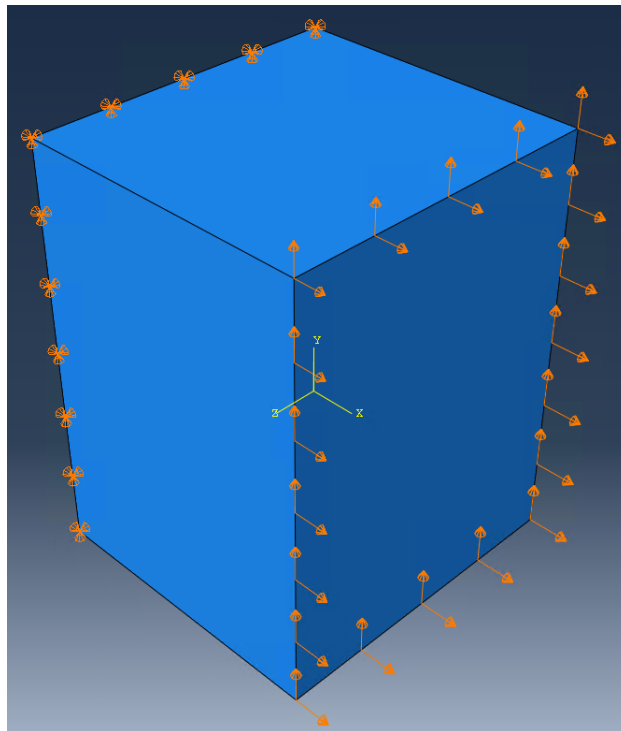


Figure 3-64: General shape and boundary condition

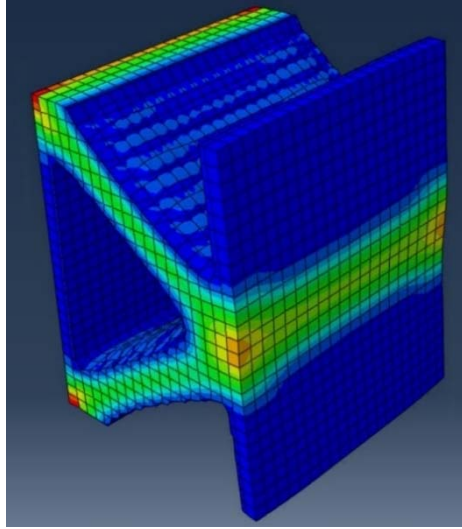


Figure 3-65: Optimized shape.

And for sake of comparison, same optimization model was developed and ran in Solid Thinking. Figure 3-66 shows results of Solid Thinking model run. ANSYS and Solid Thinking models were also run for comparison purposes. to check the results of all three programs for comparison. Figure 3-67 shows the optimized ANSYS results, which were similar to the ABAQUS results.

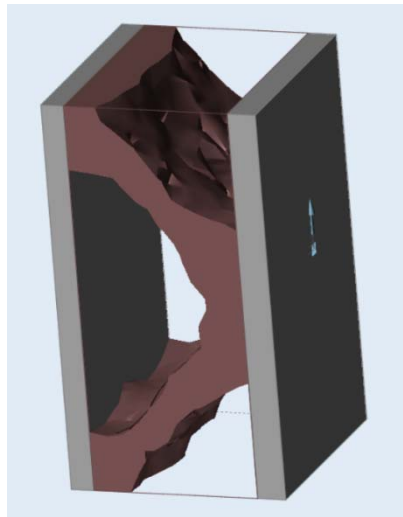


Figure 3-66: Altai (SolidThinking) optimization output

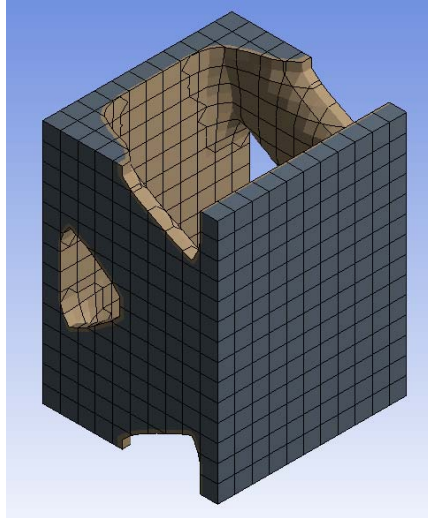


Figure 3-67: ANSYS optimization results

The analyses confirmed that the three programs had similar output regardless of the algorithms used in those programs. The analyses to determine the final optimized shapes was done using ANASYS due to the relative ease of its use. Later, ABAQUS was also used in the finite element analyses of the optimized shapes.

As a summary of the use of topology optimization, they final optimized shaped lacked symmetry about global X and Y axes that is believed to be necessary in the proposed shape. Moreover, and after running further FEM analysis, high localized plastic strain areas were present in the optimized shapes. However, when thicker material used to overcome the problem of high plastic strain, the resulted reaction forces were increased drastically. Thus, it was determined that the concept of trial and error must be used to meet the final goals of this study.

3.4 Behavior of connectors

During the initial investigation work done in this study, many different geometries were investigated, and their shapes were analyzed in ABAQUS to assess their response with respect to the study objectives. One of the major reasons that many of the early shapes are not selected for further investigation was the development of relatively high reaction force that would be exerted on the supporting shear wall members. Although higher reaction force would result in higher energy dissipation, the force has to be limited, and thus the early shapes were rejected.

3.4.1 Vertical response (Equivalent vertical springs)

3.4.1.1 Vertical response of U-shape model

Several analytical models for the U-shaped connector have been extensively discussed in sections 3.2.1 through 3.2.4.

3.4.2 Horizontal response (Equivalent horizontal spring)

It became necessary to examine the response of the U-shaped connector under horizontal displacement only and evaluate its stiffness in the horizontal direction. In the following section, the analytical models under horizontal displacement will be presented.

3.4.2.1 U-shaped connector model under horizontal displacement

The same ABAQUS model for the U-shaped connector discussed earlier was used to model the U-shape connector under horizontal displacement. The connector was fixed on one face and displacement was imposed on the opposite face as shown in Figure 3-68. The displacement cycles are shown in Figure 3-69. Figure 3-70Figure 3-128 shows the horizontal force-displacement for the U-shaped connector. As expected, the U-shaped connector offered relatively low stiffness and strength in the horizontal direction. It must be noted that the results of this analysis will be used later in this study.

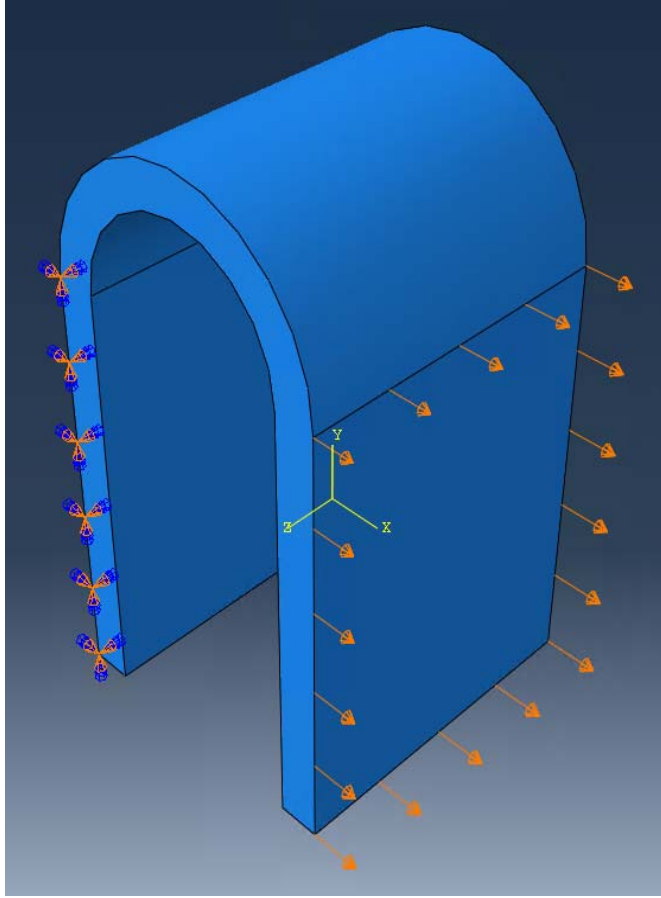


Figure 3-68: U-shape plate boundary condition

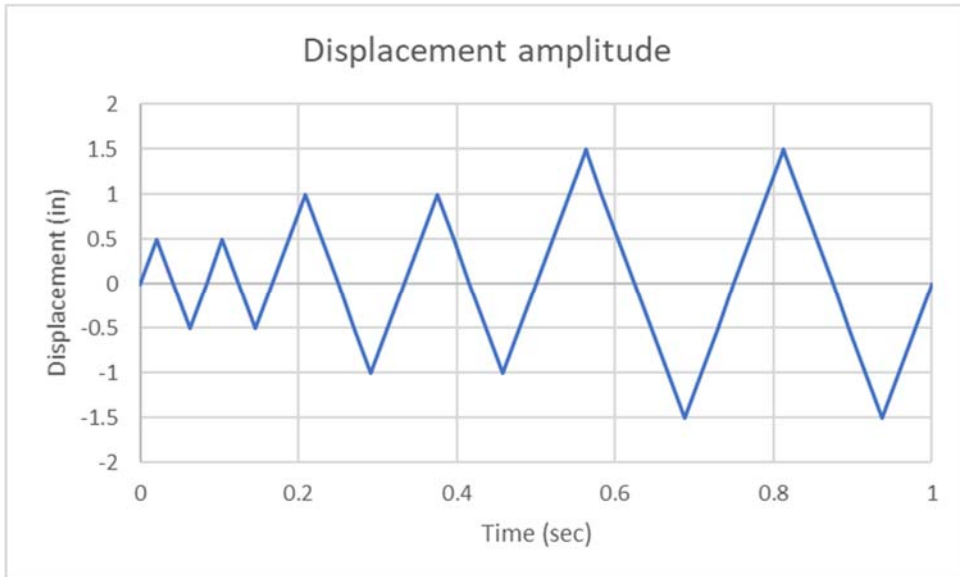


Figure 3-69: Displacement amplitude

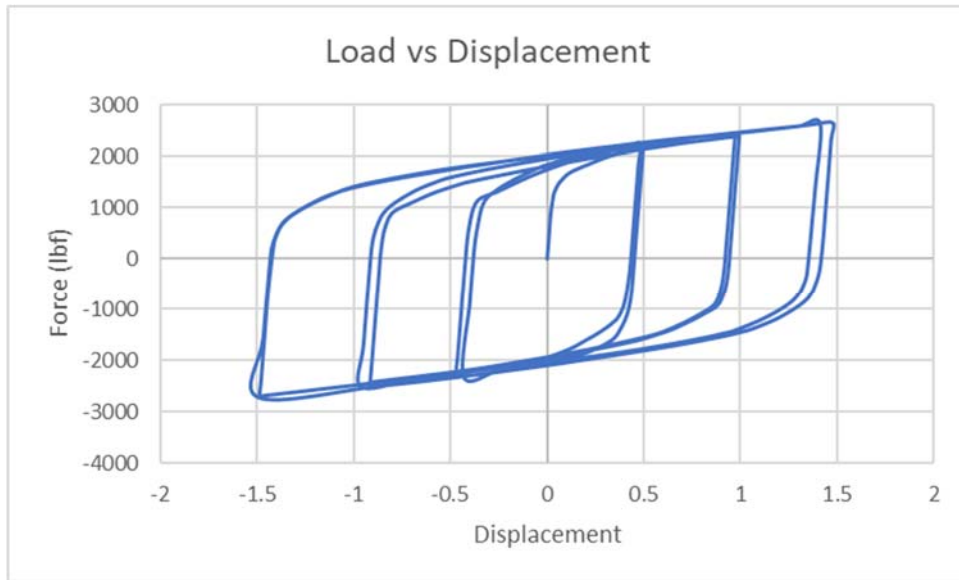


Figure 3-70: Force vs Displacement for U-shaped plate under horizontal displacement

3.5 Shape selection (Trial shapes)

For the proposed final shape, high energy dissipation, limited reaction force and adequate low-cyclic fatigue response were the important considerations. However, another consideration was to maintain symmetry in both directions (parallel and perpendicular to applied displacement). Considering the results of the optimization studies, and the above considerations, a series of trial shapes were developed. In the following, a few shapes are presented and evaluated leading to the final shapes that were selected experimental testing.

3.5.1 TSI-1 shape

An initial decision was made to this shape to use ½-in plates. Also, two plates were used for anchorage to the walls. To reduce the high reaction forces observed earlier, holes were introduced in the side plates. Also, curved or circular shapes were used as much as possible to avoid stress concentration. Figure 3-71 shows the first shape that was examined in this section. Two bars were added between the two external plates to reduce the potential for out-of-plane buckling of the outside plates. The ANSYS

element type used was Solid 186. The element mesh size used was 0.2-in and 10,325 elements were used. Non-linear elastoplastic A36 steel 36,259 psi (250 MPa) was used. The imposed displacement is the same as the one applied on the U-shape model. Figure 3-72 shows force versus displacement graph obtained from the finite element analyses. The developed reaction force for this shape was very high, which violates one of the main stated concerns. However, the force versus displacement response showed steady hysteretic behavior.

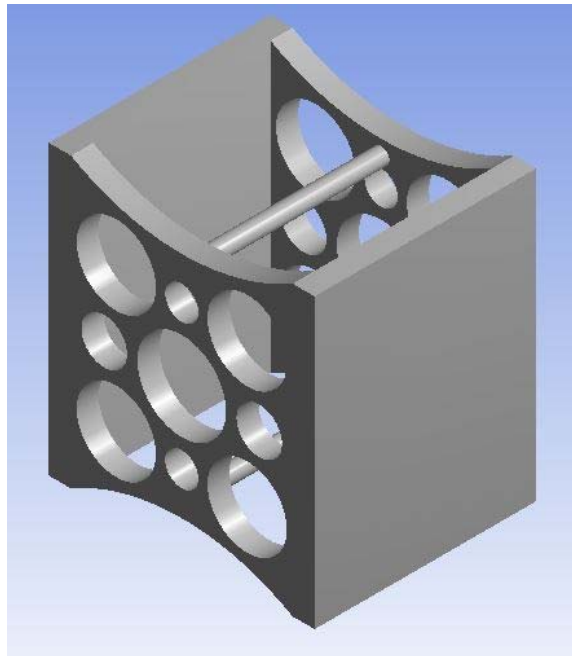


Figure 3-71: Model TSI-1; plates with holes

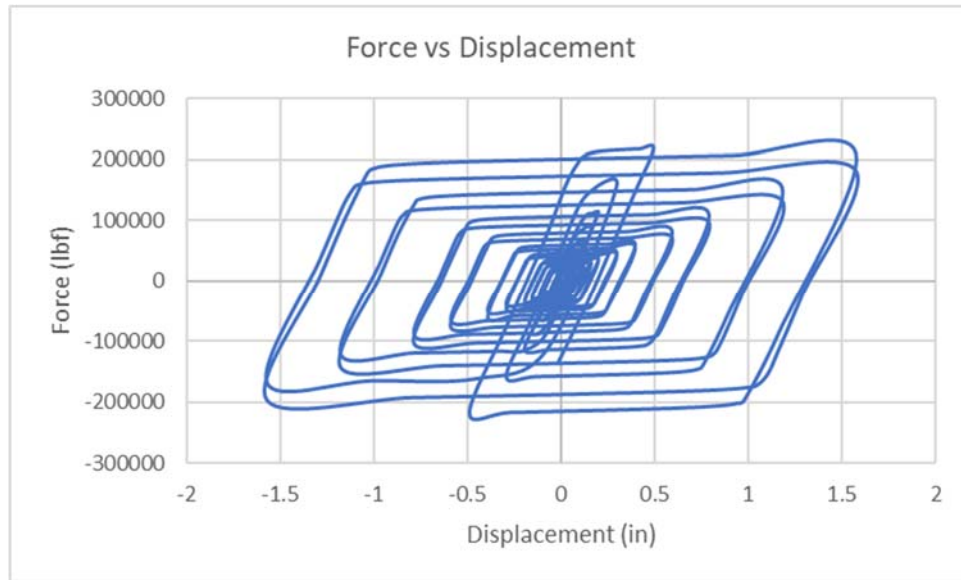


Figure 3-72: force versus displacement for TSI-1

3.5.2 TSI-2 shape

This shape was symmetric in both planes and rings (one large and four smaller) were used to reduce the reaction force and mitigate stress concentration. Figure 3-73 shows the geometry. The thickness of the rings is 5/8-inch. Figure 3-74 shows the dimensions of TSI-2.

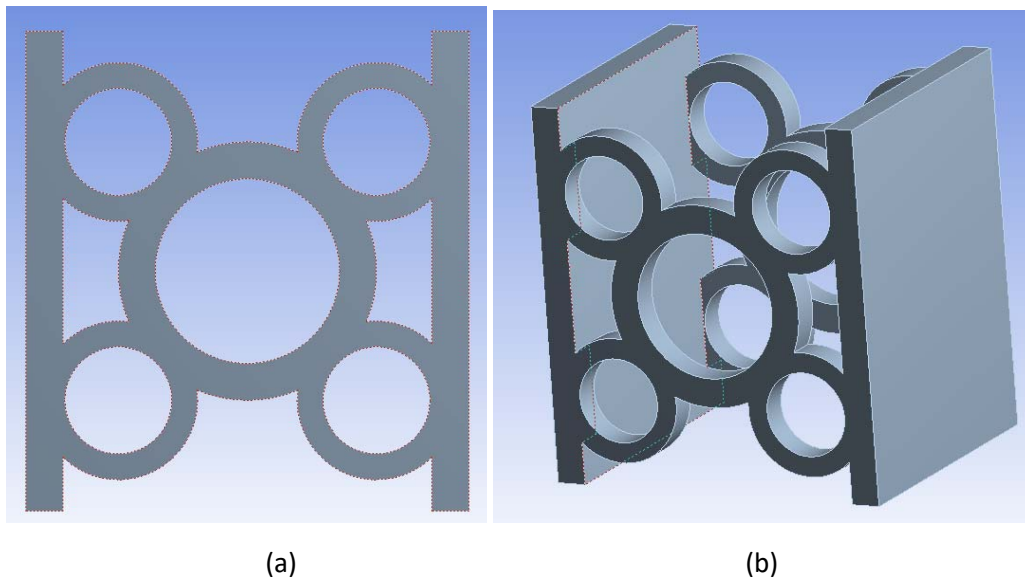


Figure 3-73: TSI-2 Geometry: (a) Elevation, (b) 3D view

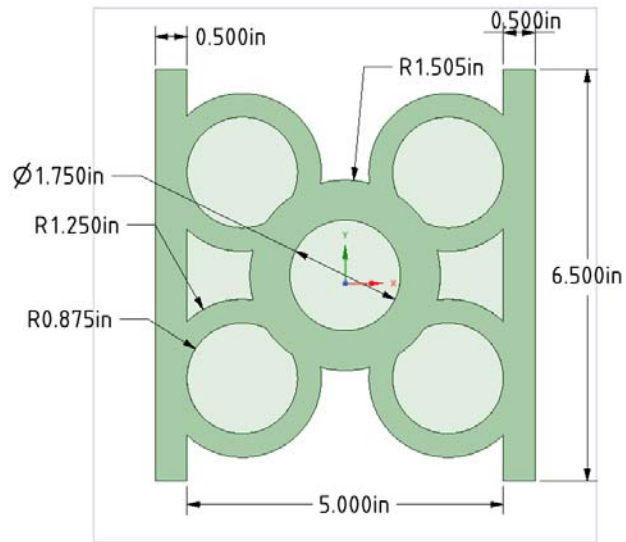


Figure 3-74: Dimensions of TSI-2

Using the same displacement profile used in the PRESSS program (shown in Figure 3-9), a finite element analysis of this shape was performed using the same ANSYS element type described earlier. Figure 3-75 shows force versus displacement graph from the analysis. The overall energy dissipated was 937,851 lbf-in (105977 J). The maximum reaction force was lower than the previous case at 78,353 lbf. Some out-of-plane buckling was noted.

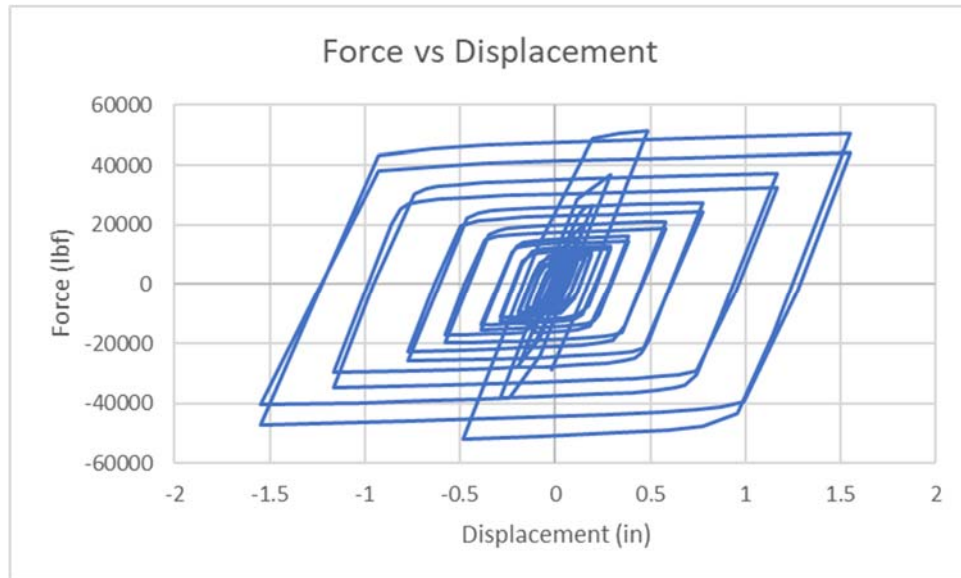
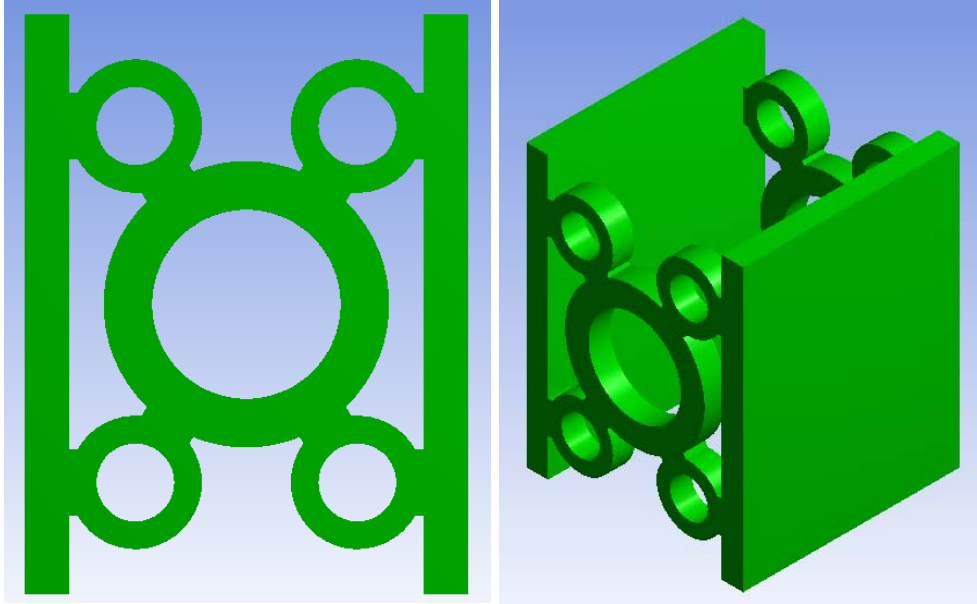


Figure 3-75: Force versus displacement of TSI-2

3.5.3 TSI-3 shape

The next shape was generated by removing some material from the rings. A different configuration was also used as shown in Figure 3-76 and Figure 3-77. The thickness of the rings is 5/8-inch. The imposed displacement profile is shown in Figure 3-9. Figure 3-78 shows the relationship between the reaction force and displacement. The performance of the shape under applied displacement was considered good and the dissipated energy (1,237,776 lbf-in or 139,869 J) was higher than in the U-shaped connector. The reaction force was relatively high (on the order of 97,567 lbf) but still acceptable. Ultimately, out-of-plane buckling was present in this model too, so mechanism to reduce out-of-plane buckling needed to solve this issue.



(a)

(b)

Figure 3-76: TSI-3 geometry: (a) elevation, (b) 3D view

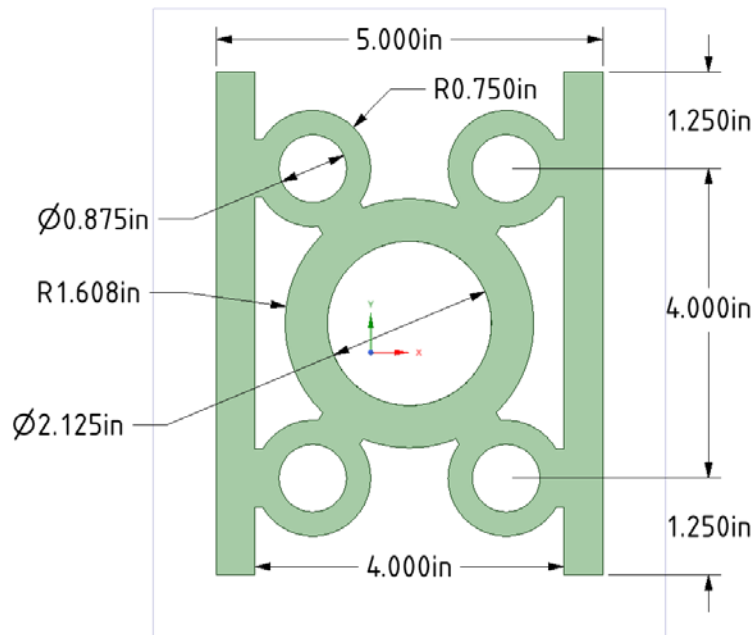


Figure 3-77: TSI-3 dimensions

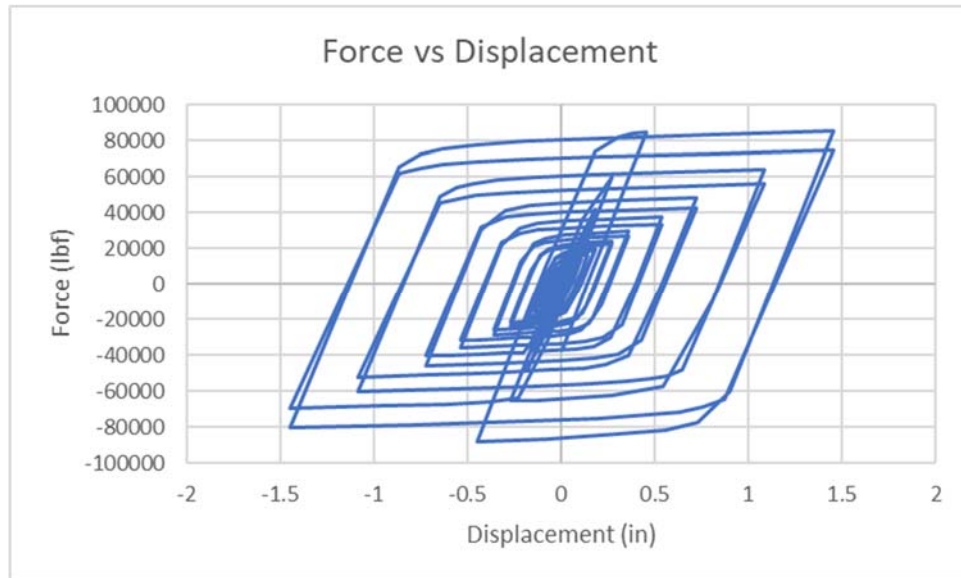


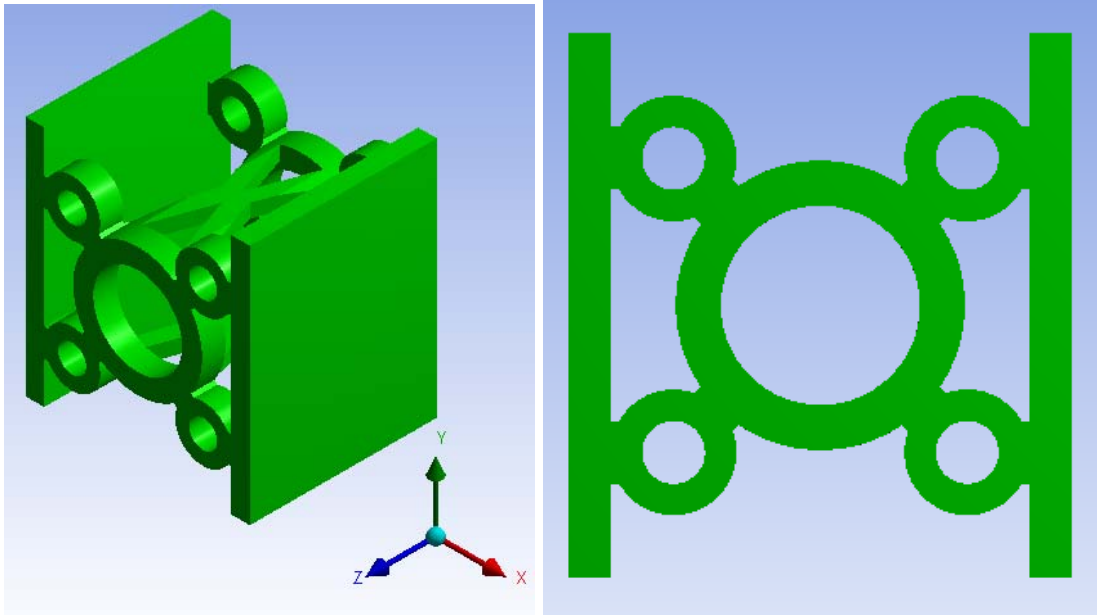
Figure 3-78: Force vs Displacement for TSI-3

3.5.4 TSI-3 with bracing

After running a few different shapes, braces to help out-of-plane buckling became needed due to the small thickness of the plates used to make the rings. As a result, different types of braces were tried. In the following section, those shapes will be presented and discussed.

3.5.4.1 TSI-4 shape

To reduce the out-of-plane buckling, braces were added to the previous shape in two different ways. First, a horizontal X-brace was added to the device between the outer rings to resist out-of-plane buckling. Figure 3-79 and Figure 3-80 show the shape with horizontal X-bracing and dimensions. The overall shape was not different from shape #2 except for some dimensions and the addition of horizontal braces.



(a)

(b)

Figure 3-79: TSI-4 geometry: (a) 3D view, (b) elevation

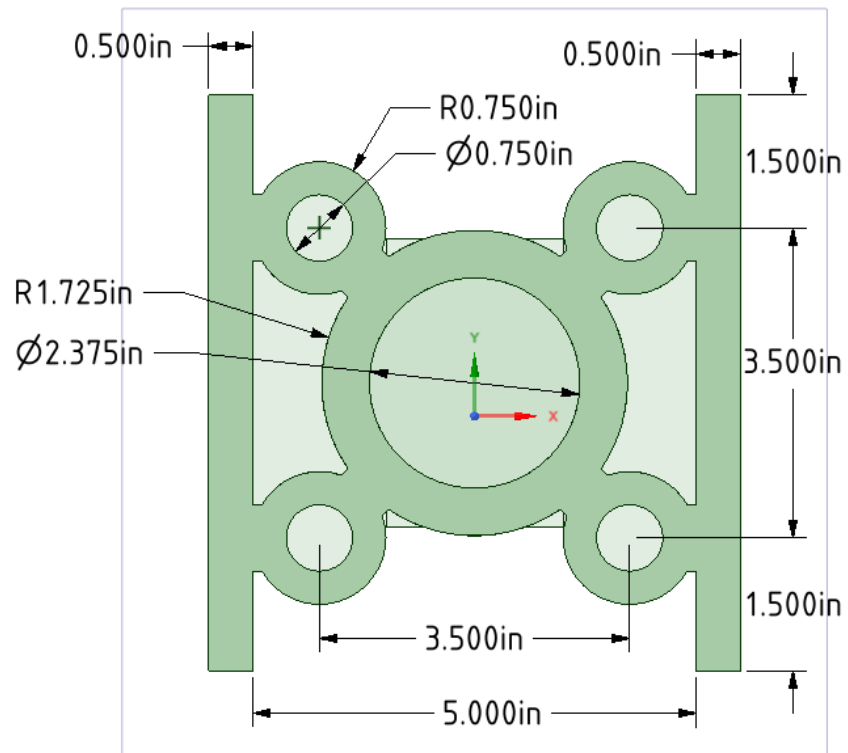


Figure 3-80: TSI-4 dimensions

Non-linear elastoplastic steel of 36,259 psi (250 MPa) was used in this simulation. The amplitude that was used to apply displacement is similar to that used by PRESSS (Figure 3-9). Figure 3-81 shows force versus displacement graph. Overall performance of the shape under applied displacement was good and dissipated higher energy than U-shaped. The resulted force was 89,626 lbf which is less than the previous shape. Also, the dissipated energy was 1,106,847 lbf-in (125,074J). Further refining needed to be conducted in order to reduce the resulted force. Ultimately, adding horizontal X-brace significantly helped the out-of-plane buckling and reduced the resulted force as well.

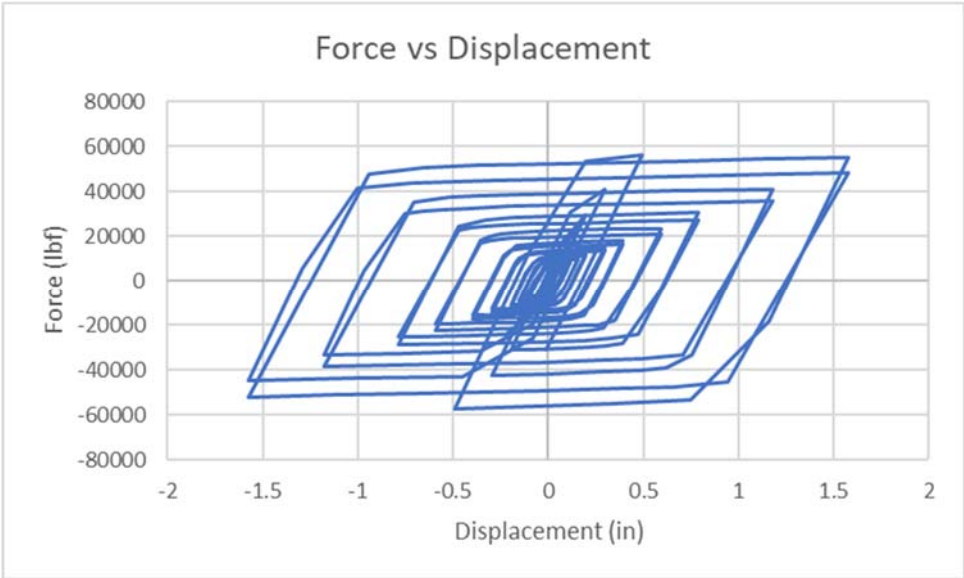
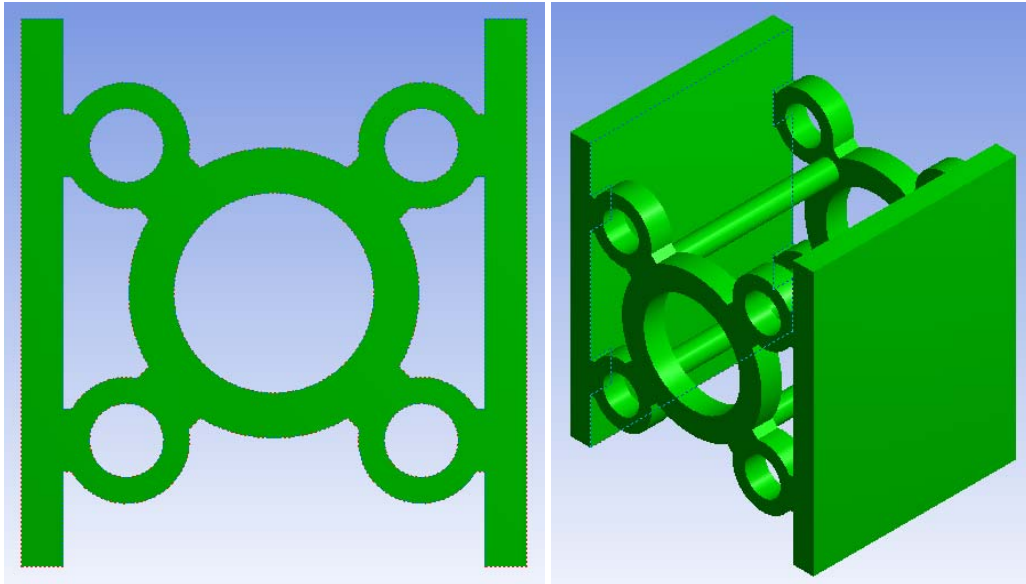


Figure 3-81: Force versus displacement for TSI-4

3.5.5 Shape (TS)

Several modifications were made to the dimensions of shape TSI-1 through TS-4 before reaching the TS shape. Figure 3-82 illustrates The TS shape. Also, Figure 3-83 shows the dimensions of TS shape. The main difference is the type of bracing used. Straight horizontal braces were used to resist the out-of-plane buckling. Initially, 3/4-inch rods were used as braces between the plates. The diameter of the rods

was ½-inch and there was not a drastic change in the reaction force or performance. Results of modeling and analysis of this shape is presented in details in Chapter 4.



(a)

(b)

Figure 3-82: ANSYS model of TS shape - Front view: (a) elevation, (b) 3D view

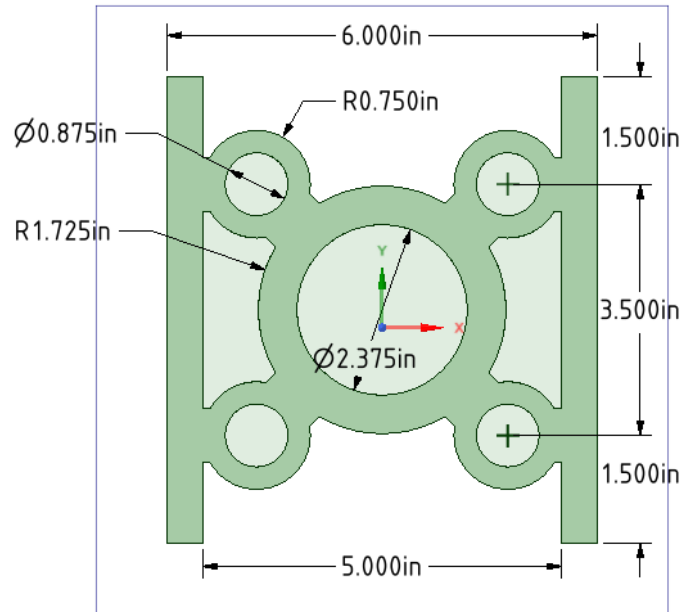


Figure 3-83: TS shape – Dimensions

The element type that was used in this analysis is Solid 186. The element mesh size used was 0.25-inch (6.35 mm) and over all 6,924 elements were used. Non-linear steel of 36,259 psi (250 MPa) was used in this simulation. Non-linear steel of 36,259 psi (250 MPa) was used in this simulation. The amplitude that was used to apply displacement is similar to that used by PRESSS (Figure 3-84).

It's been evident throughout this investigation and in order to improve the dissipated energy, the exerted force must be higher than that of U-shaped plate. Since the dissipated energy could be calculated as the area under force versus displacement and in this case, a displacement based on PRESSS amplitude is applied. Therefore, the only one way to increase and improve dissipated energy is by increasing the exerted force. However, that force should be limited to avoid local failure at the precast wall. Figure 3-85 shows the relationship between force and displacement of the TS shape.

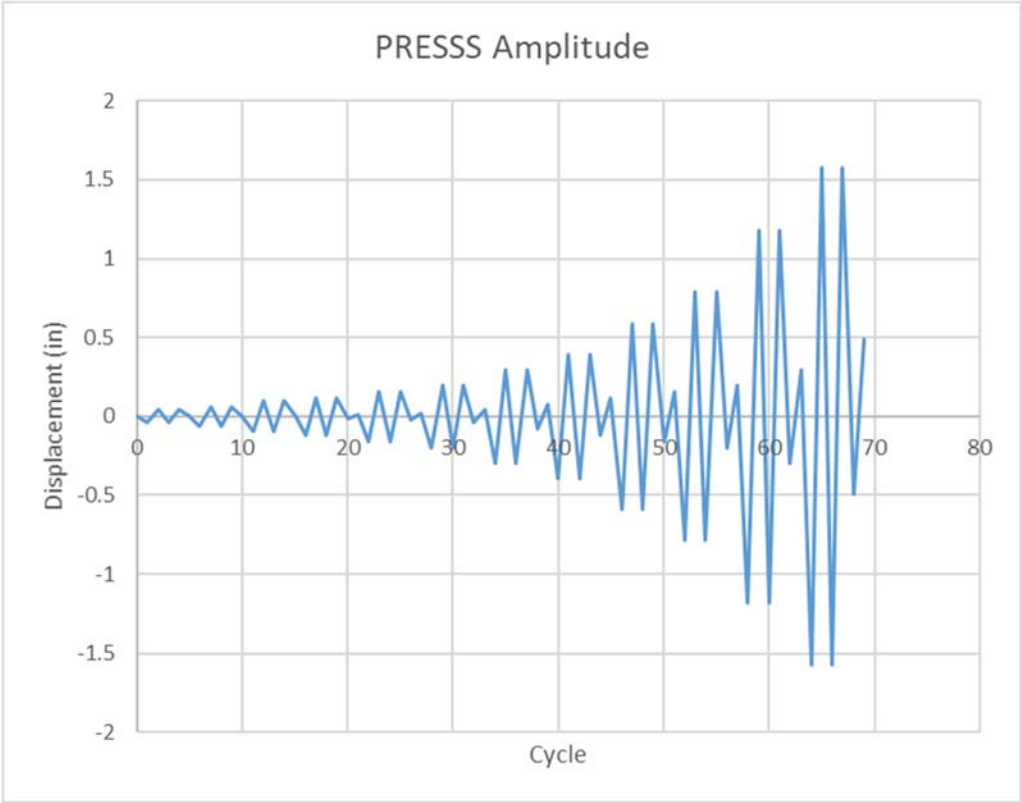


Figure 3-84: Displacement amplitude used by PRESSS to test UFP [5]

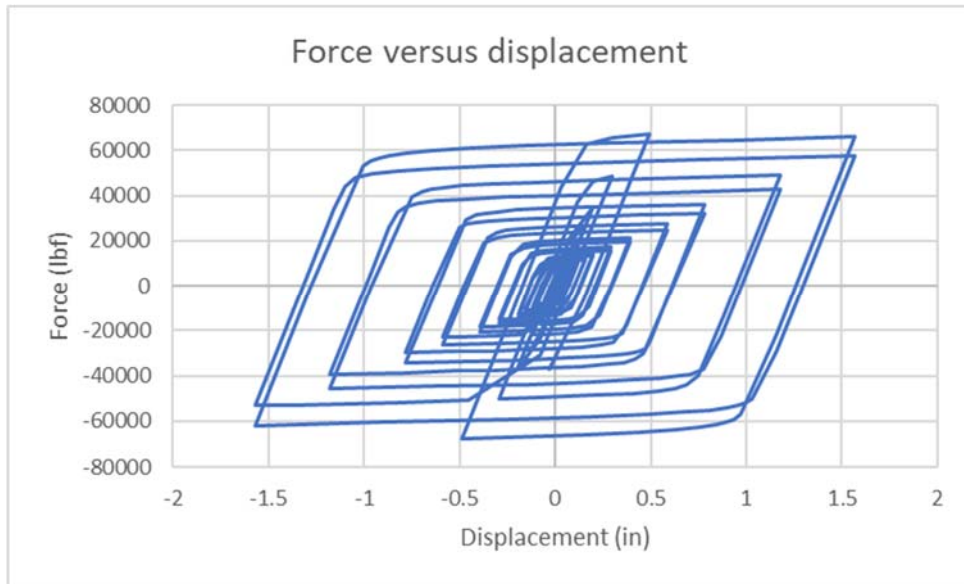
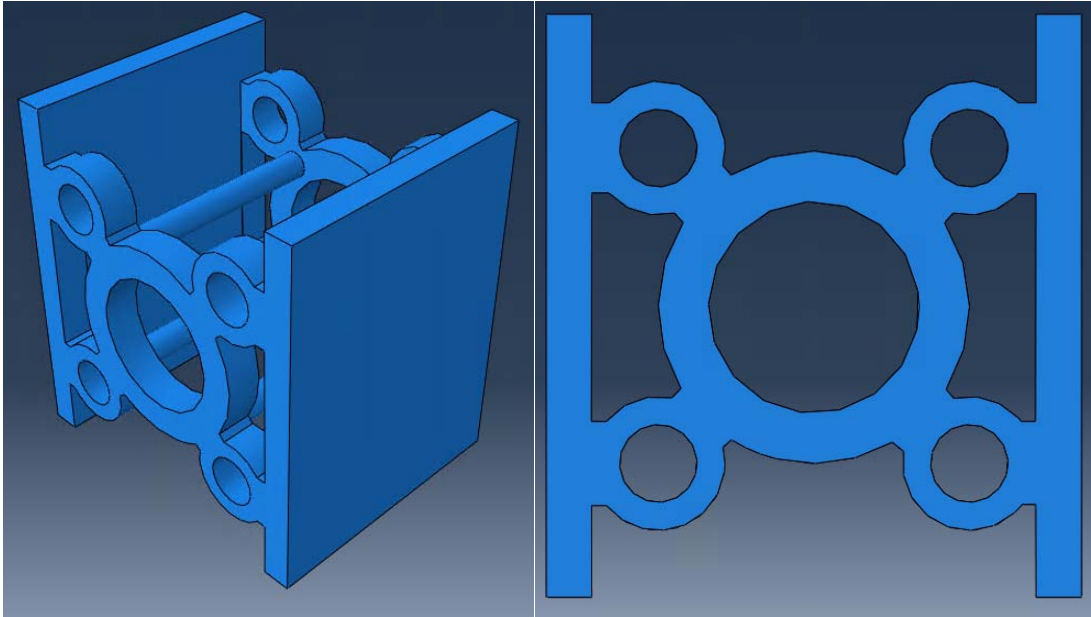


Figure 3-85: Force versus displacement of the TS shape

It could be seen that the overall performance of the shape under applied displacement is significantly higher than that of U-shaped. That applies to the dissipated energy as well, where it was 797,175 lbf-in (90,081J). The resulted force was significantly lower than those previous shapes and higher than those of the main shapes (U-shaped). Ultimately, adding vertical braces helped the out-of-plane buckling and improved the connector performance as well.

A verification of the final shape was done using ABAQUS. Figure 3-86 shows the model of the final shape in ABAQUS. The element type that was used here is C3D20R. it is 3-dimensions element with 20 nodes, reduced integration and hourglass control.



(a)

(b)

Figure 3-86: Abaqus model of TS shape: (a) 3D view. (b) elevation

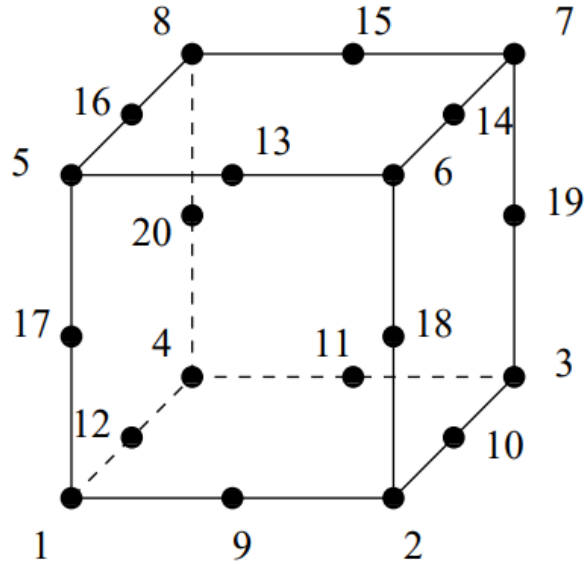


Figure 3-87: C3D20R element [38]

The C3D20R element is a general-purpose quadratic brick element, with reduced integration (2x2x2 integration points). Reduced integration uses a lower-order integration to form the element stiffness

[33]. The mass matrix and distributed loadings uses full integration. Reduced integration reduces running time, especially in three dimensions [33]. The node numbering follows the convention of Figure 3-87. It performs well for isochoric material behavior and in bending and rarely exhibits hourglassing despite the reduced integration (hourglassing generally occurs when not enough integration points are used for numerical integration and spurious modes pop up resulting in unrealistic displacement fields but correct stress fields).

The material was defined as non-linear material, data was obtained from ABAQUS library for A36 steel.

Error! Reference source not found. below shows the parameter of the material properties. Also, Figure 3-88 shows stress-strain relationship of the material that was used in this simulation.

Table 3-2: Material properties - ABAQUS

Density, ρ (slug/ft ³)	8.8E-3
Modulus of Elasticity, E (psi)	28.5e6
Poisson's ratio (ν)	0.3

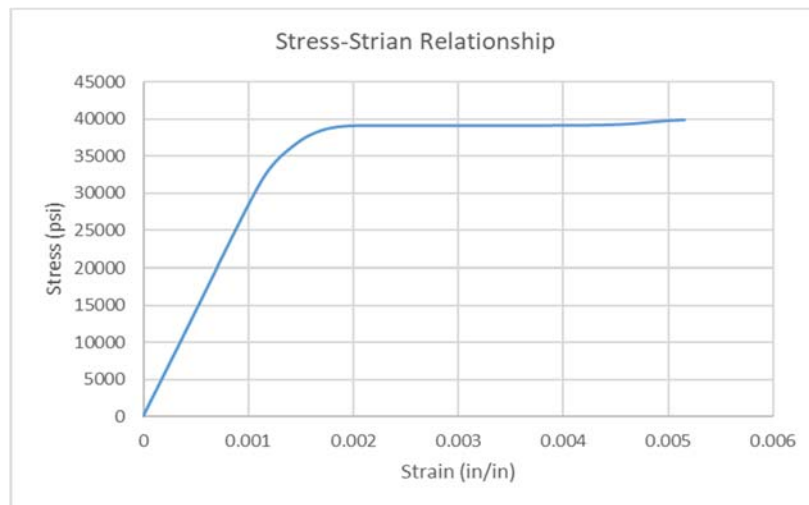


Figure 3-88: Stress - strain relationship of A36 steel

The test was done using the amplitude that was used by PRESSS and shown in Figure 3-84. Figure 3-89 shows the relationship of between force and displacement. The results were approximately similar to those obtained from ANASYS. The maximum exerted force was 59,117 lbf and overall dissipated energy was 1,927,260 lbf-in (217,780J). one of the main reasons for the difference in the results between ABAQUS and ANSYS is the type of elements and their sizes. Ultimately, those results were satisfying to the purpose of verification between the two programs.

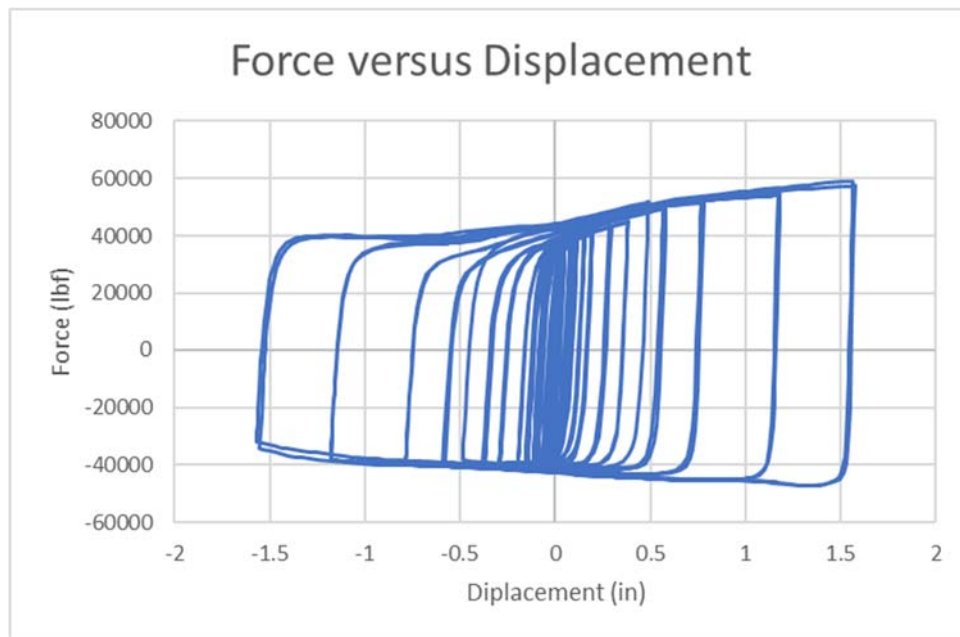


Figure 3-89: ABAQUS force versus displacement graph

After running two models in two different programs, it could be concluded, and based on the results of those models, that the final shape satisfies the main objectives of this study. It offers higher dissipated energy than that of U-shaped plate. Based upon all that, a decision was made to pursue this study and move to next step which is testing the device and determining if it will present similar results to analytical models results. Experimental description will be provided in the next chapter.

3.6 NS shape

As described earlier, several shapes were modeled to obtain a shape that meets all the stated criteria for this study. A number of trials were performed manually to come up with the shape that would limit localized high strains, which could lead to low-cycle fatigue. One of the concepts used was to employ a combination of multiple shapes. To begin with, the previous shape was used as a base for the design of the revised new shape (NS shape). Based on the experimental test (Chapter 4), it was determined that increasing the number of openings could assist to reduce localized high plastic strain. The new shape was a single plate with a thickness of 1-inch and consisting of a number of big and small circles. Symmetry was maintained about the vertical and horizontal axes. Figure 3-90 Through Figure 3-92 show the evolution of the final tested shape (NS5 shape). The first shape examined in this phase, NS1 shape, included curved openings that were used at the top and bottom of the shape. However, in the development of NS2 shape, the curved openings were removed and replaced with three smaller circles. The NS3 shape included four small circles at the top and bottom areas. The NS4 shape had the same overall number of small circles but the circles were spaced out evenly, also the middle circles diameter was reduced to reduce the plastic strain. In final shape, NS5, was similar to NS4 except a decision was made to extend the welds by approximately 1 1/8-in into the curved edges at the top and bottom areas to reduce strain concentration.

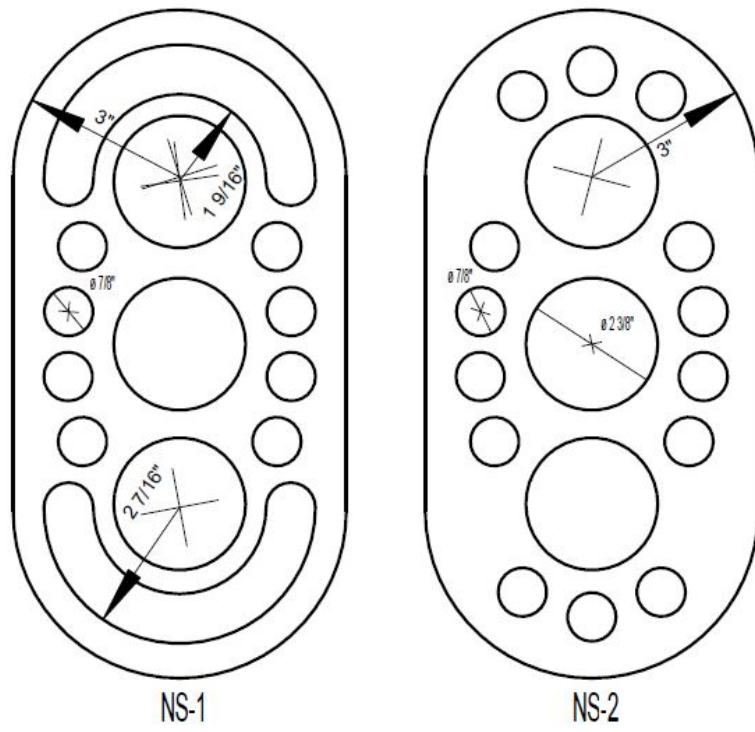


Figure 3-90: Shapes NS1 & NS2

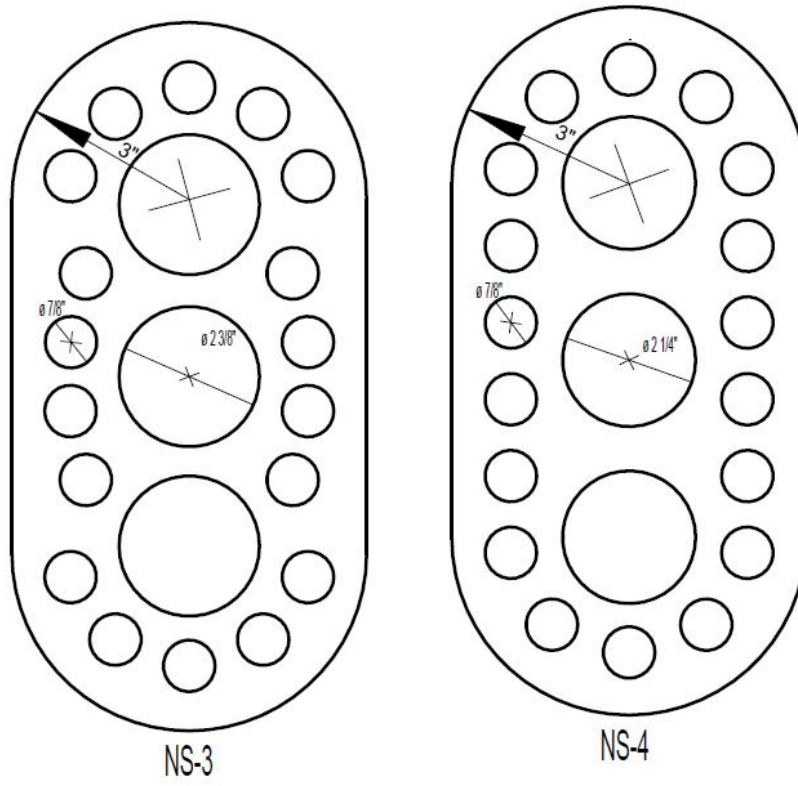


Figure 3-91: Shapes NS3 & NS4

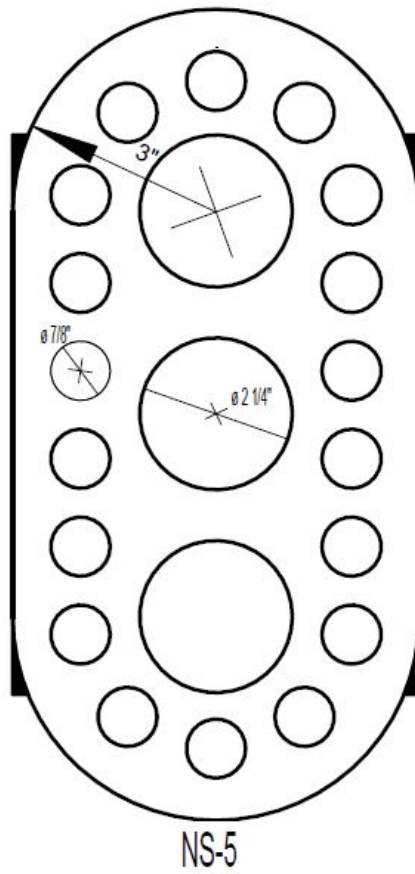


Figure 3-92: Final shape NS5

3.6.1 Shape NS1

ABAQUS FEA software was used in performing the analytical modeling and analysis of this shape. The element type that was used in this analysis is Solid C3D8R. The element mesh size used was 0.2-inch (5.080 mm) and 4,470 elements were used. Non-linear elastoplastic A36 steel 36,259 psi (250 MPa) was used. Figure 3-93 (a) Shows the mesh of ABAQUS simulation of the model.

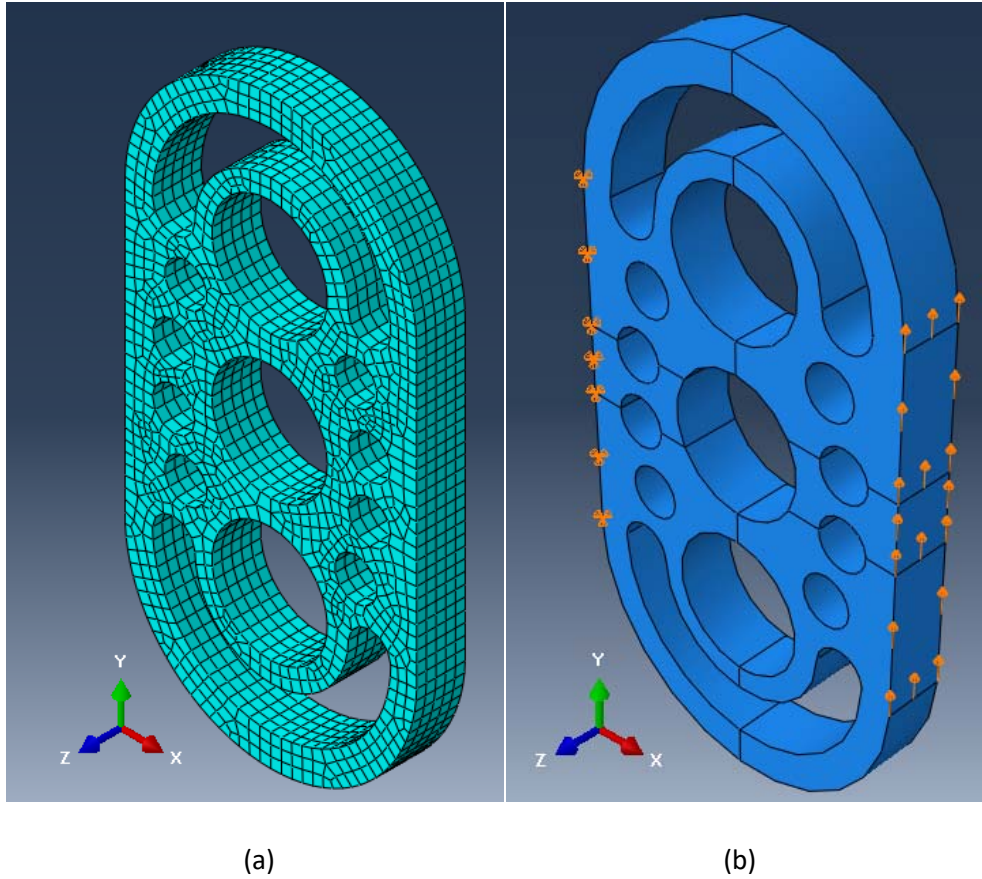


Figure 3-93: Shape NS1: (a) Meshed shape, (b) boundary conditions

Figure 3-93 (b) shows the application of boundary condition which is similar to what have been done to all models in this study. The imposed displacement is shown in Figure 3-94. It could be noticed that the maximum displacement of the modeling is 2.5-inch to match what used by PRESSS testing that was published in 2007 [44]. The plastic strain at peak displacements was monitored to improve the low-cycle fatigue. Figure 3-95 through Figure 3-98 show the plastic strain results at various positive and negative displacements.

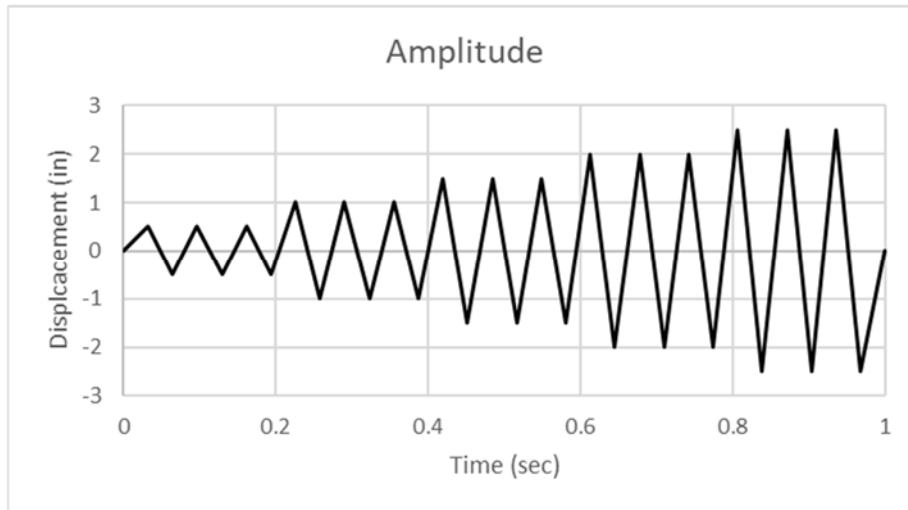


Figure 3-94: Analysis amplitude

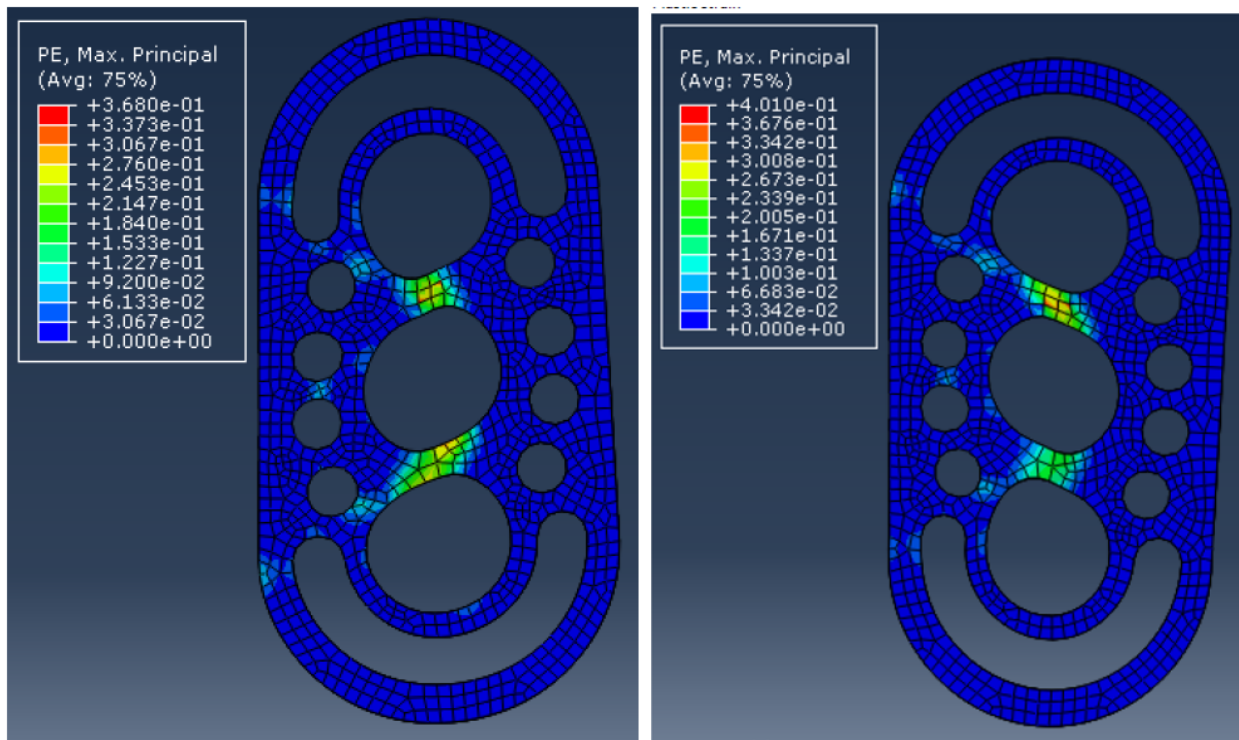


Figure 3-95: Plastic strain at 1" & -1" (left to right) NS1

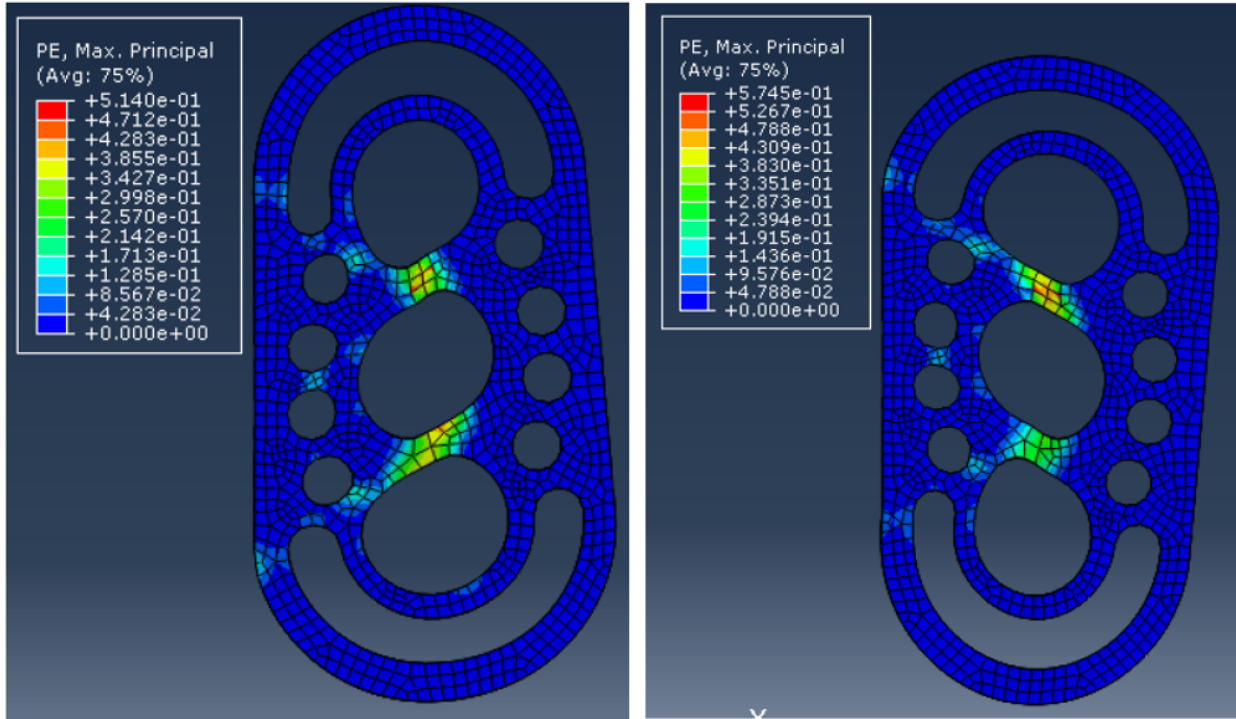


Figure 3-96: Plastic strain at 1.5" & -1.5" (left to right) NS1

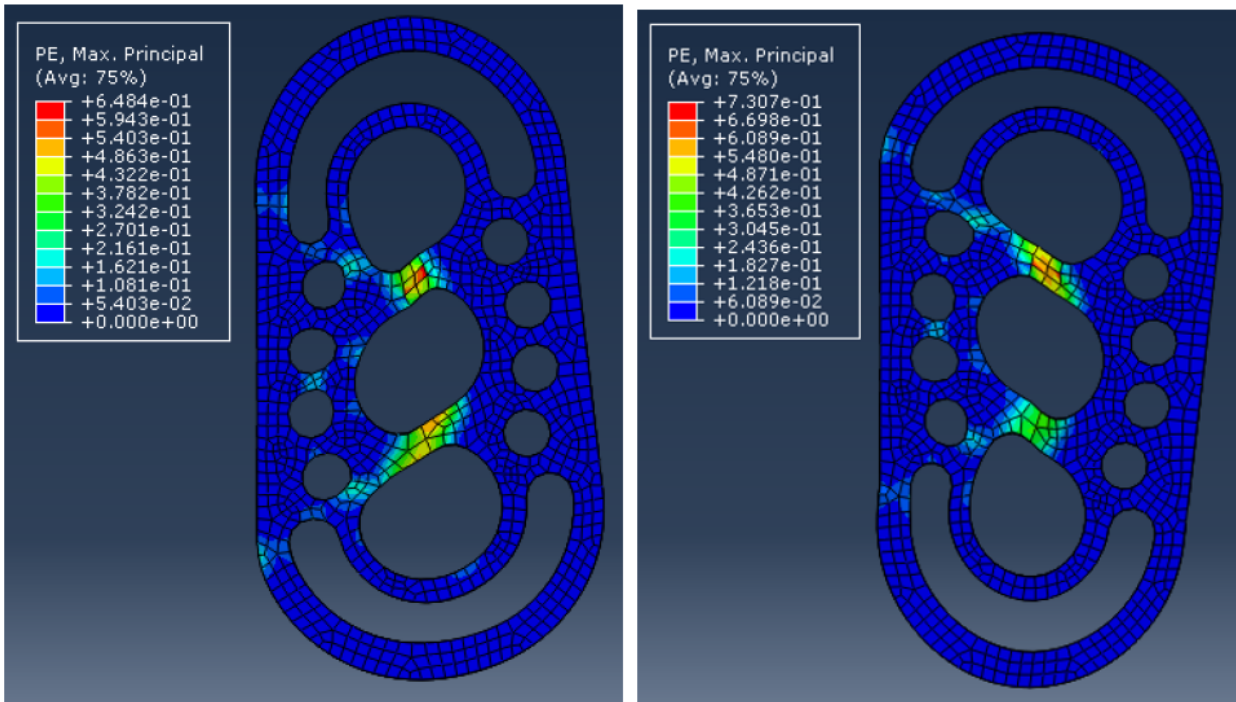


Figure 3-97: Plastic strain at 2" & -2" (left to right) NS1

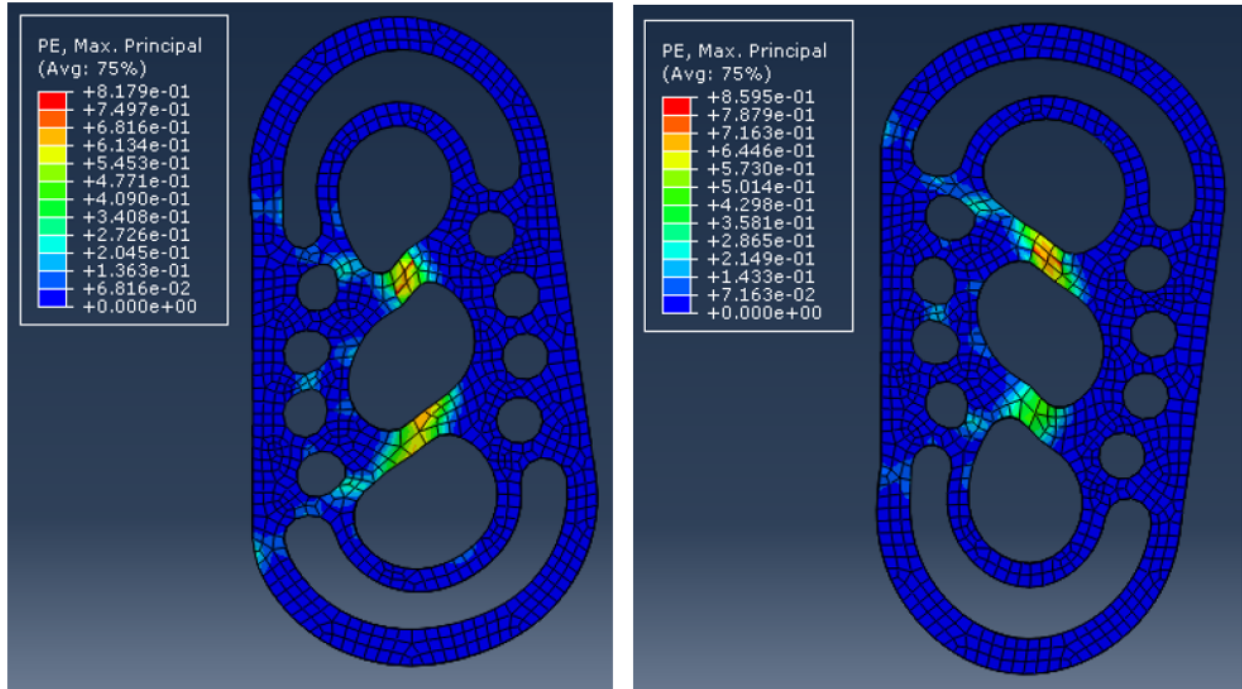


Figure 3-98: Plastic strain at 2.5" & -2.5" (left to right) NS1

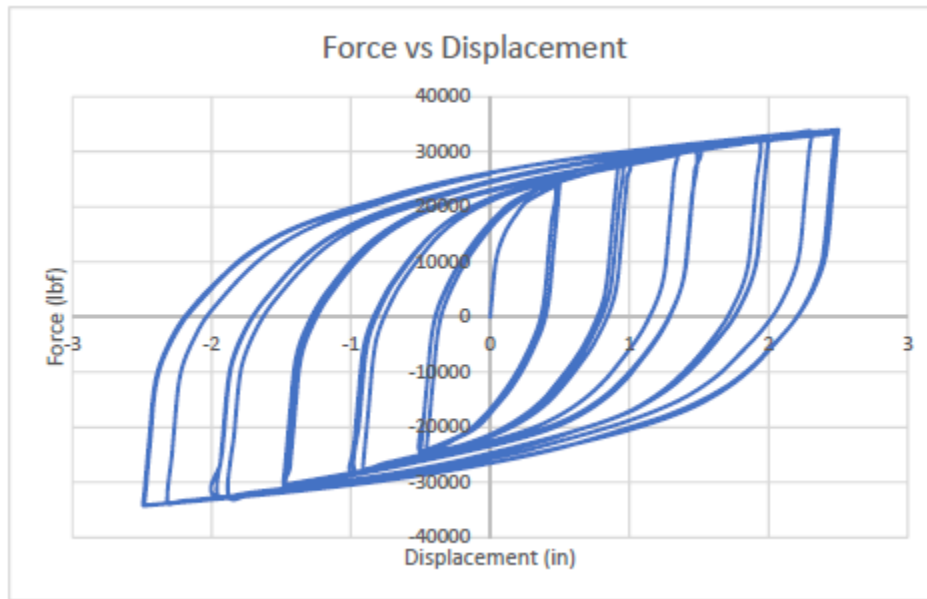


Figure 3-99: Force vs Displacement of shape NS1

Finally, Figure 3-99 exhibits the Force vs Displacement for NS1, it could be noticed that the shape has dissipated high amount of energy and the maximum reaction force is in order of 35,000lbf which is acceptable. The behavior of the model under imposed displacement confirms the findings of the topology optimization that was performed earlier in this study. As shown in Figure 3-100, the stress and strain path coincide with a triangular path between the boundary condition of both sides of the model. It was noticed that there is points of high strain at the perimeter of middle circle while the other circles are barely stressed. Thus, shape NS2 was developed to guide the stress to the upper and lower parts of the model by replacing the upper and lower curves with small circles.

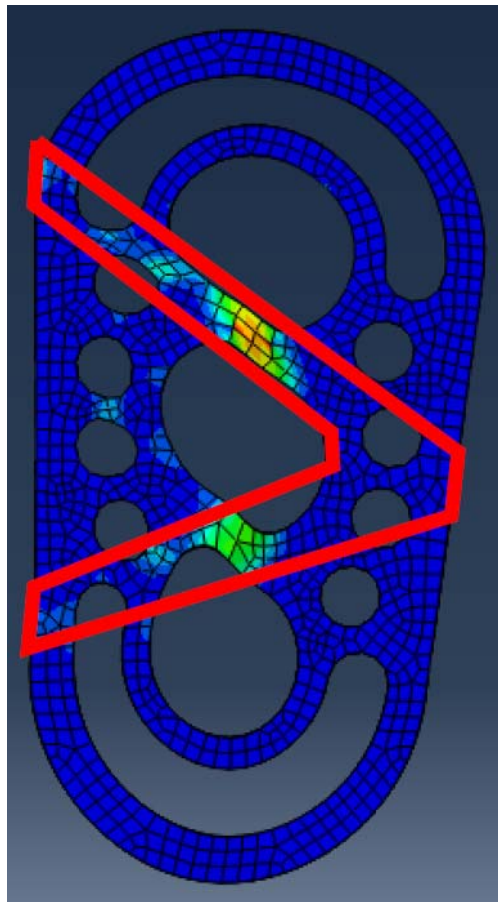


Figure 3-100: Plastic strain path of the model

3.6.2 Shape NS2

As stated previously, the top and bottom curves were replaced with smaller circles to improve the plastic strain. Similar to shape NS1, solid C3D8R was used as element type in this analysis. A finer mesh was used for this shape where 0.125-inch (3.175 mm) was used as element mesh and overall of 29,376 elements were used. Non-linear elastoplastic A36 steel 36,259 psi (250 MPa) was used.

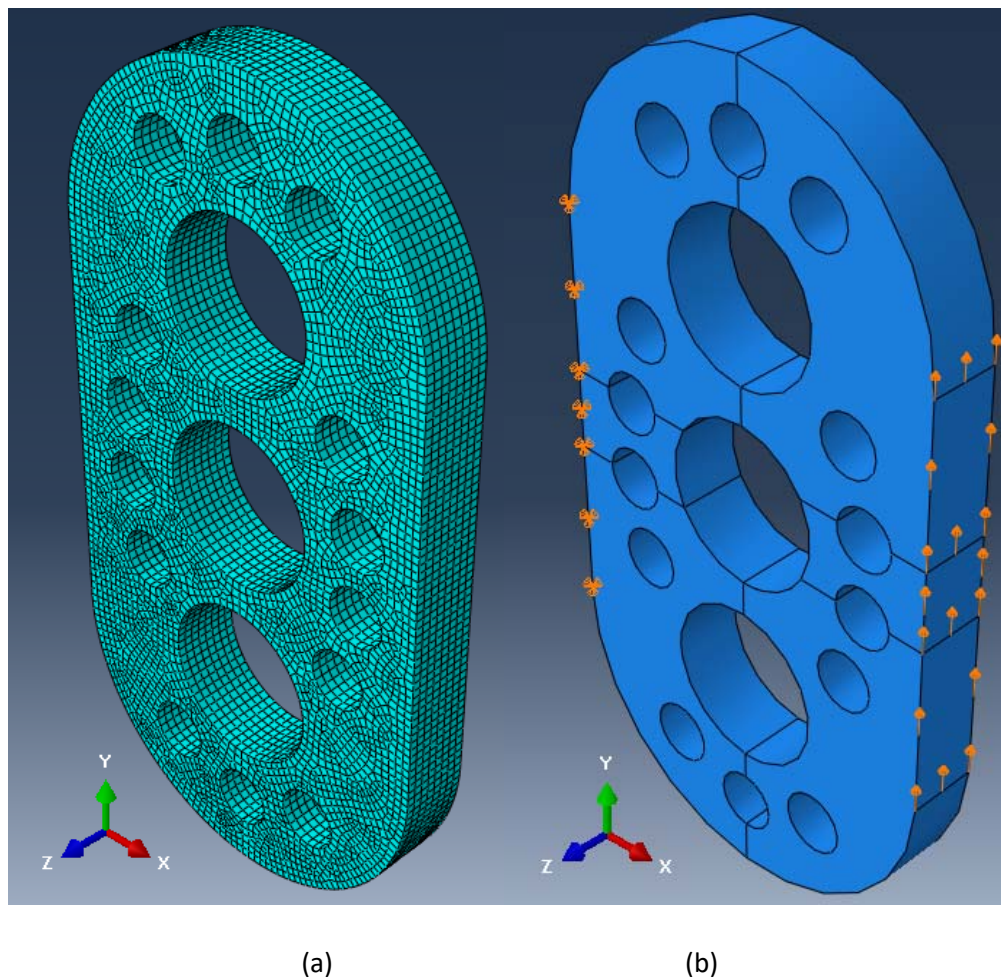


Figure 3-101: Shape NS2: (a) meshed shape, (b) boundary conditions

Figure 3-101 (a) shows the meshed NS2 shape, Figure 3-101 (b) shows a typical boundary condition where the imposed displacement is applied on one side and fixed support applied on the opposite side. The imposed displacement is applied with an amplitude that is same as the one applied to NS1 (shown

in Figure 3-94). Figure 3-102 through Figure 3-105 show the plastic strain at various peak of displacement in both negative and positive directions. It could be noticed that the strain started slightly appearing on the top and bottom portion of the model. However, it also shows areas of concern at the top and bottom ends of the fixed face of the model.

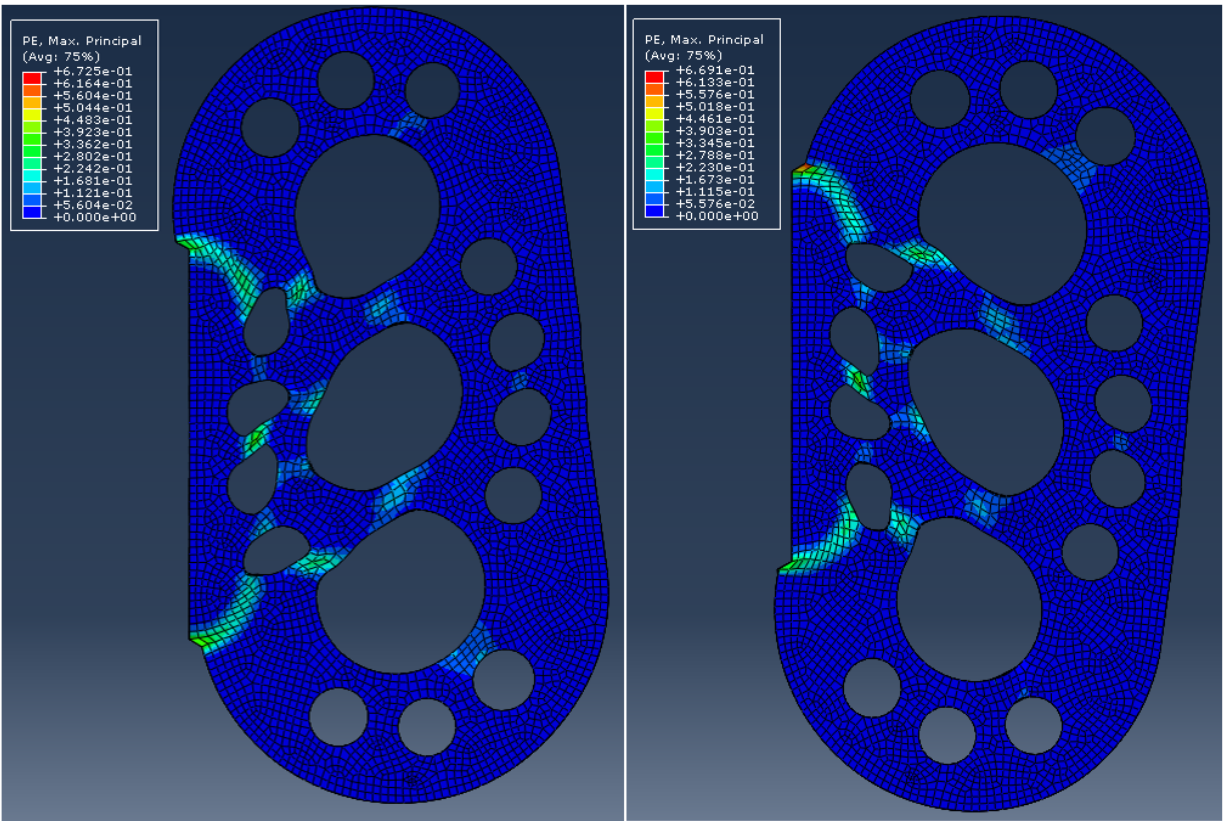


Figure 3-102: Plastic strain at 1 & -1 Displacement (left to right) NS2

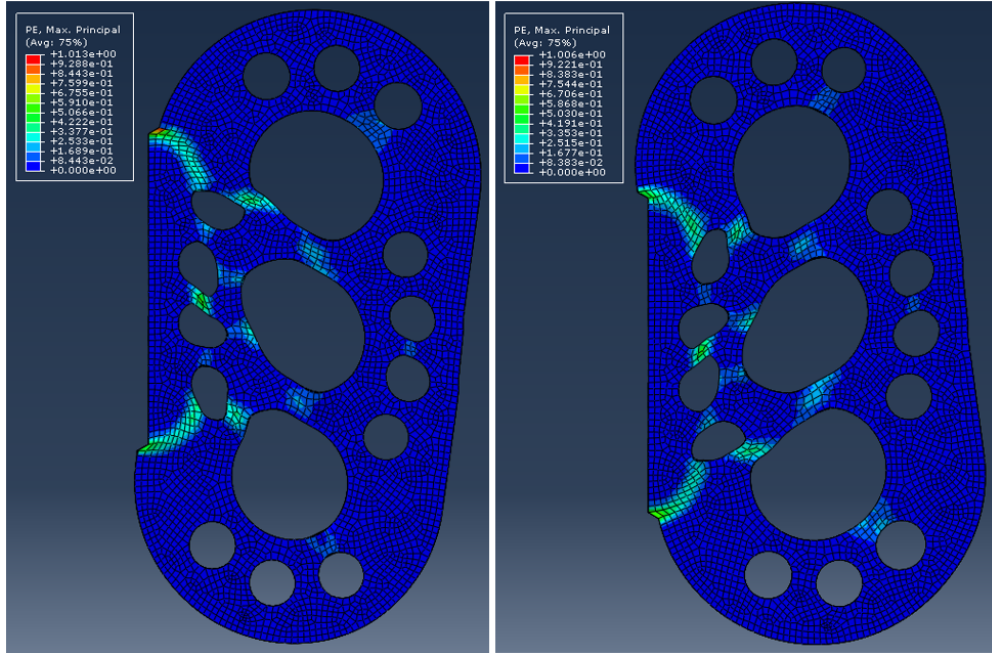


Figure 3-103: Plastic strain at 1.5 & -1.5 Displacement (left to right) NS2

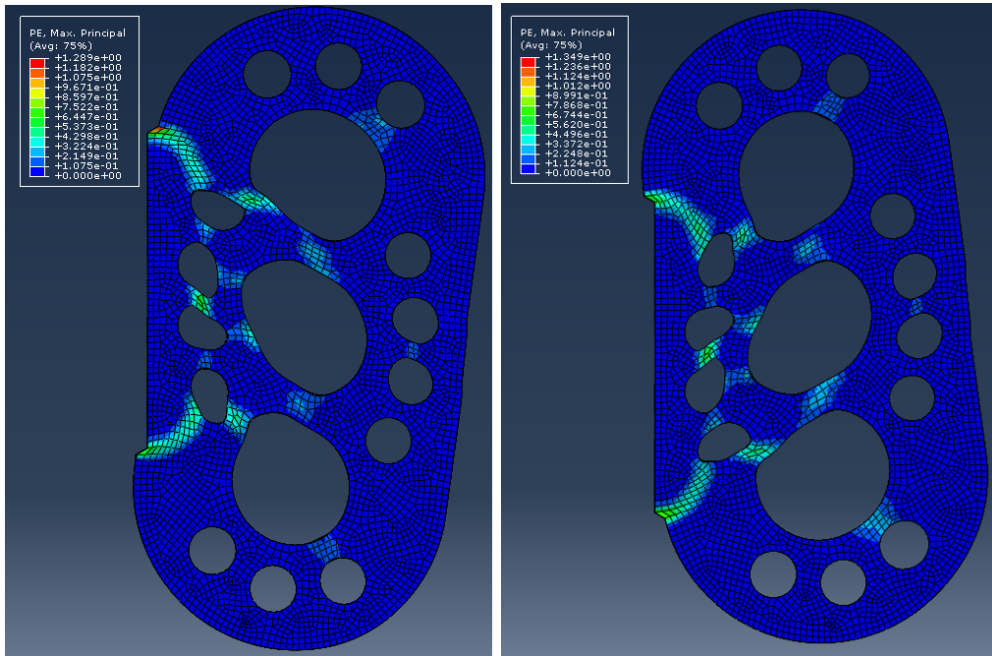


Figure 3-104: Plastic strain at 2 & -2 Displacement (left to right) NS2

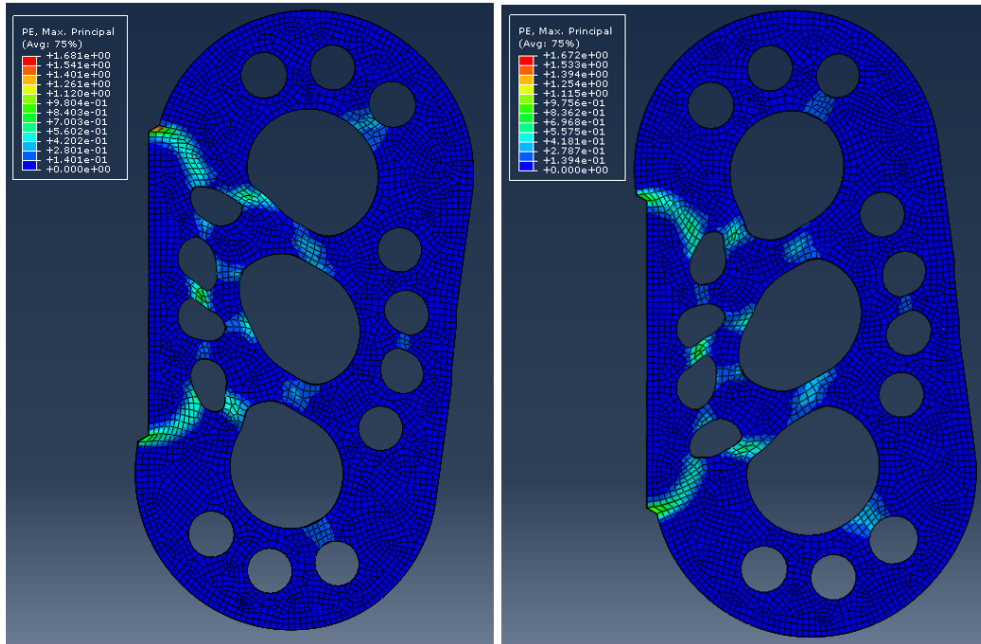


Figure 3-105: Plastic strain at 2.5 & -2.5 Displacement (left to right) NS2

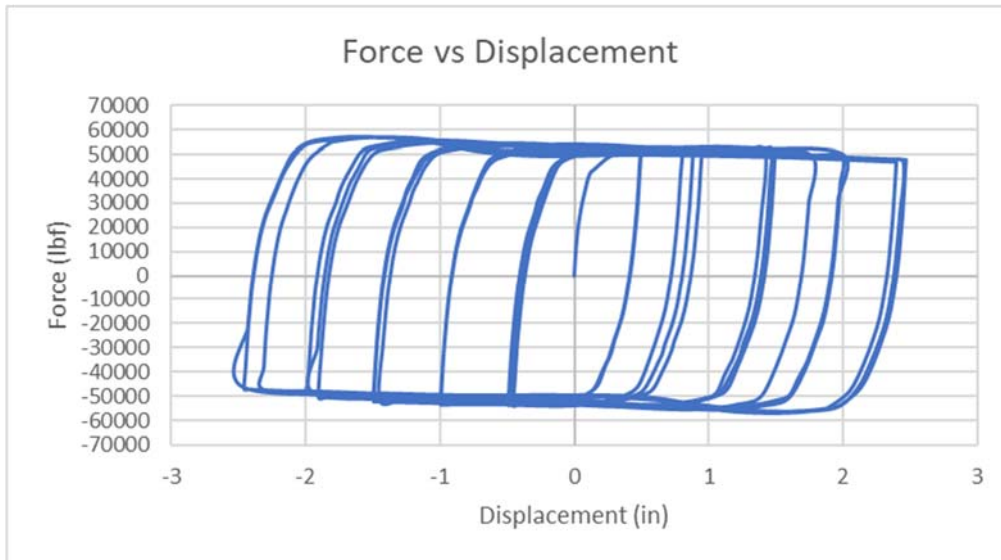


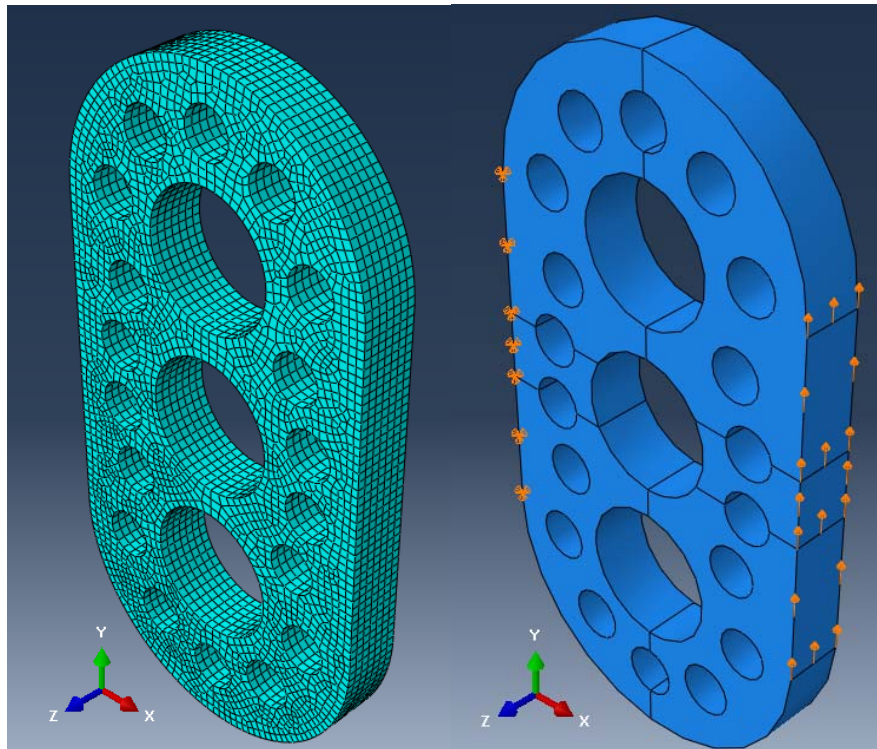
Figure 3-106: Force vs Displacement of Shape NS2

Figure 3-106 shows the Force vs Displacement response of shape NS2. The response exhibited high dissipated energy and the reaction force has increased by almost 175% than that of NS1. However, it is

still acceptable. Based on the results of the plastic strain, a modification on the model was needed to reduce the plastic strain at the top and bottom ends of the fixed face.

3.6.3 Shape NS3

Shape NS3 was developed by adding two small circles top and bottom to improve the plastic strain results. Two small circles were added to the top and bottom of NS-2 as shown in Figure 3-107 (a). The middle circles however were kept same as before. Similar to the other two shapes, solid C3D8R was used as element type in this analysis. A finer mesh was used for this shape where 0.125-inch (3.175 mm) was used as element mesh and overall of 15,624 elements were used and as shown in Figure 3-107 (a). Non-linear elastoplastic steel A36 36,259 psi (250 MPa) was used. Figure 3-107 (b) shows the boundary condition of shape NS3. The imposed displacement is applied with an amplitude that is same as the one used for NS1 and NS2 (shown in Figure 3-94). Areas of localized high strain could be seen in Figure 3-108 through Figure 3-111 at the top and bottom of the fixed support. Thus, the model requires some more improvement to reduce the plastic strain at those locations and uniformly distribute the plastic strain. Figure 3-112 show the Force vs Displacement graph which exhibits higher dissipated energy than those of both NS1 & NS2. The reaction force however was significantly increased comparing to NS1. That means the reaction force should be reduced as well.



(a)

(b)

Figure 3-107: Shape NS3: (a) meshed shape, (b) boundary conditions

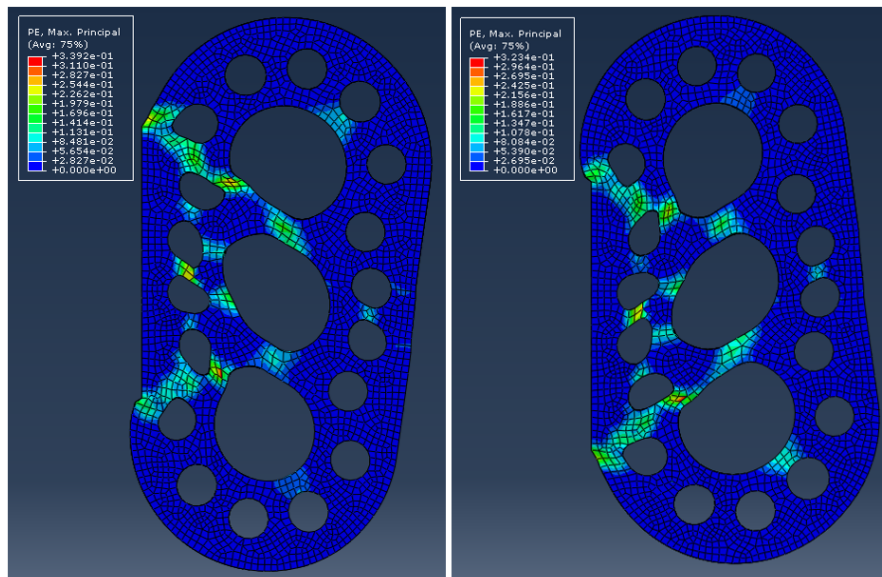


Figure 3-108: Plastic Strain at 1 & -1 Displacement (left to Right) NS3

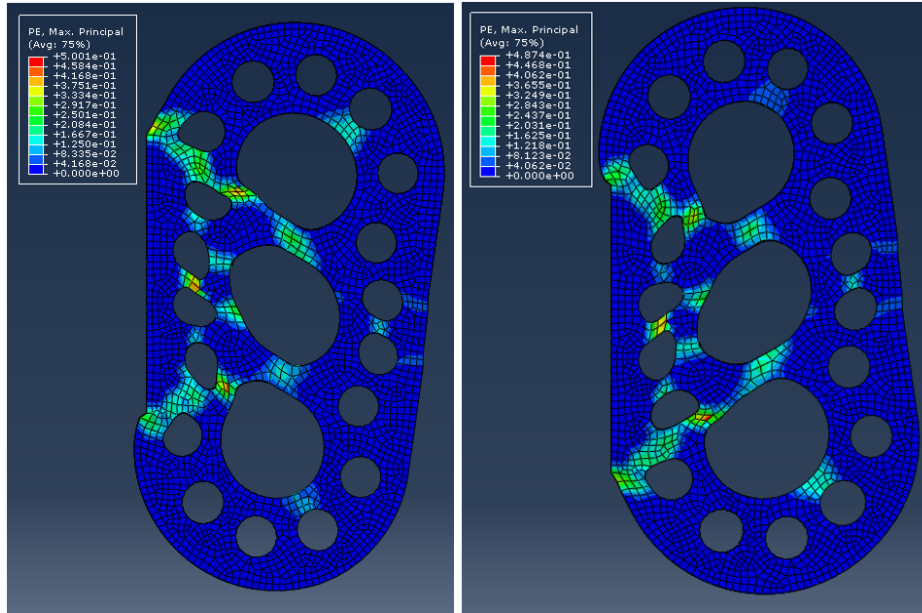


Figure 3-109: Plastic Strain at 1.5 & -1.5 Displacement (left to Right) NS3

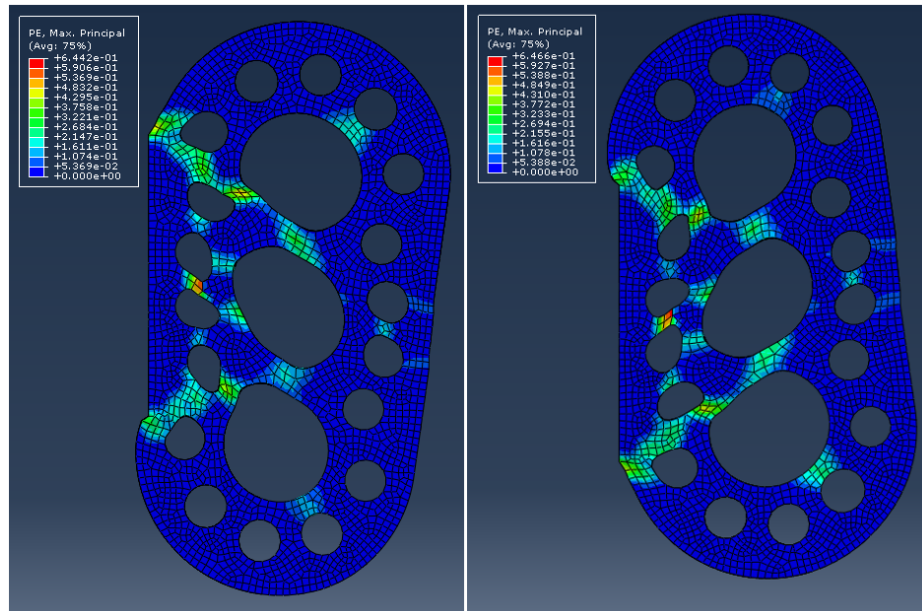


Figure 3-110: Plastic Strain at 2 & -2 Displacement (left to Right) NS3

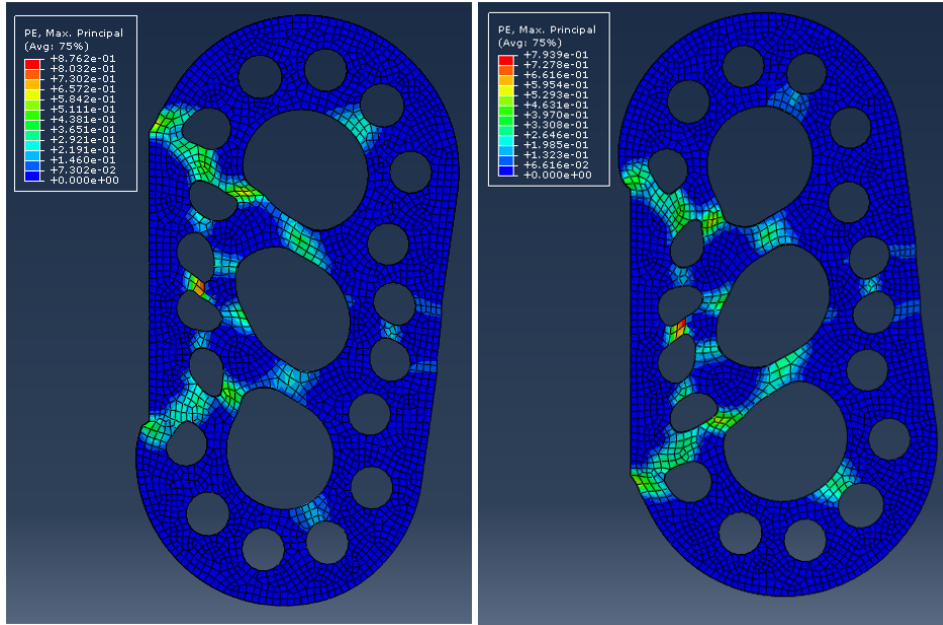


Figure 3-111: Plastic Strain at 2.5 & -2.5 Displacement (left to Right) NS3



Figure 3-112: Force vs Displacement of Shape NS3

3.6.4 Shape NS4

All previous shapes so far have exhibited high plastic strain at some localized areas. High plastic strain at some locations was expected and as stated previously, the final proposed shape could have multiple load-resisting mechanisms that would fail in sequence but not simultaneously. Shape NS4 was

developed based on the results of shape NS3 and it was noticed that the geometry needs some improvement to ensure that the strain will be distributed evenly, as much as possible. Thus, the middle four small circles were spaced evenly and in same alignment of the top and bottom small circles as shown in Figure 3-113 (a). Same as the other previous shapes, solid C3D8R were used as element type in this analysis. A mesh of 0.125-inch (3.175 mm) was used as element mesh and overall of 15,505 elements were used and as shown in Figure 3-113 (a). Non-linear elastoplastic A36 steel 36,259 psi (250 MPa) was used. Figure 3-113 (b) shows the boundary condition of shape NS4. The imposed displacement amplitude is shown in Figure 3-94.

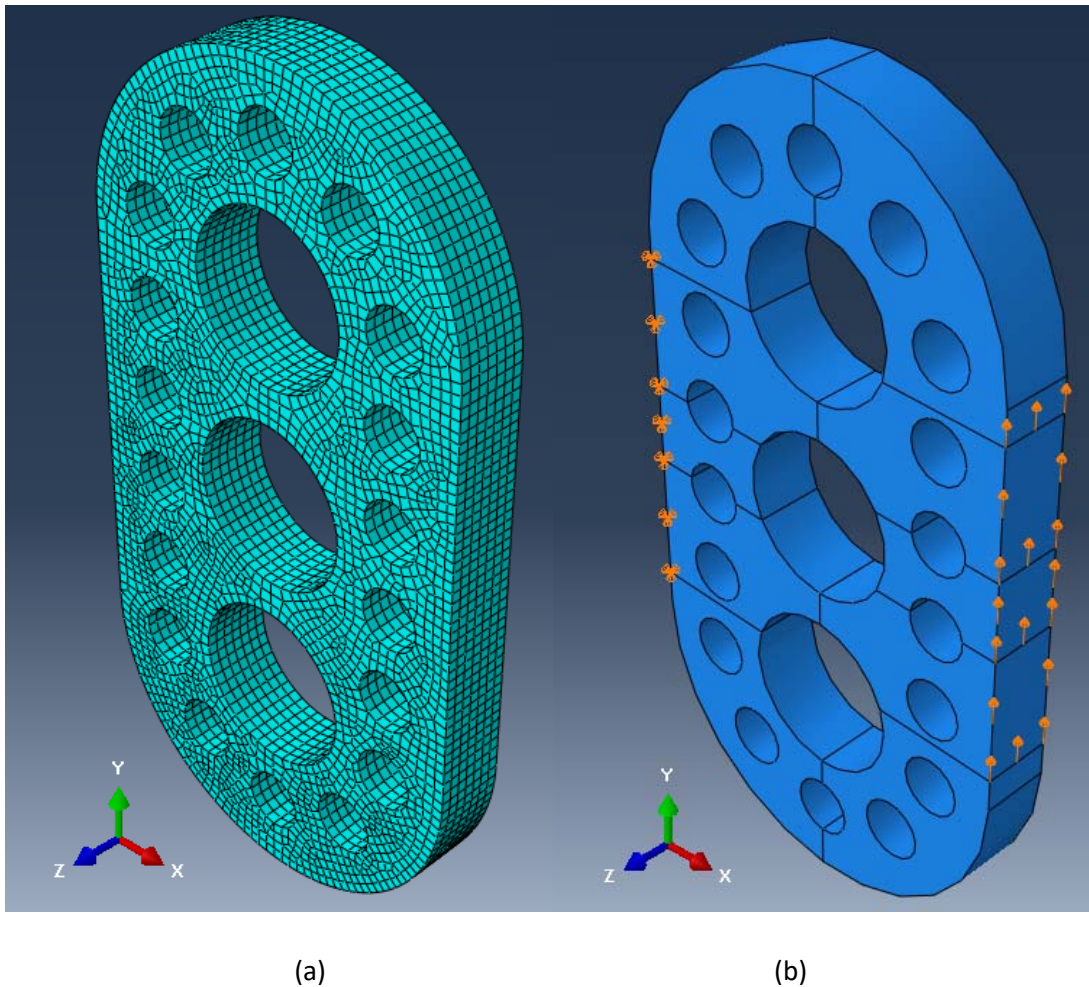


Figure 3-113: Shape NS4: (a) mesh shape, (b) boundary condition

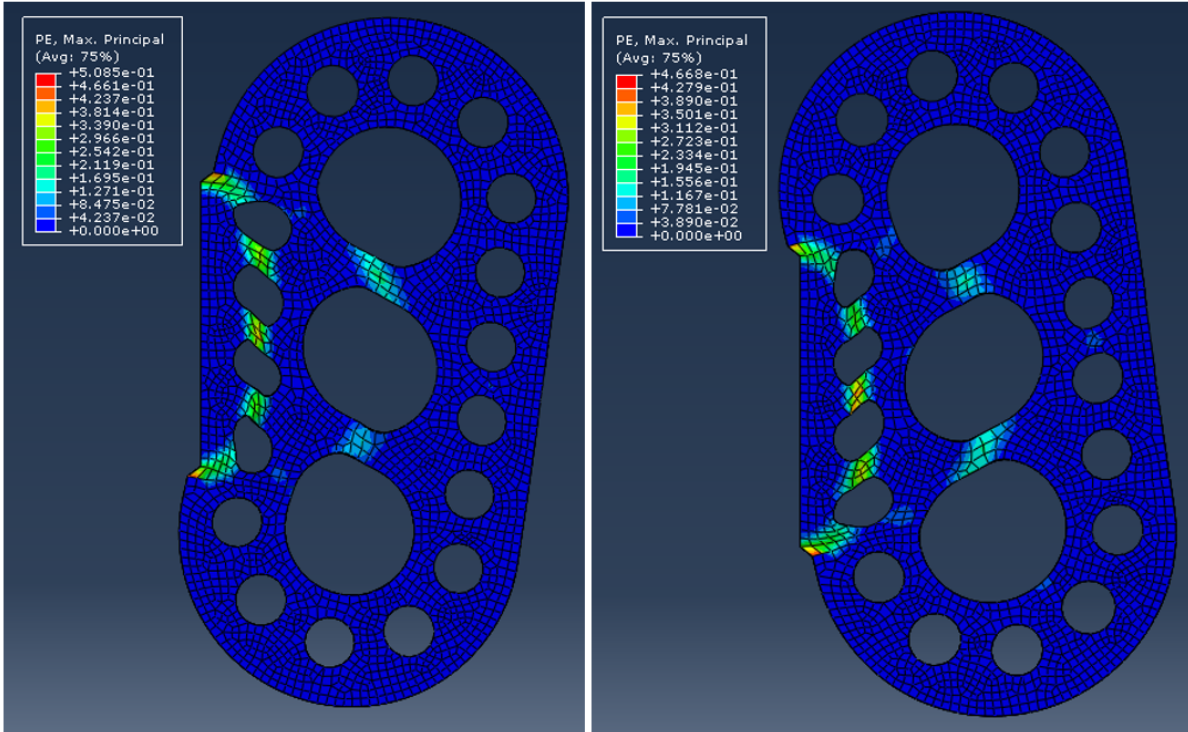


Figure 3-114: Plastic strain at 1 & -1 Displacement (left to Right) NS4

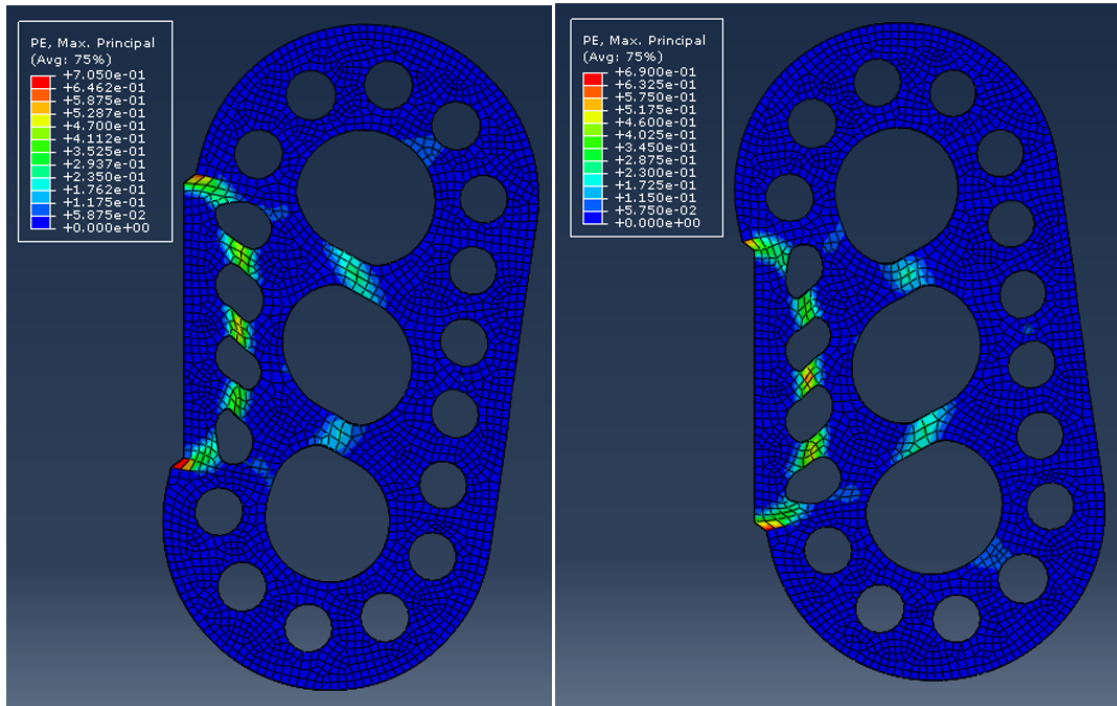


Figure 3-115: Plastic strain at 1.5 & -1.5 Displacement (left to Right) NS4

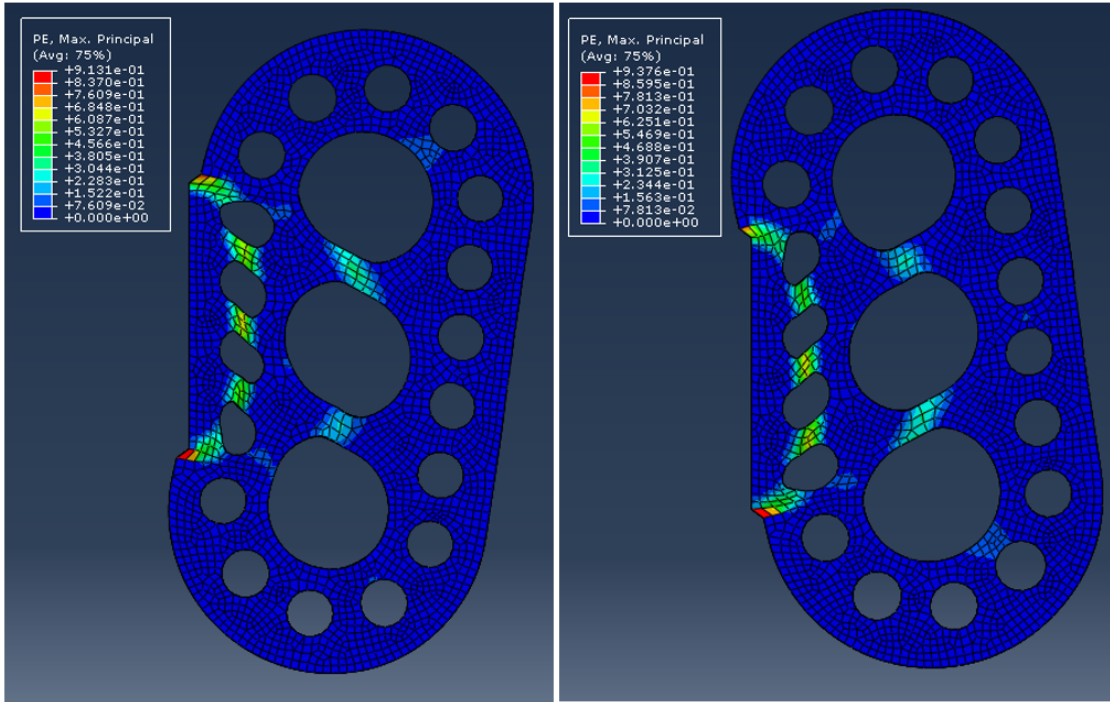


Figure 3-116: Plastic strain at 2 & -2 Displacement (left to Right) NS4

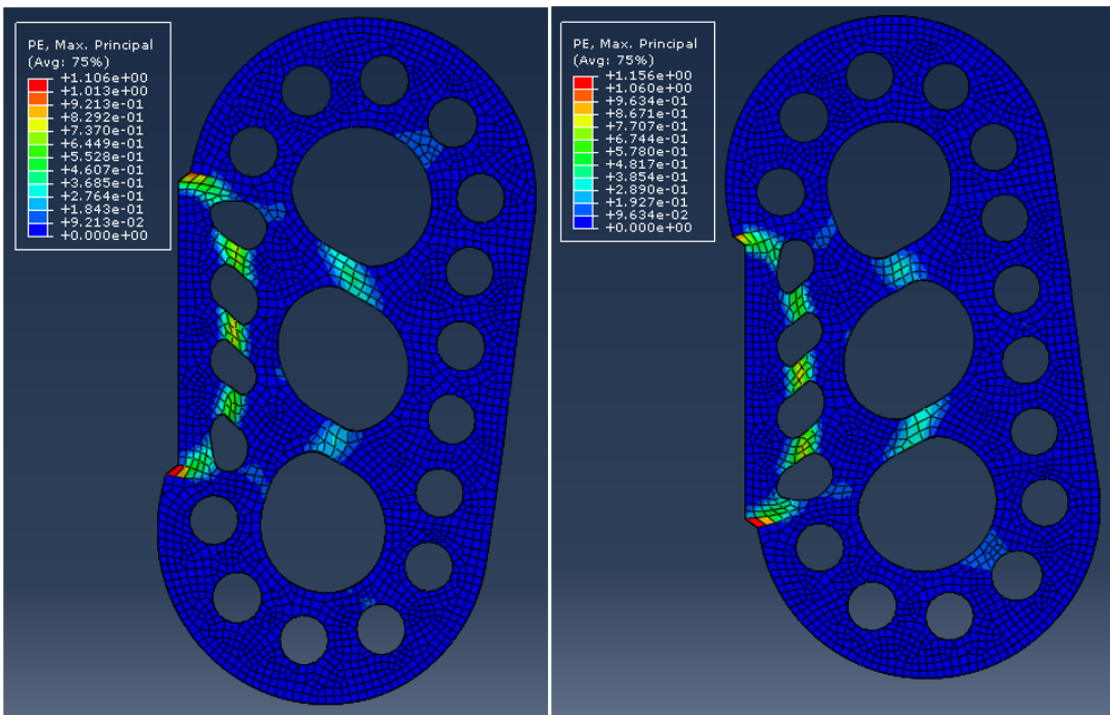


Figure 3-117: Plastic strain at ± 2.5 Displacement (+left, -Right) - NS4

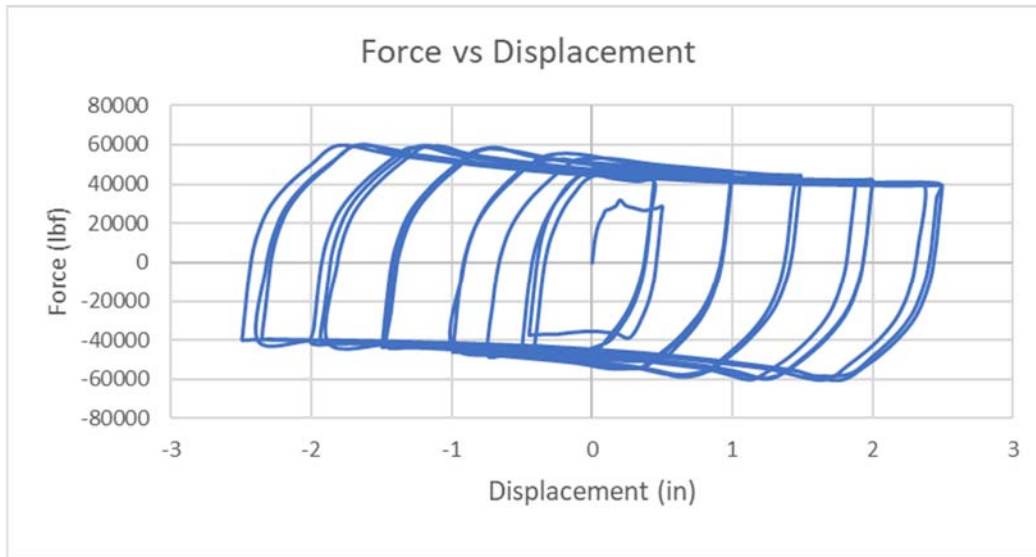


Figure 3-118: Force vs Displacement of shape NS4

Areas of localized high plastic strain at the top and bottom of the fixed end of model at the peak displacement was present as shown in the results presented in Figure 3-114 through Figure 3-117. It is evident that shape NS4 needs some more improvement to enhance the plastic strain results. Figure 3-118 show the Force vs Displacement graph which exhibits higher dissipated energy than those of both NS1 & NS2 but lower than that of NS3. The reaction force also was higher than the reaction force of shapes NS1 and NS2 but less than that of shape NS3.

3.6.5 Shape NS5

After comparing the results of all models, it was determined that by increasing the weld area to include some of the upper and lower curved edge of the connector, the plastic strain response could be improved. The actual dimensions of the model are shown in Figure 3-119. The weld was assumed to be extended for 1.125 in along both sides of upper and lower curved edges.

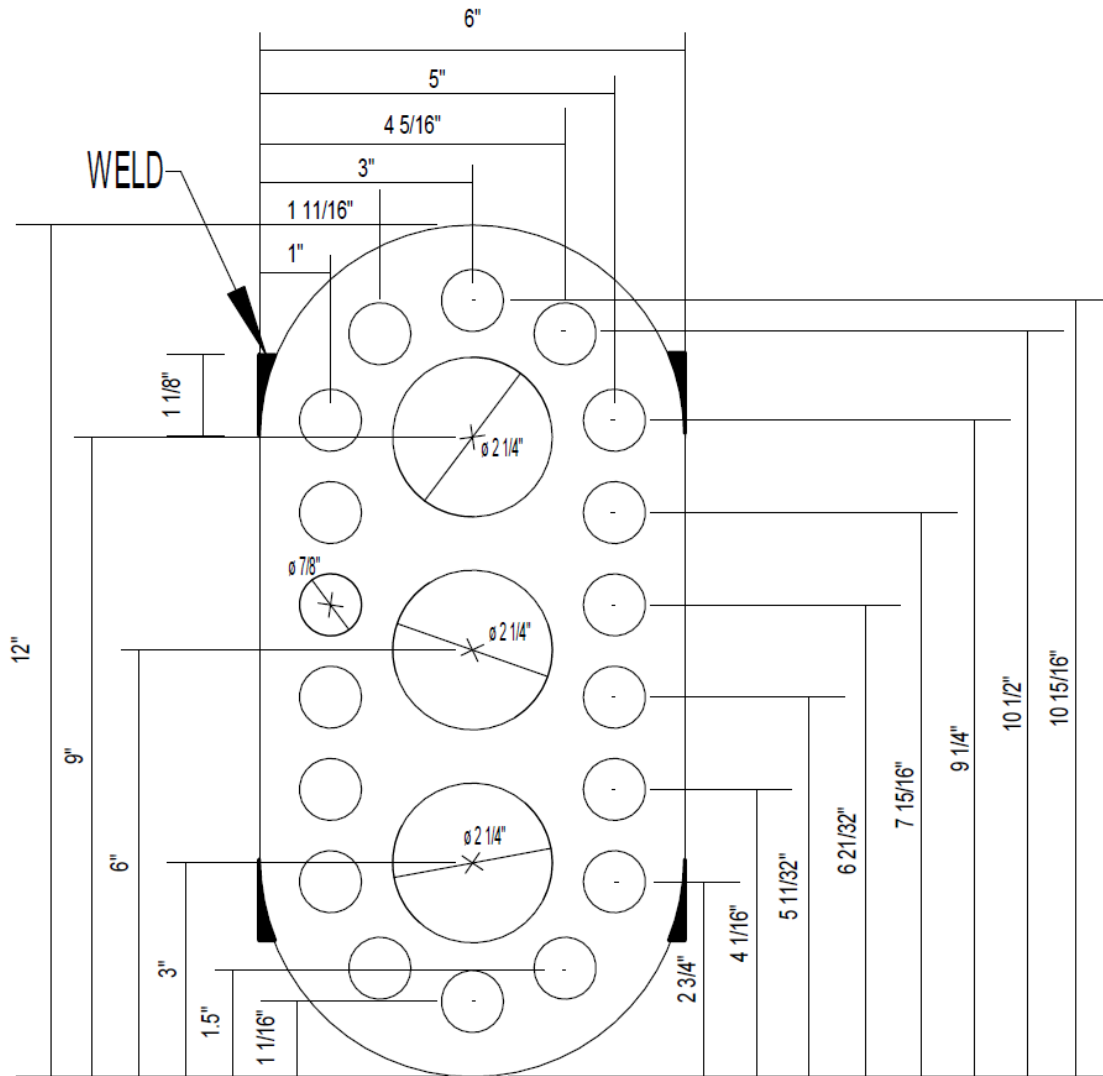
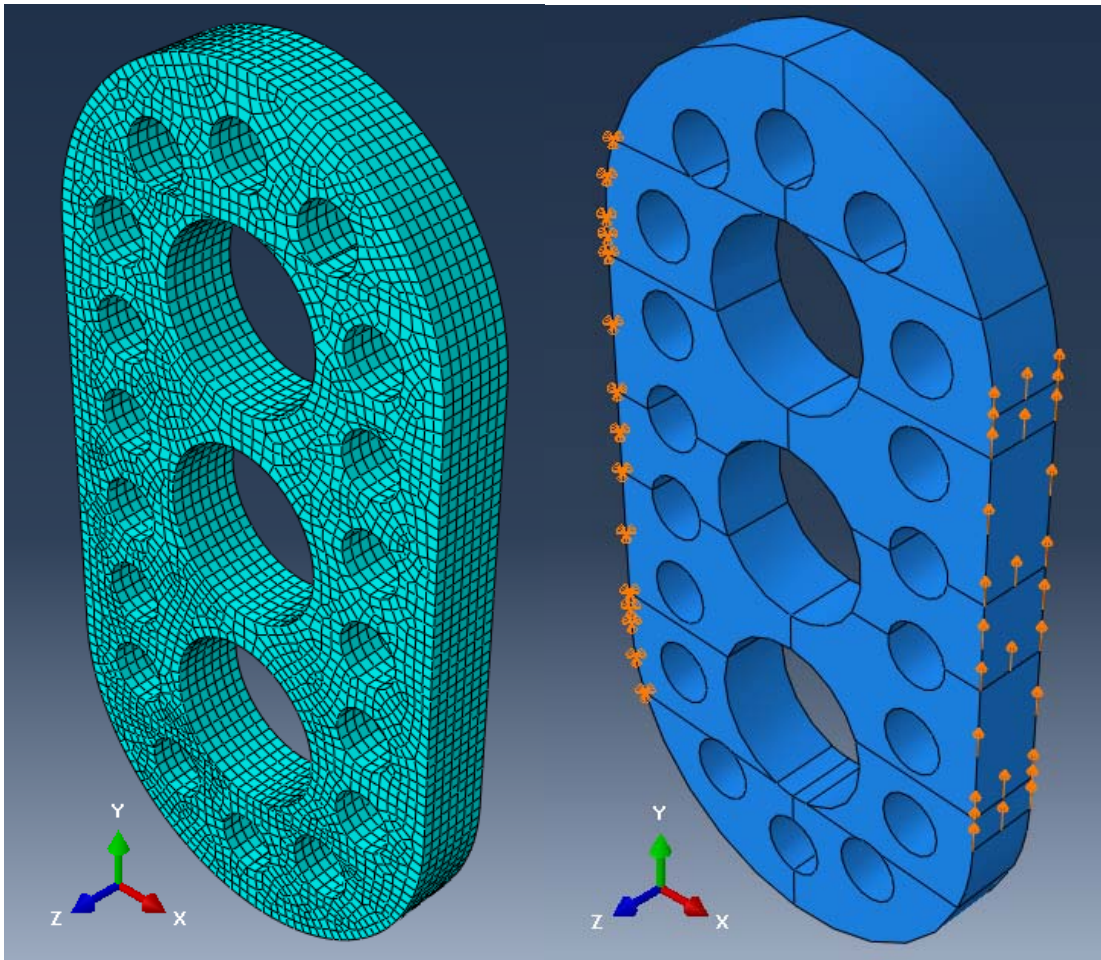


Figure 3-119: Sketch of shape NS5

Same as the other shapes, solid C3D8R was used as element type in this analysis. A mesh of 0.125-inch (3.175 mm) was used as element mesh and overall of 15,701 elements were used and as shown in Figure 3-120 (a). Non-linear elastoplastic A36 steel 36,259 psi (250 MPa). Figure 3-120 (b) shows the boundary condition of shape NS5. The imposed displacement amplitude is shown in Figure 3-94.



(a)

(b)

Figure 3-120: Shape NSS; (a) meshed shape, (b) boundary condition

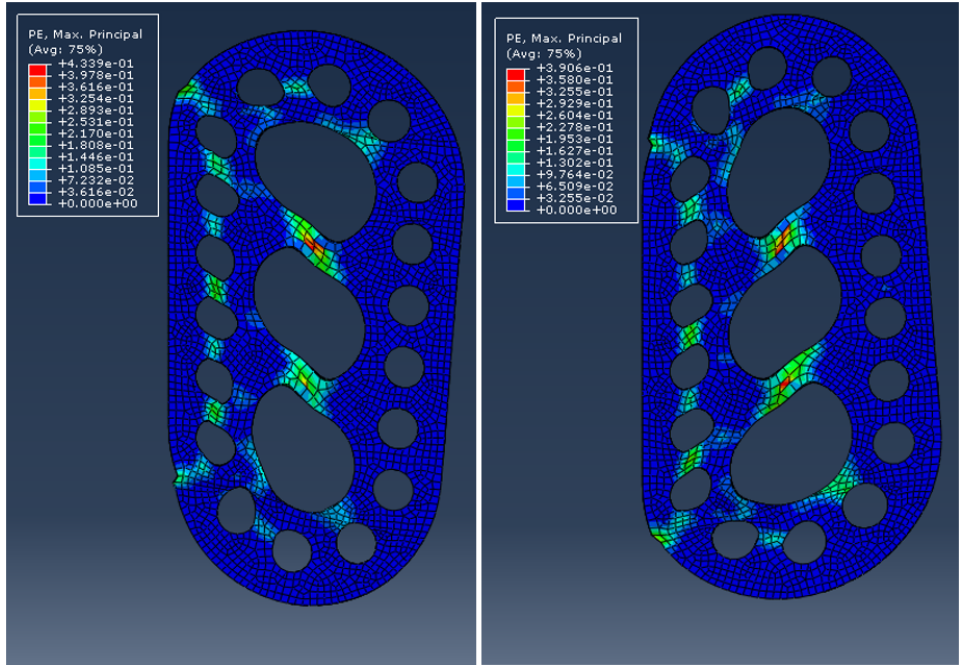


Figure 3-121: Plastic stains at -1 & 1 displacement (left to right) NS5

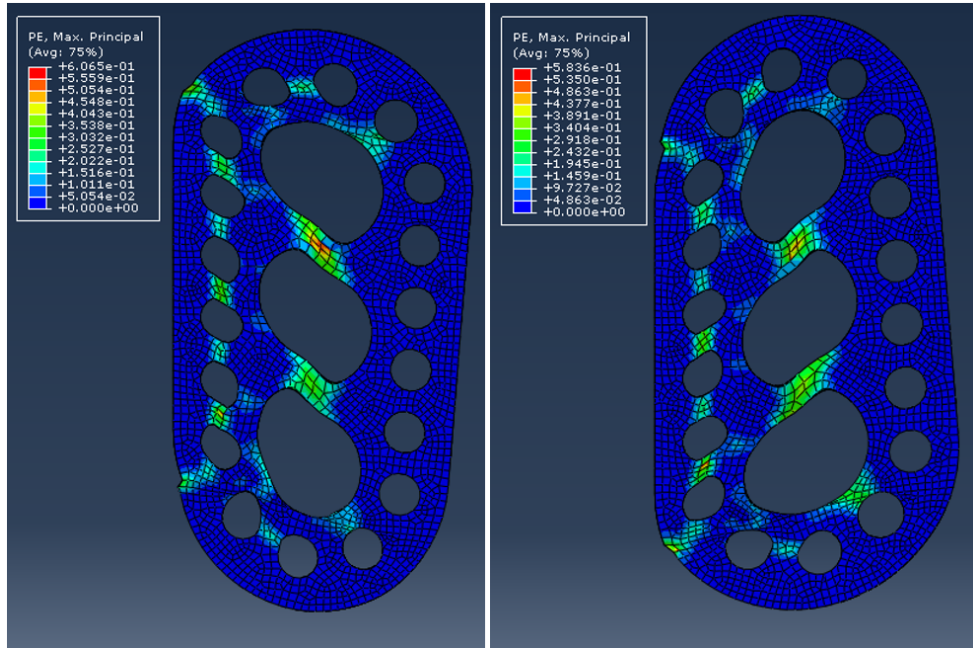


Figure 3-122: Plastic stains at -1.5 & 1.5 displacement (left to right) NS5

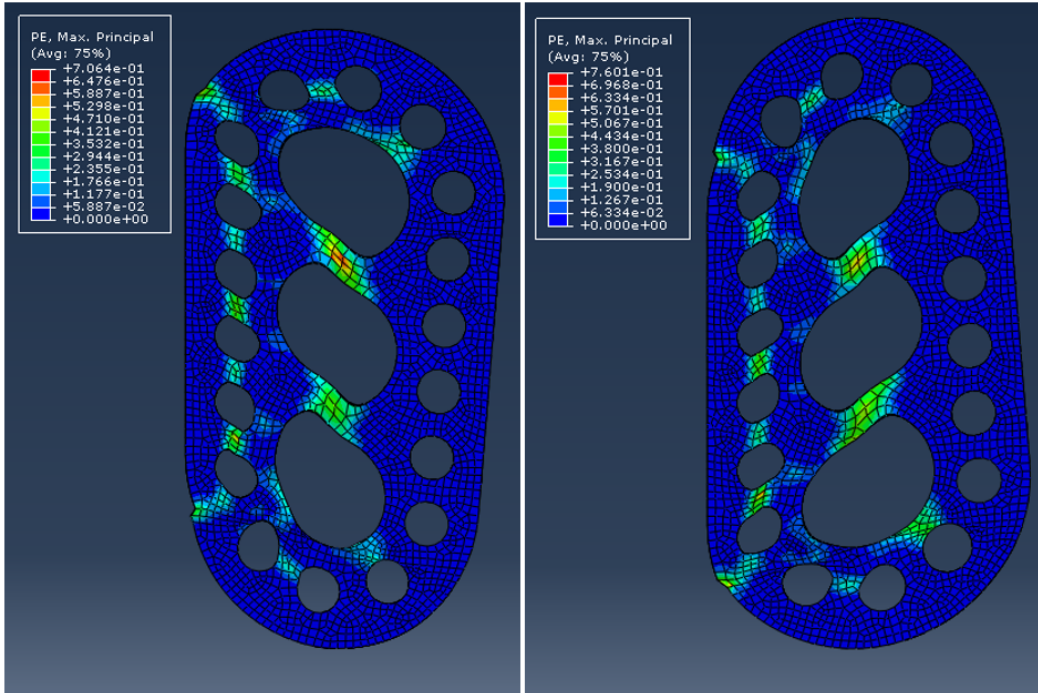


Figure 3-123: Plastic stains at -2 & 2 displacement (left to right) NS5

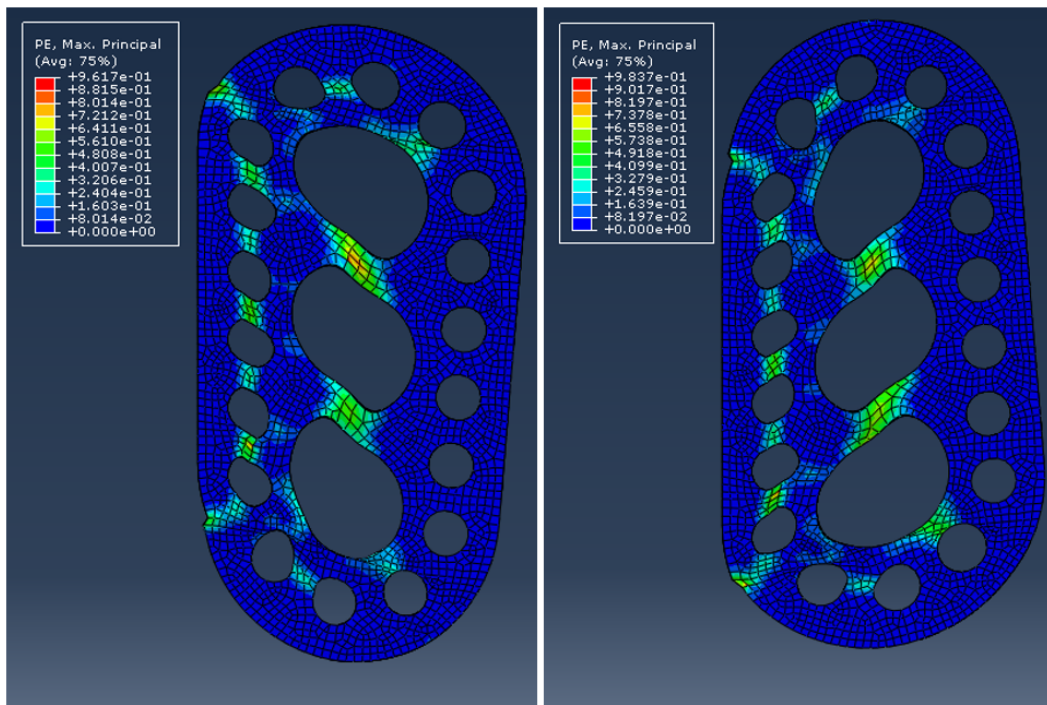


Figure 3-124: Plastic stains at -2.5 & 2.5 displacement (left to right) NS5

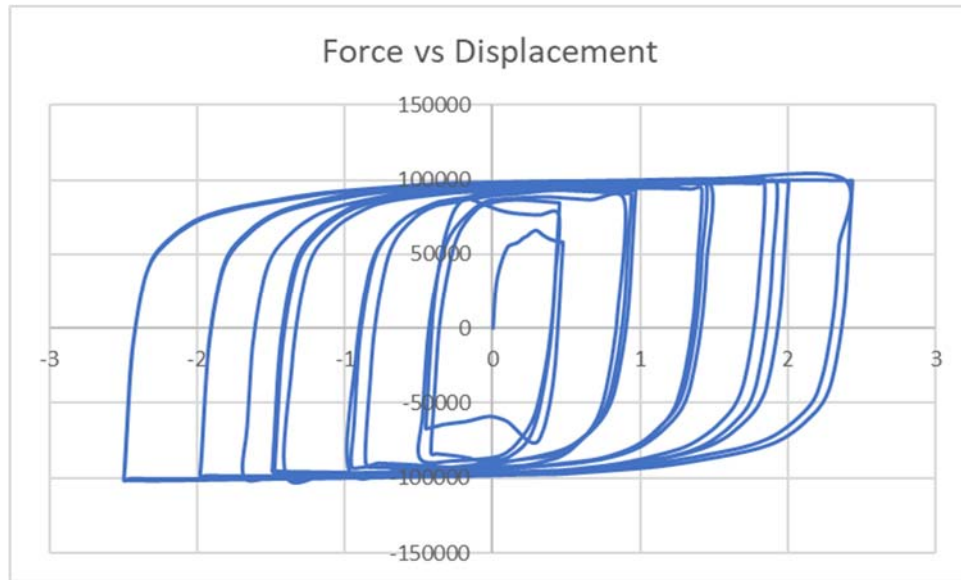


Figure 3-125: Force vs Displacement for shape NS5

High strain spots have slightly improved and the overall strain distribution has been enhanced. Since the new shape was designed based on multiple mechanisms that would fail in sequence rather simultaneously. The current shape has provided the intended aspects. The plastic strain contours of shape NS5 are shown in Figure 3-121 through Figure 3-124. Figure 3-125 show the Force vs Displacement graph which exhibits higher dissipated energy than all other shape in addition to higher reaction force.

Few other shapes were modeled and checked in attempt to get the best possible response. Main changes that have been tried is by extending the weld further or changing the sizes of middle circle. However, shape NS5 remained better than all other shapes when it comes to dissipated energy and plastic strain results. Therefore, an experimental test was conducted on shape NS5. In the next chapter (Chapter 4), a detailed description of the experimental testing will be presented.

3.6.5.1 NS5 under horizontal displacement

The same ABAQUS model for the U-shaped connector discussed earlier (in section 3.4.2.1) was used to model the NS5 connector under horizontal displacement. One side of the model was fixed while the opposite side was displaced based on the displacement cycles shown in Figure 3-127. Figure 3-126 shows the boundary conditions for the NS-5 connector model. The horizontal force-displacement response of the NS-5 connector is shown in Figure 3-128. The stiffness and strength of the NS-5 connector in the horizontal direction is significantly higher than the corresponding U-shape connector response. These results are used to develop bilinear spring models for inclusion in the building models. It must be noted that the results of this analysis will be used later in this study.

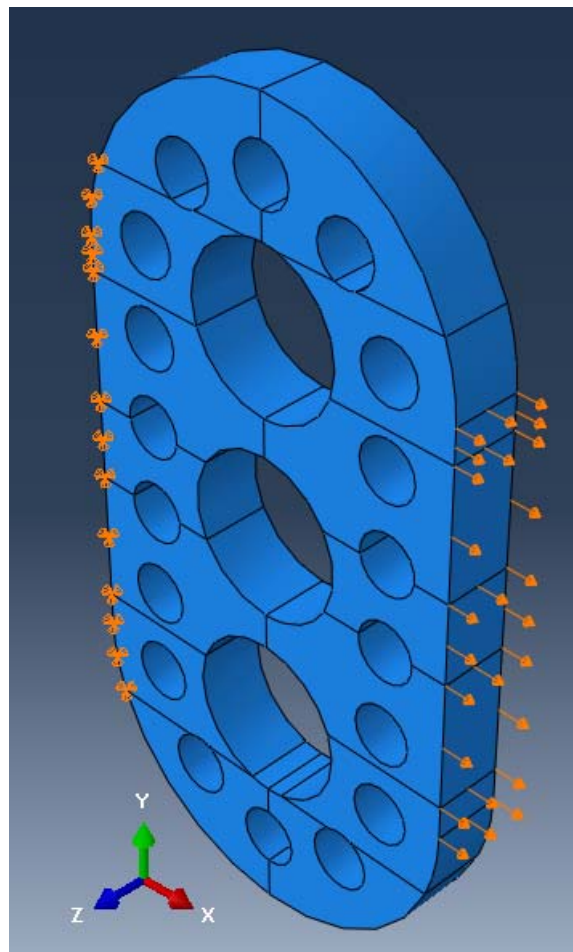


Figure 3-126: NS5 boundary condition

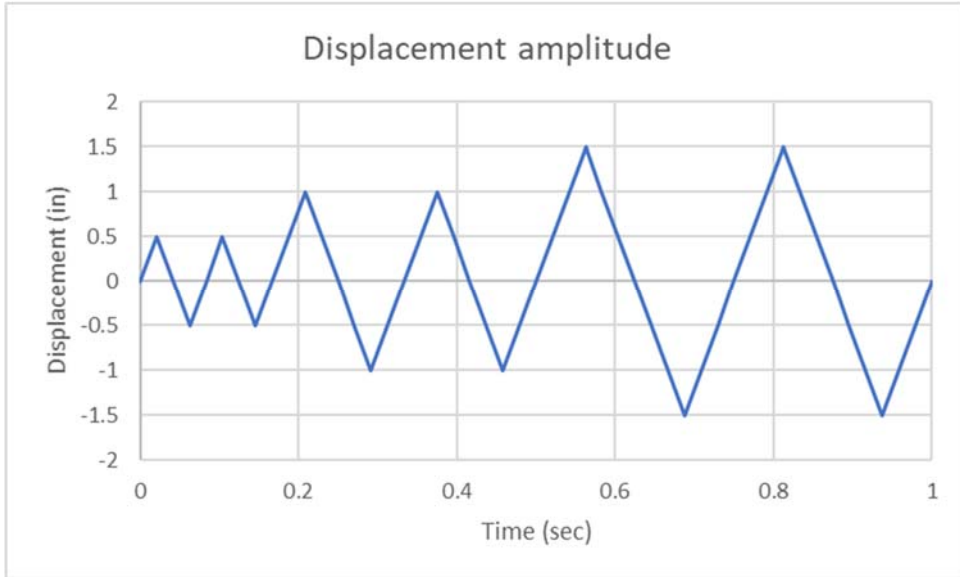


Figure 3-127: Displacement amplitude

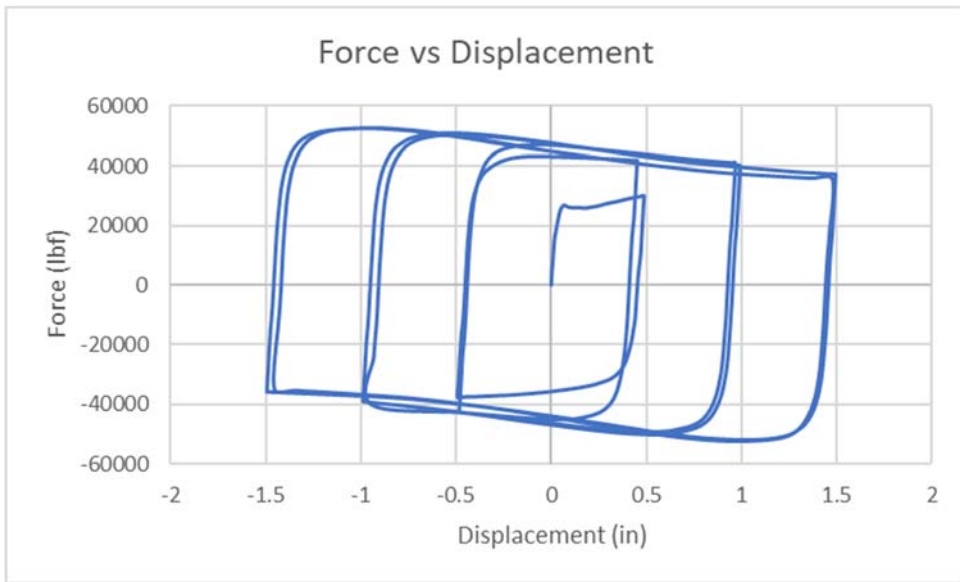
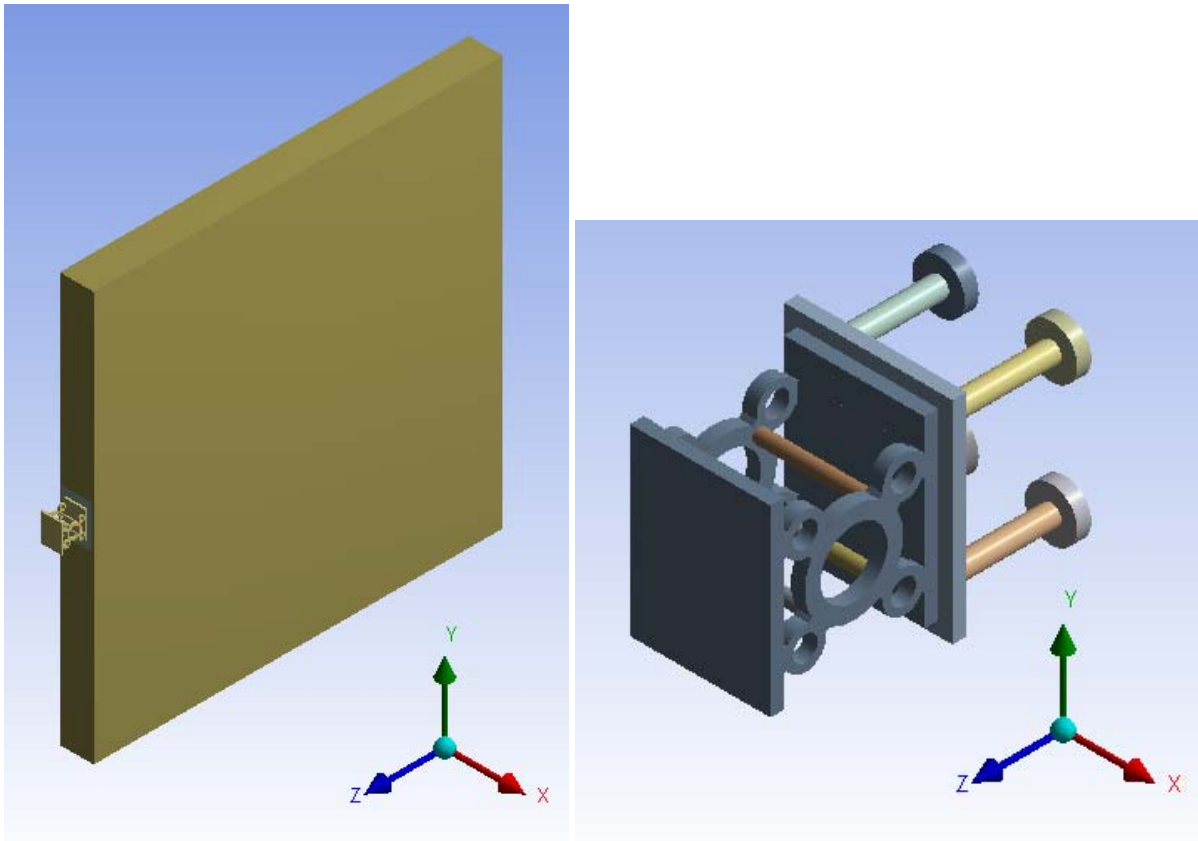


Figure 3-128: Force vs Displacement for NS5 shape

3.7 Localized resistance of concrete

A better understanding of the effect of the reaction force on the supporting shear wall is needed to make sure that the wall would not fail locally due to excessive force from the connector. There are a wide variety of connection details that could be used in the concrete. The connection detail used in these studies is an example, and therefore the results reported here do not apply to all possible connection cases.

Initially, a model of the entire wall was generated in ANSYS. The purpose of this first wall model was to determine the zone of influence of reaction force developed at the connector so that a smaller model of a portion of the wall could be developed for detailed examination. Figure 3-129 shows the model of the entire wall including the connector.



(a)

(b)

Figure 3-129: ANSYS model illustration: (a) wall with the device, (b) the device with embed plate

The ANSYS element type that was used in this analysis was Solid 186 for both the device and concrete. The concrete was reinforced with steel bars and the reinforcement was modeled as well. The element mesh sizes were 6-in for the wall and 0.25-in for the device and reinforcement. The total number of elements was 16,510. Elastoplastic steel with a yield strength of 60,000 psi was used for the reinforcement, while A36 steel was used for the device. The design compressive strength of concrete was assumed to be 4000 psi. The imposed displacement profile was similar to that used by PRESS (Figure 3-9).

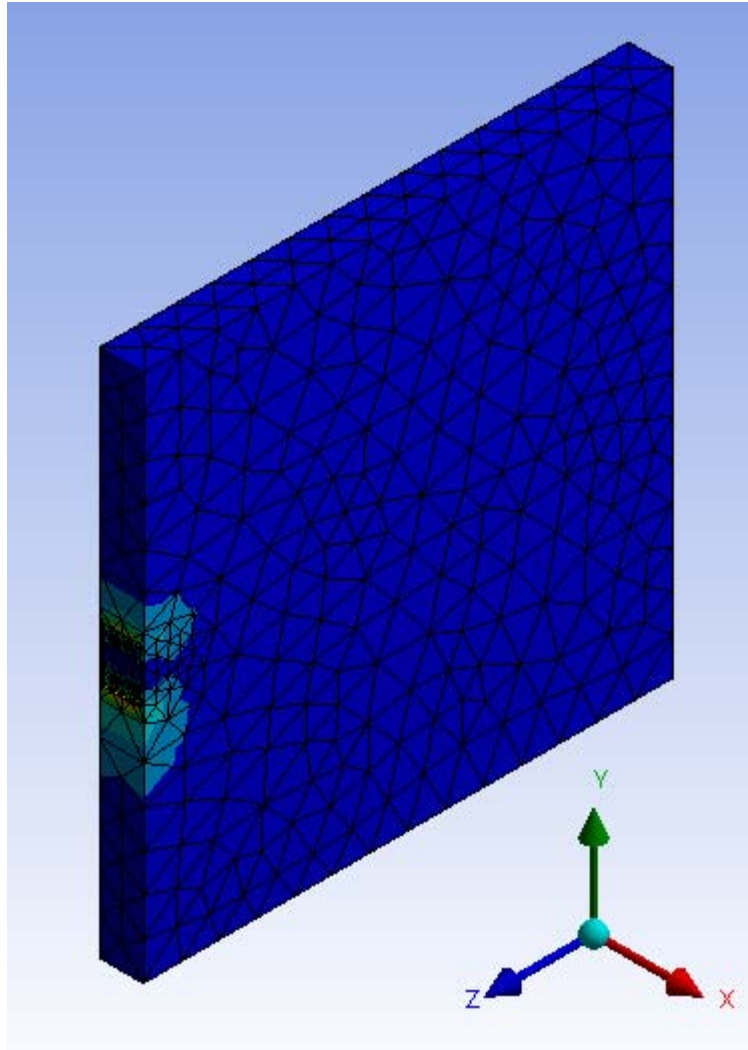


Figure 3-130: Stress contours for the wall model

Figure 3-130 shows indicates that only a limited area was substantially affected by the applied displacement. This area was within a 3'-0"x2'-0" block of the wall.

The Concrete Damage Plasticity (CDP) concrete model in the ABAQUS software was used due to the ease of modeling and familiarity. CDP includes a “combination of non-associated multi-hardening plasticity and scalar (isotropic) damage elasticity to describe the irreversible damage that occurs during the fracturing process” [39]. A full description is provided in the ABAQUS User Manual [39].

The Concrete damage plasticity parameters used in this model are shown in Table 3-3 [39].

Table 3-3: Concrete damage plasticity parameters [39]

Parameter	Description	Value
ψ	Dilation Angle	30°-40°
ϵ	Flow potential eccentricity	0.1
σ_{b0}/σ_{c0}	Ratio of initial equibiaxial compressive yield stress to initial uniaxial compressive yield stress	1.16
K_c	Ratio of the second stress invariant on the tensile meridian to that on the compressive meridian at initial yield for any given value of the pressure invariant such that the maximum principal stress is negative	0.667
μ	Viscosity parameter	N/A

3.7.1 Verification model

Before modeling the device and shear wall, a verification model was needed to gain confidence in the ability to model the anchorage behavior. The works by Segle et. al. [39] and Gross et. al. [40] provide the experimental data needed for the verification model. Gross et. al [40] conducted a series of tests on near-edge ¾-in-diameter anchors that were embedded 4-in into concrete with a spacing of 4-in between anchors and a 4-in edge distance. Three types of anchors were tested: cast-in-place, expansion and undercut anchors. of the following types of tests were conducted: static and dynamic test of single anchor in tension, static and dynamic test of group of anchors in tension, static and dynamic test of near-edge single anchors, and static and dynamic test of near-edge group of anchors [40]. Figure 3-131 shows an elevation view of one of the anchors layouts that were tested by Gross et. al. study.

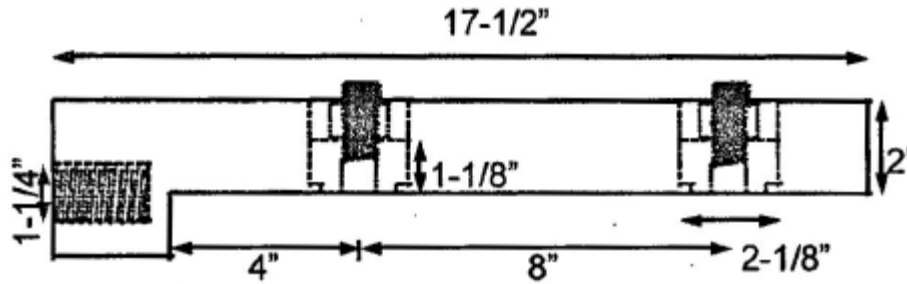


Figure 3-131: Gross et. al model; plate with two anchors [40]

Attention was focused on the modeling of group of anchors under shear loading. Segle et. al [39] modeled a block of concrete that was 87-in X 14-in X 30-in. Figure 3-132 through Figure 3-134 show the concrete block with test rigs that were used to support the block during the loading process. The distance between test rigs was 17.75 in (450mm).

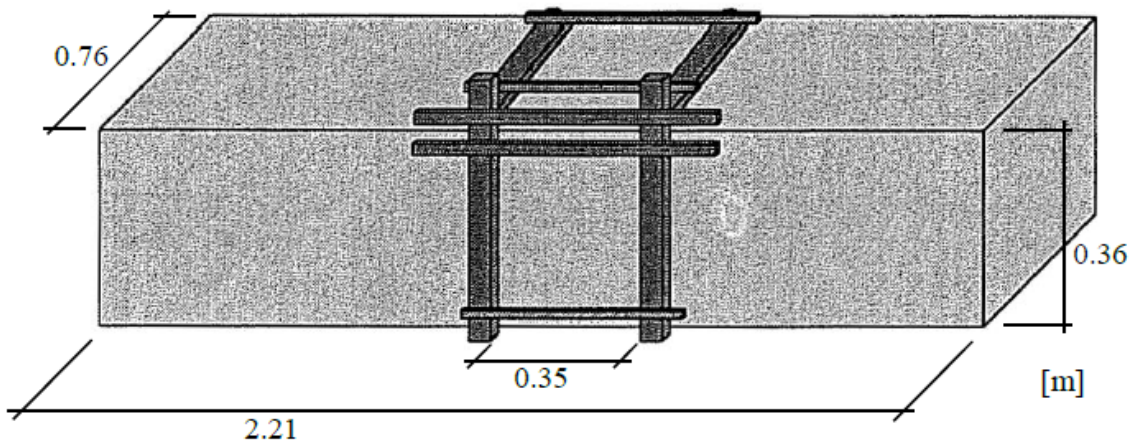


Figure 3-132: Concrete Block [39]

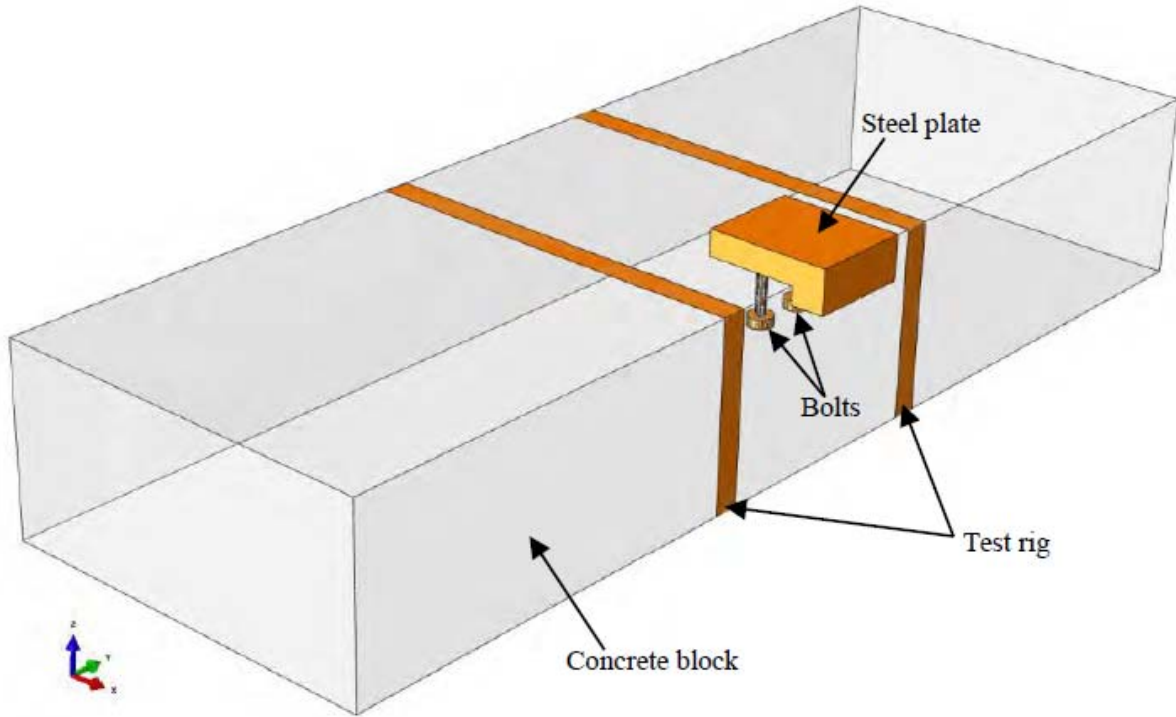


Figure 3-133: Concrete block with anchors and plate [39]

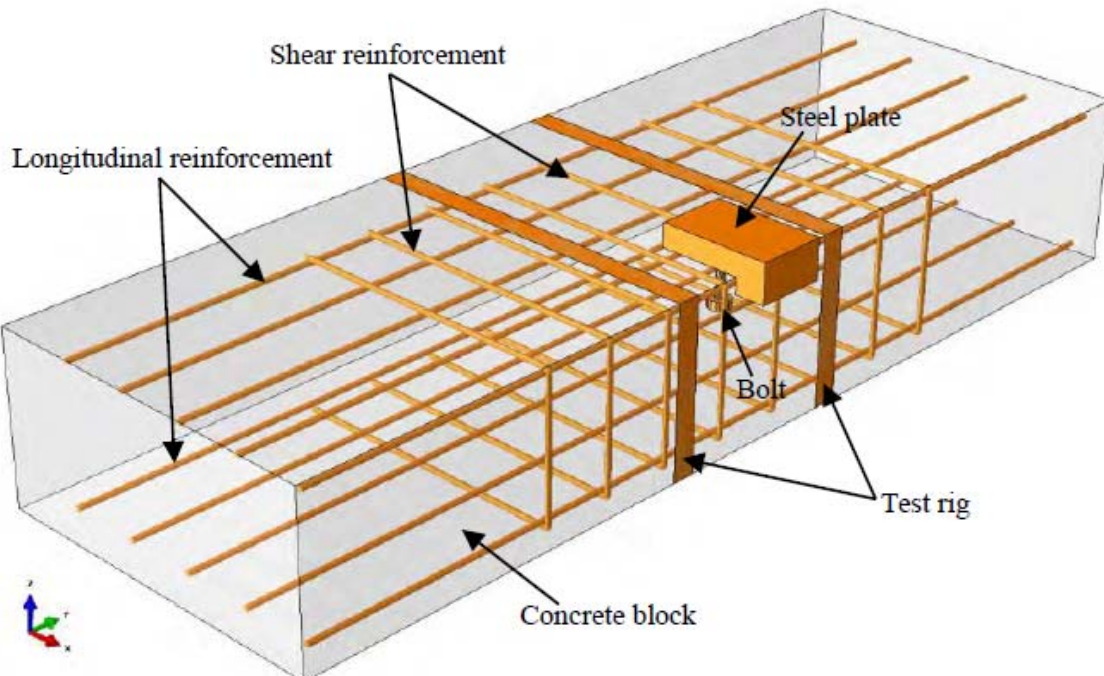


Figure 3-134: Concrete block with reinforcement [39]

The concrete was modeled using 8-node solid element (C3D8R) with reduced integration [39]. The anchor bolts and steel plate were modeled using 6-node solid elements (C3D6R) with reduced integration [39]. The rig was modelled with rigid elements type R3D4 [39].

Displacement was imposed on the steel plate near the surface of the concrete to eliminate any eccentricity. The rate of applied displacement was 30 mm/s. Figure 3-135 shows reinforcement layout and the spacing of anchors in (mm). Figure 3-136 shows the results of the testing of two anchors in shear. It is referred to as group B. The maximum exerted force in this case was approximately 18,000 lbf.

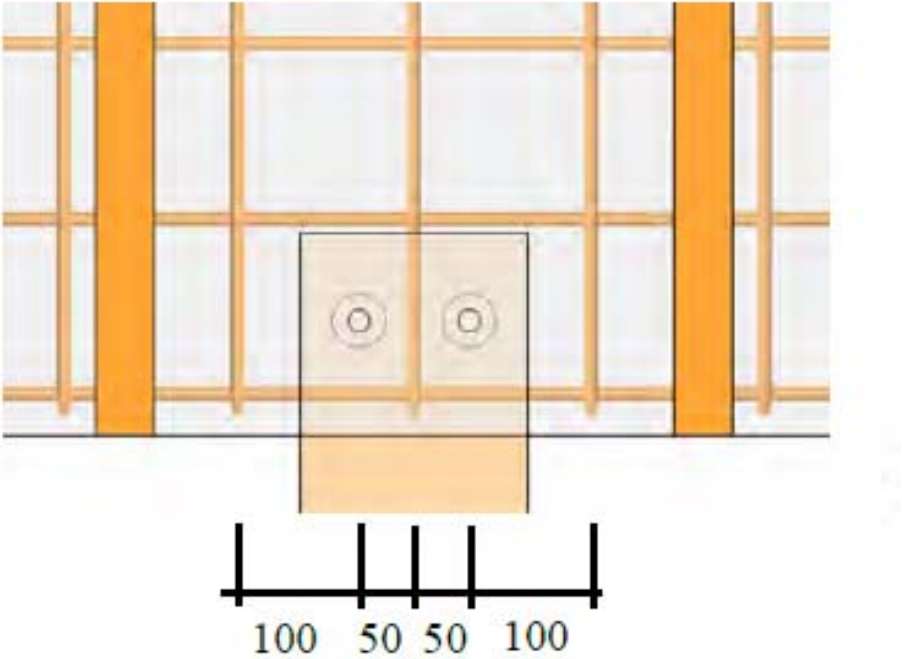


Figure 3-135: Reinforcement layout with respect to anchors [39]

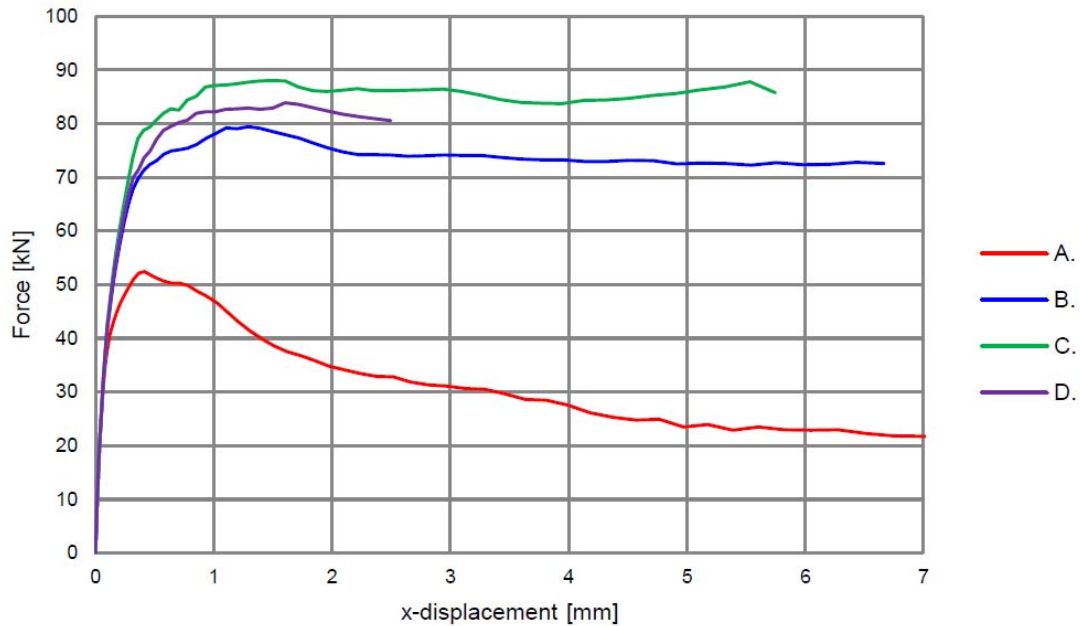


Figure 3-136: Test results of all specimens

ABAQUS was used to model the test described above. Table 3-4 and Table 3-5 show the parameters used for the concrete and steel elements in ABAQUS.

Table 3-4: Concrete modeling properties

Variable	Description	Value (20°C)
E	Modulus of elasticity	31 GPa (4.5E6psi)
ρ	Density	2400 Kg/m ³ (2.7E-3 slug/in ³)
ν	Poisson's ratio	0.2

Table 3-5: Steel modeling properties

Variable	Description	Value (20°C)
E	Modulus of elasticity	210 GPa (30E6psi)
ρ	Density	2400 Kg/m ³ (8.8E-3 slug/in ³)
ν	Poisson's ratio	0.3

As it could be noticed that the steel anchors, steel plate, and steel reinforcement all were modeled as elastic material. The Nodes at the lower surface of the concrete block were restrained to move in vertical direction only. Also, one bottom corner node was restricted from translating in the horizontal directions. Figure 3-137 show the boundary condition of the model.

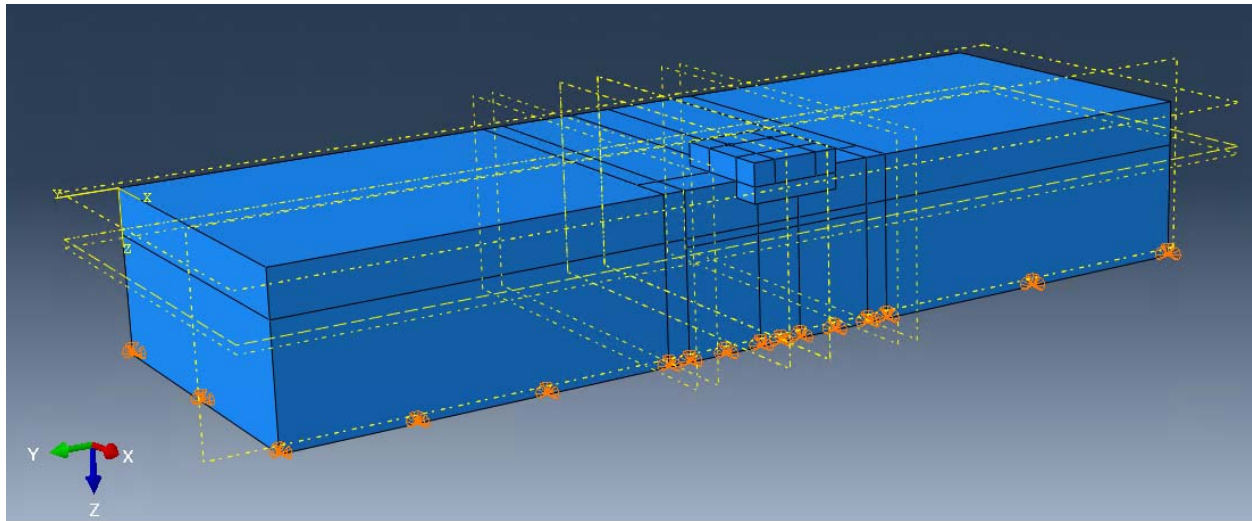


Figure 3-137: Boundary condition of the model

The types of elements used were the same as those used by Segel et al. The contacts were modeled as non-linear contact. The contact between the rigs and concrete block was defined as hard contact to restrict different parts from passing other parts but allow separation with zero tension stresses. Similar contact was defined between concrete block and anchors, and plate and anchors. Friction definition was not included in any of the contacts. Finally, Concrete was defined as slave and steel as master. Figure 3-138 and Figure 3-139 show the meshed and wireframe views of the model. The displacement was applied in at a rate 30mm/s.

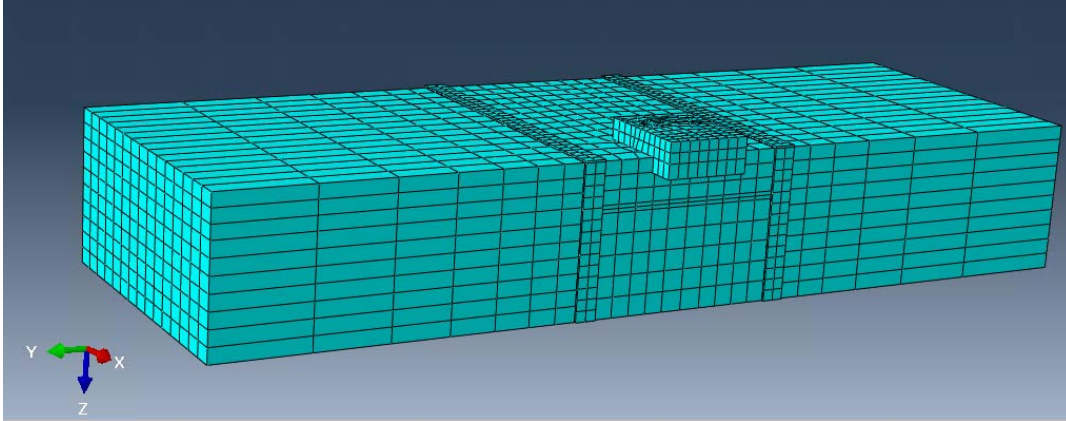


Figure 3-138: Meshed model

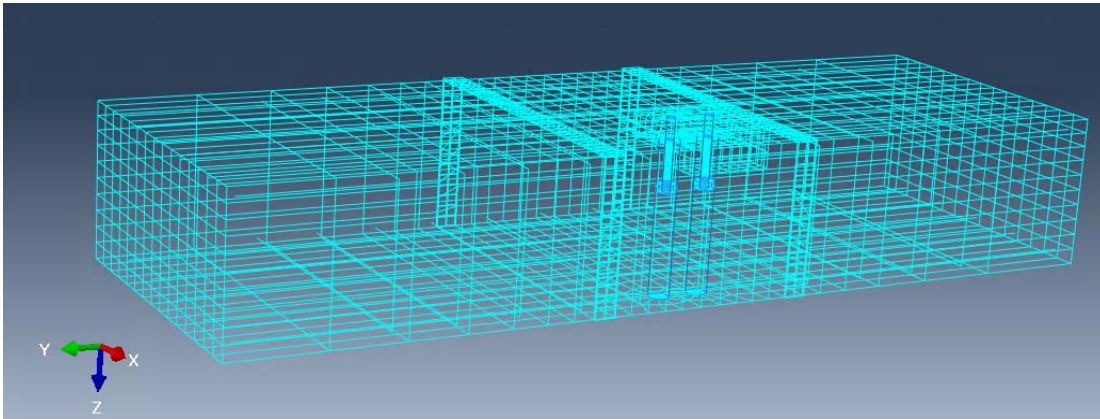


Figure 3-139: Wireframe view of the model

Figure 3-140 show the force versus displacement relationship obtained from the ABAQUS model compared results from Segle et. al. The verification model was therefore in good agreement with the test results by Segle et. al. until the yield point. The verification model shows more hardening due possibly to differences in element stiffness and CDP parameters. Ultimately, the results were considered satisfactory for the purposes of this study.

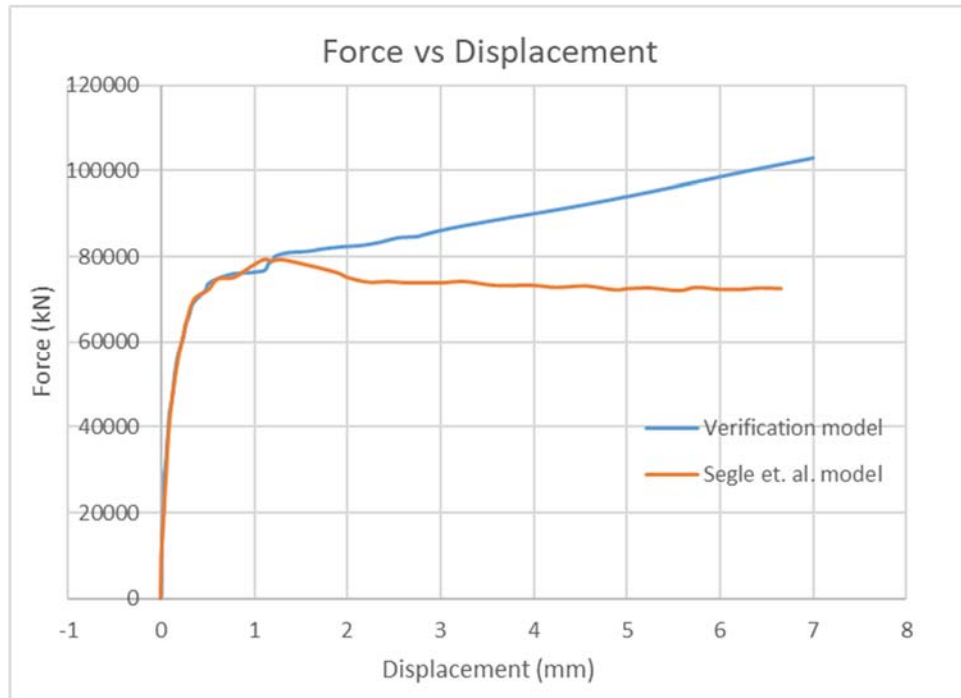
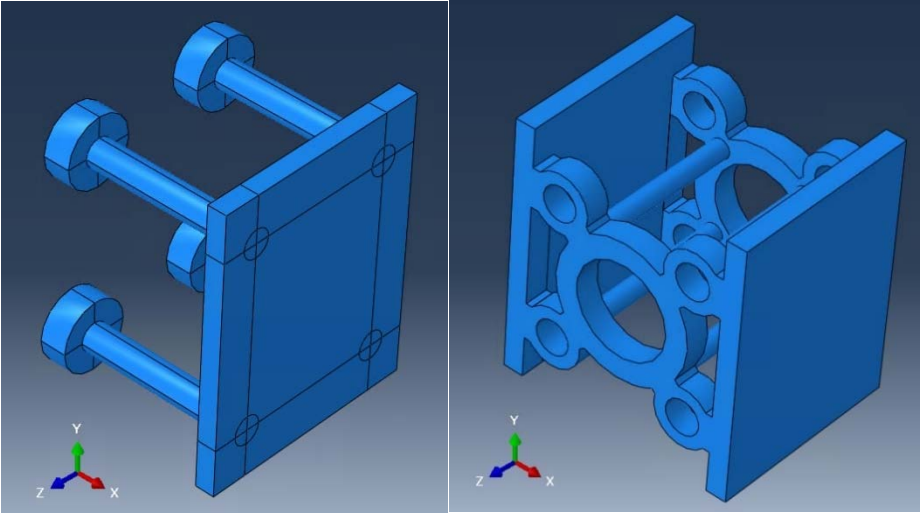


Figure 3-140: Simulation results

3.7.2 Modeling of TS connector with precast wall.

After verifying the modeling process using the available test results, a model of the TS connector together with a localized segment of the precast shear wall (with the same anchorage pattern described in the test above) was generated and subjected to displacement cycles specified by the PRESSS program. The modeled concrete block dimensions were 3'-6" x 3'-0" x 0'-8". The embedded plate was 1/2" x 6" x 7 1/2" with four 3/4-inch diameter headed anchors spaced at 4" on center horizontally and 5 in on center vertically. Figure 3-141 show the embedded plate with anchors and the TS connector. The reinforcing steel cage consisted of No. 6 bars at 6-in spacing in the horizontal direction and No. 4 bars at 12-in spacing in the transverse direction. Concrete damage plasticity type of material was used for the concrete block. Elastoplastic steel material was used for the steel reinforcement (cage), TS shape and

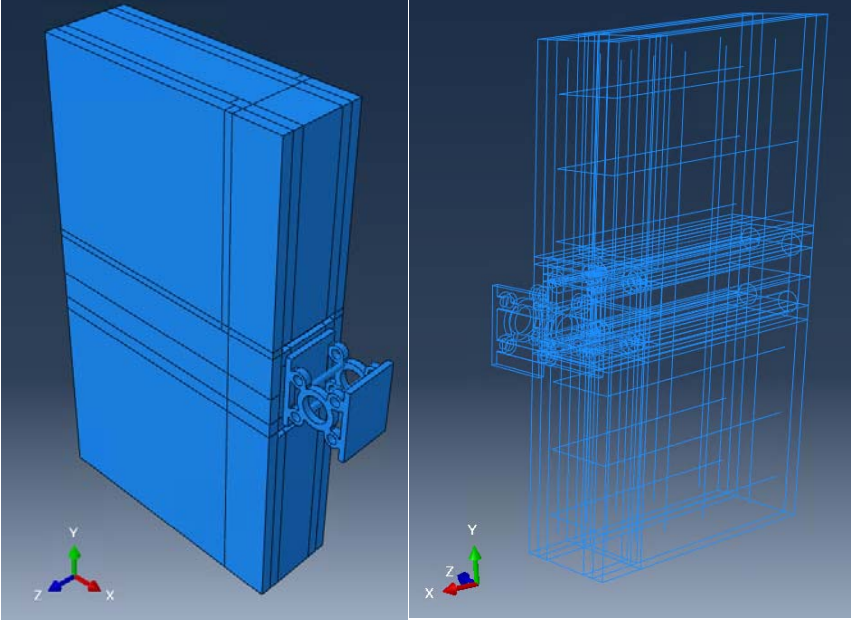
embed anchors. For the embed plate, elastic material was used based on recommendations found in the literature [39]. Figure 3-142 shows all parts after the assembly process.



(a)

(b)

Figure 3-141: Model parts; (a) Embed plate, (b) TS shape



(a)

(b)

Figure 3-142: Assembled parts: (a) solid view, (wireframe)

For boundary conditions, the back surface of the block as well as the top and bottom surfaces were fixed in translation in three direction but free to rotate. (Figure 3-143). The various parts were meshed independently. Finer mesh was used for the anchor bolts and concrete surrounding it as cracking of the concrete was expected to occur. Slightly coarser mesh was used for the other parts including the TS device. Figure 3-144 shows the mesh of concrete block and embed plate with anchors.

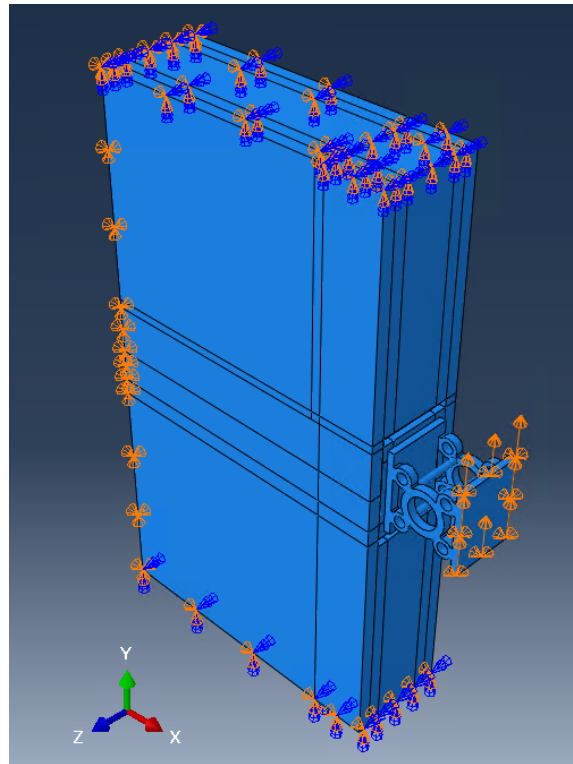


Figure 3-143: Boundary conditions of the model

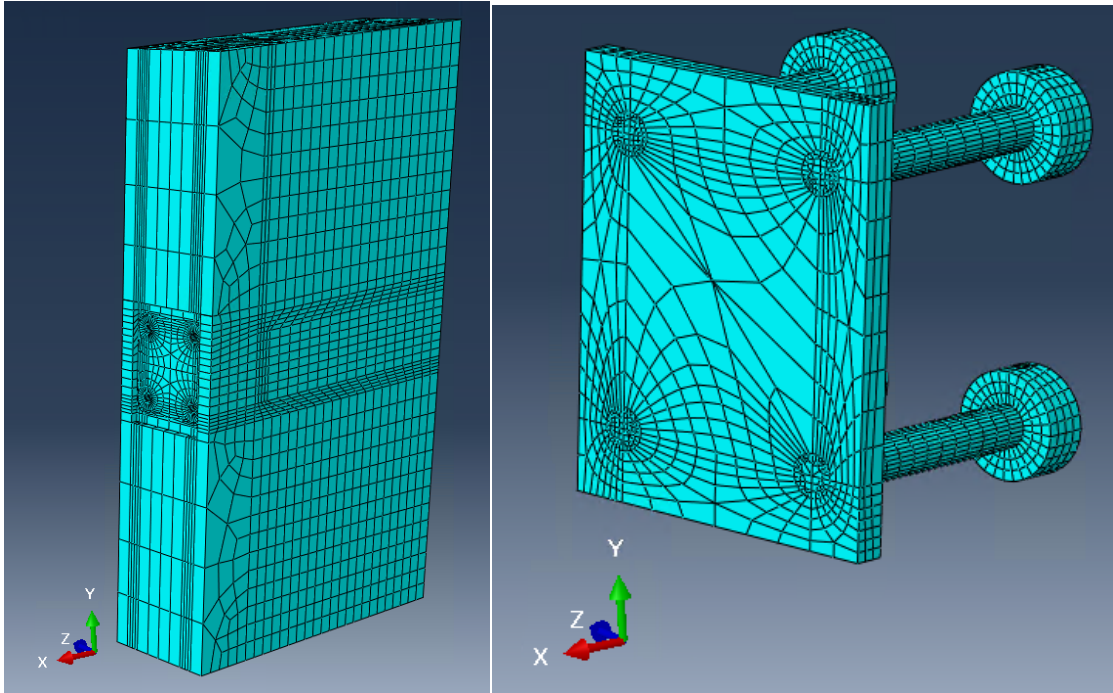


Figure 3-144: Meshed parts; (a) concrete block, (b) embed plate

A total displacement of 1.57" (40mm) was applied in increments. Figure 3-145 shows the force-displacement relationship.

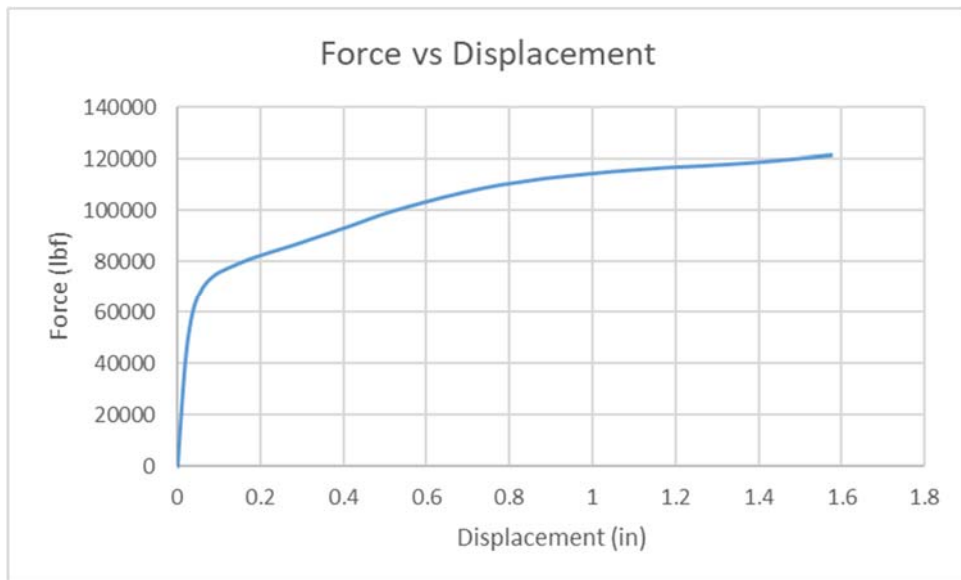


Figure 3-145: Force vs Displacement of the model

The maximum reaction developed was on the order of 75,000 lbf. The main purpose of this model was to assess the approximate effect of imposed forces by the connector on a particular anchorage system.

Figure 3-146 shows the strain amplitudes in the damaged concrete. Figure 3-147 shows the zone of damage in concrete in the vicinity of the embedded anchors.

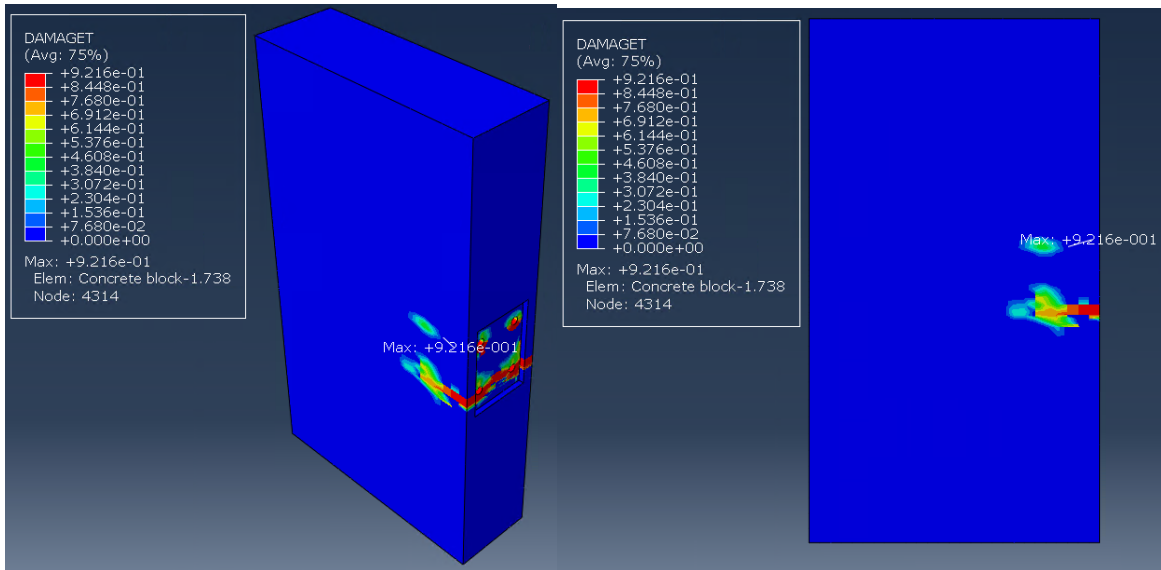


Figure 3-146: Damage effect on the concrete block

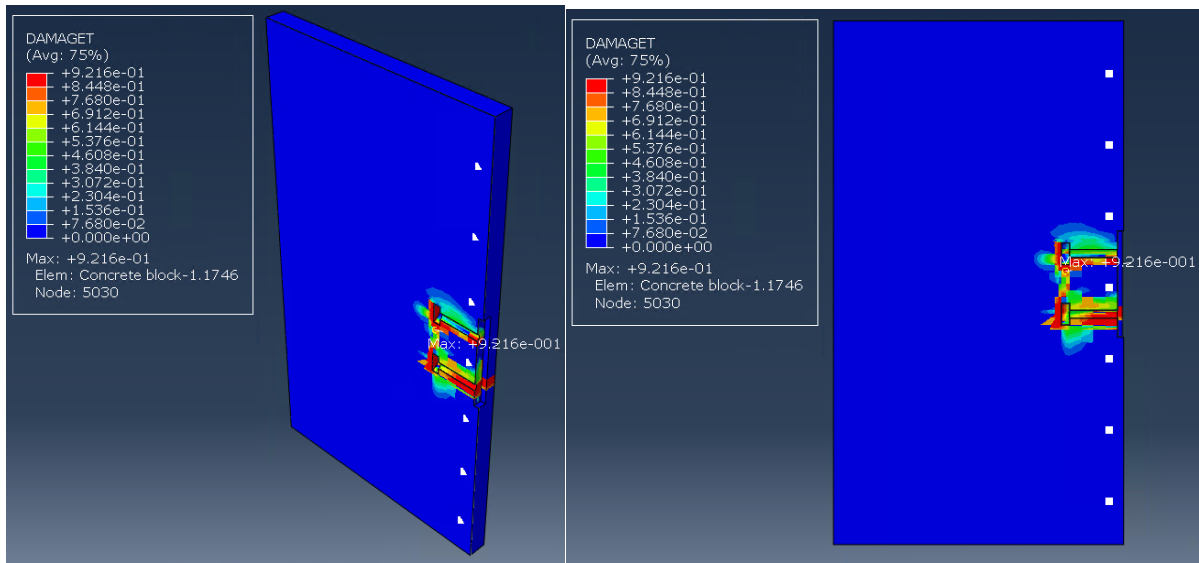


Figure 3-147: Damaged concrete around the anchors.

3.7.3 Cyclic response

In addition to the monotonic imposition of displacement described above, an analysis with cyclic displacements (Figure 3-148) was also conducted. Figure 3-149 shows the hysteretic response of the system. The maximum developed force was on the order of 78,000 lbf. Figure 3-150 and Figure 3-151 show the damage contours (DAMAGET index used by ABAQUS).

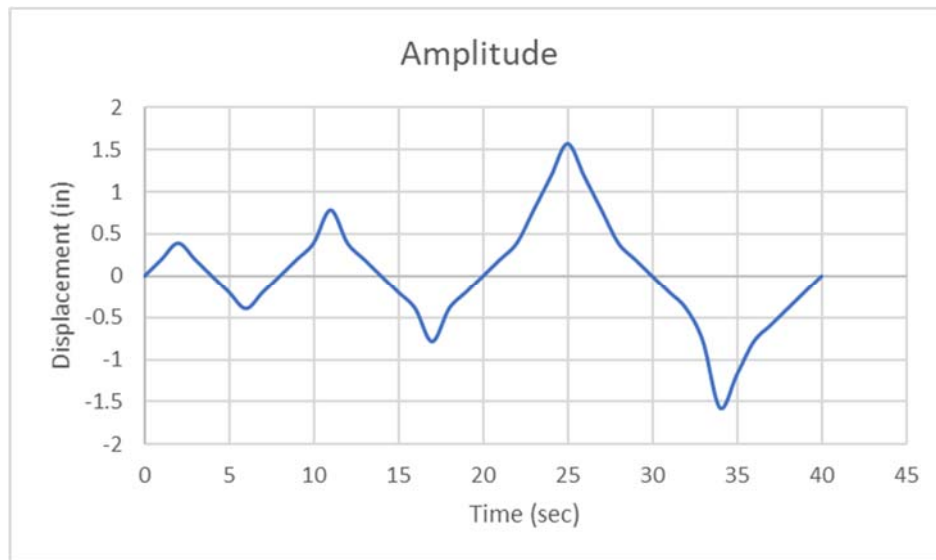


Figure 3-148: Displacement amplitude

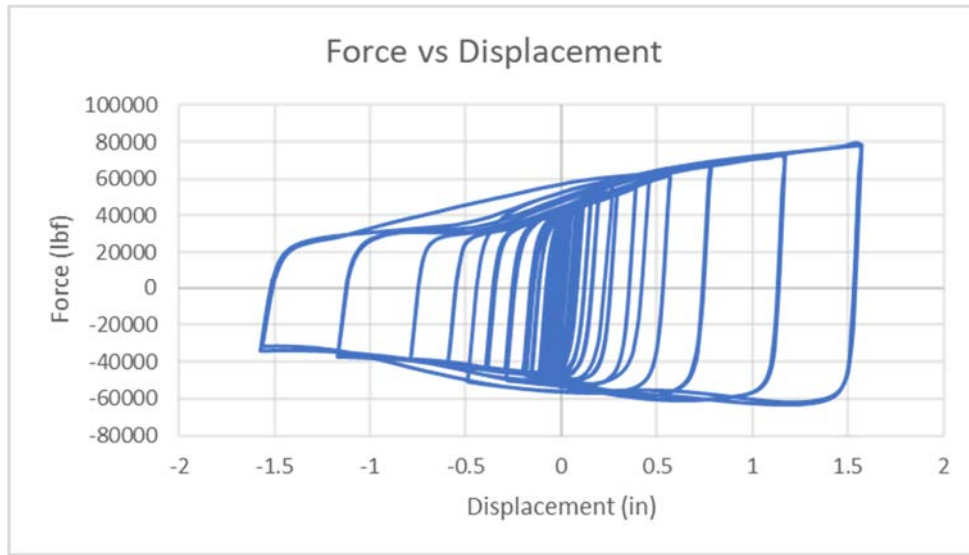


Figure 3-149: Force vs reinforcement of the cyclic model

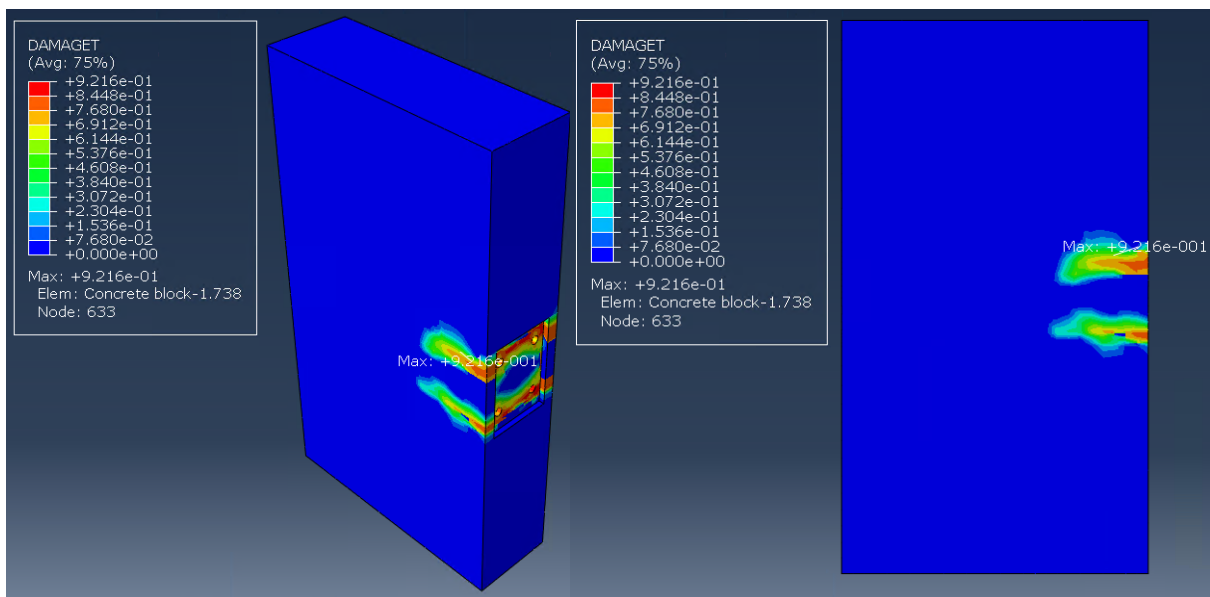


Figure 3-150: Damaged model

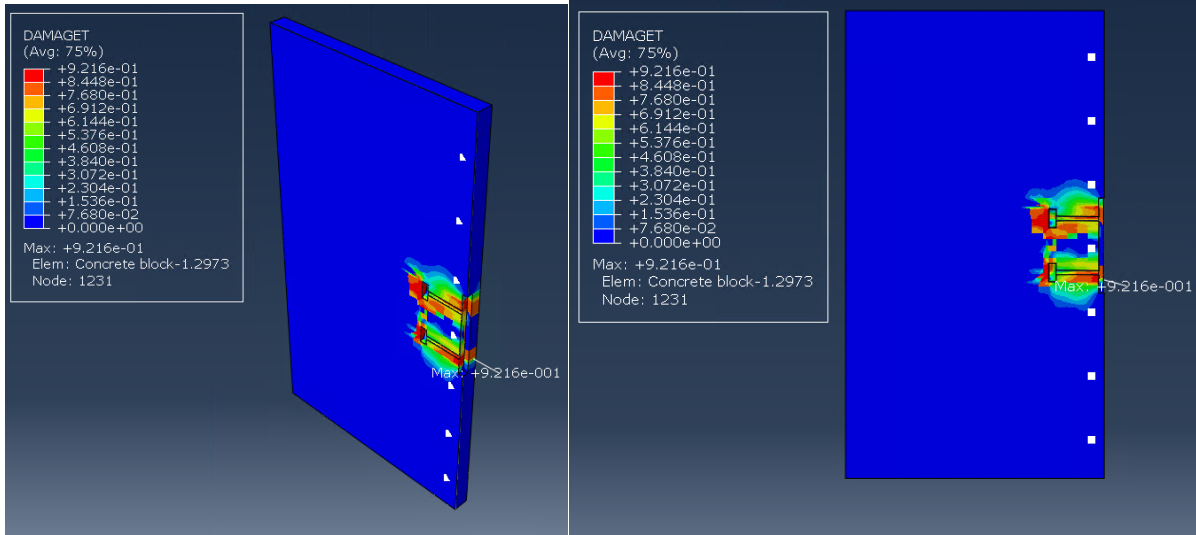


Figure 3-151: Damaged area around the anchors

3.8 Full building analytical model

A FEM model of a full building was needed to confirm the response of the connectors. Also, conduct fair comparison between proposed connectors and U-shape plate. In the following section, a discussion along with detailed description of the full building analytical model will be presented

3.8.1 Description of building model

In 2007, Sritharan S. et. al . an analytical model based on PRESSS building experimental and analytical modeling in 1996 [44]. The findings of their study confirmed PRESSS initial findings and provided additional information. Sritharan et al. concluded that the relative movement between adjacent shear wall panels could be up to approximately 2.5-in as shown in Figure 3-152.

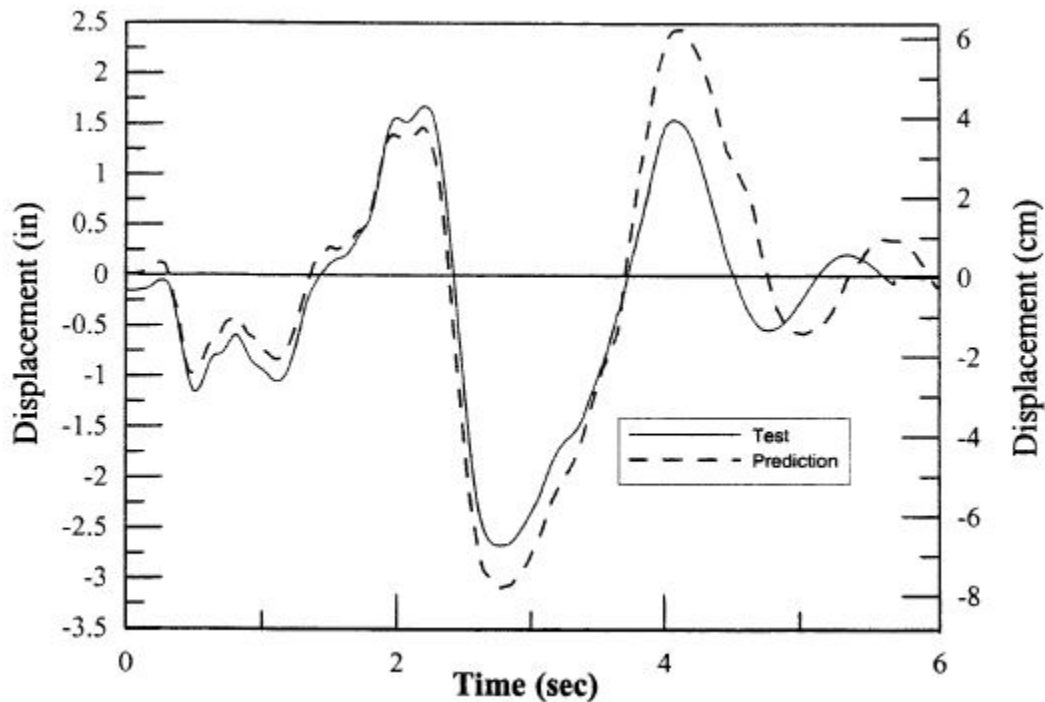


Figure 3-152: Relative vertical movement between panels [44]

It must be mentioned that the findings of Figure 3-152 are based on scaling assumptions that are discussed in Sritharan et. al. study [44]. Figure 3-153 shows the proposed analytical model in which the

two shear walls are represented by two equivalent vertical frame members and the gravity columns are collectively represented by a third vertical frame member. Rigid links connect the vertical shear wall elements to the connection points between shear walls (with rigid connection to the frame). Equivalent lumped masses to represent floor masses, and equivalent springs are used to represent post-tensioning tendons. The stiffness of the foundation is represented by compression-only springs that would allow lifting of the wall panel. Equivalent vertical springs were used to represent the force developed in the connectors between shear walls as a result of relative vertical movement.

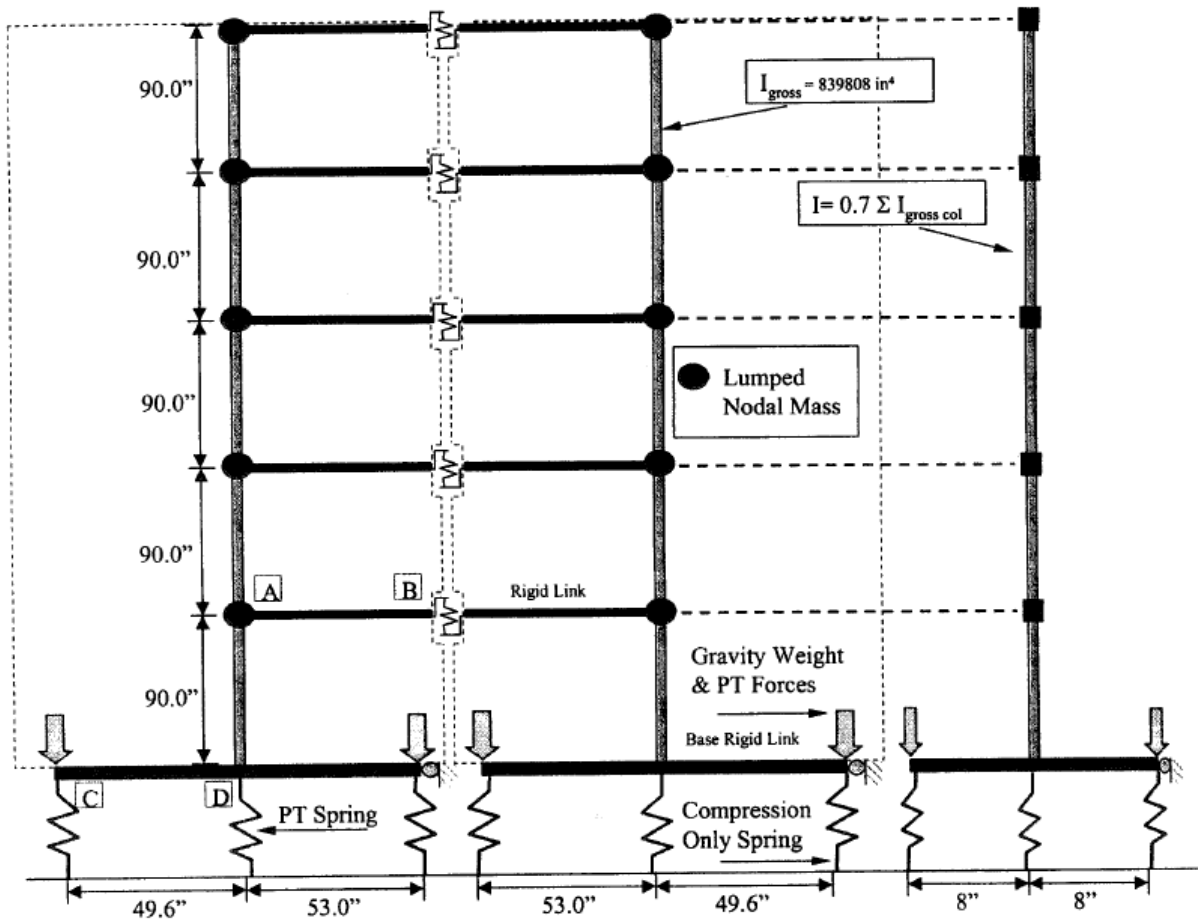


Figure 3-153: Analytical model of the PRESS Building [44]

The frame elements representing the walls were modeled as linear elastic members (no strength degradation) since the walls would be expected to undergo a rocking type motion in an earthquake. Table 3-6 and 3-8 show the equivalent section properties for the frame elements representing shear wall panels and gravity columns, respectively. The frame elements representing the columns were section properties (moment of inertia and cross-sectional area) corresponding to about 70% of the actual properties of the gravity columns Table 3-8 show the properties of rigid link elements.

Table 3-6: Equivalent Wall member section properties [44]

Property	Value
Elastic Young's Modulus	$5.2 \cdot 10^3$ ksi
Shear Modulus	$2.2 \cdot 10^3$ ksi
Cross-sectional Area	864 in ²
Effective shear area	736 in ²
Moment of Inertia	839,808 in ⁴

Table 3-7: Equivalent Column member section properties [44]

Property	Value
Elastic Young's Modulus	$5.4 \cdot 10^3$ ksi
Shear Modulus	$2.4 \cdot 10^3$ ksi
Cross-sectional Area	1814 in ²
Effective shear area	1814 in ²
Moment of Inertia	49,000 in ⁴

Table 3-8: Rigid link member properties [44]

Property	Value
Elastic Young's Modulus	$5.2 \cdot 10^3$ ksi
Shear Modulus	$2.2 \cdot 10^3$ ksi
Cross-sectional Area	86,400 in ²

Effective shear area	0 in ²
Moment of Inertia	8.39*10 ⁷ in ⁴

The rigid links meeting at the connectors were modeled with an offset of 0.01 in. to allow placement of springs representing the non-linear stiffness of the connectors. At the base, springs were used to support the walls and columns (representing the foundation) and those springs were modeled as compression-only linear springs (i.e. no energy dissipation associated with those springs). Those springs could be seen in Figure 3-153. Table 3-9 shows the characteristics of the compression-only springs.

Table 3-9: Properties of Compression-Only base spring [44]

Property	Value
Spring Stiffness in the local X-direction	10000 kip/in
Spring Stiffness in the local Y-direction	0.1 kip/in
Rotational Stiffness of the member section	0.1 kip in/rad
Bi-Linear factor for spring forces	0.0
Bi-Linear factor for rotation	0.0

The springs representing post-tensioning tendons were modeled to provide stiffness in the vertical direction only. Table 3-10 show properties of the post-tensioning springs for the walls and columns.

Table 3-10: Walls and Columns PT spring properties [44]

Property	Value
Spring Stiffness in the local X-direction (wall)	197 kip/in
Spring Stiffness in the local X-direction (Col)	154 kip/in
Spring Stiffness in the local Y-direction (both)	0.1 kip/in
Rotational Stiffness of the member section (both)	0.1 kip in/rad
Bi-Linear factor for spring forces (both)	0.02
Bi-Linear factor for rotation (both)	0.0

The shear connectors were modeled as non-linear springs and connected the rigid links between different walls. The bi-linear force versus displacement response for the connector were determined based on the tests of the connector. The results were scaled to conform to the scale of the test building. The connector that was used in the PRESSSS tests was the U-shaped connector. Table 3-11 shows the data used for the bi-linear data in PRESSSS analytical model [44].

Table 3-11: Scaled properties of the bi-linear spring representing the U-shaped connector [44]

Property	Value
Spring Stiffness in the local X-direction	186.6 kip/in
Spring Stiffness in the local Y-direction	0.1 kip/in
Rotational Stiffness of the member section (both)	0.1 kip in/rad
Bi-Linear factor for spring forces (both)	0.015
Bi-Linear factor for rotation (both)	0.0
Positive ALFA Longitudinal direction	0.001
Negative BETA Longitudinal direction	0.001

components. A lumped mass equivalent to 175.5 kips was applied at each node in each floor level as shown in Figure 3-153.

To develop the spring properties for the shear connector, the U-shaped connector was subjected to cyclic displacements and the developed reaction forces were measured. Figure 3-154 shows the scaled hysteretic force versus displacement responses for the U-shaped connector based on the experiment and prediction models. The maximum reaction force was on the order of 13000 lbf. The maximum displacement obtained from the test was approximately 3 in. It should be noted that, because of the relatively low stiffness of the U-shaped connector in the transverse direction (horizontal in the model discussed in 3.4.2.1), a horizontal spring was not included in the building model (in addition to the vertical spring) to represent the transverse stiffness. As discussed later, other connectors may offer

substantial resistance in both directions, and the addition of a second horizontal spring may be warranted in such cases.

A scaled ground excitation (acceleration versus time shown in Figure 3-155) was applied at the base of the structure in the analytical model. Figure 3-156 shows the base shear versus time relationship obtained from the analytical model and its comparison with the experimental data [44]. The base shear was calculated at each time step by summing each floor force in the analytical model.

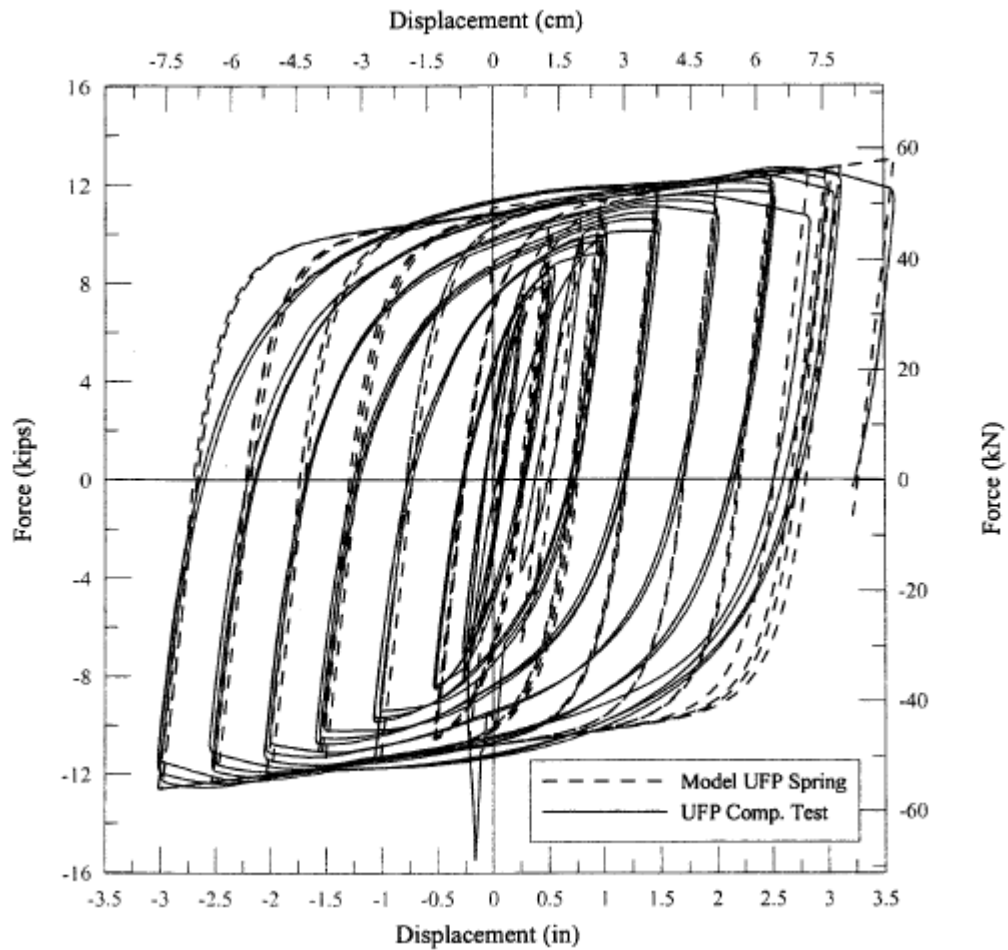


Figure 3-154: Force vs Displacement of full building model

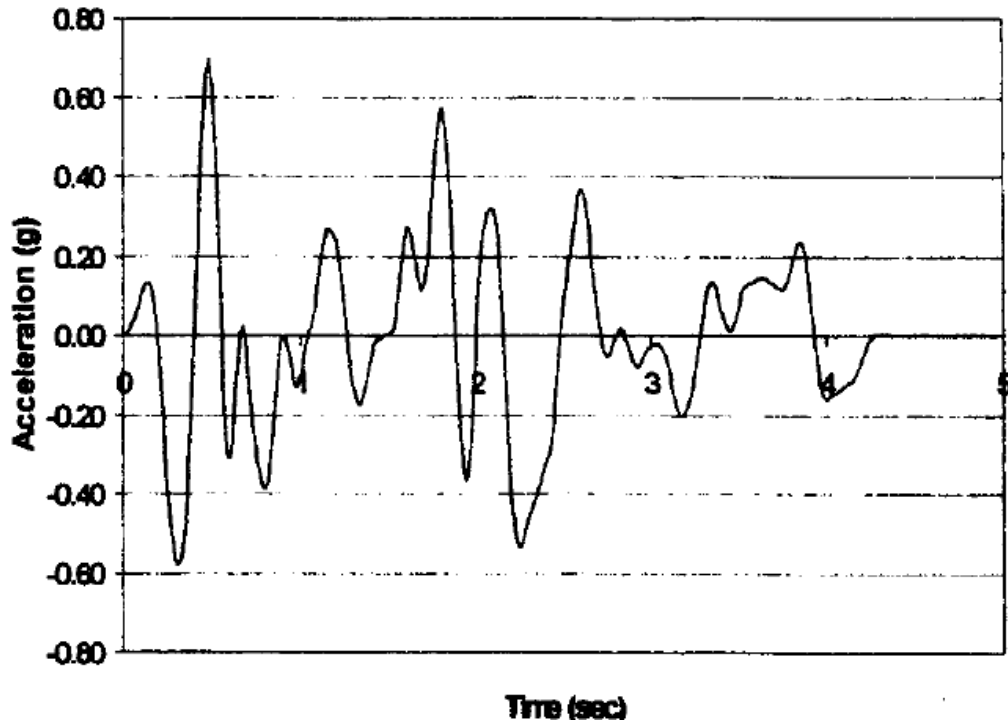


Figure 3-155: Ground excitation [44]

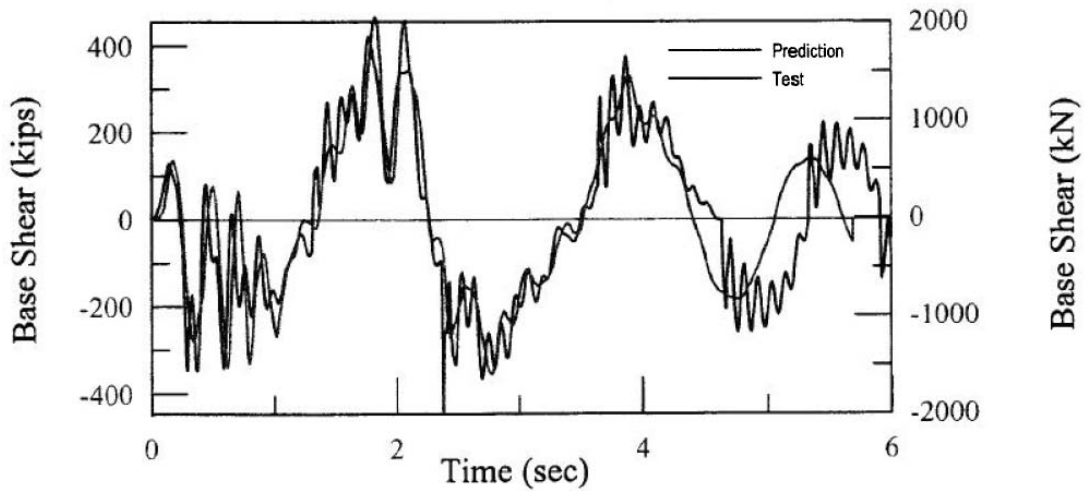


Figure 3-156: Base shear [44]

3.8.2 Analysis with vertical springs only

In this study, the ANSYS finite element software was used to recreate the same building model proposed by Sritharan et al. [44] as shown in Figure 3-157 (a) and (b). Member properties are as presented in

Table 3-6 and Table 3-7. Lumped masses were added at the nodes (labeled A through J) as shown in Figure 3-157 (b). All elements and material properties were provided and the base springs (compression only) were defined as a “Body to Ground” type of spring with properties shown in Table 3-9. For the PT springs, they were modeled in a similar manner, and ANSYS spring elements were used with the properties shown in Table 3-10 as shown in Figure 3-158 and Figure 3-160. The model was subjected to base excitation with acceleration shown in Figure 3-159.

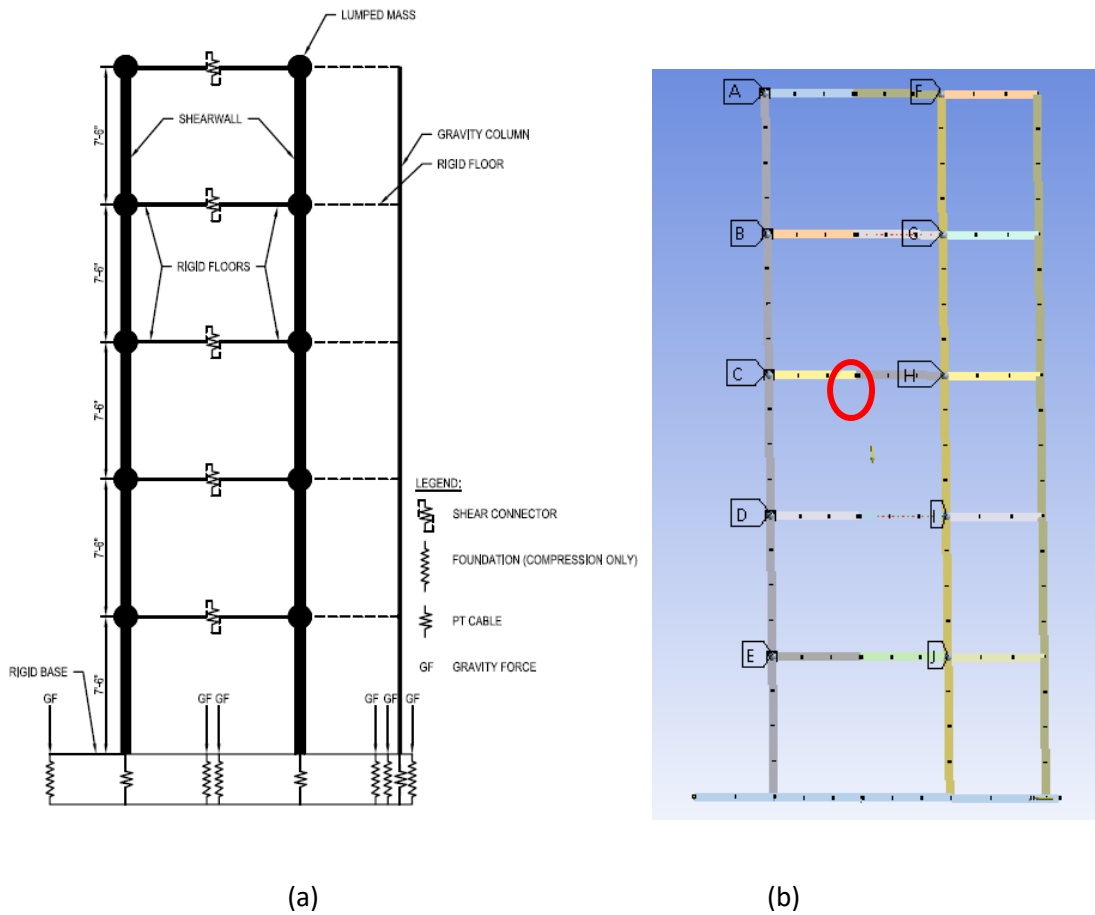


Figure 3-157: ANSYS building model; (a) concept model, (b) Ansys presentation

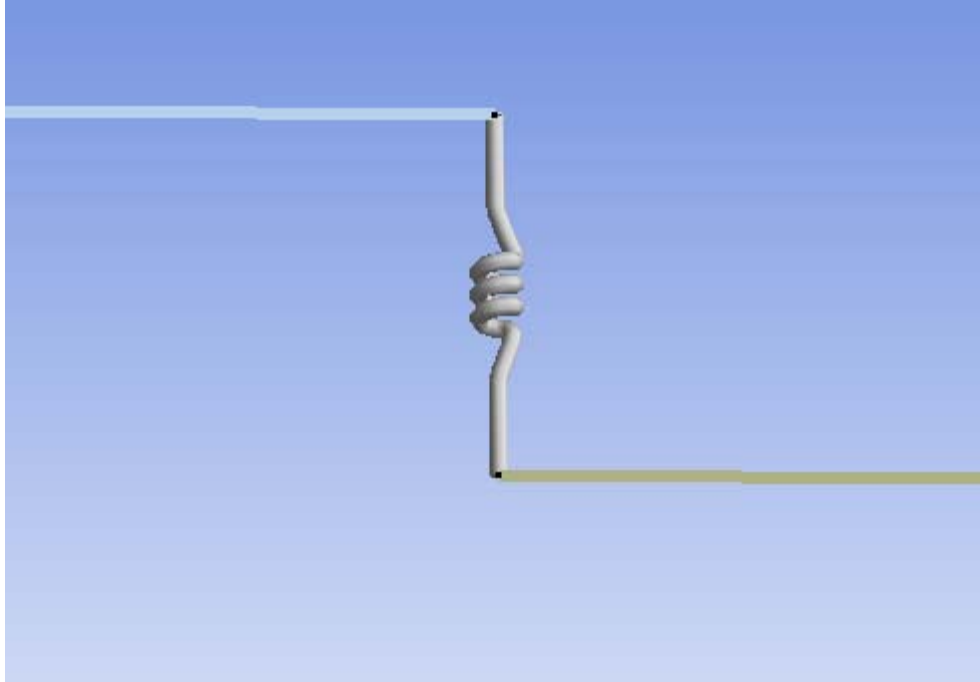


Figure 3-160: Typical spring connector

The force versus displacement data for the U-shaped springs were obtained from actual test results that was performed by the PRESS program. A scale of 2/3 was applied to the prototype connector test results since the test specimens were scaled [5] & [44].

3.8.2.1 U-shaped connector model

Figure 3-161 shows the bilinear data of the U-shape connector that was used in ANSYS software. After running the model, results were gathered as it will be compared later in this study. Figure 3-162 shows force vs displacement relationship of the U-shaped connector inside the building model. It could be seen that the maximum displacement is in the order of ± 1.4 in. and the maximum force is approximately 21,500lbf. The overall response of the building (drift and base shear) for various connectors including the U-shaped connector are discussed and compared in Section 3.8.2.5. Figure 3-163 shows Story drift of the model, the maximum drift is at the top of the building and it is 4.32 in. Figure 3-164 exhibits the

base shear, the base shear is 2175 kips. Lastly, Figure 3-165 shows the accumulated dissipated energy throughout the analysis. The total dissipated energy is 1,097,605 lbf-in.

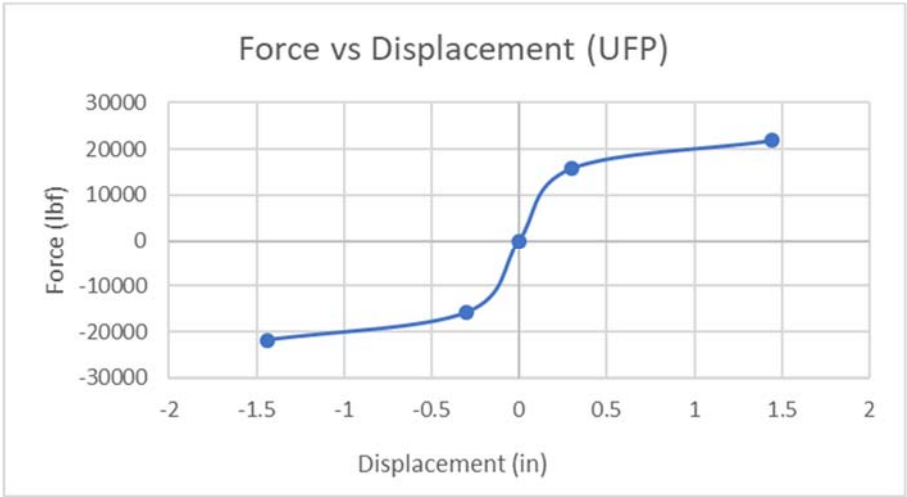


Figure 3-161: Bilinear data of U-shape connector

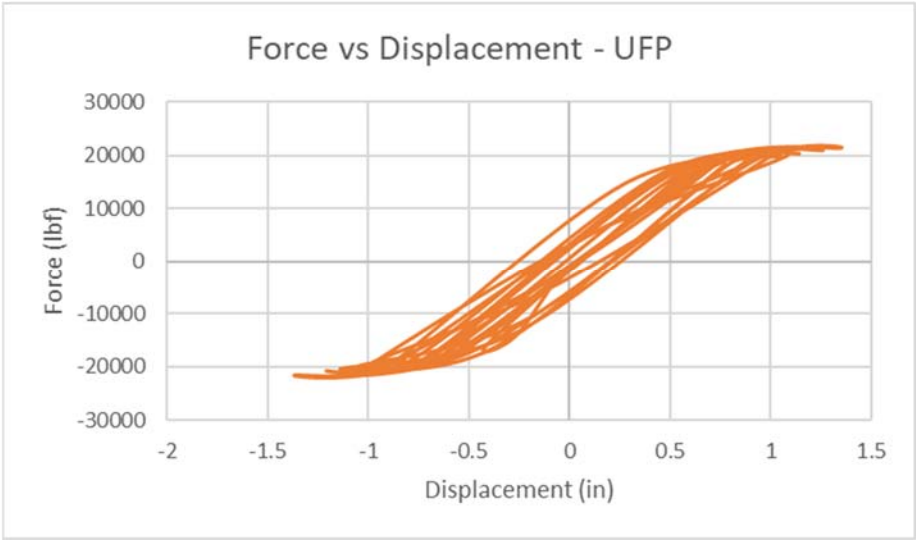


Figure 3-162: Force vs displacement of the full building model with U-shape connector

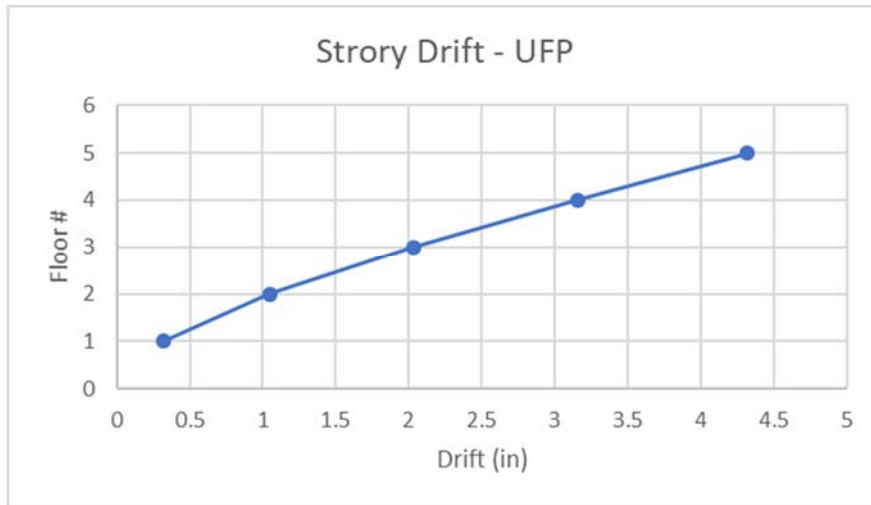


Figure 3-163: Story drift of the full building model with U-shape connector

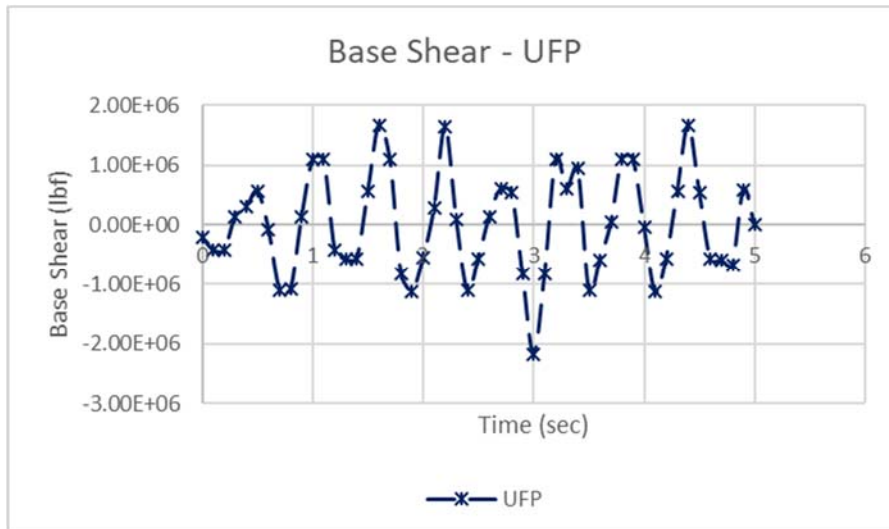


Figure 3-164: Base shear of the full building model with U-shape connector

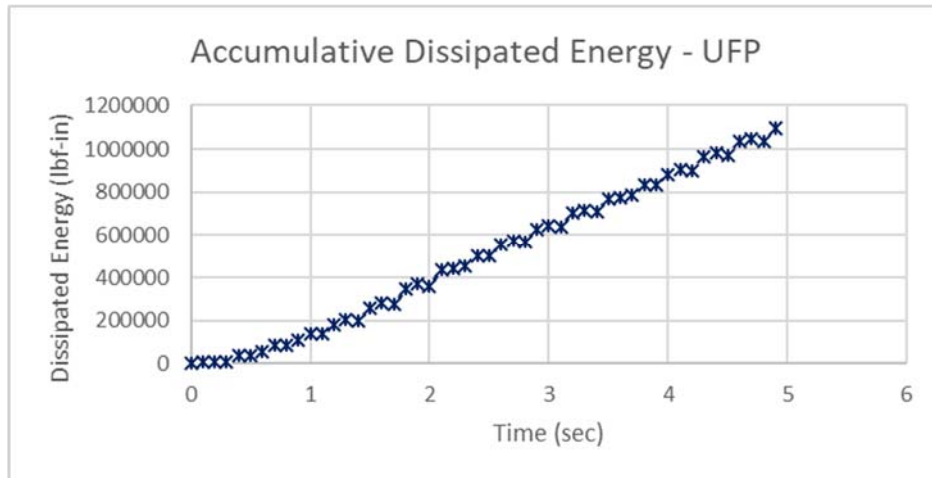


Figure 3-165: Accumulated dissipated energy of the full building model with U-shape connector

3.8.2.2 Shape NS-5 modeling

The building model described above was revised to include the vertical spring representing the NS-5 connector. The vertical spring properties for the NS5 connector were obtained from experimental test results that are discussed in Chapter 4. Scaling laws were used to convert loads and displacements from the 1/2-scale test to the 2/3-scale building test. Figure 3-166 shows the bilinear data of the NS5 springs. Figure 3-167 shows the force vs displacement relationship for one of the NS5 connectors in the building model. The maximum force was on the order of 46,700 lbf at a maximum displacement of approximately 1.2 in. Figure 3-168 shows the story drift of the model, maximum drift at the top of the building is 3.68 in. Figure 3-169 exhibits the base shear, the base shear is 1834 kips. Lastly, Figure 3-170 shows the accumulated dissipated energy throughout the analysis. The total dissipated energy is 2,157,428 lbf-in.

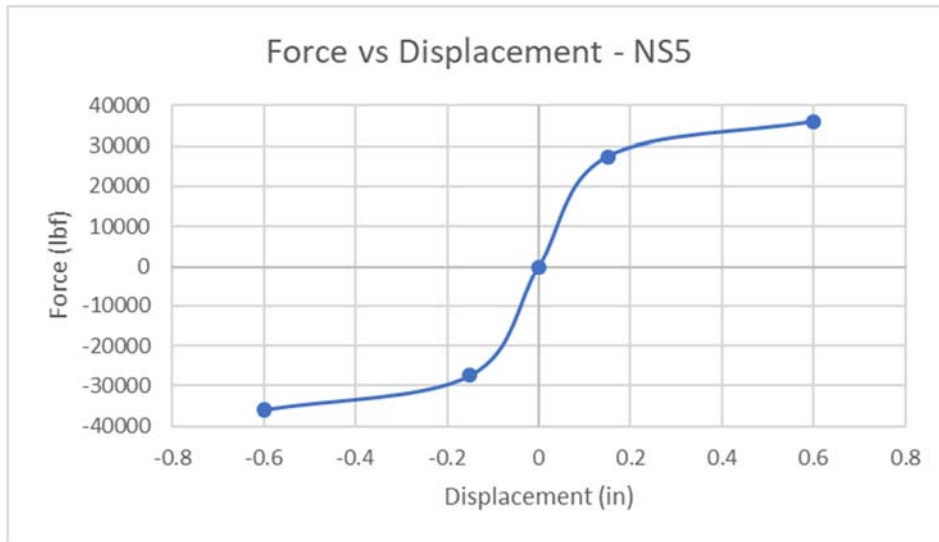


Figure 3-166: Bilinear data of NS5 shape

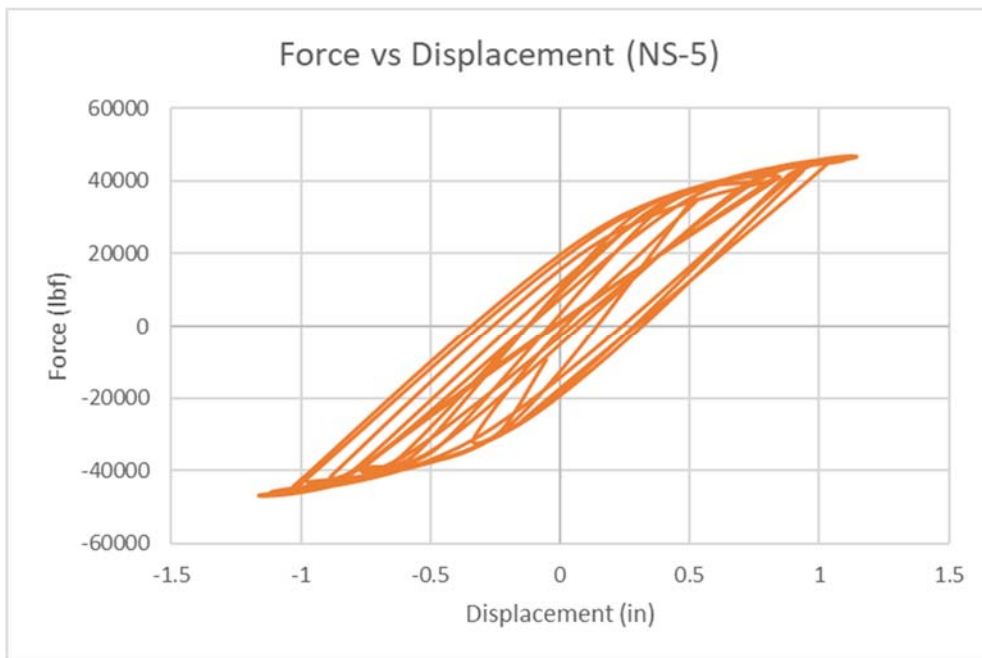


Figure 3-167: Force vs Displacement for shape NS5

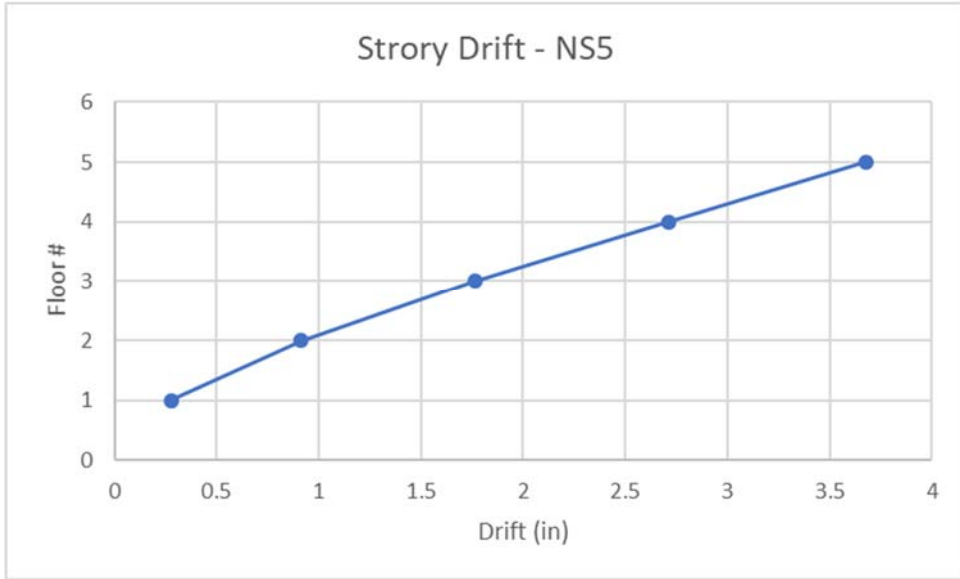


Figure 3-168: Story drift of the full building model with U-shape connector

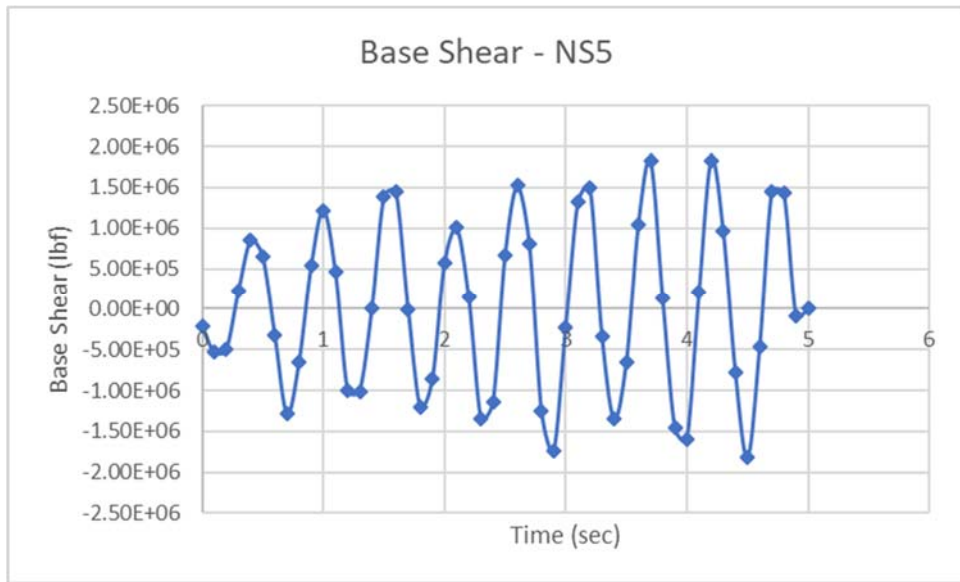


Figure 3-169: Base shear of the full building model with NS5 connector

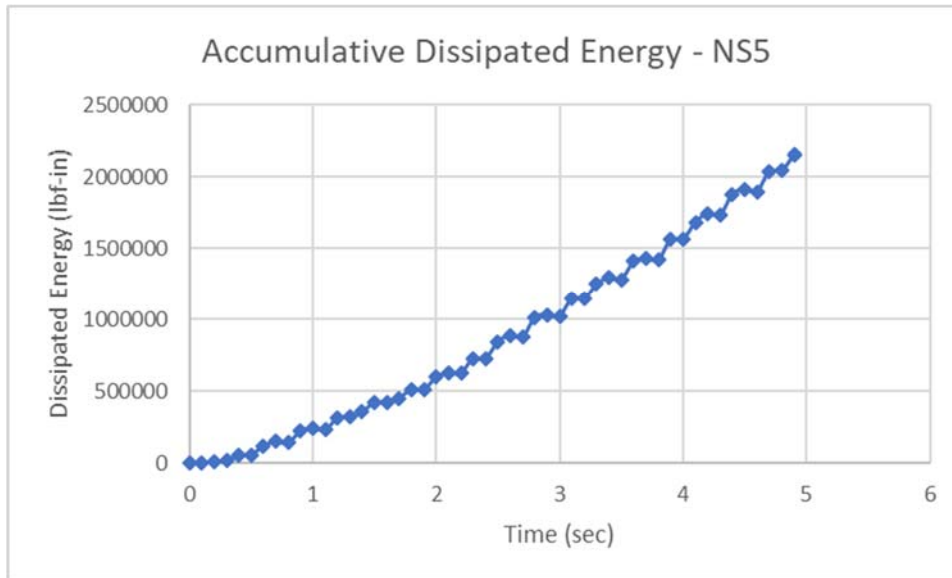


Figure 3-170: Accumulative dissipated of the full building model with NS5 connector

3.8.2.3 Rigid model

The full building model discussed earlier was further revised to evaluate the response of the building when the connection between the shear walls is a rigid point connection. This, along with the free connection discussed next, was intended to bracket the connector behavior. The connector springs were removed and replaced with rigid beam elements. The overall response of the building (drift and base shear) for various connectors including the rigid connection are discussed and compared in Sections 3.8.2.5 and 3.8.3. It must be noted that since no bilinear data present in this model, no force vs displacement nor dissipated energy responses were obtained from this model. Maximum drift is at the top of the building and it is 0.86 in (as shown in Figure 3-171). While maximum base shear is 2.7E8 and as shown in Figure 3-172.

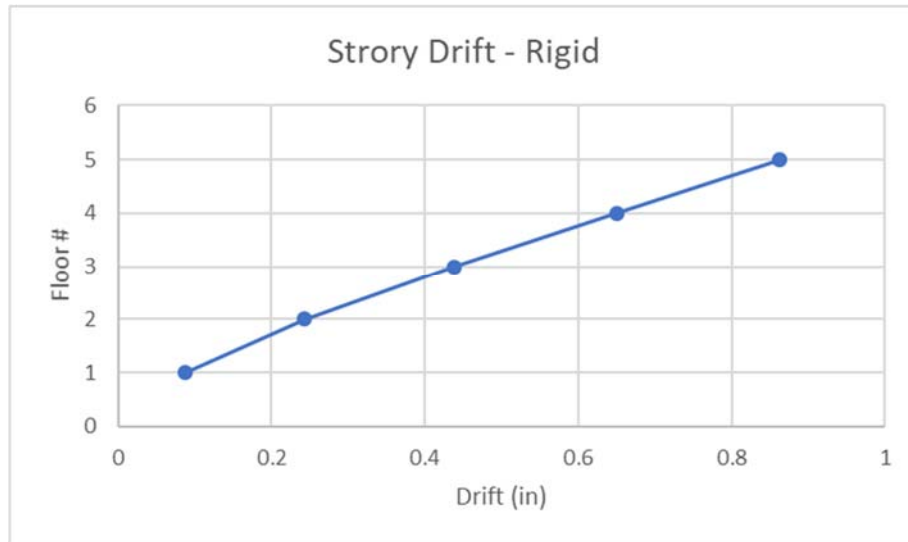


Figure 3-171: Story drift of the full building model with Rigid connector

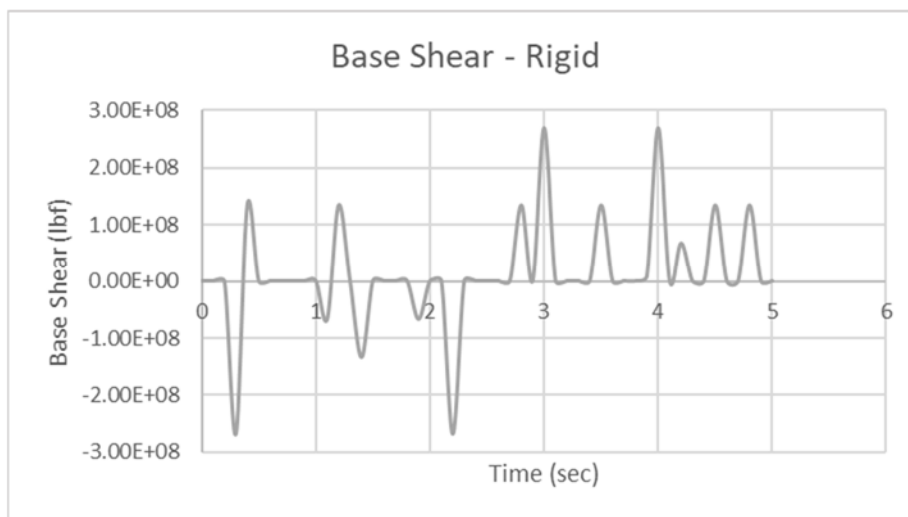


Figure 3-172: Base shear of the full building model with Rigid connector

3.8.2.4 Free model

Another model was created for sake of comparison where there were no connectors in between the shear wall. The results of this model will be used for comparisons only and it will be presented in the last section of this chapter. It must be noted that since no bilinear data present in this model, no force vs displacement nor dissipated energy responses were obtained from this model. Maximum drift is at the

top of the building and it is 4.81 in (as shown in Figure 3-173). While maximum base shear is 1,085 kips and as shown in Figure 3-174.

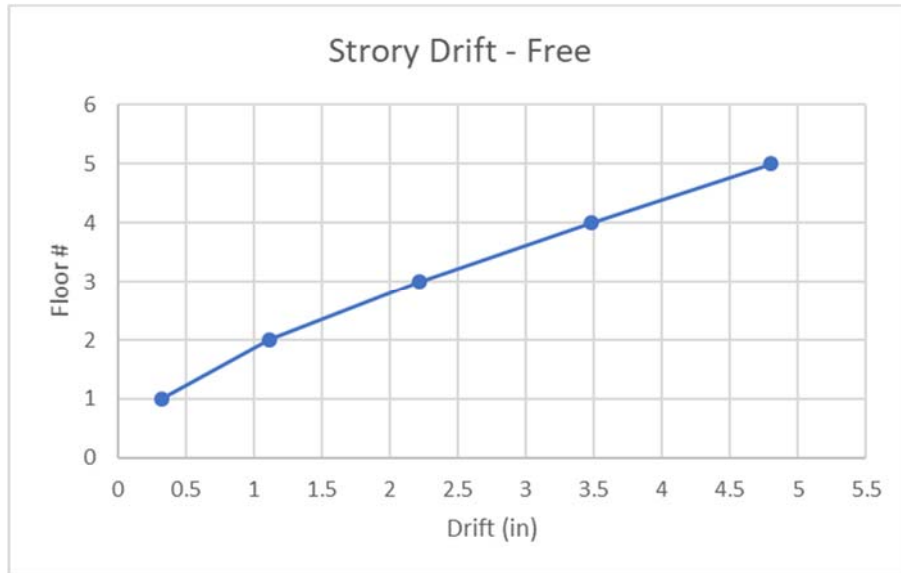


Figure 3-173: Story drift of the full building model with no connector (free)

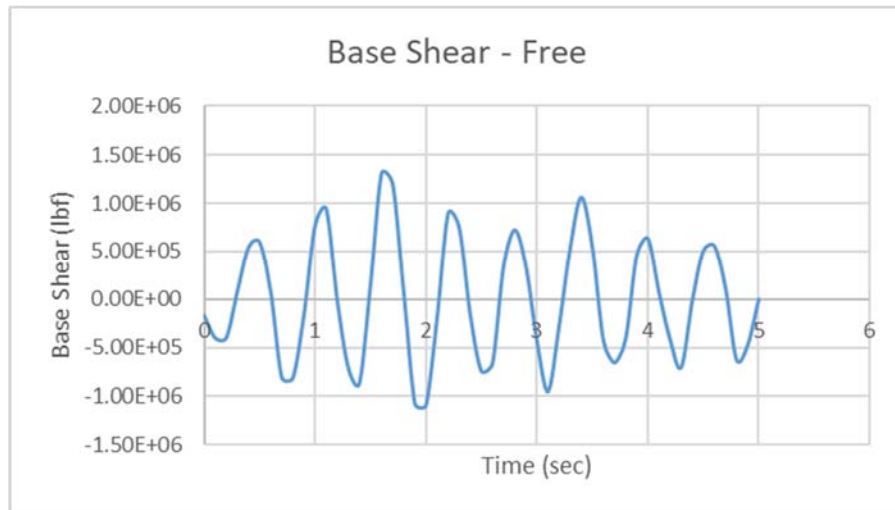


Figure 3-174: Base shear of the full building model with no connector (free)

3.8.2.5 Overall building response – comparison between different connectors

Overall building responses (drifts and base shear) from all building models discussed above were analyzed and compared with each other to better understand the influence of the type of shear

connector on the seismic response in a representative building (PRESS building). Figure 3-175 shows a comparison between the force-displacement responses of U-shaped and NS-5 connectors at one connection point in the building. The U-shaped connector itself endured higher displacement and lower reaction force (connector force) than the NS-5 connector. More importantly, the NS5 shape dissipated much higher energy (area under the load-displacement curve) than the U-shaped connector. Both shaped exhibited steady hysteresis curves.

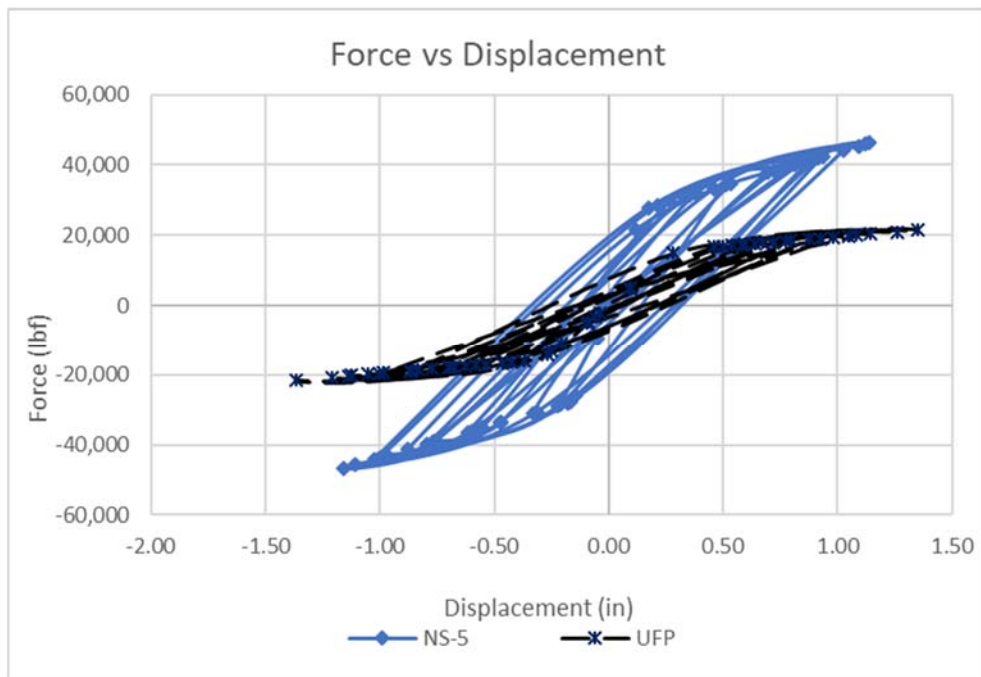


Figure 3-175: Force vs Displacement for UFP and NS5

Figure 3-176 shows the maximum story drifts for all building models at various floor levels. As expected, the rigid model had the lowest drift and the free model had the highest drift. The building with rigid connection acts as a unit with no energy dissipation at the connections. The NS-5 connector exhibited lower drift compared to the U-shaped connector. The higher stiffness and strength of the NS-5 connector is an important contributing factor.

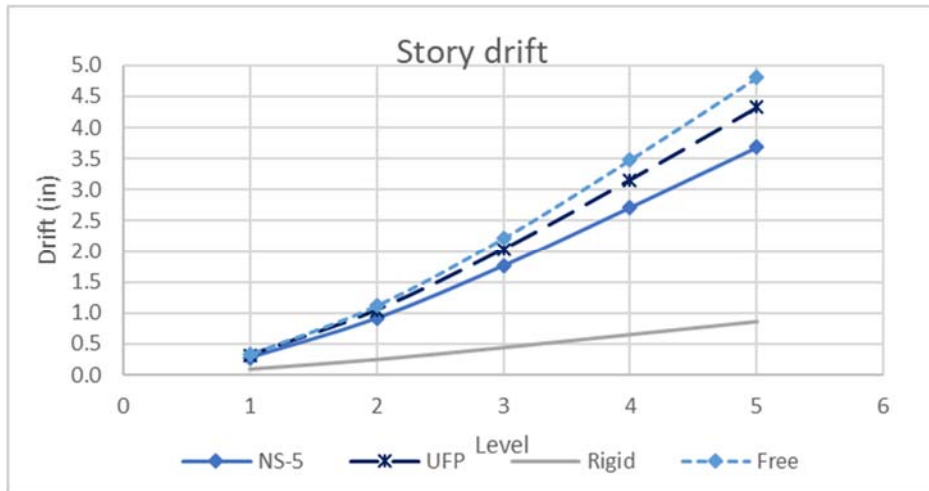


Figure 3-176: Story drift of all models

Figure 3-177 shows the drifts for all models with time. As expected, the rigid model resulted in the smallest displacement at the top of the building. The overall movement of the top of the building for the U-shaped model was slightly more than of the model with the NS-5 connector. The base shear of all building models was determined as shown in Figure 3-178. The rigid model exhibited significantly higher base shear compared to the other models.

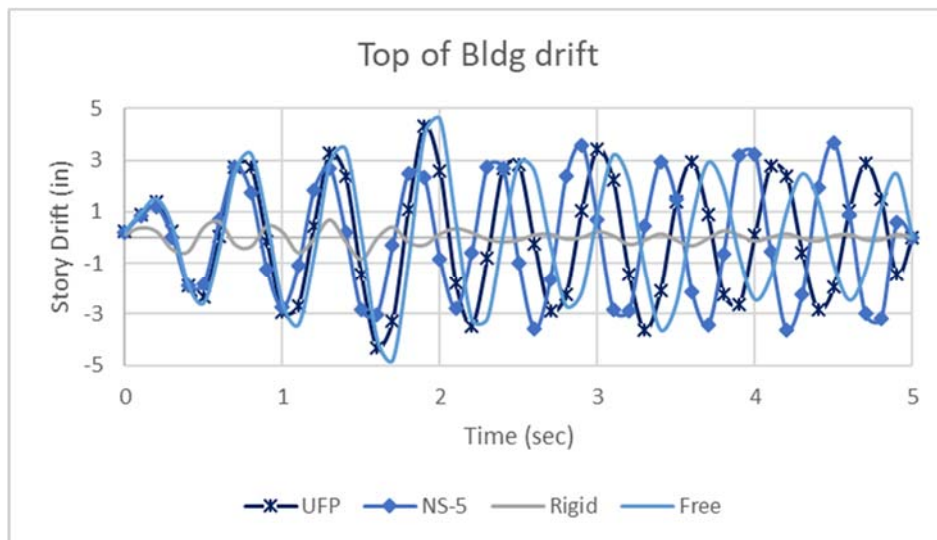


Figure 3-177: Top of building drift for all models

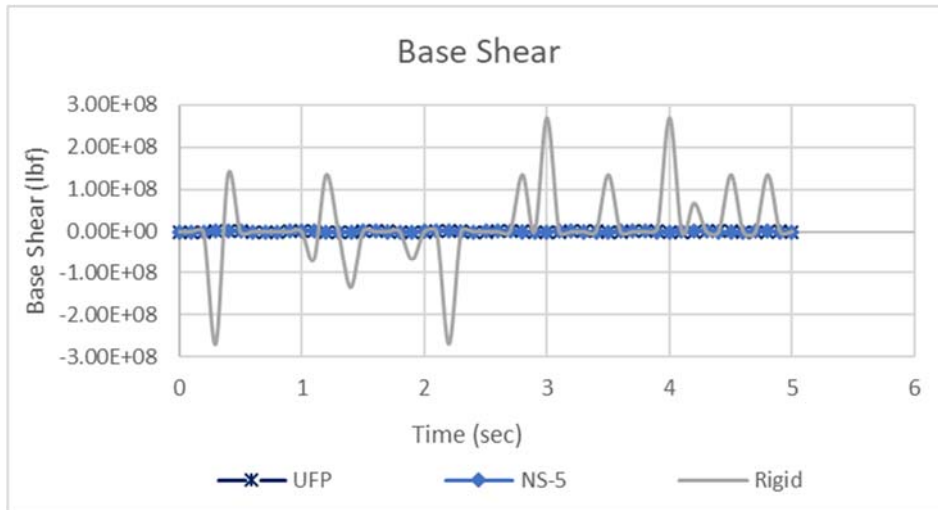


Figure 3-178: Base shear for all models

Due to the high magnitude of the base shear for from the rigid model, Figure 3-179 (without the rigid model) was added to better illustrate the differences between the models with U-shaped and NS-5 connectors. The NS-5 model developed slightly higher base shear compared to the U-shaped model.

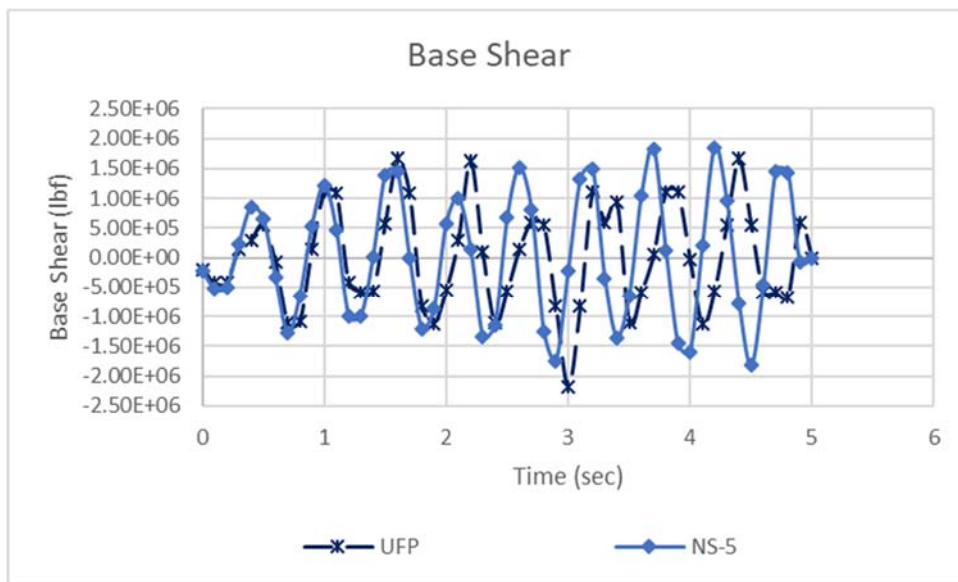


Figure 3-179: Base shear for U-shaped and NS5

The incremental energy in the NS-5 and U-shape models were calculated as shown in Figure 3-180. It is clear that the model with the NS-5 connector dissipated significantly higher energy than the model with

U-shaped connector especially as the time progressed. It is believed that the NS-5 reached yield early and developed higher force resulting in higher energy. Figure 3-181 shows a comparison between the building models based on the cumulative dissipated energy. The total energy dissipated by the building with the NS-5 connector was significantly higher than the building with the U-shaped plate (almost double).

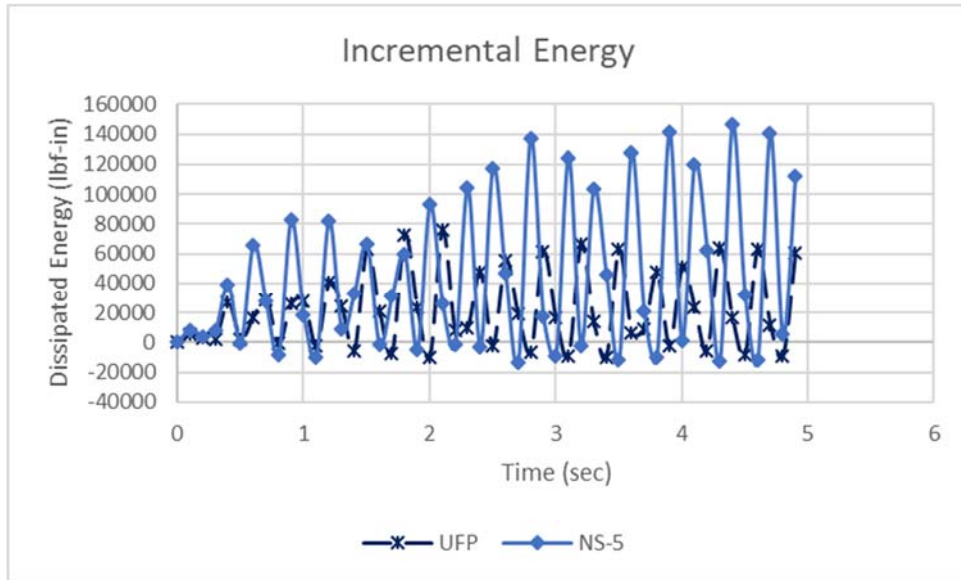


Figure 3-180: Incremental energy dissipation of shear connectors for U-shape and NS5

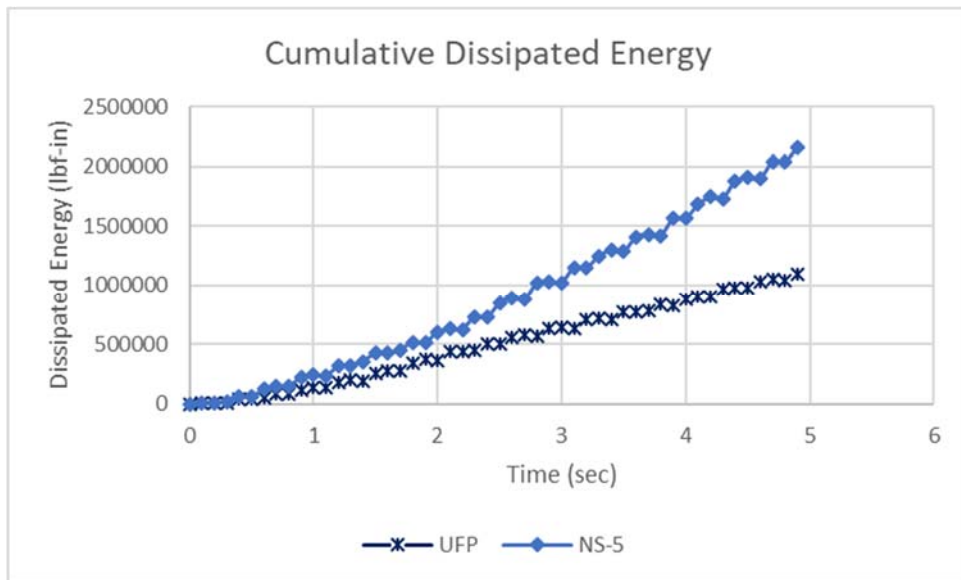


Figure 3-181: Cumulative dissipated energy

3.8.3 Analysis with vertical and horizontal springs

The U-shaped connector has relatively small stiffness and strength in the transverse direction (horizontal in a building) while the NS-5 connector can offer relative high stiffness and energy dissipation in the horizontal direction. To assess the behavior, and to develop spring models, for the horizontal direction, the connectors were analyzed for movement in the horizontal direction alone. In the following section, the connector responses (not part of building model) are analyzed and discussed.

Two building models were generated, each incorporating both vertical and horizontal springs, for the U-shaped and NS-5 connectors. These new models are similar to the models described in sections 3.8.2.1 and 3.8.2.2 except that horizontal springs were added based on the data obtained in sections 3.4.2.1 and 3.6.5.1. Figure 3-182 and Figure 3-183 exhibit the bilinear data of the NS5 and U-shape connectors, respectively. Figure 3-184 shows that both connectors exhibited steady hysteresis and energy dissipation. Figure 3-185 exhibits the story drift for all models. It could be seen that the Free and Rigid models bracketed the responses of the NS5 and U-shape modes. The performance of the model with NS-5 connector (horizontal and vertical springs) is significantly better with a total drift of 3.32-in compared with 4.54-in for the model with U-shaped connector. Figure 3-186 shows the top of building drift for all models throughout the analysis. Base shear for all models is shown in Figure 3-188. Due to the high base shear of the Rigid model, Figure 3-188 was added to emphasize the response of the NS5 and U-shape connectors. There was only a slight difference in base shear with the U-shaped model exhibiting higher base shear. Figure 3-189 compares the incremental energy with each time step in the analysis. This figure indicates that the NS-5 connector resulted in higher dissipated energy. Finally, Figure 3-190 shows that the cumulative energy dissipation obtained from the model with the NS-5 connector was significantly higher than the U-shaped connector. It is believed that the NS-5 reached yield early and developed higher force resulting in higher energy. The total energy dissipated by the

building with the NS-5 connector was significantly higher than the building with the U-shaped plate (70% higher).

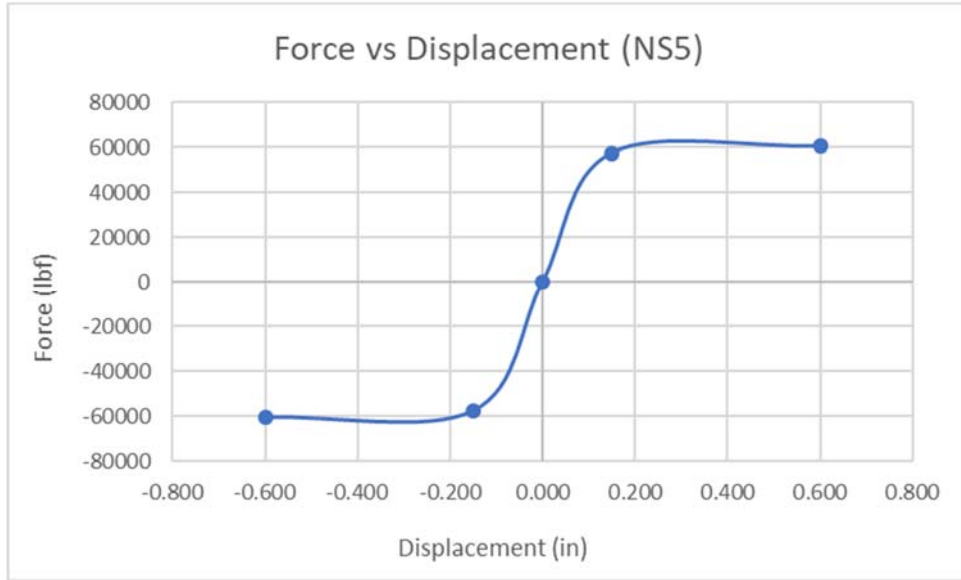


Figure 3-182: Bilinear data of NS5 connector in the horizontal direction

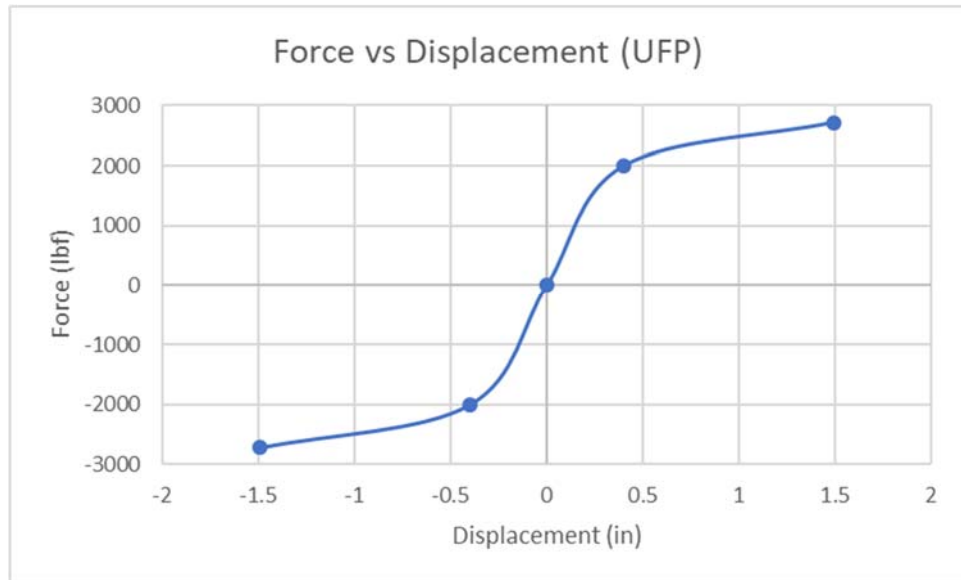


Figure 3-183: Bilinear data of UFP connector in the horizontal direction

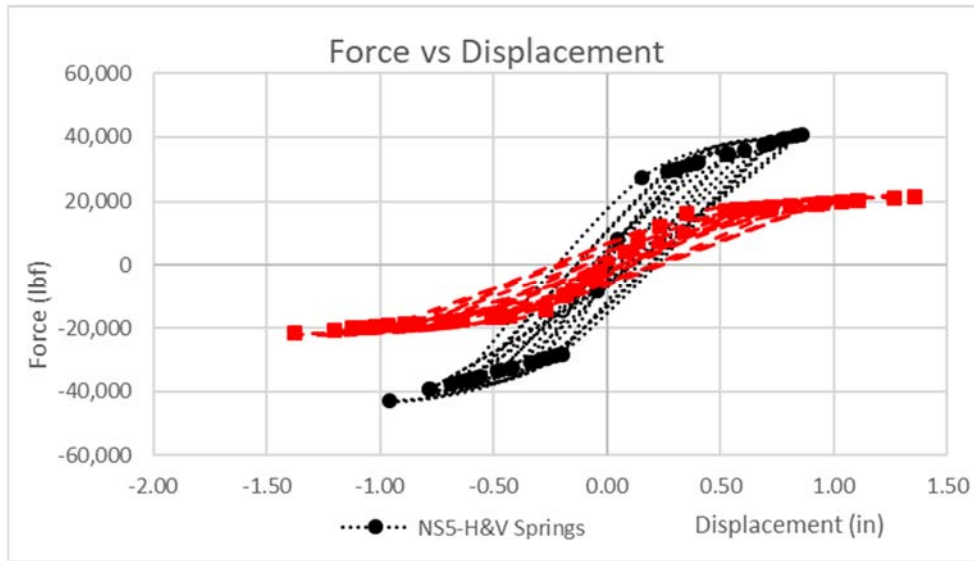


Figure 3-184: Force vs displacement responses for single r U-shaped and NS-5 connectors located in the building model with horizontal and vertical springs

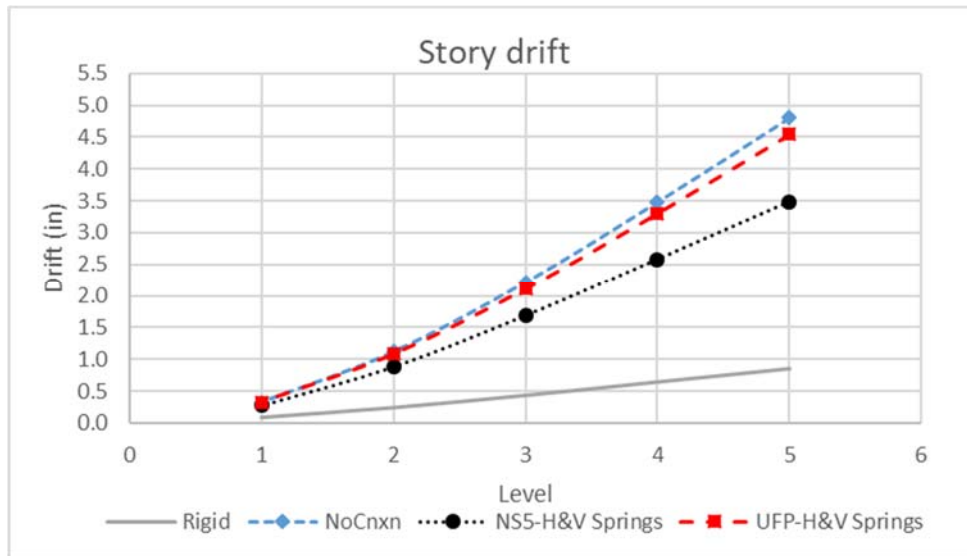


Figure 3-185: Story drift for U-shaped and NS-5

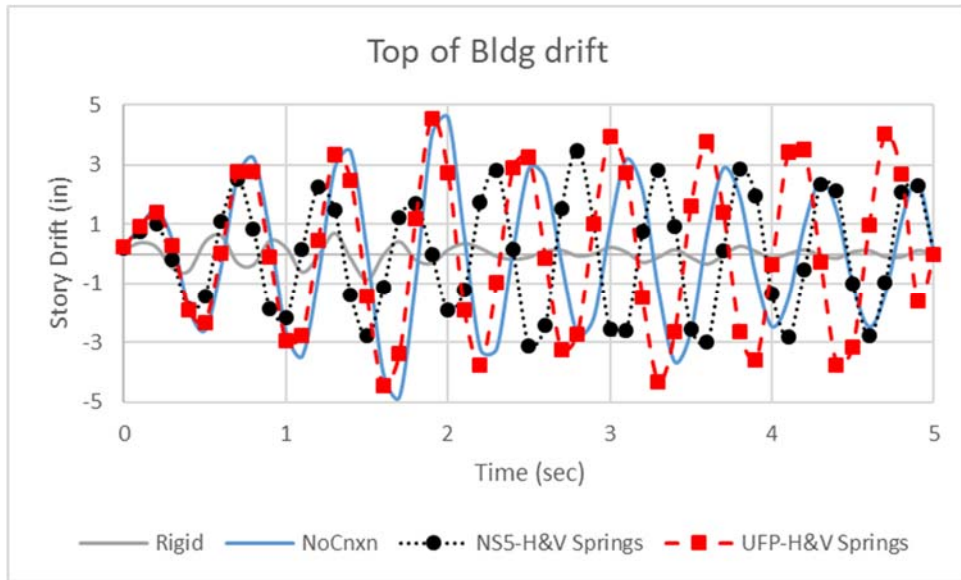


Figure 3-186: Top of building drift with U-shaped and NS-5 springs in the horizontal and vertical directions.

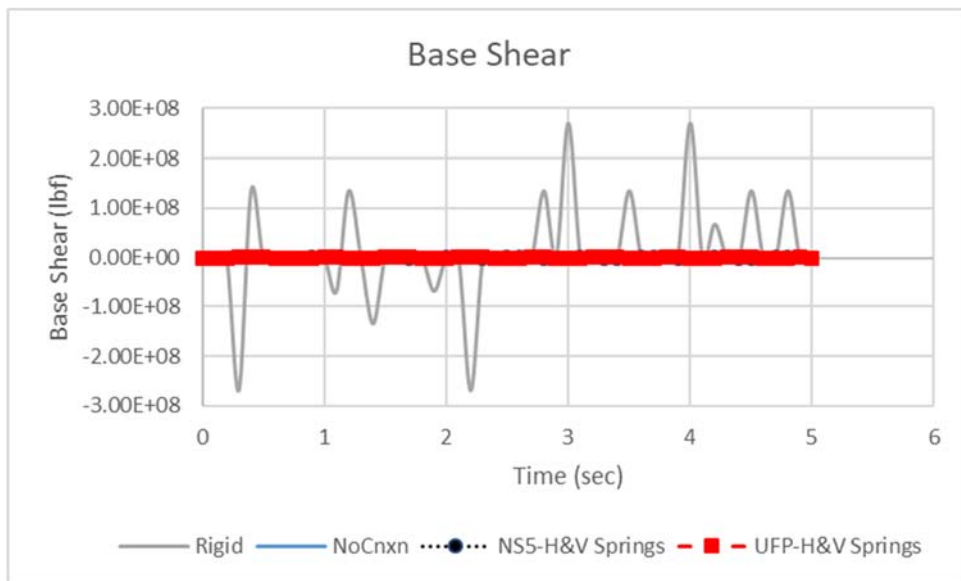


Figure 3-187: Base shear for all models

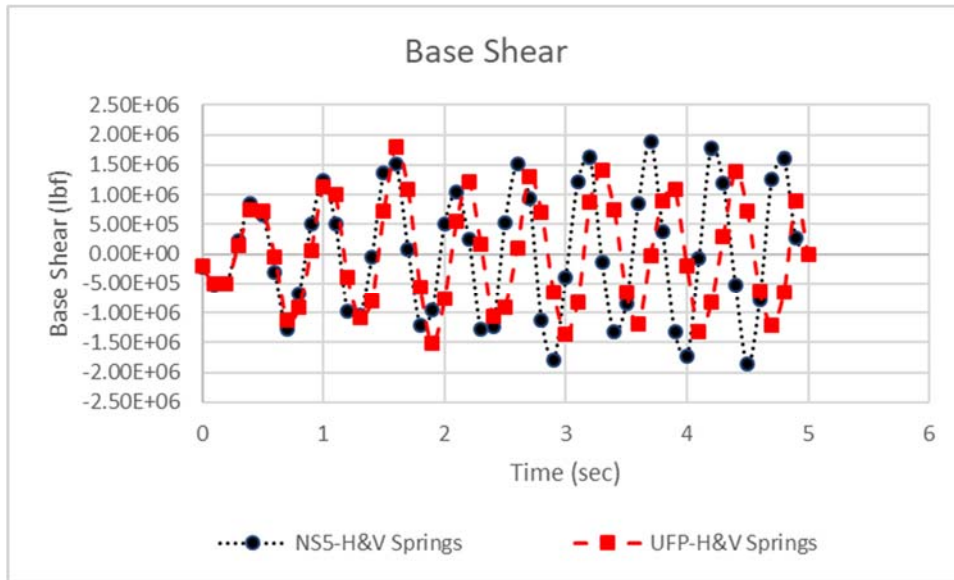


Figure 3-188: Base shear for NS-5 and U-shaped connectors in building models with horizontal and vertical springs

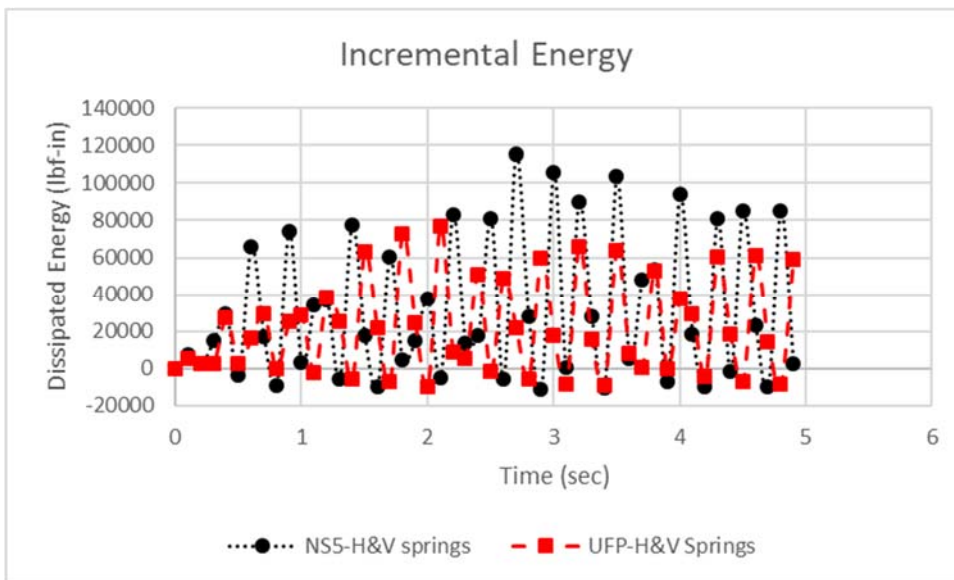


Figure 3-189: Incremental energy in building with U-shaped and NS-5 springs in the horizontal and vertical directions.

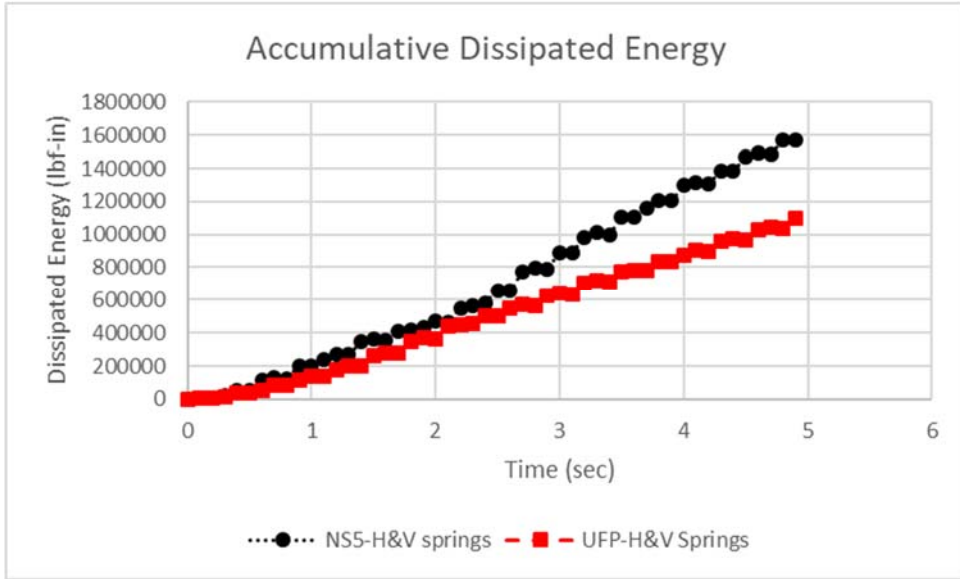


Figure 3-190: Cumulative dissipated energy for U-shaped and NS-5

CHAPTER 4: Experimental work

4.1 Background

As discussed previously, finite element analyses (using ABAQUS and ANSYS software) were performed, under a prescribed displacement protocol, on various shapes that were evaluated under the analytical program. Scaled physical models of the two proposed shapes (TS and NS-5) were subjected to testing to verify the analytical results and to assess low-cycle fatigue resistance. Finite element analyses had indicated the potential for significant energy dissipation and acceptable reaction forces for these two shapes. Nevertheless, experimental testing was deemed necessary to verify the validity of analytical predictions. A full description of the testing program is presented in this chapter.

4.2 Test Setup and protocol

The two proposed connector shapes were presented in Chapter 3 along with computer models of those shape under a prescribed displacement profile. Six half-scaled specimens were fabricated and tested for each of the TS and NS-5 shapes. The test setup was designed to include two specimens at a time. This was done to prevent specimen bending and to apply a pure shear force on each of the two specimens in the setup. All dimensions were one-half the corresponding prototype dimensions, except for the plate thickness, which was $\frac{1}{4}$ of the prototype thickness. This was done because two specimens were being tested simultaneously. This arrangement would allow the scaling rules to be applied based a scale factor of one-half.

The steel that was used in the fabrication of the specimens and test setup was A36 steel. An MTS universal servo-hydraulic test machine with a capacity of 110 kips was used for the tests. Figure 4-1 and Figure 4-2 show the test setup, and Appendix B includes detailed drawings for the setup. Specimens were welded to plate #2, 3 and 4. The displacement was applied through plate #4, which was attached to the test machine's piston. Plate #1 was stationary and connected through the MTS machine's bottom

grips. Plate #5 was designed to provide out-of-plane support to the specimens and to prevent any torsion or twist in the test setup.

As shown in Figure 4-2 (a) and (c), there was a bar on each side of the specimen that was welded to plate #5 to prevent buckling. However, there was also a gap of approximately 1/8-in to not hinder the up and down movement of the specimens during testing. Lastly, a 1/4-in x1-in plate was bolted to plate # 2 to help measure the displacement of specimens (Figure 4-2 (c)). Figure 4-2 shows the detail sections of the test setup. Figure 4-2 (a) is a section through plate #5 and shows cross sections of plates #1 in the middle and plates # 2 &3 on the sides. Also, it shows the bars that used for out-of-plane buckling. Figure 4-2 (b) is a section through the cover plate and shows a cross section of plates # 2&3 on the sides and plate # 1 in the middle. Lastly, Figure 4-2 (c) is a horizontal section through plates #5 and the cover plates.

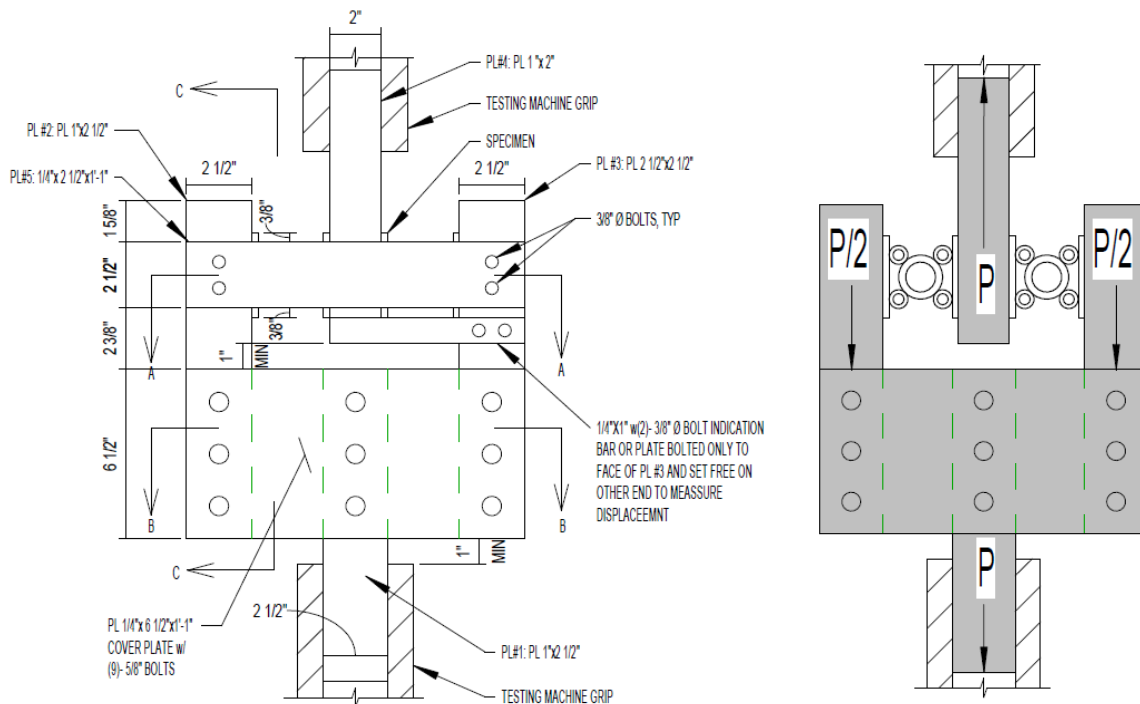
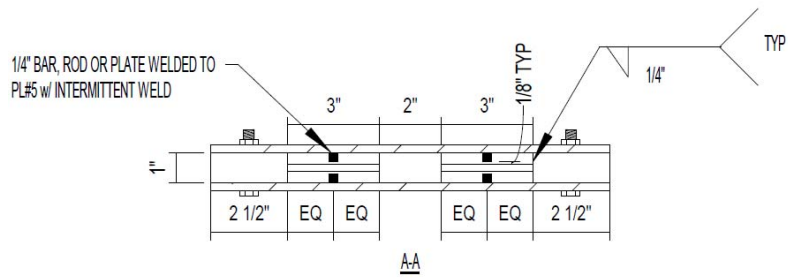
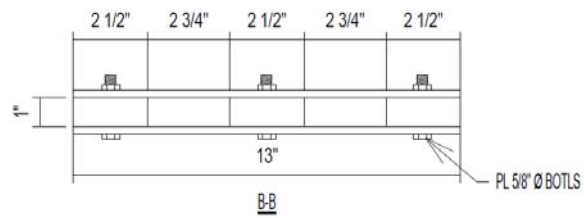


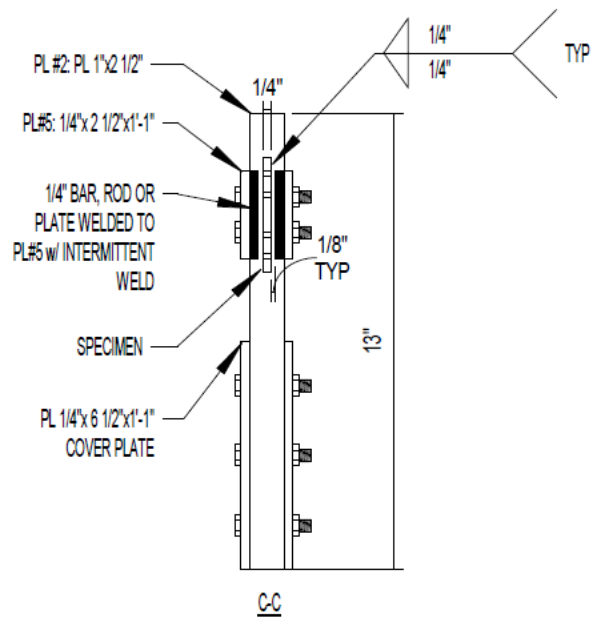
Figure 4-1:TS shape test setup layout



(a)



(b)



(c)

Figure 4-2: Section details of test setup; (a) section A-A, (b) section B-B, (c) section C-C

The inner faces of plates #5 and 4 were treated with grease to lubricate the surface and allow the specimens and those plates to move up and down. However, one #5 plate was removed after the first set of testing, which is the front plate, due to no signs of out-of-plane buckling and to be able to observe the specimens and assess crack initiation and propagation. Furthermore, it was evident that the specimens had not experienced out-of-plane buckling or deformation.

Figure 4-3 (a) shows the full scaled dimensions of shape TS, while Figure 4-3 (b) shows the half-scaled dimensions of shape TS. Prior to testing, actual measurements of the six specimens were made. Refer to Appendix B for each specimens' actual measurements. The tests are identified with the letters TS and 1 through 3 since there was three conducted tests. Also, the specimens are identified with letters A and B. The specimen on the left (as seen facing the test machine) was designated as A while the specimen on the right as B.

The imposed (scaled) displacement cycles used in the tests were based on the protocol used by PRESSS and the Structural Engineers Association of California (SEAOC) [5], [43] and [44]. The scaled test protocol is shown in Figure 4-4 and Table 4-1. The intent was to run a minimum of two cycles at each displacement amplitude.

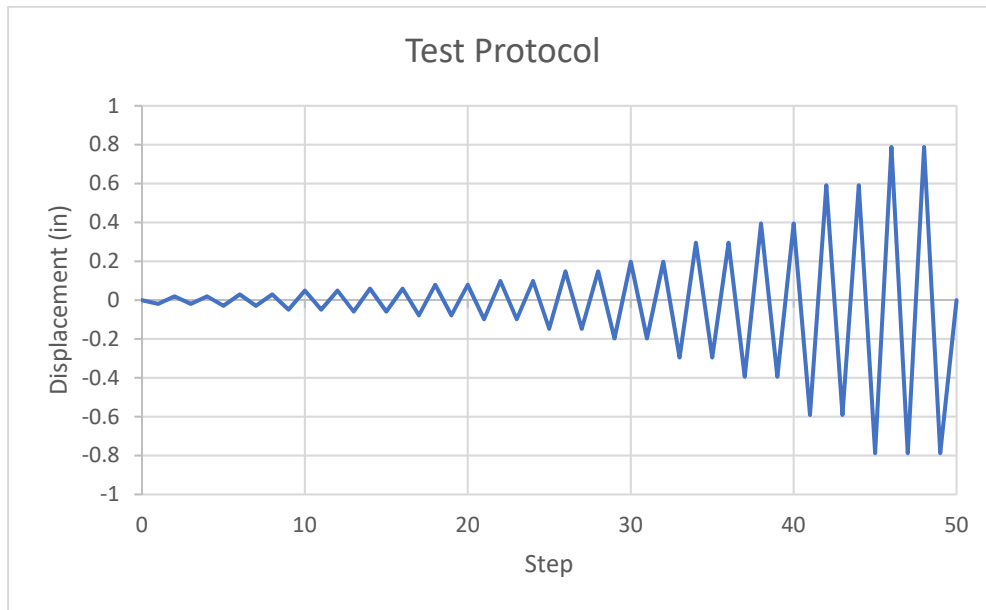


Figure 4-4: Imposed vertical displacements (scaled)

Table 4-1: Test protocol for TS specimens (scaled)

Step #	Δ (in)	Step #	Δ (in)	Step #	Δ (in)	Step #	Δ (in)	Step #	Δ (in)
0	0	11	-0.049	22	0.098	33	-0.295	44	0.591
1	-0.020	12	0.049	23	-0.098	34	0.295	45	-0.787
2	0.020	13	-0.059	24	0.098	35	-0.295	46	0.787
3	-0.020	14	0.059	25	-0.148	36	0.295	47	-0.787
4	0.020	15	-0.059	26	0.148	37	-0.394	48	0.787
5	-0.030	16	0.059	27	-0.148	38	0.394	49	-0.787
6	0.030	17	-0.079	28	0.148	39	-0.394	50	0
7	-0.030	18	0.079	29	-0.197	40	0.394		
8	0.030	19	-0.079	30	0.197	41	-0.591		
9	-0.049	20	0.079	31	-0.197	42	0.591		
10	0.049	21	-0.098	32	0.197	43	-0.591		

Three Linear Variable Differential transformer devices (LVDTs) were used as shown in Figure 4-5 to measure displacements. LVDTs #1 and #2 were used to confirm that there was no twist or differential movement between the two sides of the test setup. LVDT #3 was used to measure the imposed displacement. LVDT #3 was in contact with an angle (that was clamped to plate #4) to measure the displacement of the specimens. Appendix A contains additional information including pictures of the testing process.

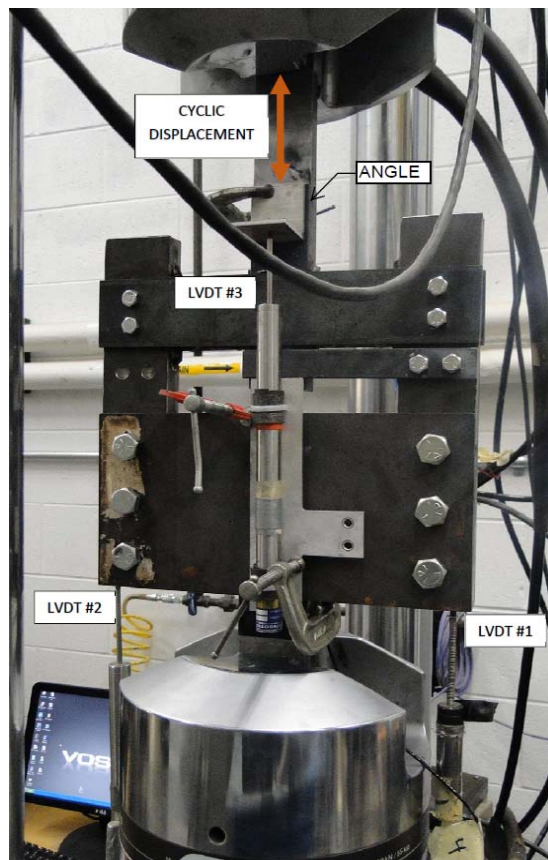


Figure 4-5: Test setup in the MTS Test machine

4.3 TS Specimens – Results and Discussion

In this section, test details and results for all TS specimens are discussed.

4.3.1 First set of specimens of TS shape – TS1

An initial test was first performed to make sure that the displacements were reasonable and in agreement with machine piston displacements. The test setup containing two specimens were subjected to the cyclic displacements shown in Figure 4-5 and Table 4-1

Specimens TS1-A experienced cracks initiating at the middle large ring as shown in Figure 4-6 (labeled #1) at a displacement of 0.294 in. Following that, specimen TS1-B failed at the weld as shown in Figure 4-6 (labeled #2). Results are reported until the first crack was noted.

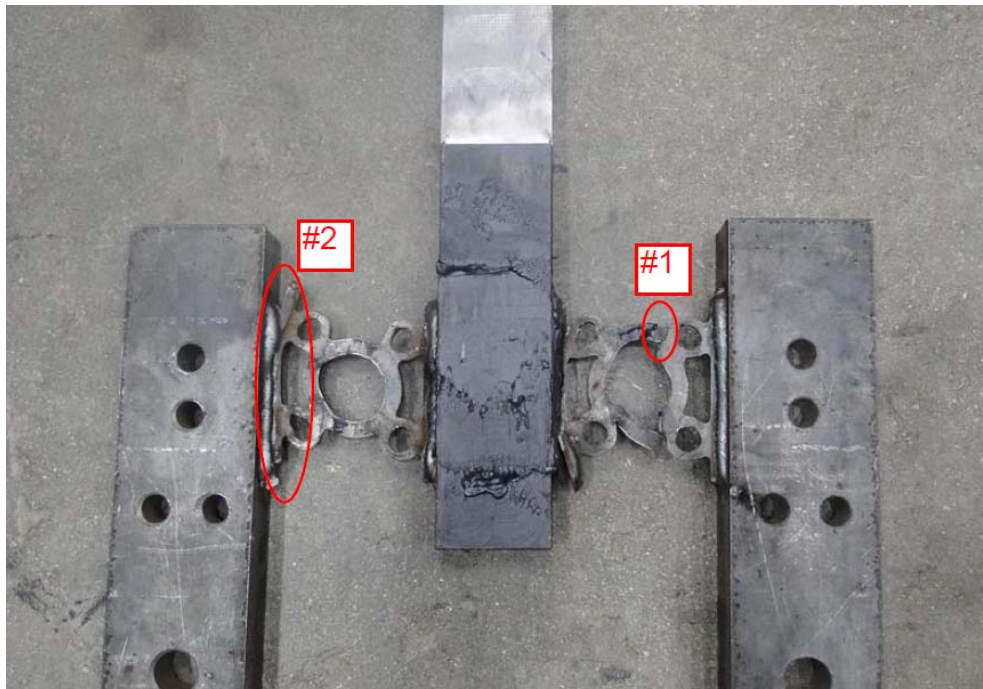


Figure 4-6: TSI fractures sequence

Figure 4-7 shows the force vs displacement relationship for the first set of specimens. It shows that the specimen reached a maximum of approximately 0.3-in displacement before it encountered a sudden decrease in load in the last two cycles before it fractured at a displacement of approximately 0.5-in. It could be seen that the overall behavior of the specimens was ductile and exhibits high energy dissipation. However, the failure mode of the specimens was low-cycle fatigue fracture due to large strains where the material already passed the yield point. It should be noted that according to the

scaling laws, the prototype force would be 4 times the scaled model force, and the prototype displacement would be twice the scale model displacements. Figure 4-8 shows a comparison between the experiment and FEM results. There is some variation at the load values which is believed due to the strength degradation of the specimens throughout the test that the FEM model did not count for.

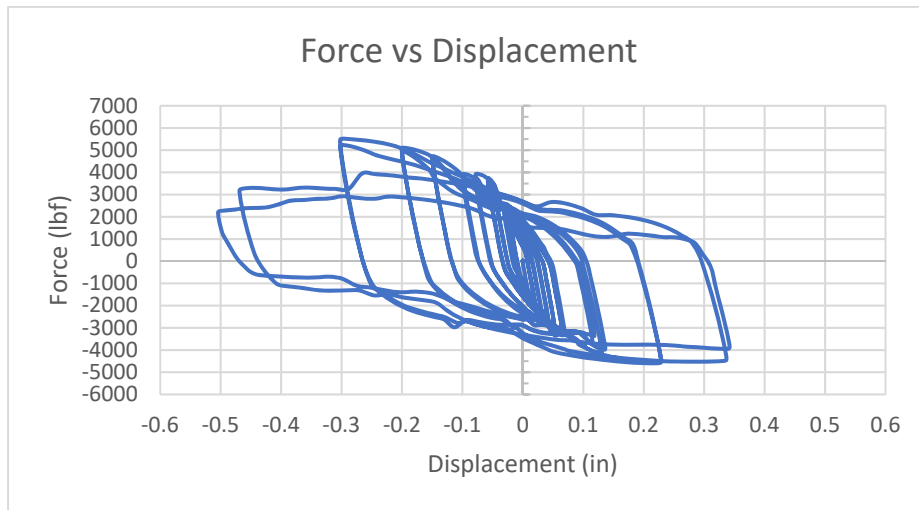


Figure 4-7: Experimental force vs displacement results for first set of specimens

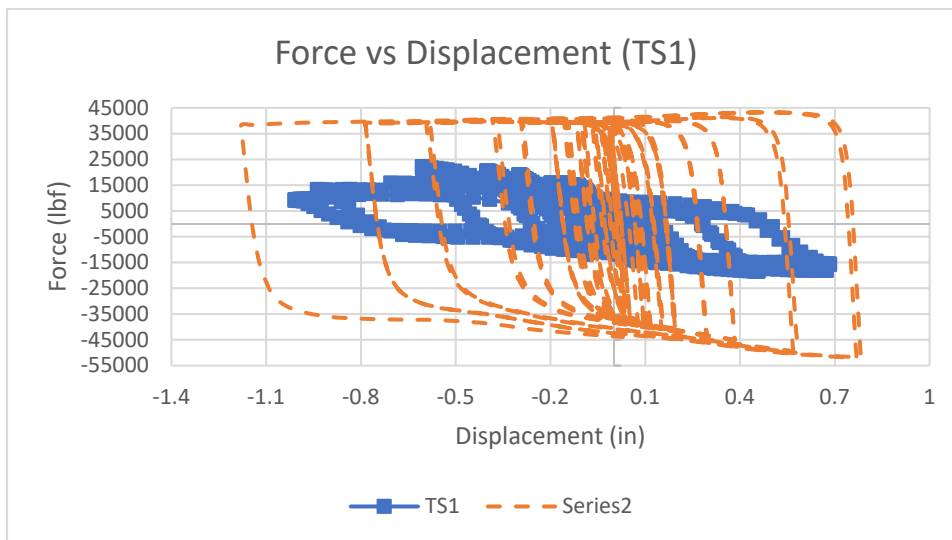


Figure 4-8: Experiment vs FEM results of TS1

4.3.2 Second set of specimens of TS shape – TS2

The second set of tests was done in a similar manner as in the first set of tests and with the same test protocol. During this test, the front plate (plate #5) was removed in order to monitor the test process and to be able to fully observe the crack initiation and propagation. However, the back plate was kept to provide bracing for plates #2 and #3. Figure 4-9 shows the second set of specimens, also, the front plate #5 was removed due to no observation of out-of-plane buckling on the first set of specimens.

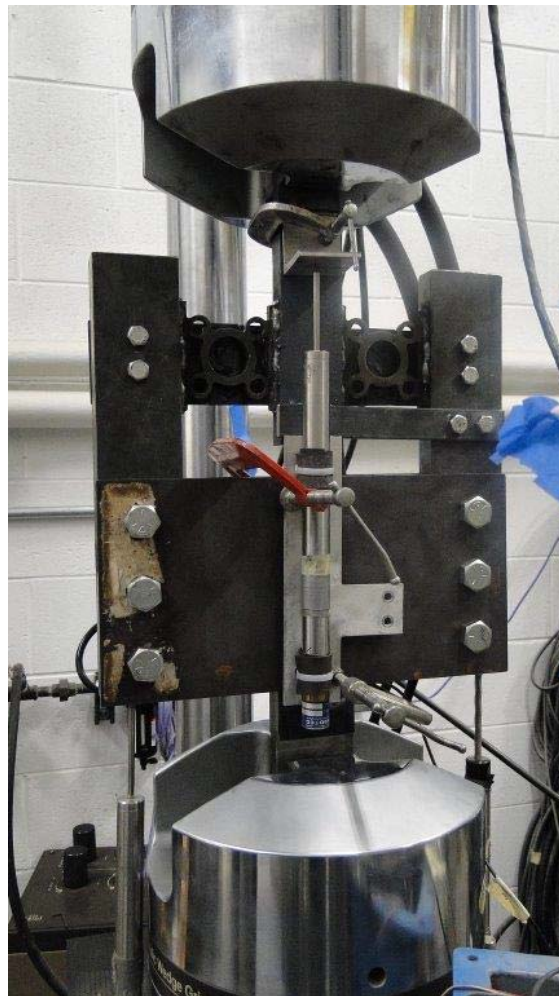


Figure 4-9: Test setup TS2

The test ran until both specimens, TS2-A and TS2-B, experienced cracks initiating at the top and bottom of the middle ring in a diagonal manner as shown in Figure 4-10. The first fractures are labeled #1.

Following that, fractures on the opposite sides (labeled #2) began developing and propagating as shown in Figure 4-10. Results are reported till both specimens failed completely.

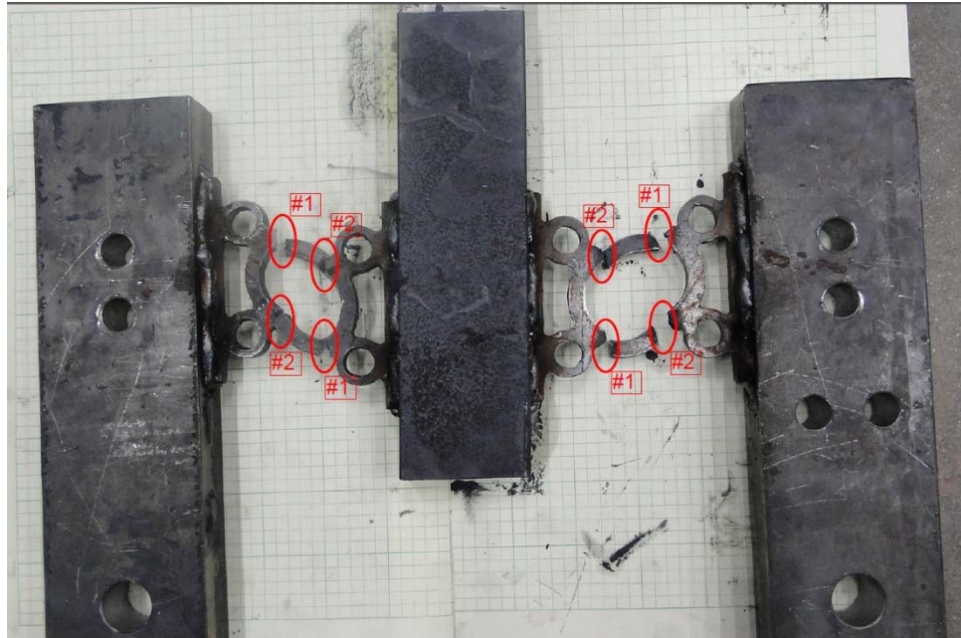


Figure 4-10: TS2 fractures sequence

Force vs displacement relationship of TS2 is shown in Figure 4-11. It could be seen that the specimen reached a maximum displacement of approximately 0.3- before it encountering a reduction in stiffness with relatively high strain in the last cycles before it had the first fracture at approximately 0.4 in. The overall response of the specimens was ductile. Furthermore, it exhibits substantial energy dissipation is noted. The failure was due to low-cycle fatigue and was similar to the first test. Figure 4-12 shows a comparison between the experiment and FEM results. There is some variation at the load values which is believed due to the strength degradation of the specimens throughout the test that the FEM model did not count for.

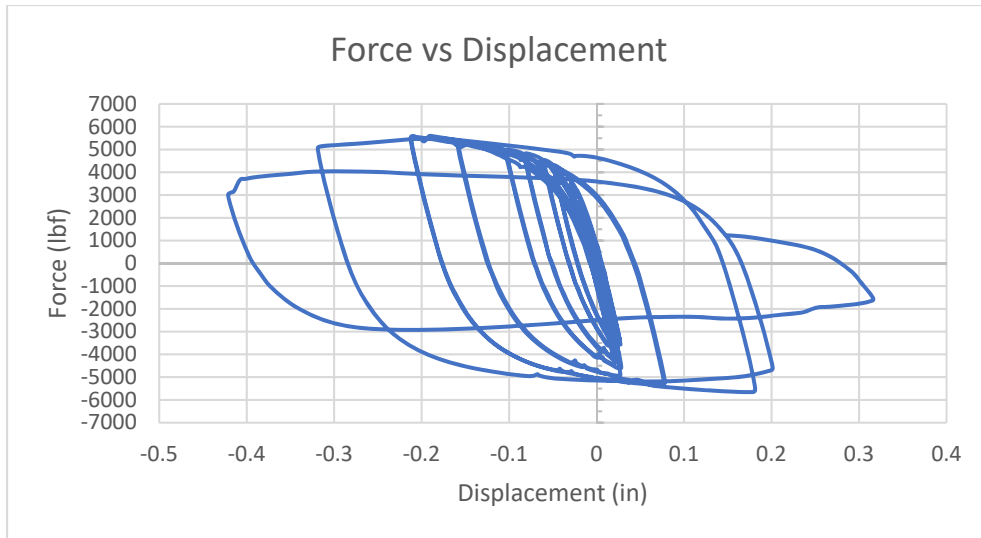


Figure 4-11: Force vs Displacement of TS2

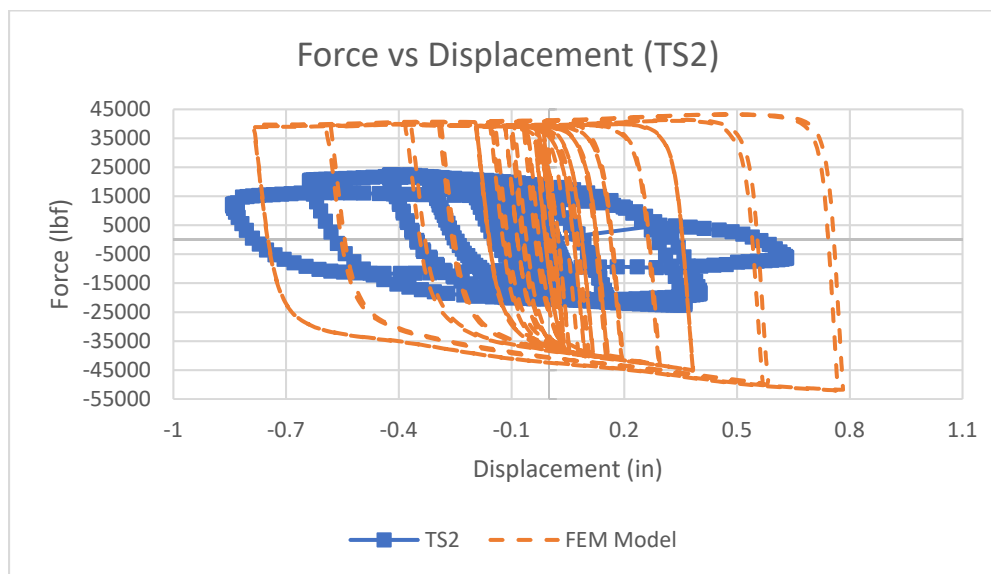


Figure 4-12: Experiment vs FEM results of TS2

4.3.3 Third set of specimens of TS shape – TS3

Similar to TS2, the three LVDT's were calibrated prior to do the testing of TS3. However, the rest of the test procedure was the same of the previous two tests. Also, the front plate (plate number five) was removed in order to monitor the test process and be able to observe crack initiation and propagation.

However, the back plate was kept to provide bracing for plates #2 and #3. Figure 4-13 shows the test setup of TS3

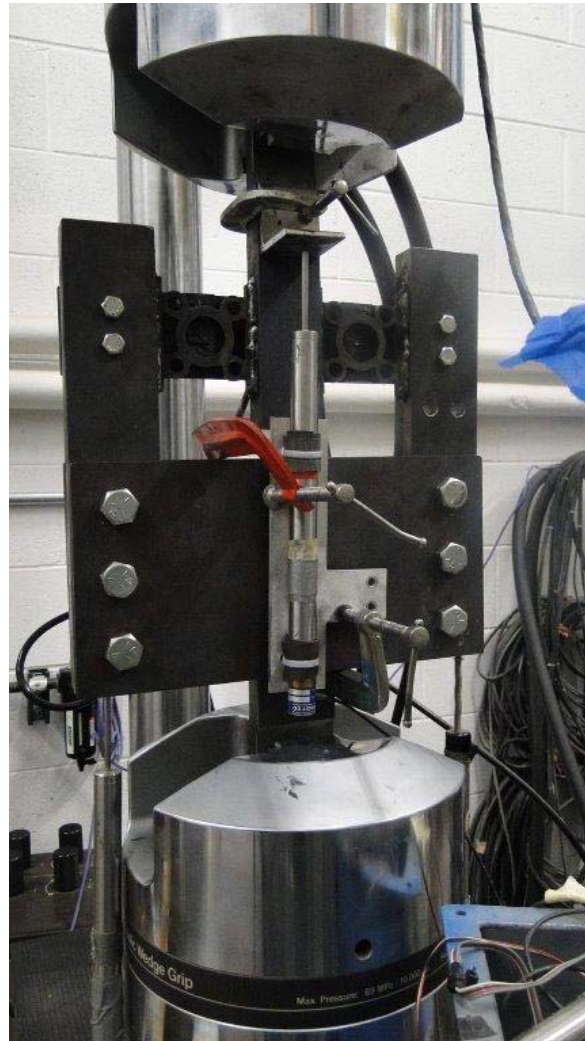


Figure 4-13: Test setup TS3

The test ran till both specimens TS3-A and TS3-B experienced crack initiating at the top and bottom of the middle large ring in a diagonal manner simultaneously as shown in Figure 4-14. First fractures were labeled (#1) in the latter figure. Following that, fractures on the opposite directions of fractures #1 started initiating and propagating, they are labeled (#2) in Figure 4-15. Results are reported till both specimens failed completely.

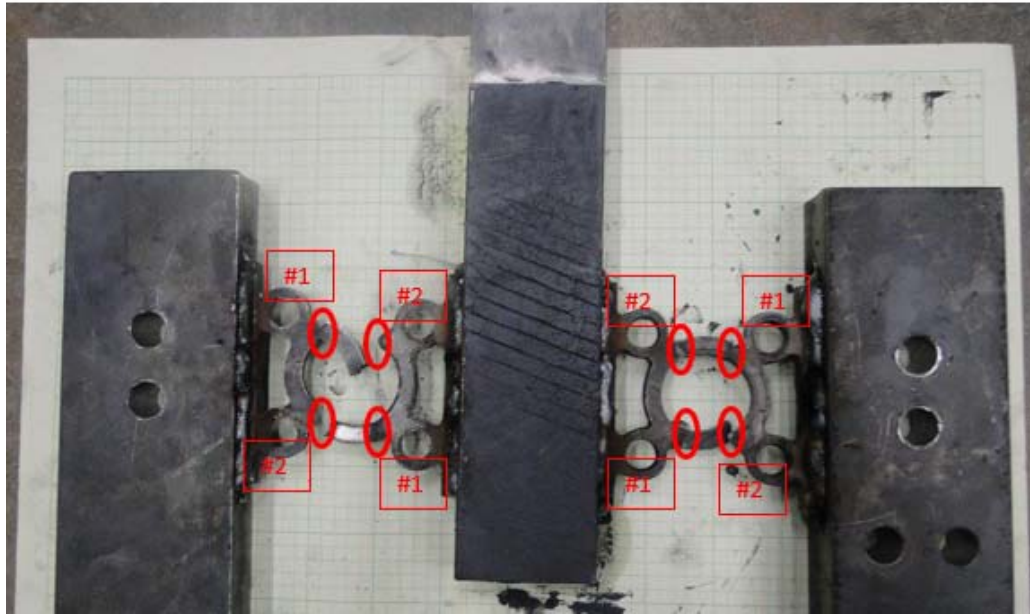


Figure 4-14: TS3 fractures sequence

Result of Force vs displacement relationship of TS3 test are shown in Figure 4-15. It could be seen that the specimen reached a maximum of approximately 0.3-inch displacement before it encounters a reduction in stiffness with relatively high strain in the last cycles before it had the first fracture at approximately 0.45-inch. It could be seen that the overall behavior of the specimens was ductile. Furthermore, it exhibits high energy dissipation. However, the failure mode is similar to first set which is low-cycle fatigue fracture was similar to the first test. Figure 4-16 shows a comparison between the experiment and FEM results. There is some variation at the load values which is believed due to the strength degradation of the specimens throughout the test that the FEM model did not count for.

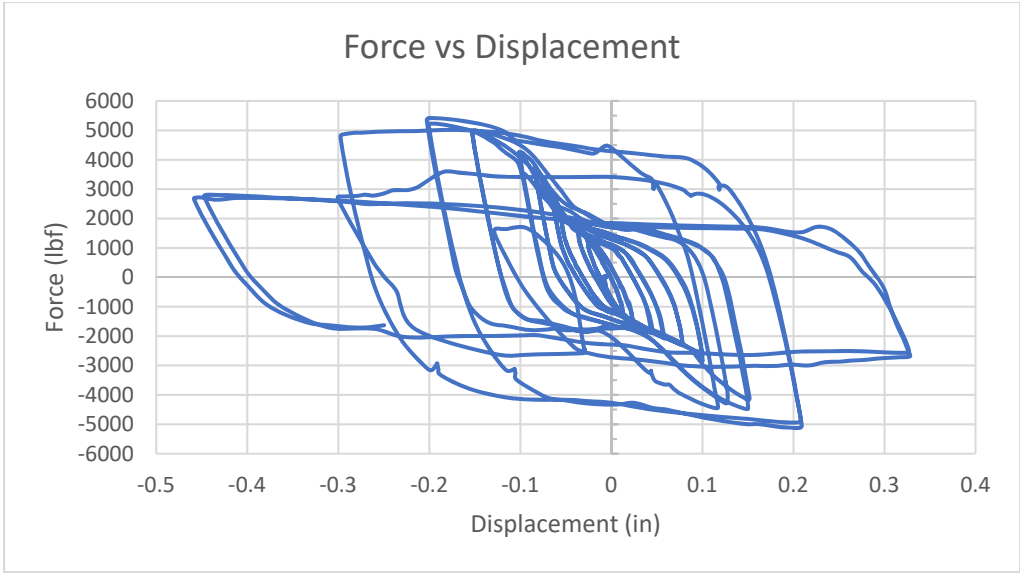


Figure 4-15: Force vs Displacement of TS3

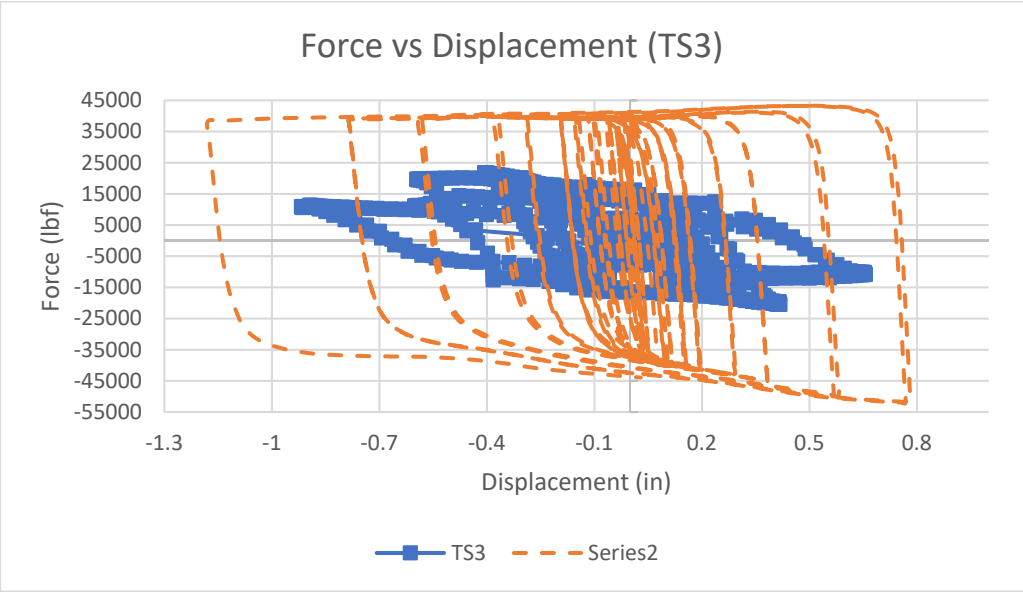


Figure 4-16: Experiment vs FEM results of TS3

4.4 Summary of TS shape testing

Overall behavior of first tested shape shows ductile behavior and high dissipated energy. However, all specimens failed to meet the requirement of resisting higher displacement. It was also noticed that the specimens have failed due to low cyclic fatigue. Comparison between the test versus FEM model results indicated that there is some variation especially for the force magnitude. It is believed that it is due to strength degradation of the shape once first cracks initiated which was not fully captured in the FEM model. As a result of the findings of first shape testing. Second and final shape (NS-5) was proposed, modeled and tested. In the following section the final shape (NS-5) will be discussed in details.

4.5 Testing, Results, and Discussion of NS5

The proposed connector NS5 was presented and discussed in Chapter 3. Testing of shape NS5 was same of that of the TS shape (TS1, TS2, and TS3). It has become a necessity to test this model experimentally to verify its behavior and compare it to the computer model analysis and to the previous shape analytical and experimental results. Six half-scaled specimens have been fabricated and tested. The test setup has been designed to test two specimens at a time, to minimize specimen bending and apply pure shear effect on specimens. All dimensions were one-half the corresponding prototype dimensions, except for the plate thickness, which was $\frac{1}{4}$ of the prototype thickness. This was done because two specimens were being tested simultaneously. This arrangement would allow the scaling rules to be applied based a scale factor of one-half. The steel that was used in the fabrication of the specimens and test setup was A36 steel. An MTS universal servo-hydraulic test machine with a capacity of 110 kips was used for the tests. Figure 4-17 shows the test setup, Appendix B includes detailed drawings of test setup. Specimens are welded to plates # 2, 3 and 4. The displacement is applied to plate # 4. Plate # 1 is stationary and the MTS machine grip is applied to it. Similar to the previous test setup, plate No.5 is designed to provide out-of-plane support to the specimens and to prevent and torsional or twist in the test setup. There are two rods or bars on each side or the specimen that are welded to plate No. 5 to prevent buckling. However, there is also a gap of approximately 1/8-inch so the bars will not hinder the up and down movement of the specimens during the testing. Figure 4-18 shows the test setup in the MTC machine. Three LVDT's were used in this testing. LVDT's #1 and 2 were solely used to confirm that there is no twist or differential movement between the model's sides. LVDT #3 is used to read the displacement. LVDT #3 was in contact with an angle (that was clamped to plate #4) to measure the displacement as shown in Figure 4-18. At first, a check and calibration were done on the readings of LVDT number three to match the recorded and actual displacements.

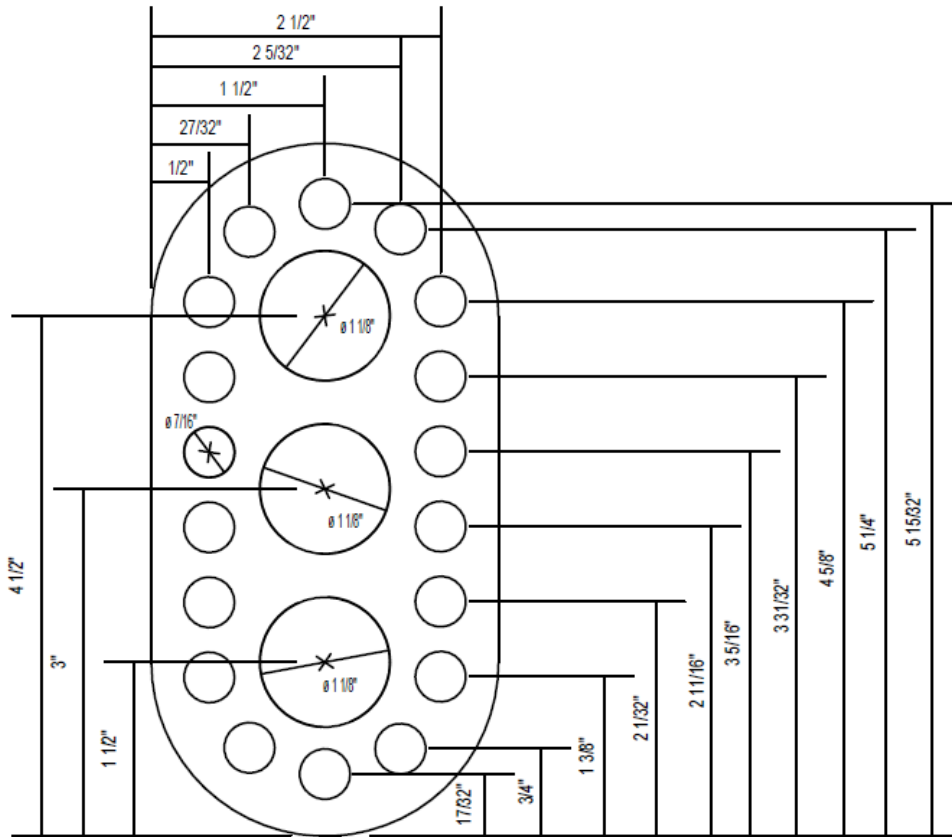


Figure 4-19: Half-scaled test specimen

The specimens are identified with NS5 in addition to a number 1, 2 or 3 referring to the test sequence. The specimen on the left (as seen facing the test machine) was designated as A, while the specimen on the right as B. Figure 4-19 shows the half-scaled dimensions of shape NS5. The imposed (scaled) displacement cycles used in the tests were based on the protocol used by PRESSS and the Structural Engineers Association of California (SEAOC) [5], [43] and [44]. The scaled test protocol is shown in Figure 4-20 and Table 4-2. The intent was to run a minimum of two cycles at each displacement amplitude.

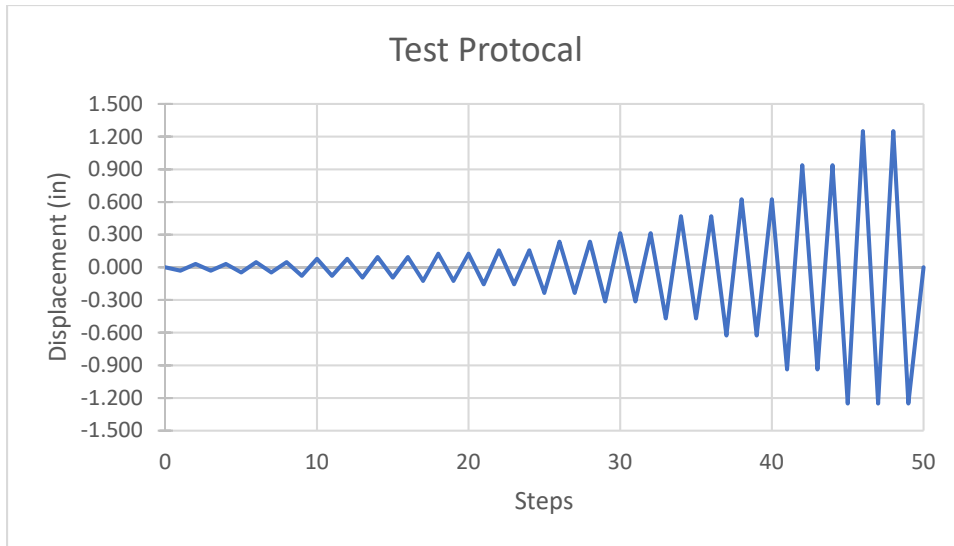


Figure 4-20: Test protocol of shape NS5

Table 4-2: Test protocol of shape NS5

Step #	Δ (in)	Step #	Δ (in)	Step #	Δ (in)	Step #	Δ (in)	Step #	Δ (in)
0	0.000	11	-0.078	22	0.156	33	-0.469	44	0.938
1	-0.031	12	0.078	23	-0.156	34	0.469	45	-1.250
2	0.031	13	-0.094	24	0.156	35	-0.469	46	1.250
3	-0.031	14	0.094	25	-0.234	36	0.469	47	-1.250
4	0.031	15	-0.094	26	0.234	37	-0.625	48	1.250
5	-0.047	16	0.094	27	-0.234	38	0.625	49	-1.250
6	0.047	17	-0.125	28	0.234	39	-0.625	50	0.000
7	-0.047	18	0.125	29	-0.313	40	0.625		
8	0.047	19	-0.125	30	0.313	41	-0.938		
9	-0.078	20	0.125	31	-0.313	42	0.938		
10	0.078	21	-0.156	32	0.313	43	-0.938		

4.5.1 Test NS5-1

At the beginning of this test, an initial test was conducted to calibrate the readings of all LVDT's in general and LVDT #3 in particular to verify that recorded displacement matches actual displacement.

Two specimens were subjected to cyclic displacements shown in Figure 4-20 and Table 4-2.

Specimen NS5-1-A experienced crack initiating at the right top corner of left specimen as shown in Figure 4-21 and Figure 4-22 and that was at displacement 0.313-inch. However, the test continued till max displacement of 0.51-inch and that when all side circles failed and as shown in Figure 4-22.

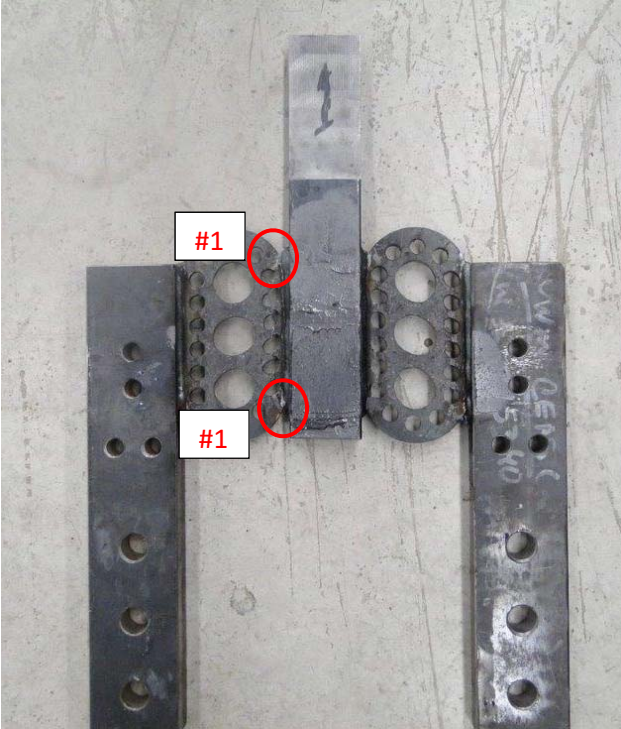


Figure 4-21: Failure mode of NS-1



Figure 4-22: Failure model of NS-1

Figure 4-23 shows the force vs displacement relationship of first set of specimens. It shows that the specimen reached a maximum of approximately 0.510-inch displacement before it encounters a gradual decrease in stiffness with relatively high load before it fails. It could be seen that the overall behavior of the specimens was ductile. Moreover, it exhibits steady hysteresis with high energy dissipation. However, the failure mode of the specimens was similar due to low-cycle fatigue. Ultimately, it showed improvement in the performance and higher capacity of first tested shape in addition to high exerted reaction force. Figure 4-24 shows a comparison between experiment and FEM model results. It could be seen that the results are close to perfect match and FEM model was able to capture the strength degradation of the model.

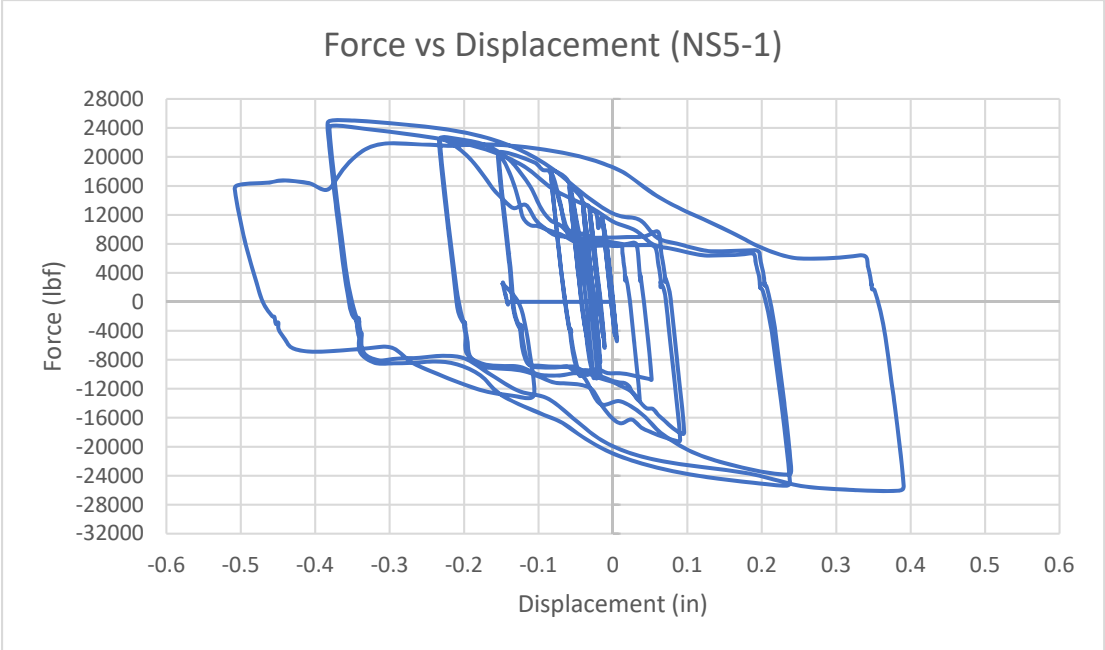


Figure 4-23: Force vs displacement of shape NS5-1

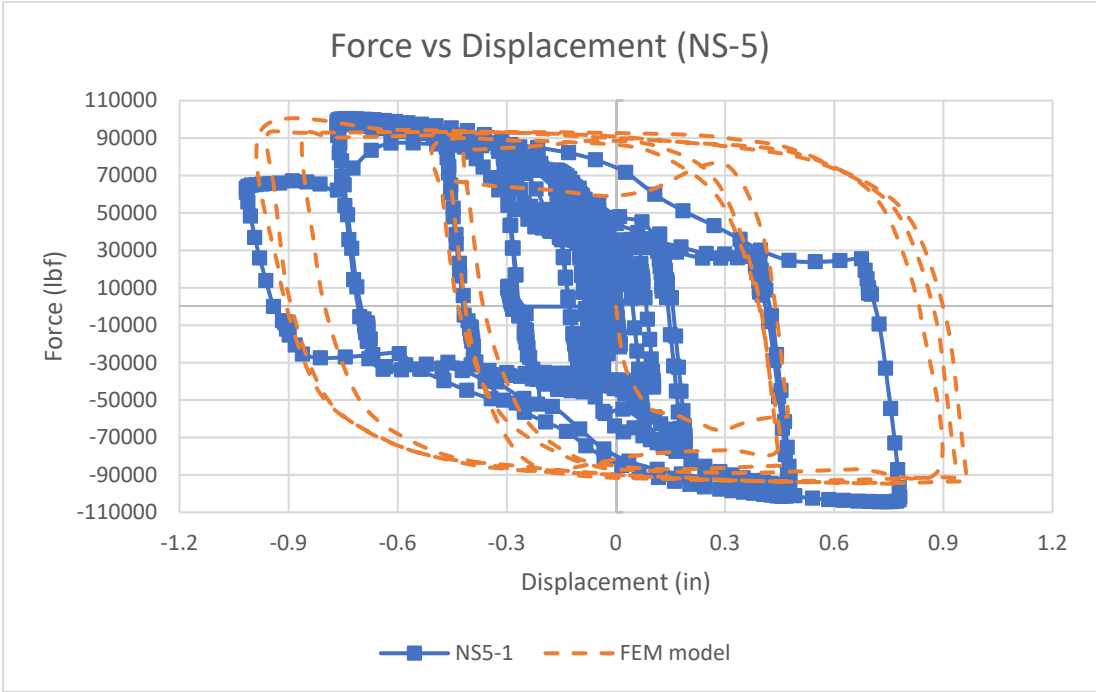


Figure 4-24: Experiment vs FEM results of NS5-1

4.5.2 Test NS5-2

After finishing first test, a calibration was performed on all three LVDT's prior to test the second set of specimens. The test was done in similar manner that was followed in testing first set with the same protocol. During this test, the front plate (plate #5) was removed in order to monitor the test process and be able to observe crack initiation and propagation. However, the back plate was kept to provide bracing for plates 2 & 3. The test continued till both specimens (NS5-2A & NS5-2B) experienced crack initiating at the top and bottom of right hand-side of both specimen simultaneously as shown in Figure 4-25 and Figure 4-26. First fractures occurred at displacement 0.313-inch and the test went on till failure which occurred at maximum displacement of 0.540-inch. Figure 4-26 shows the progressed failure of NS-2.

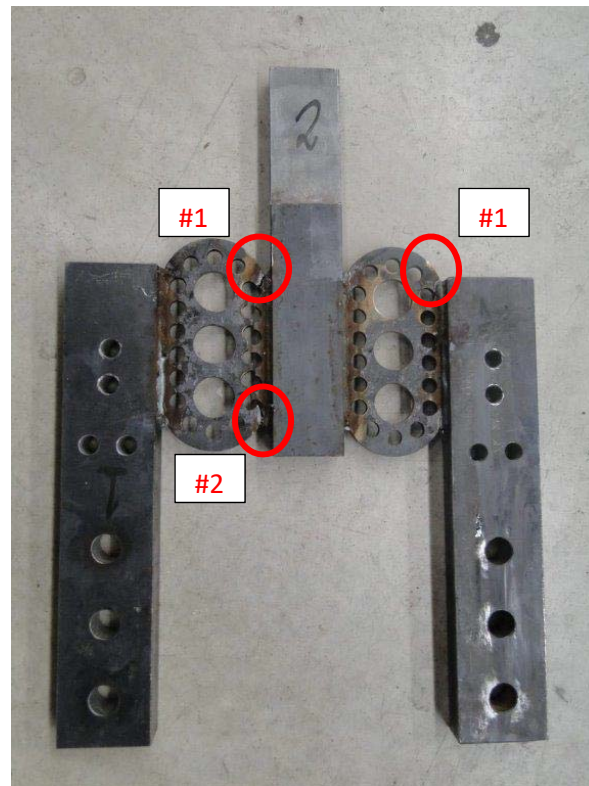


Figure 4-25: Failure mode of NS5-2



Figure 4-26: Failure mode of NS5-2

Figure 4-27 shows the force vs displacement relationship of first set of specimens. It shows that the specimen reached a maximum of approximately 0.540-inch displacement before its stiffness decreases with relatively high higher load. It could be noted that the overall behavior of the specimens was ductile. Also, it exhibits steady hysteresis with high energy dissipation. However, the failure mode of the specimens was similar to NS5-1 which is low-cycle fatigue. Ultimately, it showed improvement in the performance and higher capacity of first tested shape in addition to high exerted reaction force. Figure 4-28 shows a comparison between experiment and FEM model results. It could be seen that the results are close to perfect match and FEM model was able to capture the strength degradation of the model.

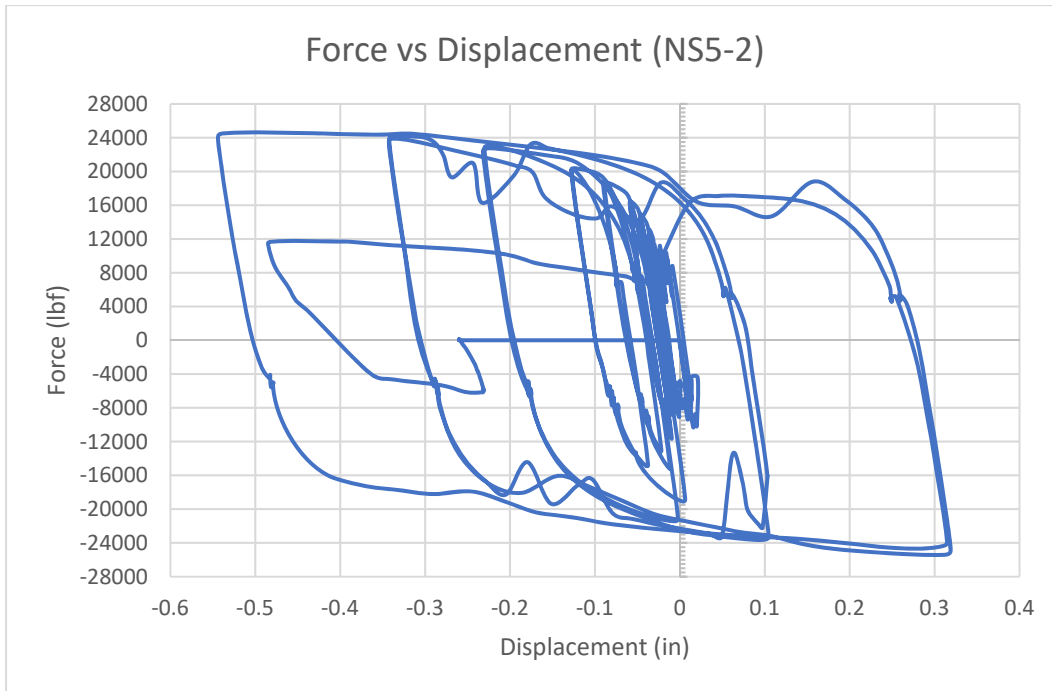


Figure 4-27: Force vs Displacement for shape NS5-2

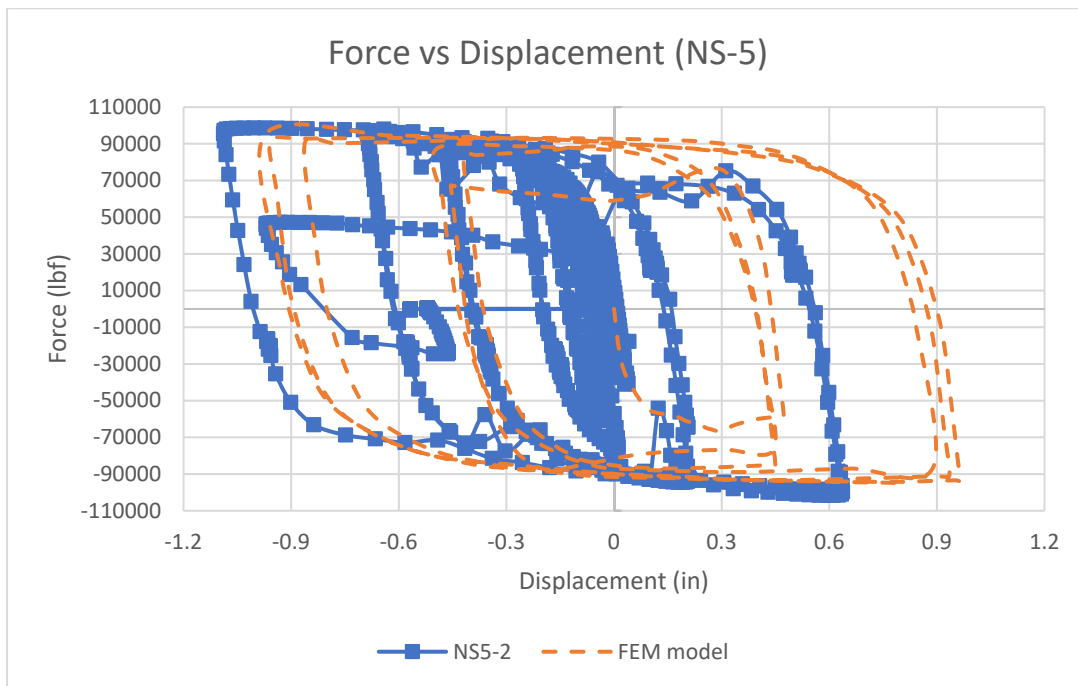


Figure 4-28: Experiment vs FEM results of NS5-2

4.5.3 Test NS5-3

Similar to previous tests, the three LVDT's were calibrated prior to do this testing. However, the rest of the test procedure of the previous sets was the same. Also, the front plate (plate #5) was removed in order to monitor the test process and be able to observe crack initiation and propagation. However, the back plate was kept to provide bracing for plates #2 & #3. Similar to first two tests (NS5-1 and NS5-2), the crack initiation appeared at displacement 0.313-inch. Cracked appeared first at the top and bottom corners of both specimens before it progresses to complete failure. The specimen completely separated from the test setup and as shown in Figure 4-29 and Figure 4-30. The maximum displacement at failure was 0.569-inch.



Figure 4-29: Failure mode of NS5-3



Figure 4-30: Failure mode of NS5-3

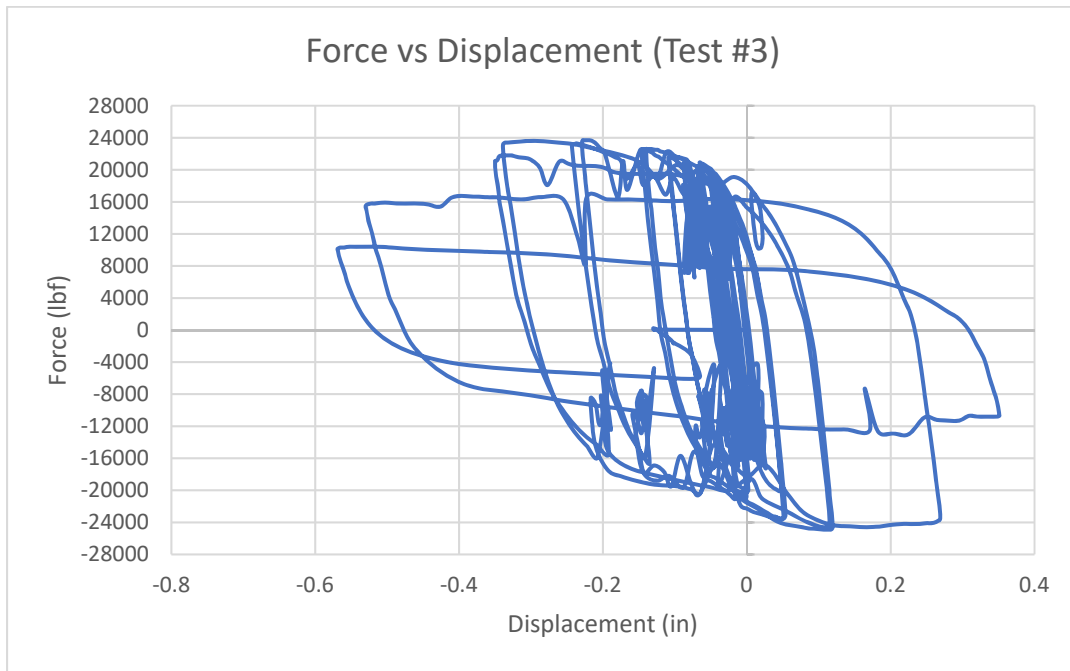


Figure 4-31: Force vs Displacement of test NS5-3

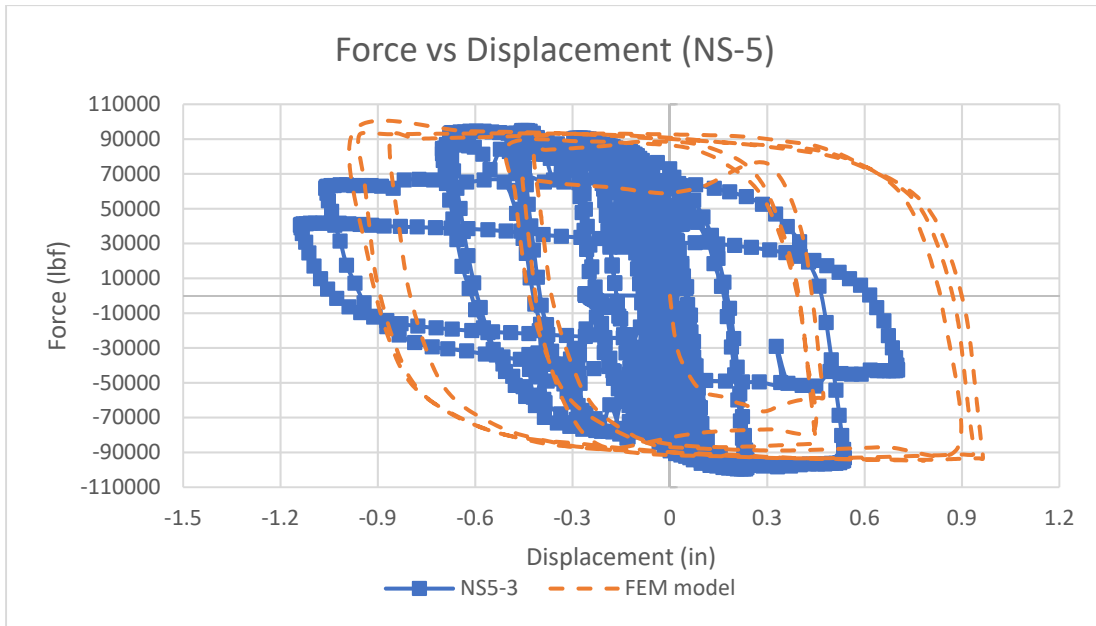


Figure 4-32: Experiment vs FEM results of NS5-3

It could be noted from Figure 4-31 that the specimens have experienced strength degradation after the crack initiation at 0.313-inch. In general, as shown in Figure 4-31 that specimen reached a maximum of approximately 0.313-inch displacement before its stiffness decreases with relatively high load. The ultimate failure occurred at 0.569-inch displacement. It could be noted that the overall behavior of the specimens was ductile and exhibited steady hysteresis with high energy dissipation. However, the failure mode of the specimens was similar to tests NS5-1 and NS5-2 which is low-cycle fatigue. Ultimately, it showed improvement in the performance and higher capacity of first tested shape in addition to high exerted reaction force. Figure 4-32 shows a comparison between experiment and FEM model results. It could be seen that the results are close to perfect match and FEM model was able to capture the strength degradation of the model.

4.6 Summary of NS-5 shape testing

Overall behavior of first tested shape shows ductile behavior and high dissipated energy. Also, the displacement has increased comparing to TS shape. It could be noticed that this shape has exhibited steady force versus displacement hysteresis and high energy dissipation. The displacement results could be considered promising and further analysis will reveal that this shape could provide feasible solution.

4.7 Comparison between various models

4.7.1 Background

Several shapes and geometries have been modeled and analytically examined in this research in order to find a shear connector that would dissipate higher energy and yield in shear under high seismic loads. Two shapes, however, were experimentally evaluated and their performance and behavior were closely analyzed to determine their efficiency. In the following section, a comparison between those shapes and the U-shape connector will be presented to draw a final conclusion for this study.

4.8 Comparison of tested shapes

Based on the test and analytical results, it could be concluded that NS5 shape has performed better than first tested shape (TS shape). It exhibited higher energy dissipation and better steady hysteresis than those of the first test Figure 4-33 and Figure 4-34. The first shape had first crack initiation at approximately 0.6-inch and total failure at an average 0.9-inch. On the other hand, NS5 shape had crack initiation at an average of 0.626-inch and total failure at 1.079-inch. That means there is roughly 20% improvement. Figure 4-35 shows TS shape, NS shape and full-scaled data of U-shape. It could be well seen that NS5 shape has dissipated significantly more energy than first tested shape. Moreover, shape NS5 exhibits higher plasticity range. Ultimately, the average dissipated energy calculated from first shape test data is approximately 165,540 lbf-in while it was 665,380 lbf-in for shape NS5. It means that

NS5 has dissipated about 400% higher energy than first shape. It worth mentioning that the U-shaped analytical data have yielded to a total of 182097 lbf-in. and that could be very well noticed in Figure 4-35.

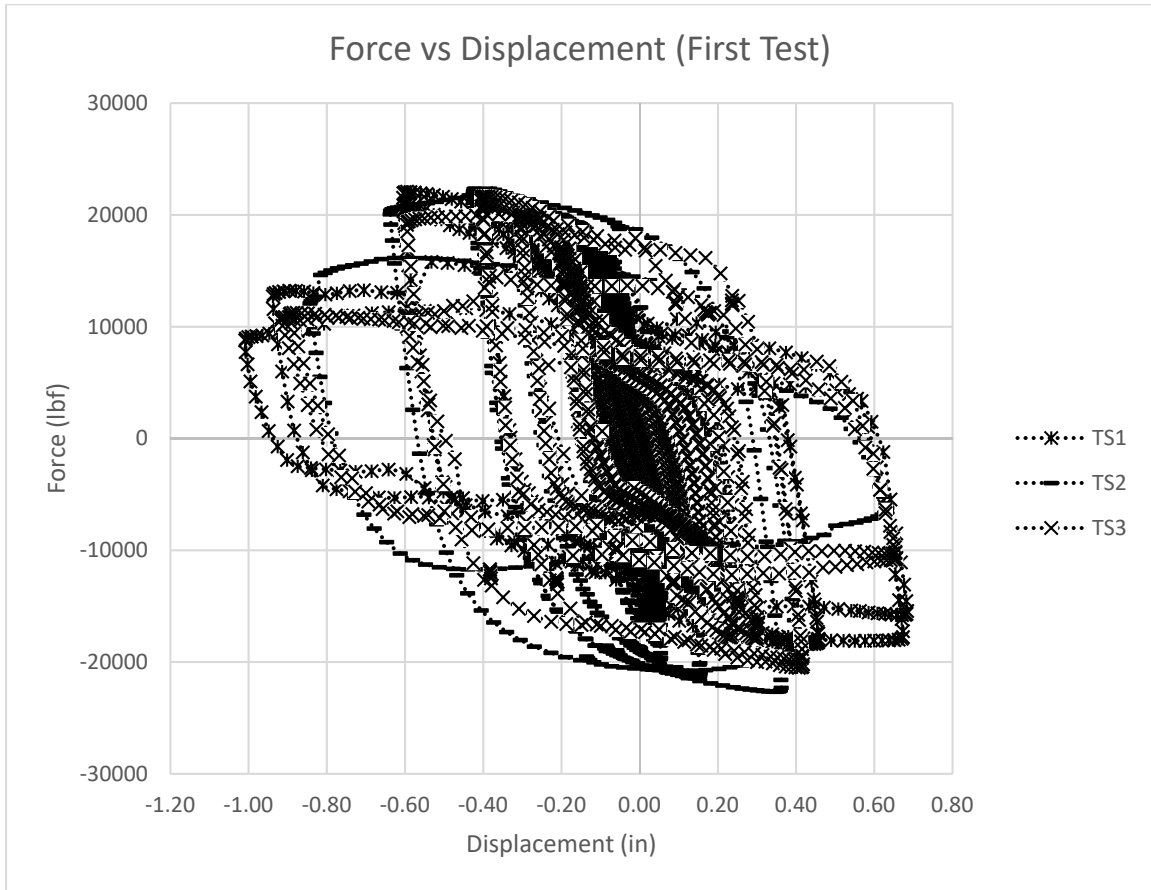


Figure 4-33: Force vs Displacement for first tested shape

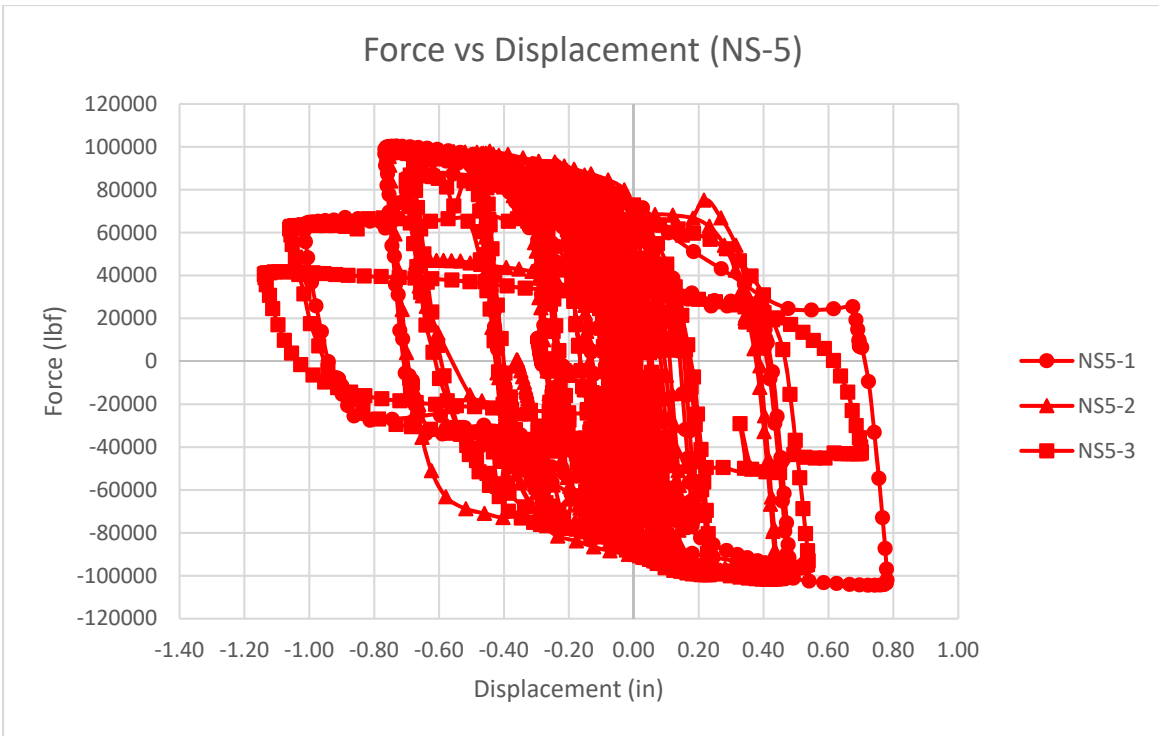


Figure 4-34: Force vs Displacement for Shape NS5

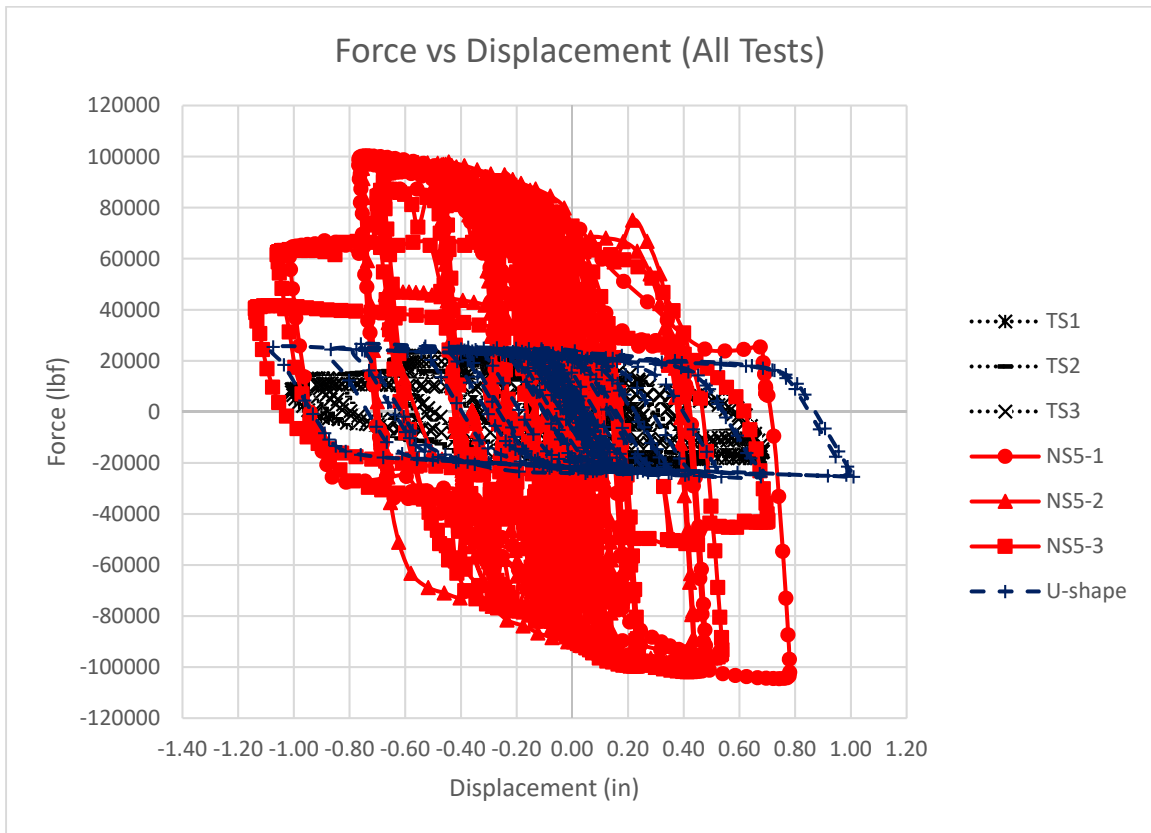


Figure 4-35: Force vs Displacement for all tests

CHAPTER 5: Summary and Conclusion

5.1 Summary and conclusions

Precast concrete shear wall systems are widely used in building structures. Precast structures are sometimes preferred over conventional cast-in-place concrete structures due to ease of construction and rapid implementation. In seismic regions, Precast concrete structures must have enhanced connection systems to address the inherent discontinuity between the various precast components. The main objective of this research was to find an improved connector between precast shear walls to increase energy dissipation and improve the overall behavior of precast shear walls when resisting seismic loads. Several shapes with different geometries were modeled (using finite element analyses) to meet the objectives of this study. For a given imposed displacement, an increase in the developed reaction force is required to substantially improve the energy dissipation of the shear connector. The developed reaction forces must be compatible with the available shear/tension strength in the concrete shear wall at the connection point.

To develop a more effective energy-dissipating connection system, a series of optimization steps were taken to come up with two alternative shapes. Subsequently, half-scale models of both shapes were physically tested in the laboratory to assess the level of energy dissipation and low-cycle fatigue resistance. Laboratory tests and finite element analysis results indicate that one of the two shapes, designated NS-5 and shown in Figure 5-1, can significantly enhance energy dissipation when compared with the conventional U-bar system. A comparison of the vertical load-displacement response for the NS-5 and U-bar connectors is shown in Figure 5-2. The finite element analyses of NS-5 indicate that shear yielding would occur between the openings in the connector, and there is a rapid increase in force to the maximum level. However, the maximum displacement achieved by the NS-5 connector in the load tests was lower than that reported for the U-bar due to low-cycle fatigue. Nevertheless, the achieved

maximum displacement was acceptable. If the displacement demand is higher than that achievable with the NS-5 connector, a combination of two or more NS-5 connectors (placed in series as shown in Figure 5-3) may be considered.

A nonlinear reinforced concrete FE model was analyzed, and conventional structural strength calculations were performed to assess the impact of higher reaction force on the concrete shear wall. The typical minimum steel reinforcement provided for embedment/anchorage within the zone around the connection in the shear wall would likely not be sufficient to handle the higher reaction forces exerted by the NS-5 device. However, adding additional steel anchorage reinforcement or increasing the bar size could provide the required strength. Finally, a simplified frame model of a 4-story shear wall building that was developed by PRESS [44] was used to assess the relative performance of the new NS-5 connector compared to the conventional U-bar device.

Results have shown that the shear walls incorporating the NS-5 connectors dissipated higher energy and exhibited lower drift when compared to the same structure with U-shaped connectors. The NS-5 shape performed better due to the higher stiffness and energy dissipation. This can be seen in the hysteretic force versus displacement results.

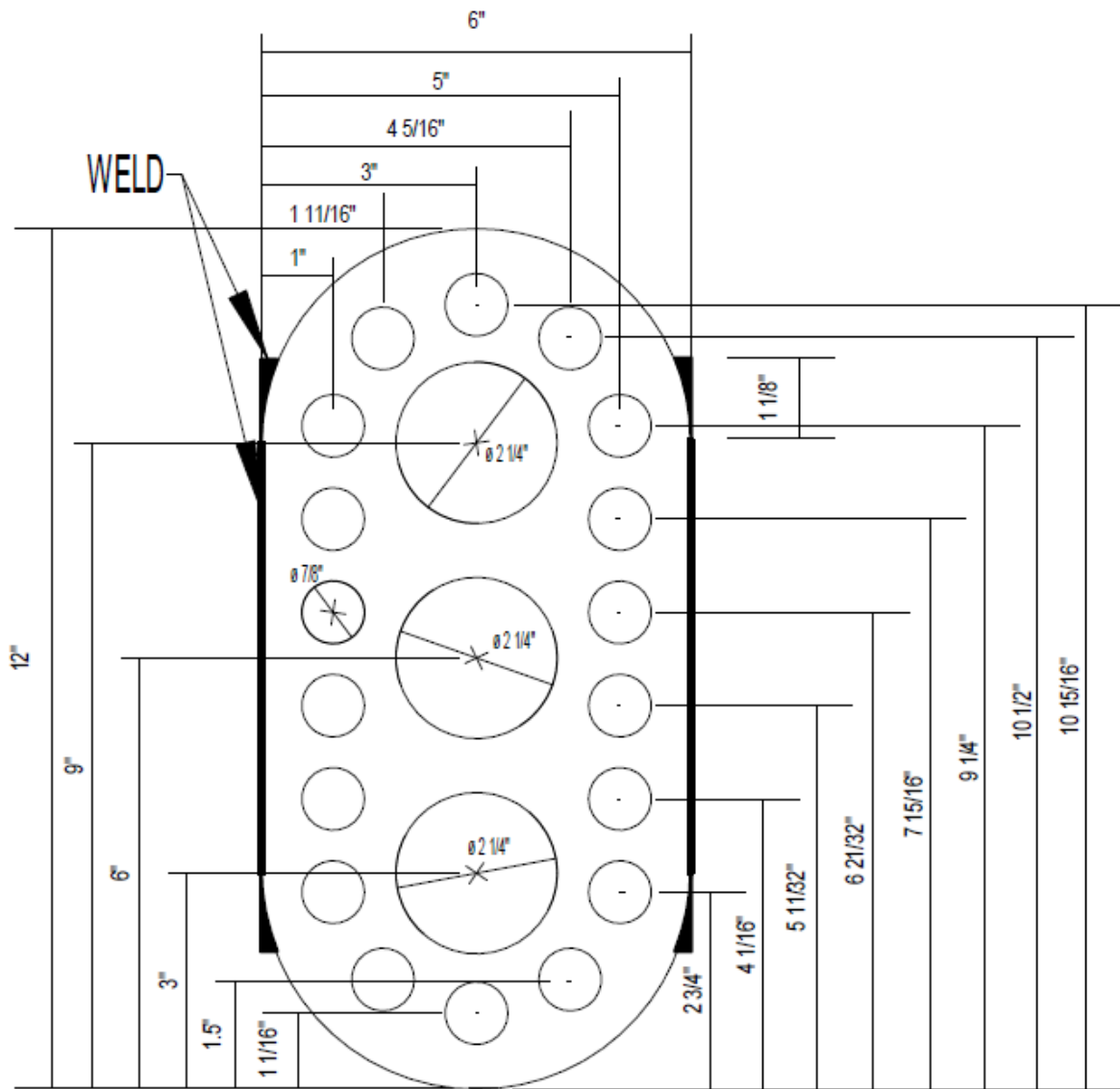


Figure 5-1: Shape NS-5

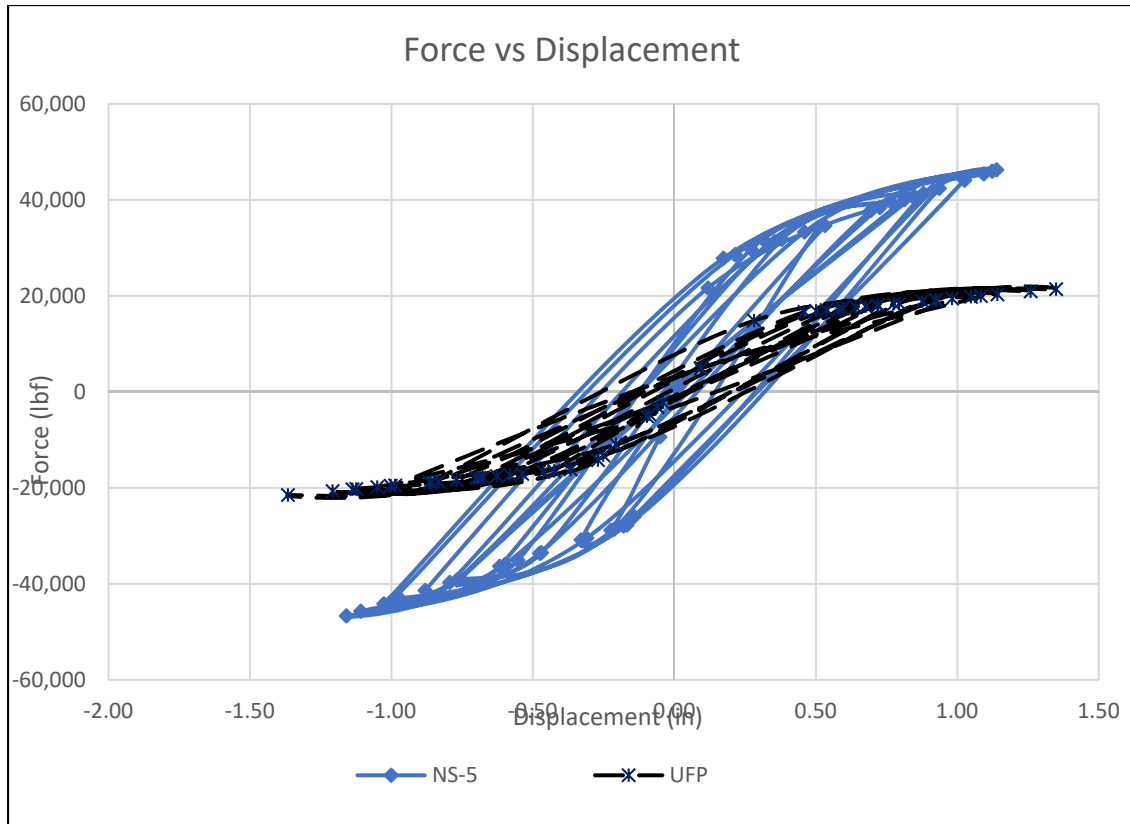


Figure 5-2: Vertical force vs Displacement for NS-5 and U-shaped plate

Another important advantage of the NS-5 connector over the conventional U-bar is its ability to provide substantial energy dissipation and resistance in the transverse (horizontal) direction in addition to the vertical direction. The U-bar connector, on the other hand, offers very little resistance in the horizontal direction. Figure 5-4 shows a comparison of horizontal load-displacement responses for the two connector systems based on finite element analyses.

Finite element analyses using a simplified shear wall building model (frame model) indicated that the horizontal relative movements between shear wall segments were not insignificant, and the addition of horizontal resistance can further reduce drift and base shear (Figure 5-5 and Figure 5-6)

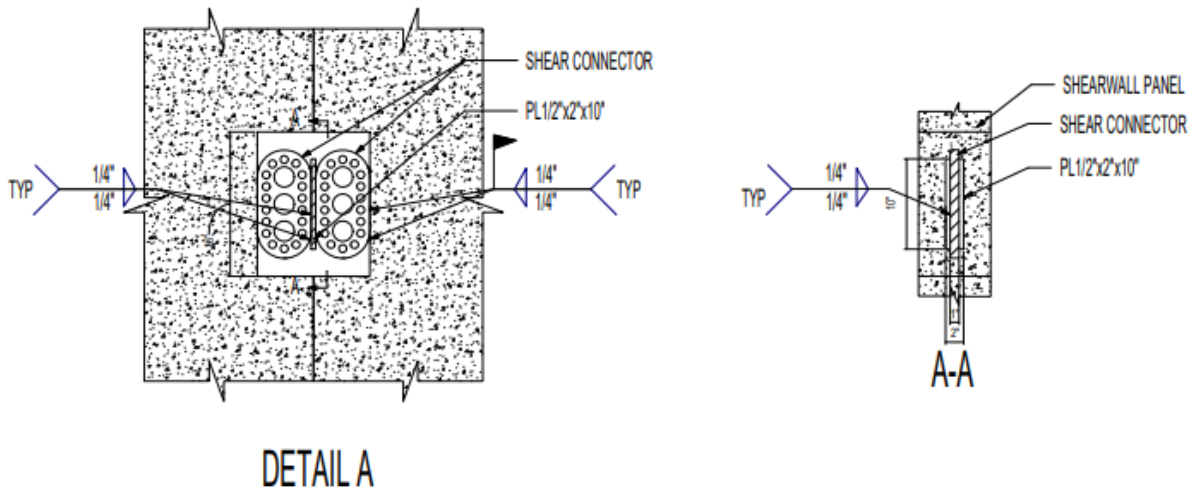


Figure 5-3: Two NS-5 shapes parallelly connected

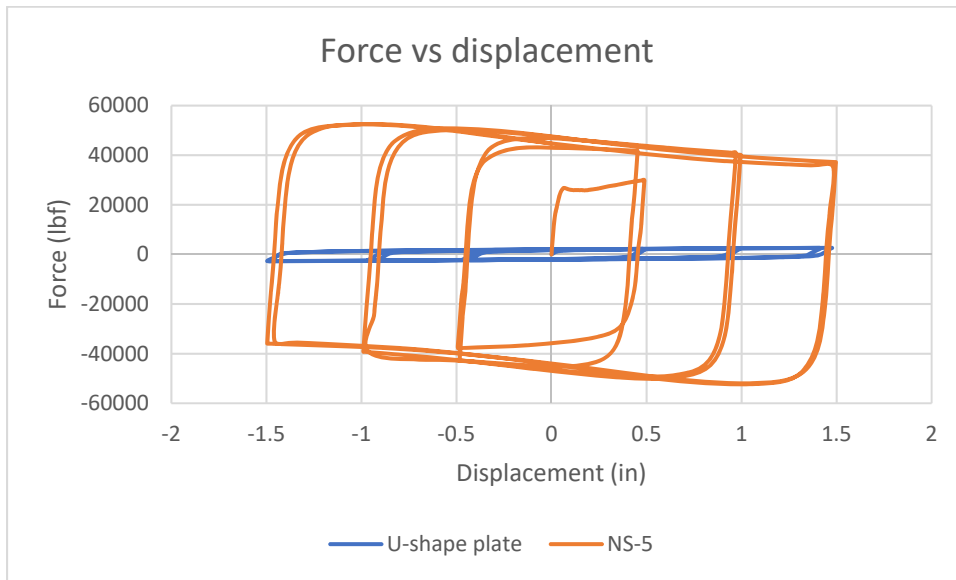


Figure 5-4: Horizontal force vs displacement for NS-5 and U-shaped connector under horizontal displacement

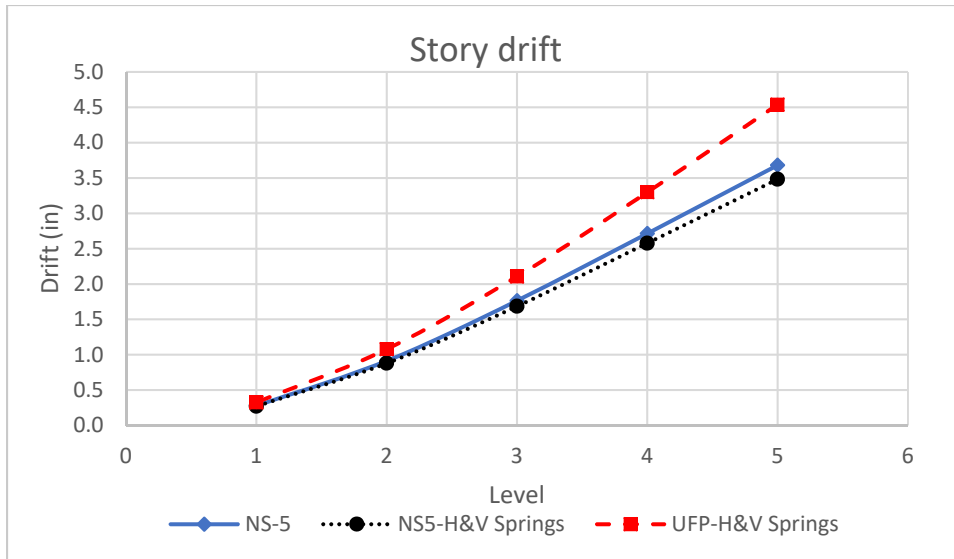


Figure 5-5: Story drift for U-shaped and NS-5 (With or without horizontal springs)

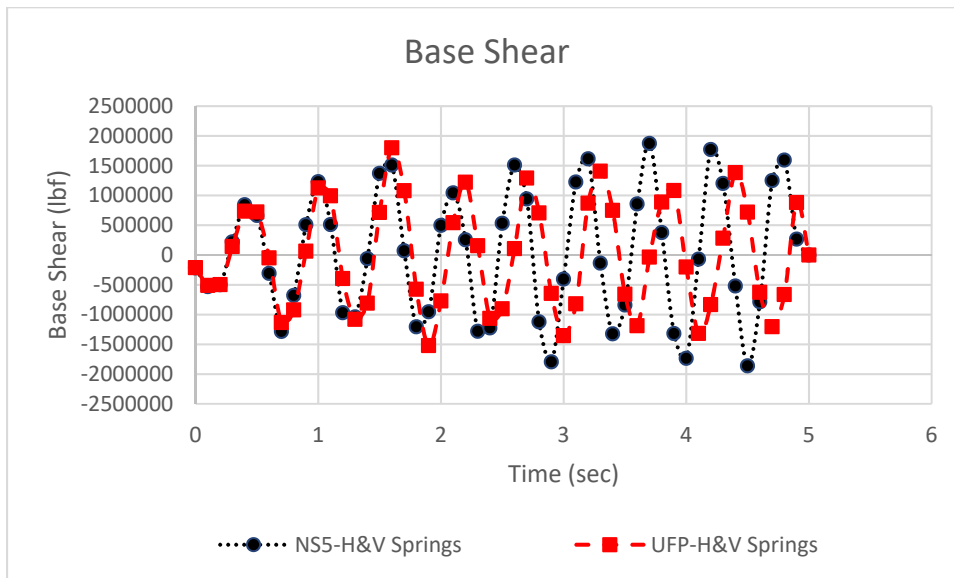


Figure 5-6: Base shear for U-shape plate and NS-5

Based on the results of experimental and analytical studies that were presented in this study, it is recommended that the proposed NS-5 shape be considered because of its high energy dissipation capability under relative vertical and horizontal displacements. The fabrication of the new NS-5 connector device is expected to be relatively easy because of the common A36 steel plate used and the

fact that the NS-5 shape could be easily produced by fabrication shops. Moreover, typical 6-in x 12-in Styrofoam or wood block outs could be used.

Future study

Perform a scaled model test of shear walls connected with NS-5 connectors.

Generate a FEM model and conduct laboratory tests on the use of two devices connected in series and subjected to lateral movement to enhance the maximum displacement capability when needed.

Perform a comprehensive analysis of the performance of NS-5 connectors using a 3-dimensional nonlinear finite element model of an entire building subjected to earthquake excitation at its base.

Assess the use of different types of steel and aluminum to fabricate the NS-5 shape and its effect on the overall performance of the connector.

CHAPTER 6: REFERENCES

- [1] http://www.pci.org/design_resources/about_precast/walls/. Accessed by 2016/08/30 6:15PM.
- [2] Li H-N, Li G., and Wang S-Y, "Study and Applications of Metallic Yielding Energy Dissipation Devices and Buildings", Tenth U.S. National Conference on Earthquake Engineering, Frontiers of Earthquake Engineering, July 21-25, 2014, Anchorage, Alaska,
- [3] B. J. Smith and Y. C. Kurama, "Seismic Design Guidelines for Special Hybrid Precast Concrete Shear Walls", Report #NDSE-2012-02.
- [4] R. A. Hawileh, E. I. Saqan, and J. A. Abdalla, "Simplified Optimum Design Procedure for Special Unbonded Posttensioned Split Precast Shear Walls", ASCE Technical Note.
- [5] A. E. Shultz and R. A. Magana, "Seismic Behavior of Connections in Precast Walls".
- [6] Kelly, J. M, Skinner, R. I., and Heine, A. J., "Mechanism of Energy Absorption in Special Devices for use in Earthquake Resistant Structures," Bulletin of the New Zealand Society for Earthquake Engineering, Vol. 5, No. 3, Sept., 1972, PP.63-88.
- [7] M. J. Nigel Priestley, "Overview of PRESSS Research Program". PCI Journal July-August 1991, PP 50-57.
- [8] Stanton, J. F. Anderson, R. G., Dolan, C. W., and McCleary, D. E., "Moment Resistant Connections and Simple Connections", Research Report No. ¼, Restressed Concrete Institute, Chicago, IL 1986.
- [9] Grigorian, C. E, Tang, T.-S., and Popov, E. P., "Slotted Bolted Connection Energy Dissipators" Report No. UCB/EERCE-92/10, Earthquake Engineering Research Center, University of California, Berkeley, July, 1992.
- [10] Stanton, J. F., and Nakaki, S. D. (2002). "Design guidelines for precast concrete seismic structural systems." PRESSS report No. 01/03-09 and Report No. SM02-02, PCI, Chicago, IL, and University of Washington, Seattle.
- [11] Elias I. Saqan and Rami A. Hawileh, "Non-dimensional Design Charts for Unbonded, Post-tensioned, Split Precast Concrete Walls". PCI journal Fall 2010 PP 78-99.
- [12] C. Bora, M. G. Oliva, S. D. Nakaki, and R. Becker, "Development of a Precast Concrete Shear-Wall System Requiring Special Code Acceptance". PCI Journal January-February 2007, PP 122-135.
- [13] Freedman, S "Loadbearing Architectural Precast Concrete Panels" PCI Journal, V.44, No. 5 (September-October): PP. 92-115
- [14] PCI Ad Hoc Committee on Precast Walls. 1997. "Design with Precast Concrete Shear-Walls. PCI Journal, V. 42, No. 5 (September-October): PP. 44-65.
- [15] Sritharan, S., and Aaleti, S. "Seismic Design of Jointed Precast Concrete Wall Systems" 4th International conference on Earthquake Engineering, Taipei, Taiwan, October 12-13, 2006.
- [16] Thomas, D. J., and Sritharan S., "An Evaluation of Seismic Design Guidelines Proposed for Precast Jointed Wall Systems. ISU-ERI-Ames Report ERI-04643, Department of Civil Engineering, Iowa State University, Ames, Iowa.
- [17] Perez, F. J., Pessiki, S., and Sause R., "Seismic Design of Unbonded Post-Tensioned Precast Concrete Walls with Vertical Joints Connectors", PCI Journal (January-February) 2004. PP 58-79.
- [18] Perez, F. J., Pessiki, S., and Sause R., "Lateral load behavior of Unbonded Post-Tensioned Precast Concrete Walls with Vertical Joints Connectors", PCI Journal (March-April) 2004. PP 48-64.

- [19] Kurama, Y., Pessild, S., Sause, R., Lu, L.-W., and El-Sheikh, M., "Analytical Modeling and Lateral Load Behavior of Unbonded Post-Tensioned Precast Concrete Walls," Research Report No. EQ-96-02, Department of Civil and Environmental Engineering, Lehigh University, Bethlehem, PA, 1996, 191 pp.
- [20] Ajrab J. J., Pekcan G., and Mander J. B., "Rocking Wall-Frame Structures with Supplemental Tendon Systems", Journal of Structural Engineering, ASCE, June 2004.
- [21] Housner G.W., "The Behavior of inverted Pendulum Structures during Earthquake", Bull. Seismol. Soc. Am., 53(2), 403-417.
- [22] Mander, J. B., and Cheng, C-T. "Seismic Resistance of Bridge Pier Based on Damage Avoidance Design" Tech. Rep. NCEER-97-0014, 1997, National Center for Earthquake Engineering Research, Buffalo, NY.
- [23] Seymore D. and Laflamme S., "Quasi-Static Analysis of Rocking Wall Systems", Department of Civil Engineering and Environmental Engineering, Massachusetts Institute of Technology, Cambridge MA.
- [24] Sun J., Qiu H., Yang Y. and Lu B., "Experimental and Analytical Studies on the Deformability of a Precast RC Shear Wall Involving Bolted Connections", Science China, Technological Science, August 2015, Vol. 58, No. 8:1439-1448
- [25] Sun J., Qiu H., and Xu J., "Experimental Verification of Vertical Joints in an Innovative Prefabricated Structural Wall System", Advances in Structural Engineering, Vol. 18 No. 7, 2015, PP. 1071-1086.
- [26] ANSYS Software help, ANSYS help viewer, Release 16.1.
- [27] Asger N. C, J. Andreas B., Morten N, Niels A, and Ole S., "Combined shape and topology optimization of 3D structures", Technical University of Denmark, Denmark.
- [28] "https://en.wikipedia.org/wiki/Topology_optimization", Accessed by 2017/08/15 6:30PM.
- [29] Mats Werme, "On Methods for Discrete Topology Optimization for Continuum Structures", Stockholm, Sweden 2008.
- [30] Jaejong P, Alok, S, "A multi-resolution method for 3D multi-material topology optimization", Department of Mechanical and Aerospace Engineering, The Ohio State University, Columbus, OH, 43210, USA.
- [31] Massimo Pola "A Study of Nodal Regions in Strut and Tie Models" MAsc thesis, Department of civil engineering, University of Toronto, Canada 1992.
- [32] Daniel K, Sukit Y. Thomas N, Jaso "Experimental Validation of Strut-and-Tie Method for Complex Regions", ACI Structural Journal, Vol. 105, Issue 4, 2008, PP578-589.
- [33] SIMULIA User assistance 2017
file:///C:/SIMULIA/Documentation/2017SE/English/DSSIMULIA_Established.htm?show=SIMACAECAERefMap/simacae-m-Hlp-sb.htm accessed 2018-08-15, 7:16PM (ET)
- [34] Bendsoe M. P., Sigmund O. "Topology Optimization theory, methods, and applications" Springer, Berlin, 2003.
- [35] Altair Hyperworks, User manual 2017, accessed by 04/13/2018 5:30PM.
- [36] Henry R. S., Aaleti S., Sritharan S. and J.M Ingam "Design of a shear connector for a new self-centering wall system"
- [37] Twigden K. M., Henry R.S., "Experimental response and design of O-connector for rocking wall system"
- [38] Dhondt Guido, "CalculiX CrunchiX USER'S MANUAL version", July 34, 2016

- [39] Segle P., Strombro J., Wulff A., Kolfors J., Larsson A., Persson R. "Numerical Simulations of Headed Anchors Break in Reinforced and Non-Reinforced Concrete Structures", Swedish Radiation Safety Authority.
- [40] Gross J., Klingner R., and Graves H. III, "Dynamic Behavior of Single and Double Near-Edge Anchors Loaded in Shear", ACI Structural Journal, Volume: 98, Issue: 5, Sept 2001, PP.665-676.
- [41] Lee J, Fenves G "Plastic-Damage model for cyclic loading concrete structures" Journal of Engineering mechanics, 1998, Volume 124, No. 8, PP. 892-900.
- [42] Lubliner J, Oliver J, Oller S, Onate E. "A plastic-damage model for concrete" International journal of solids and structures, 1989, volume 25, PP. 299-329
- [43] Krawinkler, Helmut "Loading Histories for Cyclic Tests in Support of Performance Assessment of Structural Components"
- [44] Sritharan, S., Aaleti, S., and Thomas, D. J. "Seismic Analysis and Design of Precast Jointed Wall Systems" ISU-ERI-Ames report ERI-07404, Iowa State University of Science and Technology.
- [45] R. A. Haweeleh, A. Rahman, H. Tabatabai "Nonlinear finite element analysis and modeling of a precast hybrid beam-column connection subjected to cyclic loads", Applied Mathematical Modeling journal, 2010, Volume 34, Issue 9, PP. 2562-2583
- [46] R. A. Haweeleh, H. Tabatabai, A. Rahman, A Amro "Non-dimensional design procedures for precast, prestressed concrete hybrid frames", PCI journal, 2006, Volume 51, Issue 5 , PP. 110-130.
- [47] E. I. Saqan, R. A. Haweeleh, "Non-dimensional design charts for unbonded, post", PCI journal, 2010.
- [48] A. Rahman, H. Tabatabai, R. A. Haweeleh "Simplified Design Procedures for Precast Hybrid Frames " University of Wisconsin – Milwaukee, Department of Civil Engineering and Mechanics, 2004

APPENDICES

APPENDIX A. EXPERIEMENT PHOTOS



Figure A- 1: Test setup

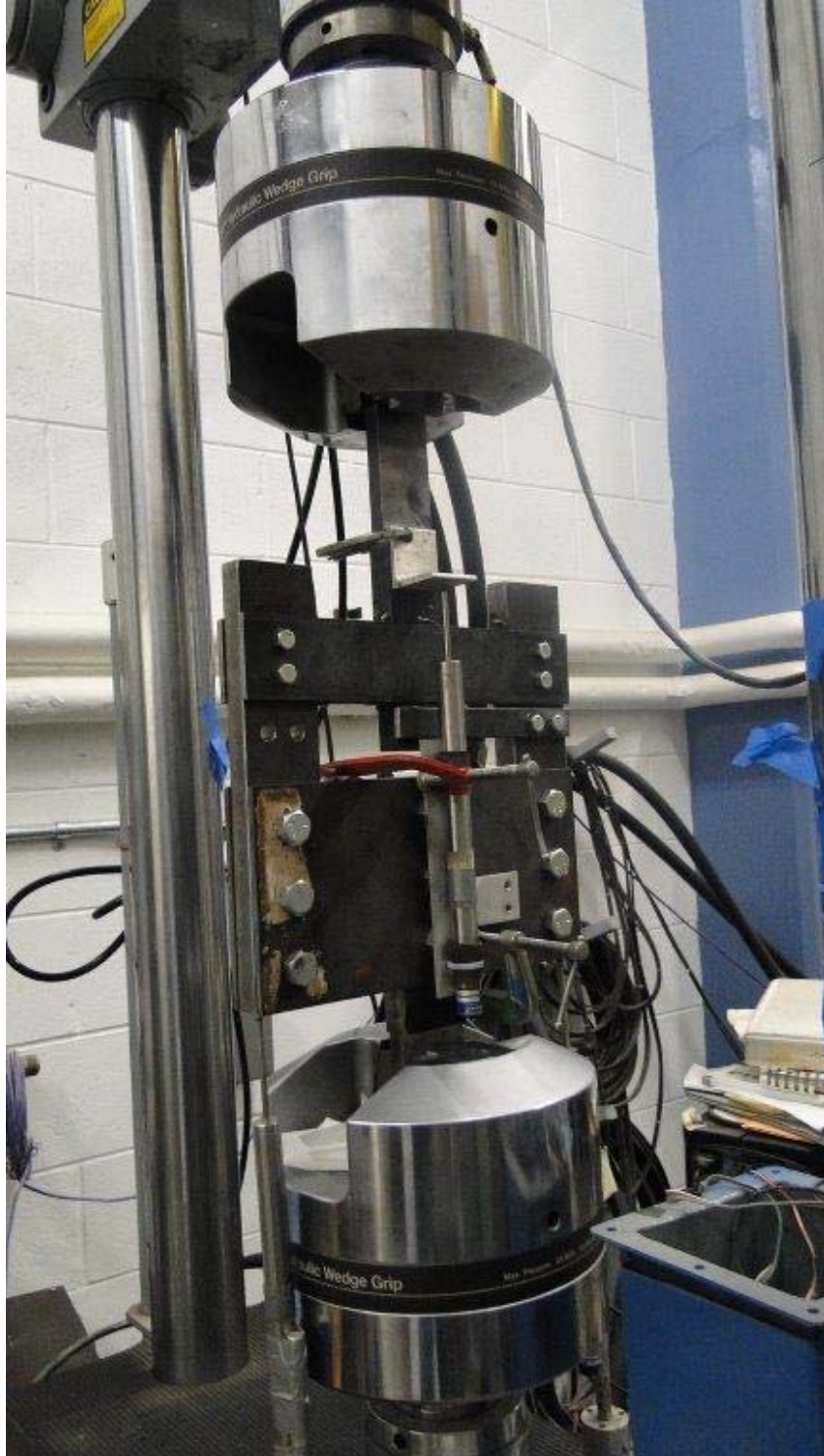


Figure A- 2: MTS with the test setup

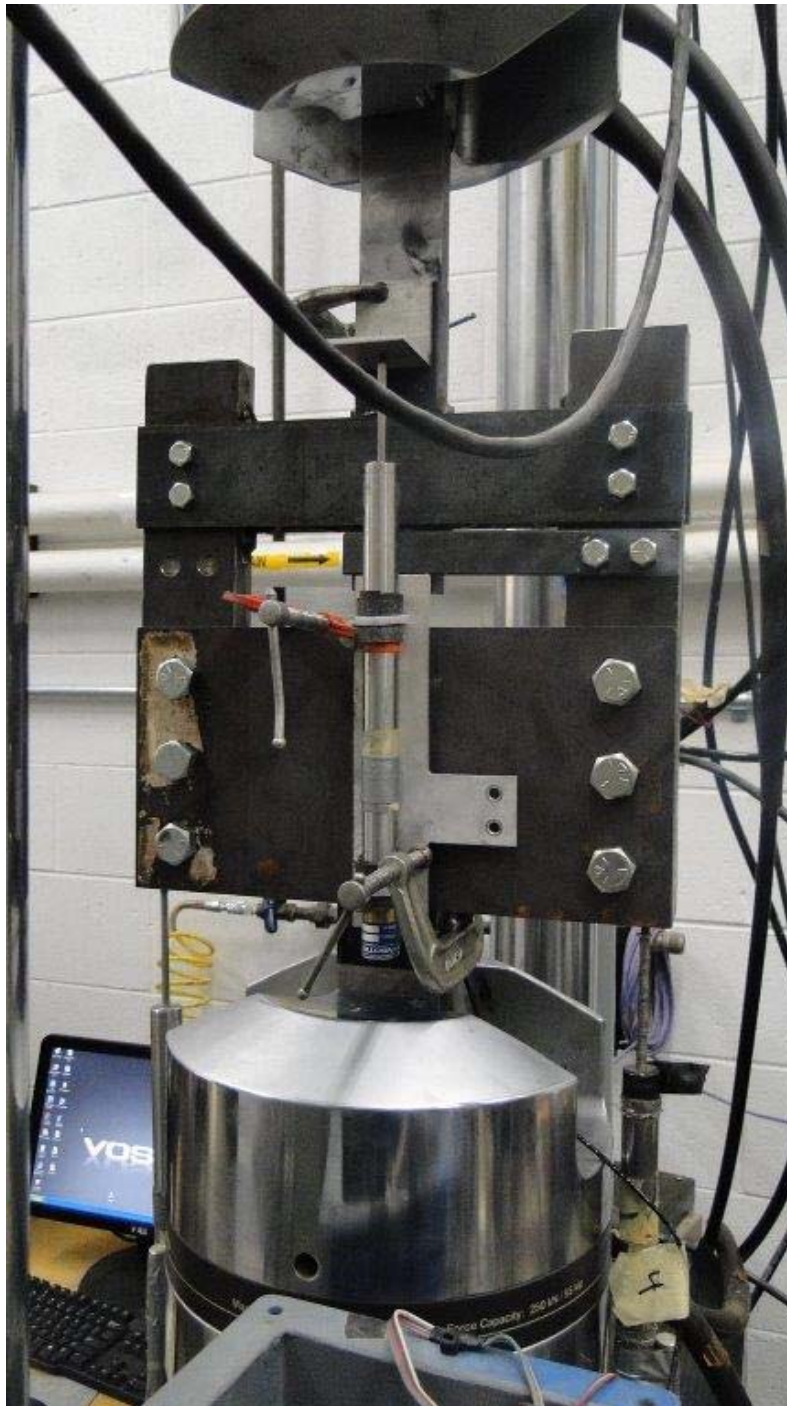


Figure A- 3: LVDT's are set and ready for the test to start



Figure A- 4: First tested devices

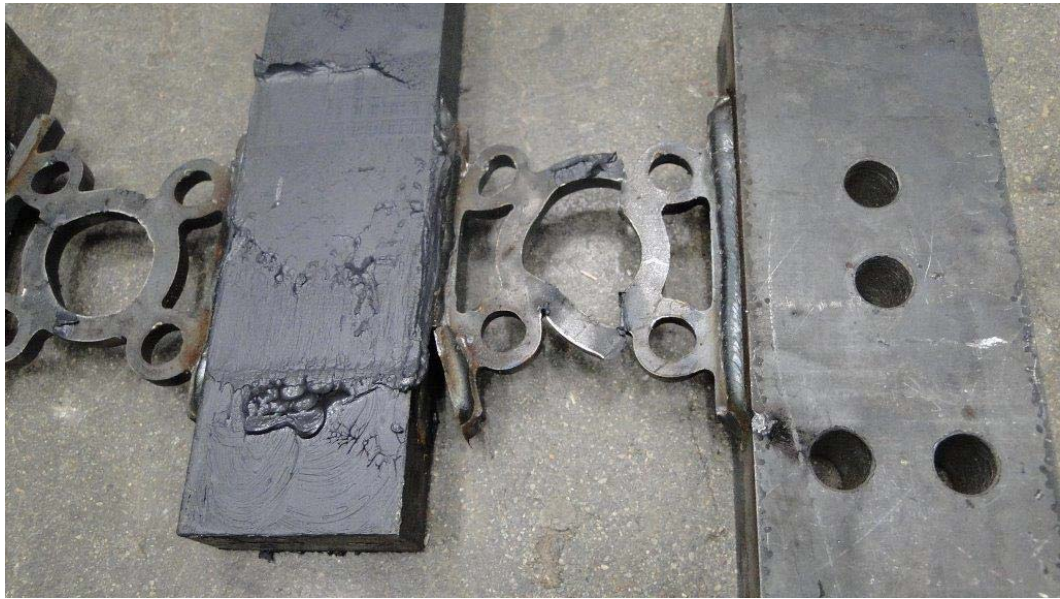


Figure A- 5: Close-up of the first tested device shows the failure mode

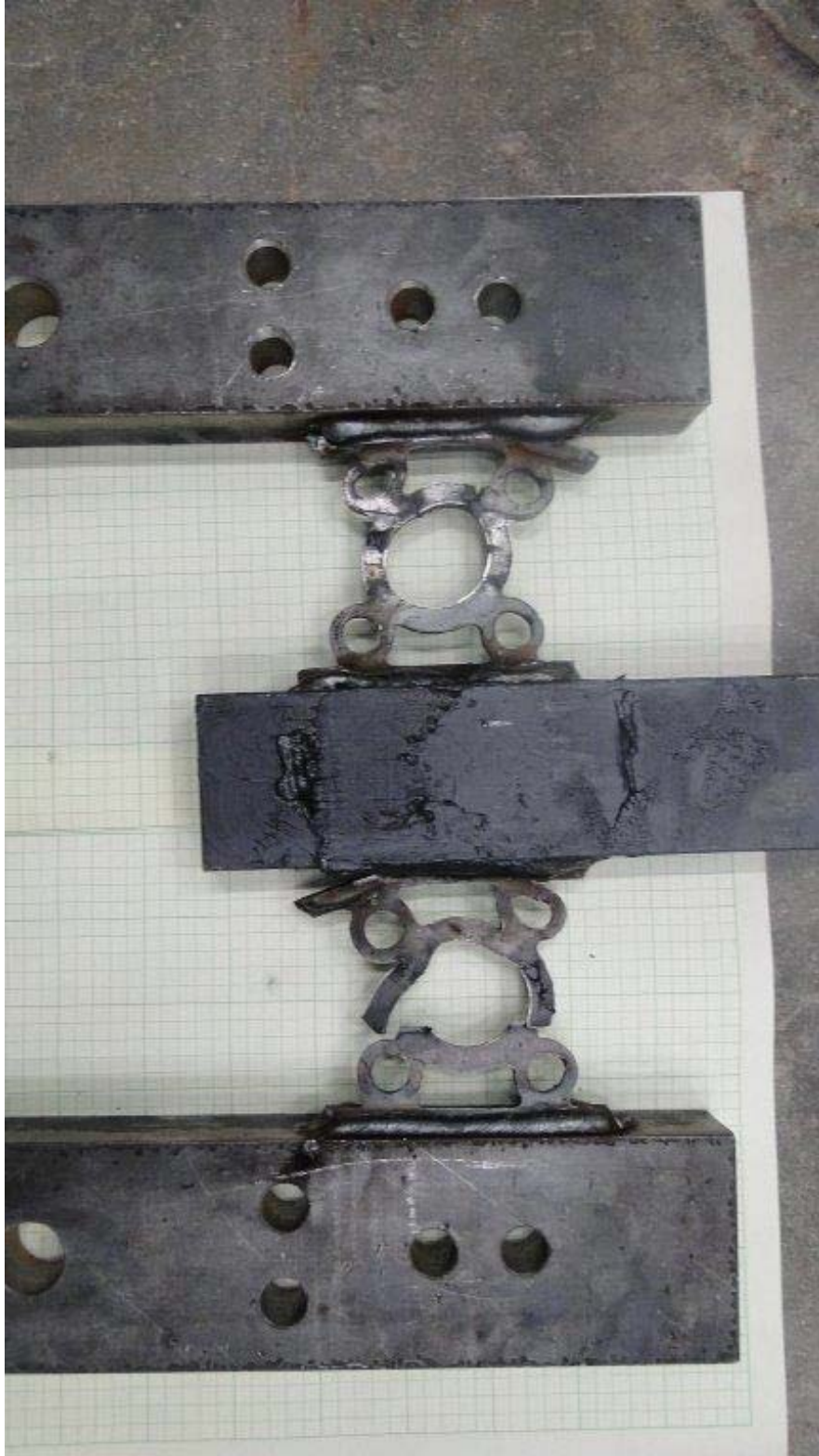


Figure A- 6: Failure mode of first tested devices



Figure A- 7: Close-up of the fist tested device shows the failure mode



Figure A- 8: Close-up of the fist tested device shows the failure mode



Figure A- 9: Failure mode of second tested devices



Figure A- 10: Close-up of the second tested device shows the failure mode



Figure A- 11: Close-up of the second tested device shows the failure mode



Figure A- 12: Close-up of the second tested device shows the failure mode



Figure A- 13: Failure mode of third set of tested devices



Figure A- 14: Close-up of the third set of tested device shows the failure mode



Figure A- 15: Close-up of the third set of tested device shows the failure mode



Figure A- 16: Close-up of the third set of tested device shows the failure mode



Figure A- 17: Test setup of Shape NS-5



Figure A- 18: Failure mode of first set of tested NS-5 shapes

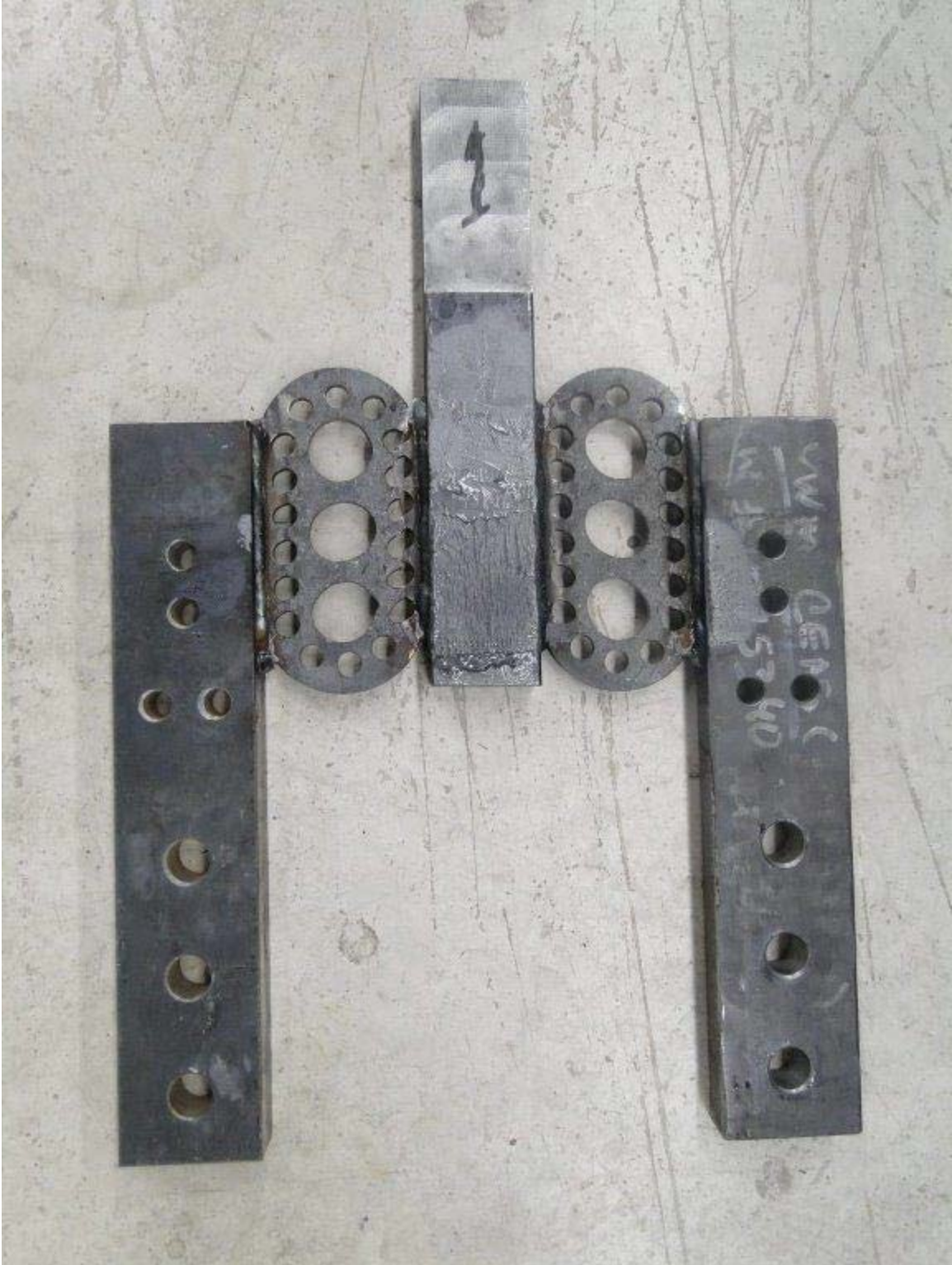


Figure A- 19: Failure mode of first set of tested NS-5 shapes shows the failure mode



Figure A- 20: Close-up figure shows the failure initiation of first set of NS-5 shapes



Figure A- 21: Failure mode of second set of tested NS-5 shapes



Figure A- 22: Failure mode of second set of tested NS-5 shapes shows the failure mode



Figure A- 23: Close-up figure shows the failure initiation of second set of NS-5 shapes



Figure A- 24: Failure mode of third set of tested NS-5 shapes



Figure A- 25: Failure mode of third set of tested NS-5 shapes shows the failure mode



Figure A- 26: Close-up figure shows the failure initiation of third set of NS-5 shapes

APPENDIX B. TEST SETUP DRAWINGS

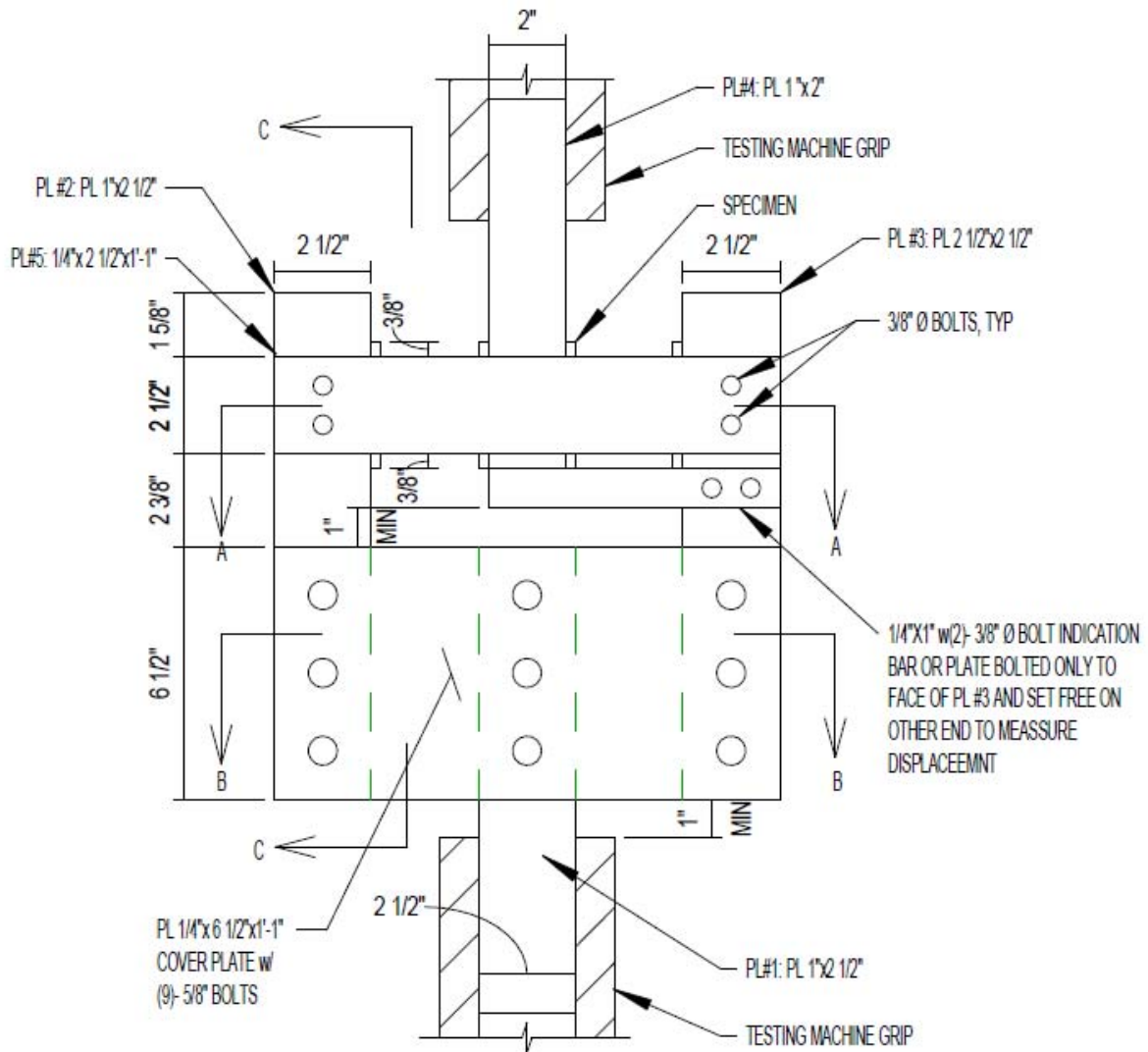


Figure B- 1: General view of test setup

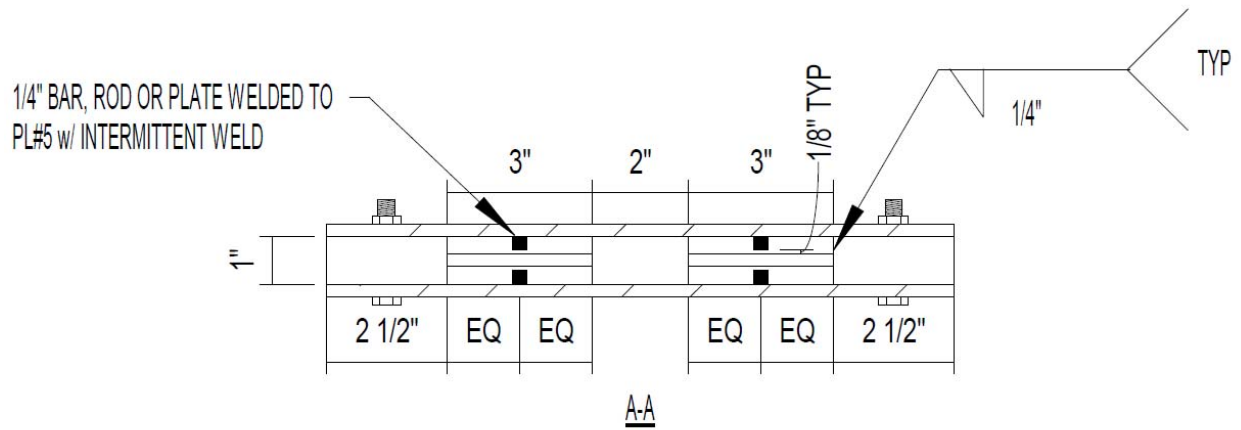


Figure B- 2: Section A-A

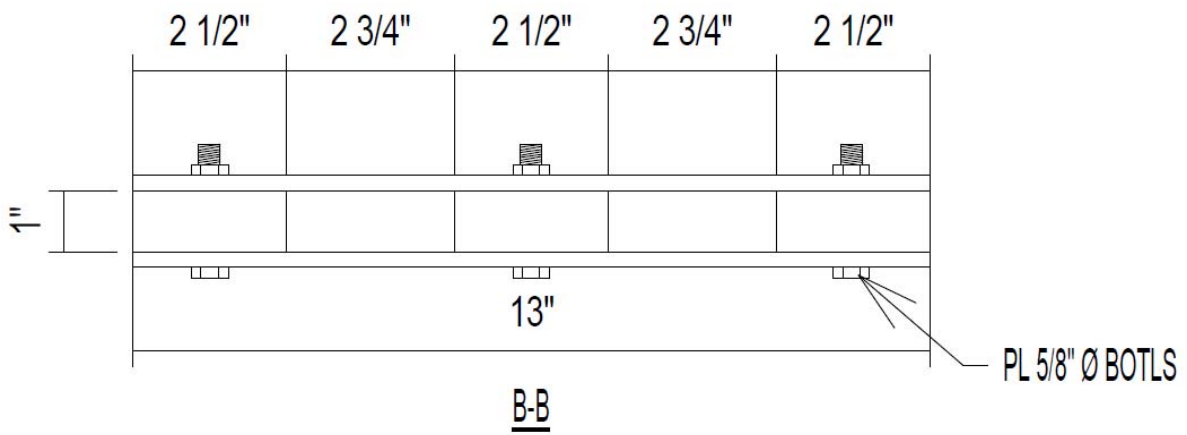


Figure B- 3: Section B-B

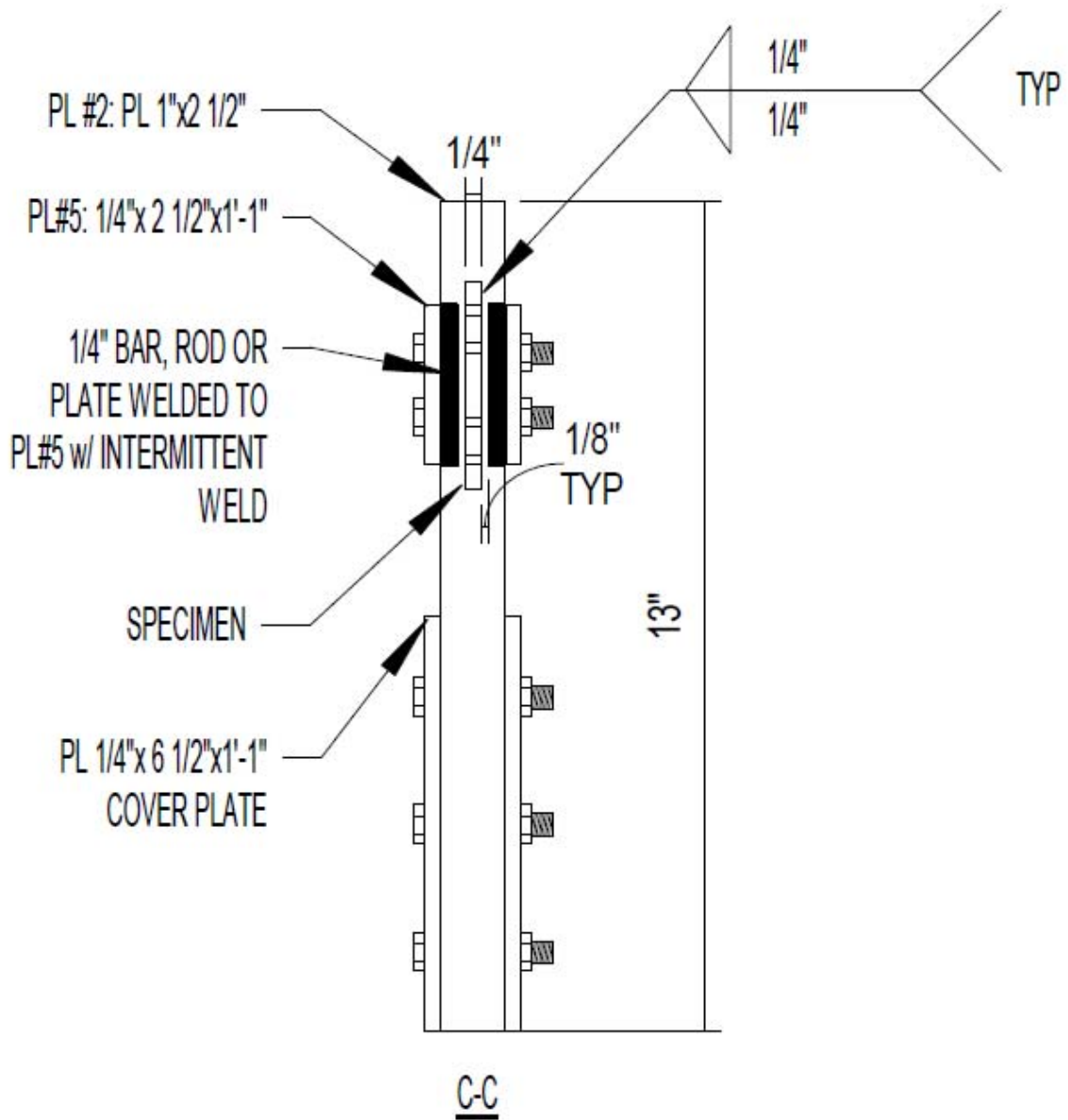
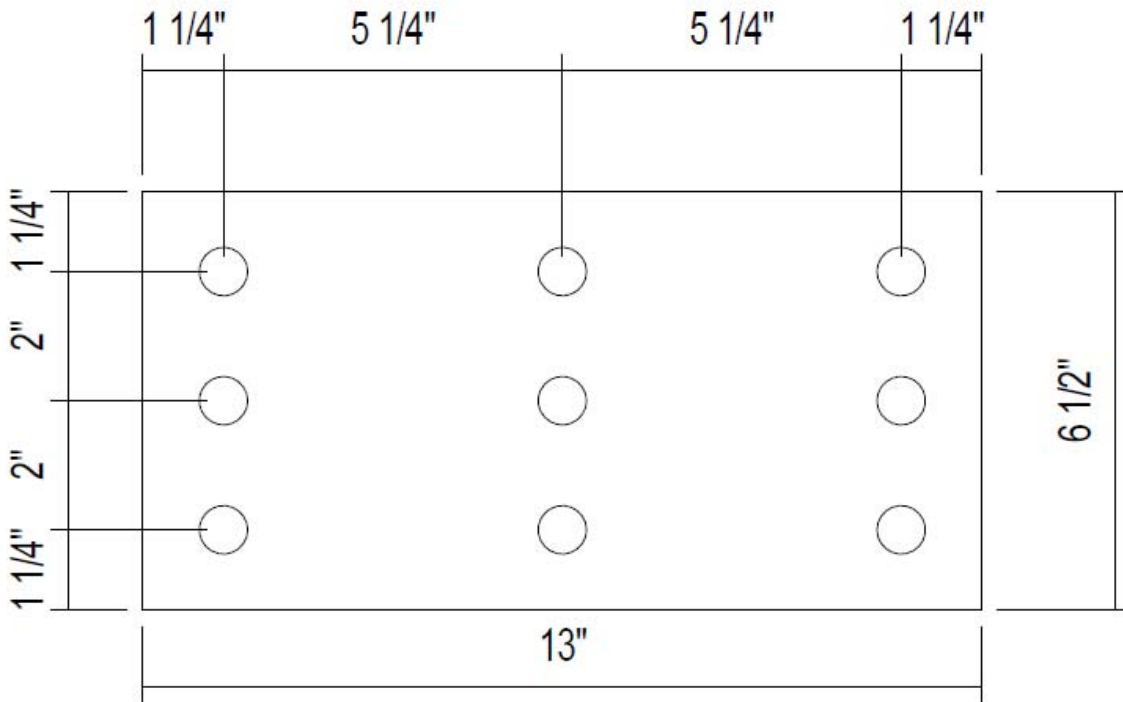
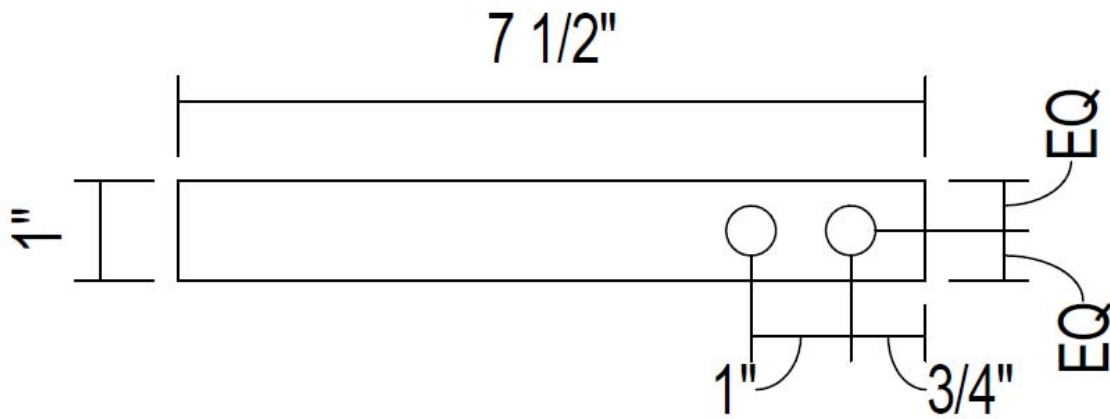


Figure B- 4: Section C-C



PL 1/4"x6 1/2"x1'-1" COVER
 PLATE w/ (9) - 3/4" HOLES.
 QUANTITY = 2 EA

Figure B- 5: Cover plate detail



INDICATION BAR OR
 PLATE: PL 1/4"x1"
 w/ (2) - 1/2" HOLE
 QUANTITY = 1 EA

Figure B- 6: Indication bar details

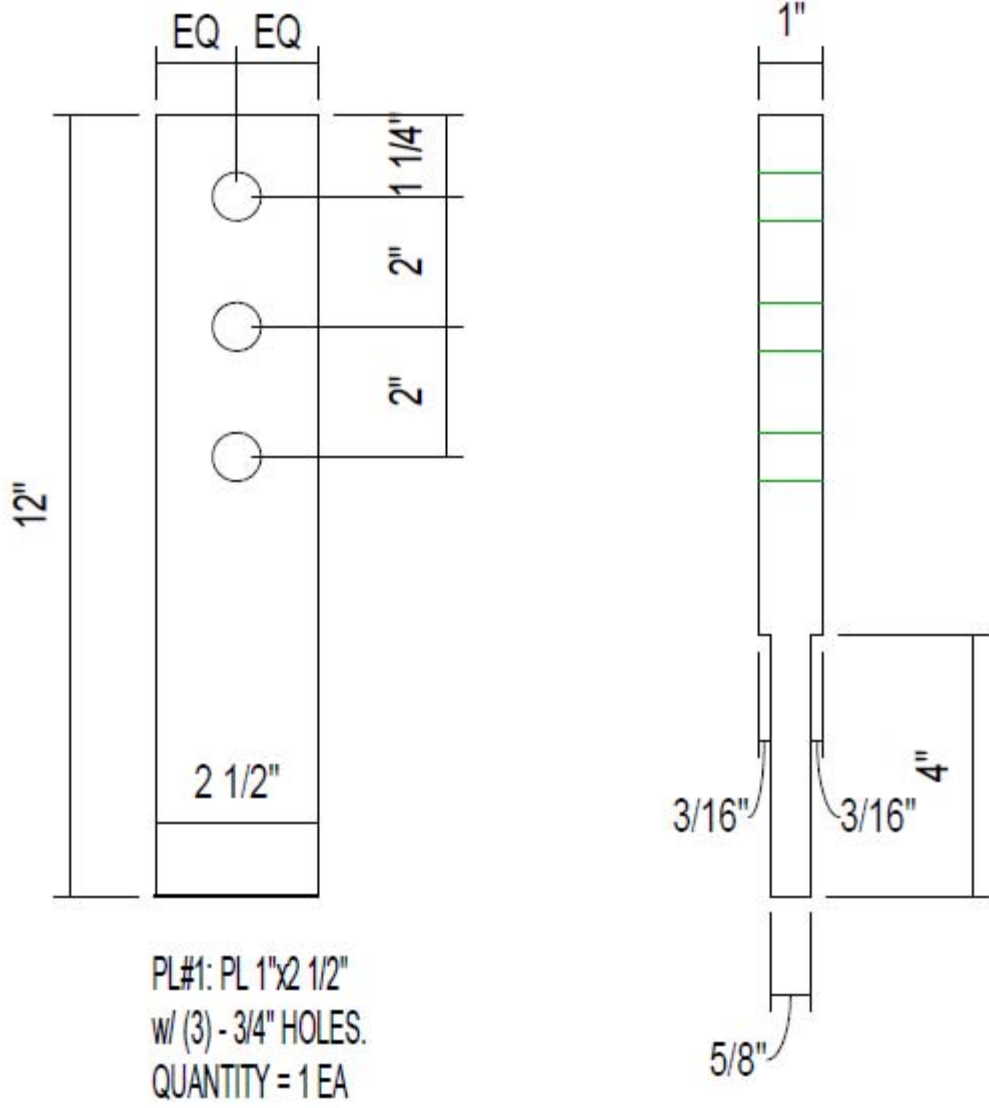
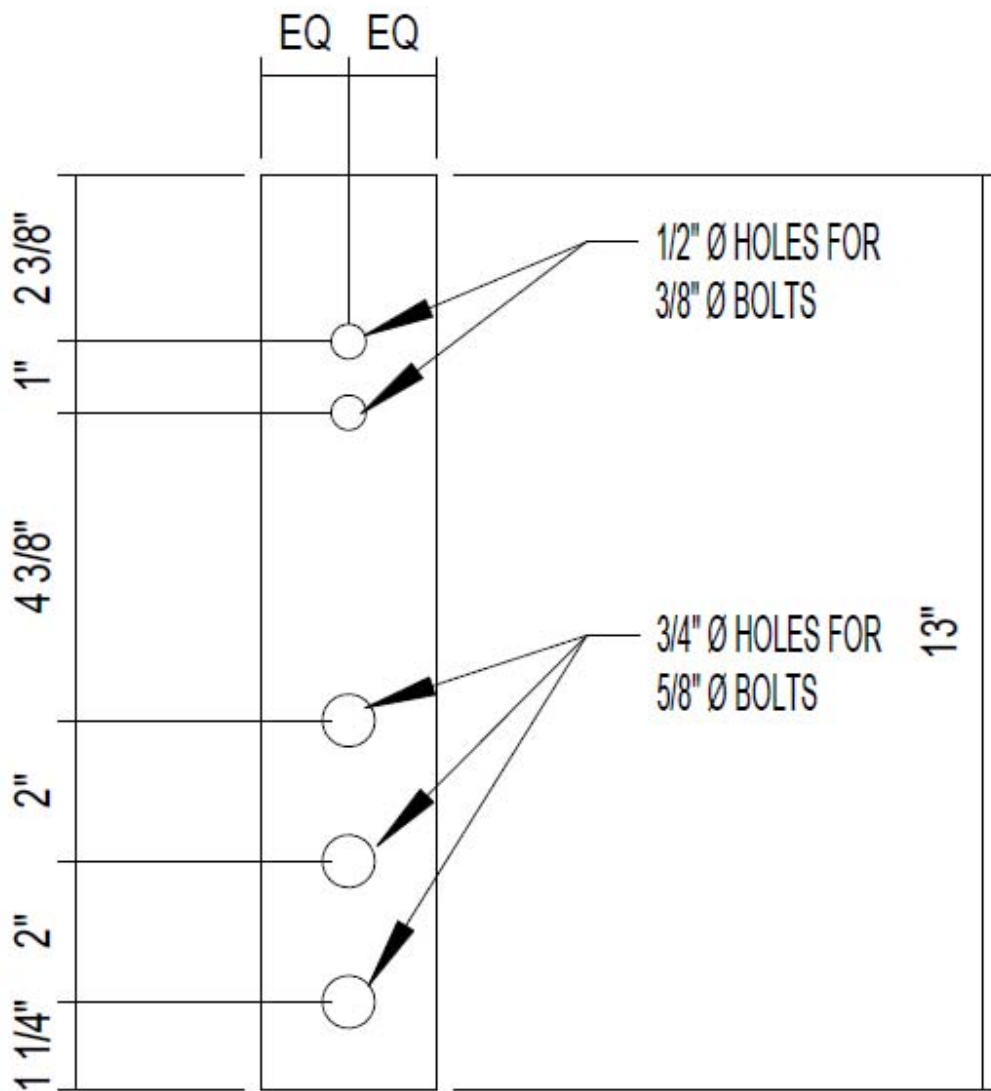
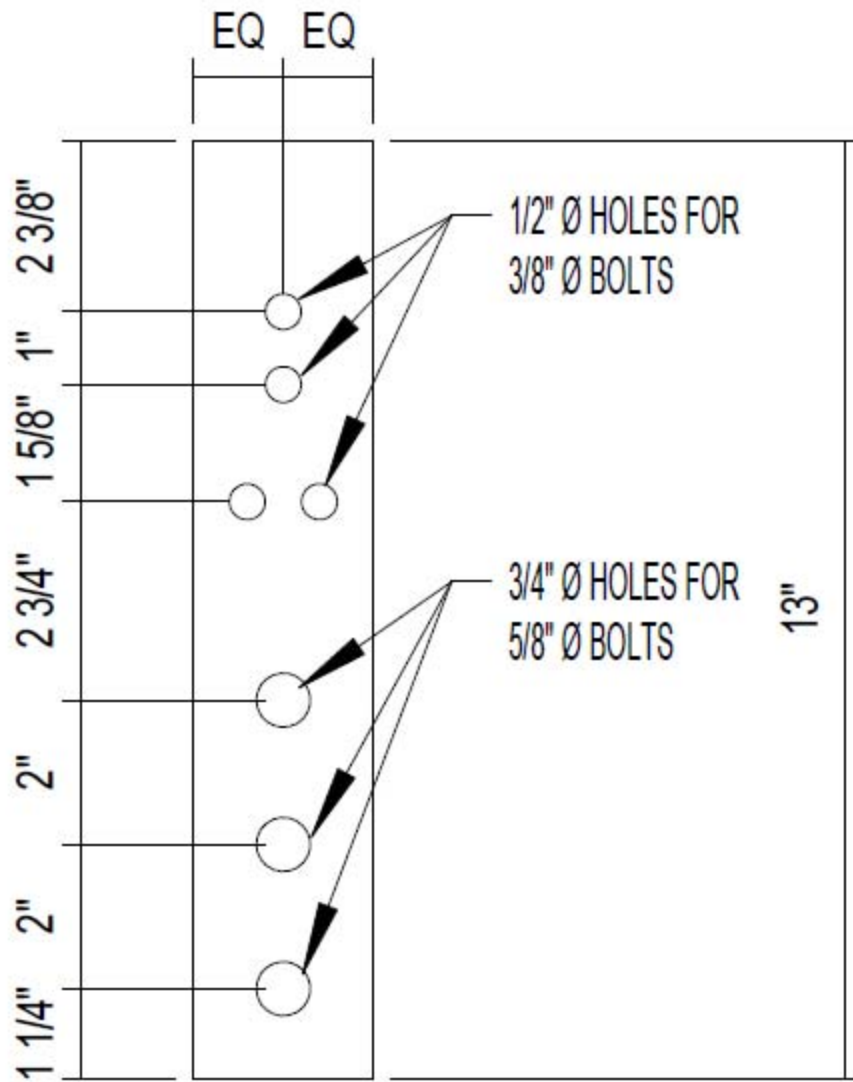


Figure B- 7: Plate number 1 details



PL #2: PL 1"x2 1/2"
 w/ (3) - 3/4" HOLES
 &w/ (2) - 1/2" HOLES
 QUANTITY = 3 EA

Figure B- 8: Plate number 2 details



PL #3: PL1"x2 1/2"
 w/ (3) - 3/4" HOLES
 &w/ (4) - 1/2" HOLES
 QUANTITY = 3 EA

Figure B- 9: Plate number 3 details

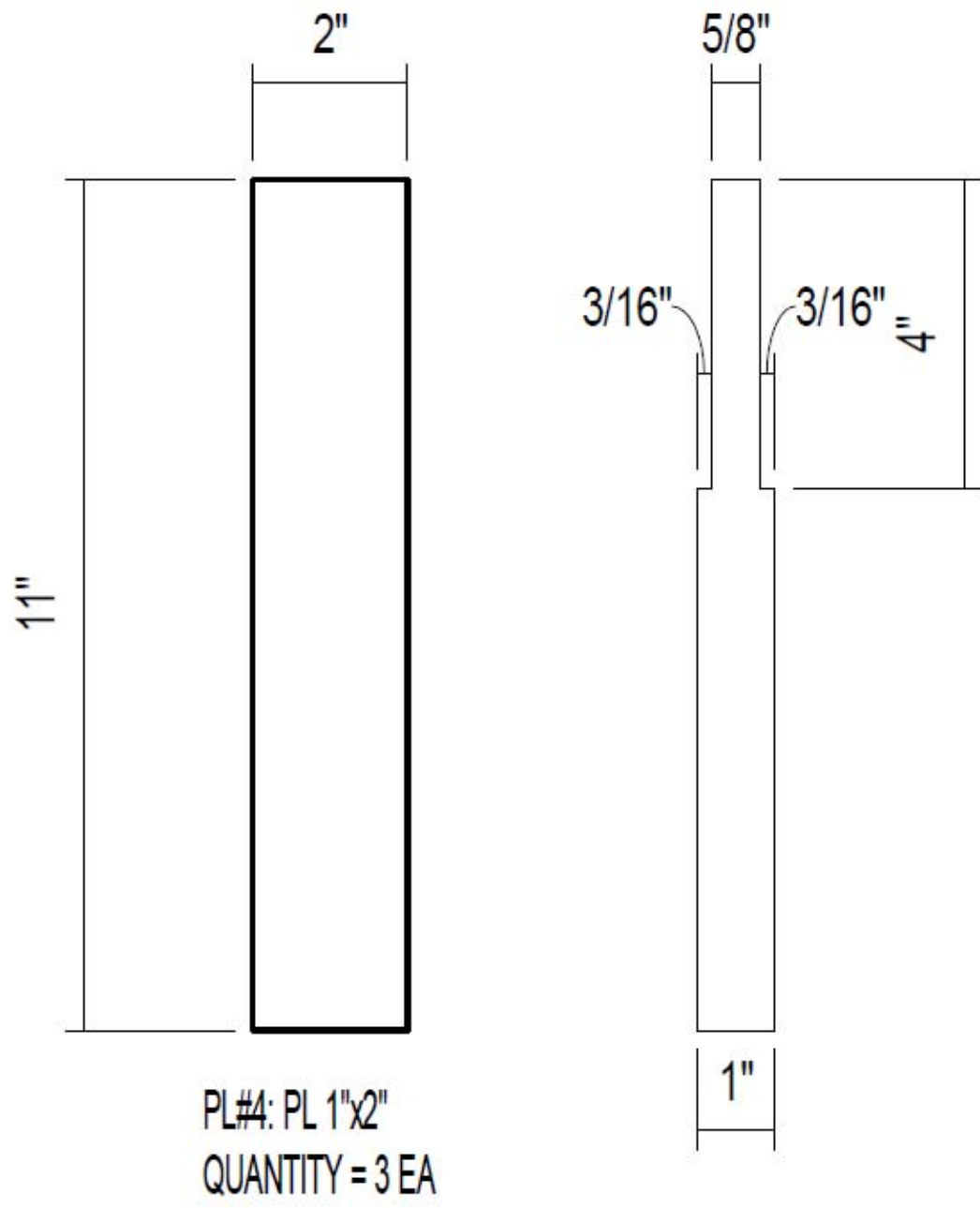
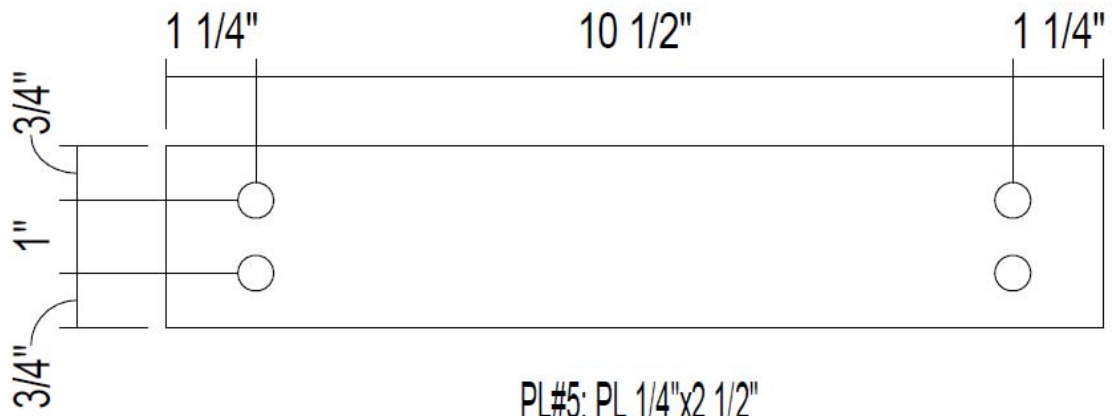


Figure B- 10: Plate number 4 details



PL#5: PL 1/4"x2 1/2"
w/ (4) - 1/2" HOLE
QUANTITY = 2 EA

Figure B- 11: Plate number 5 details

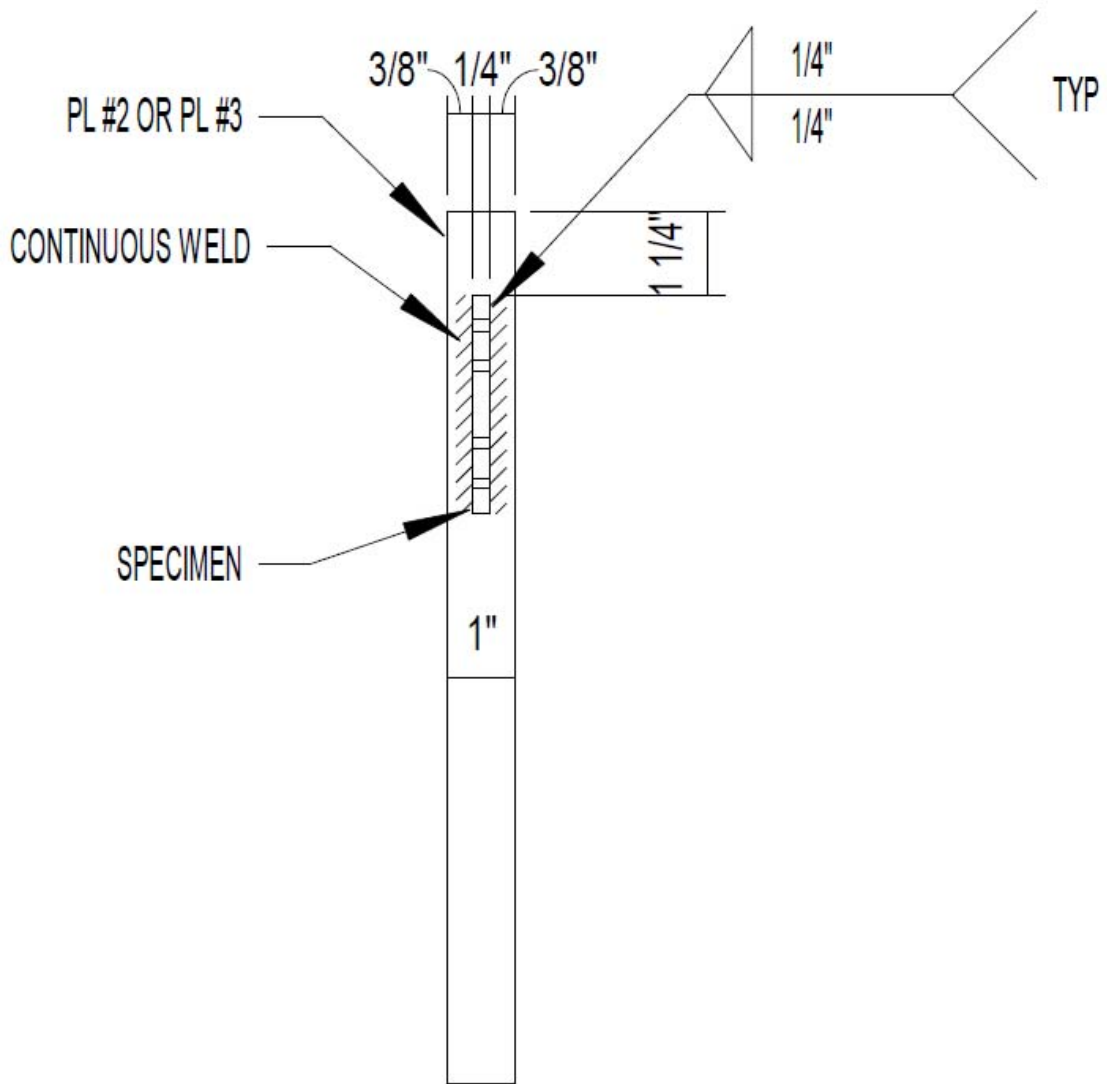


Figure B- 12: Plate number 2 & 3 details

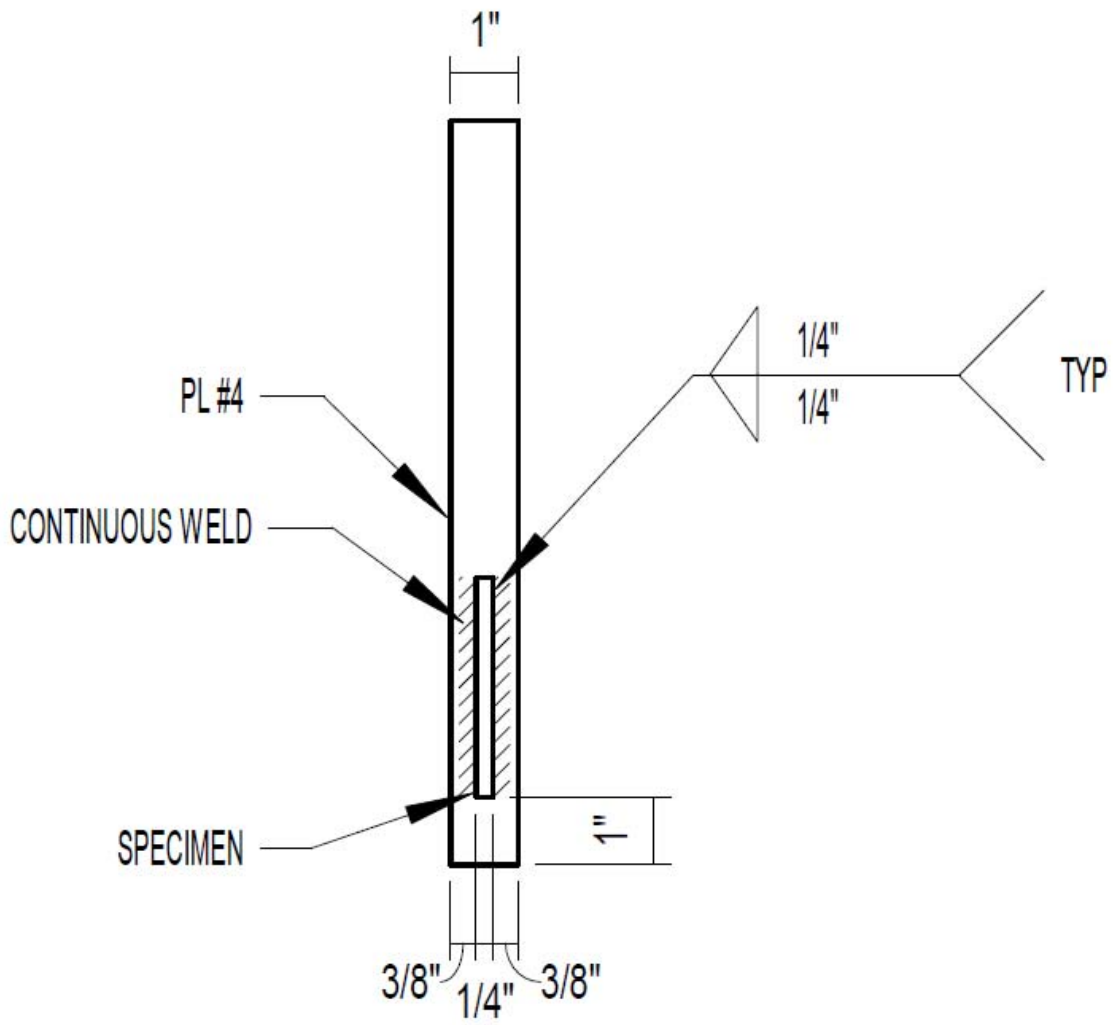


Figure B- 13: Plate number 4 details

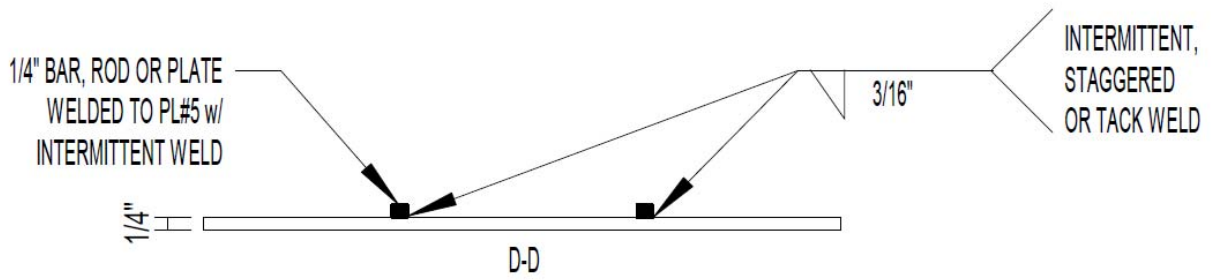
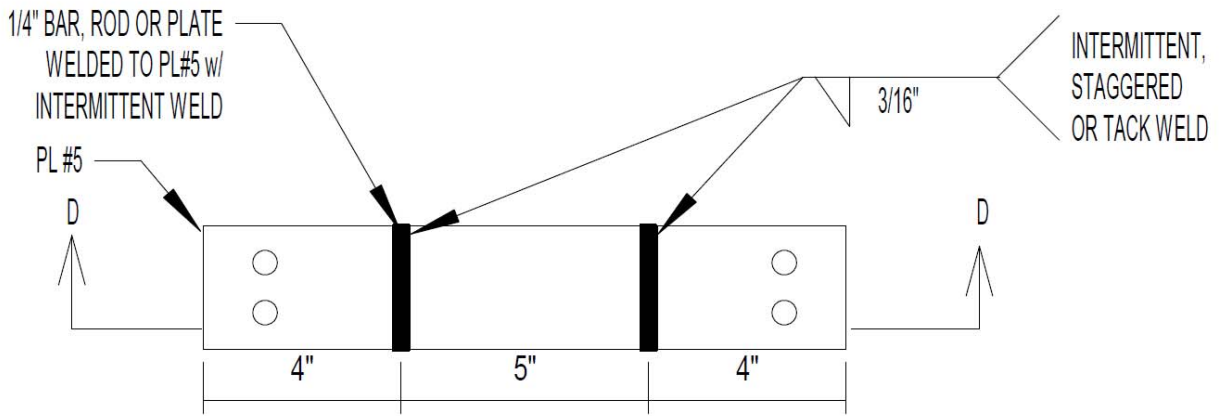


Figure B- 14: Plate number 5 details

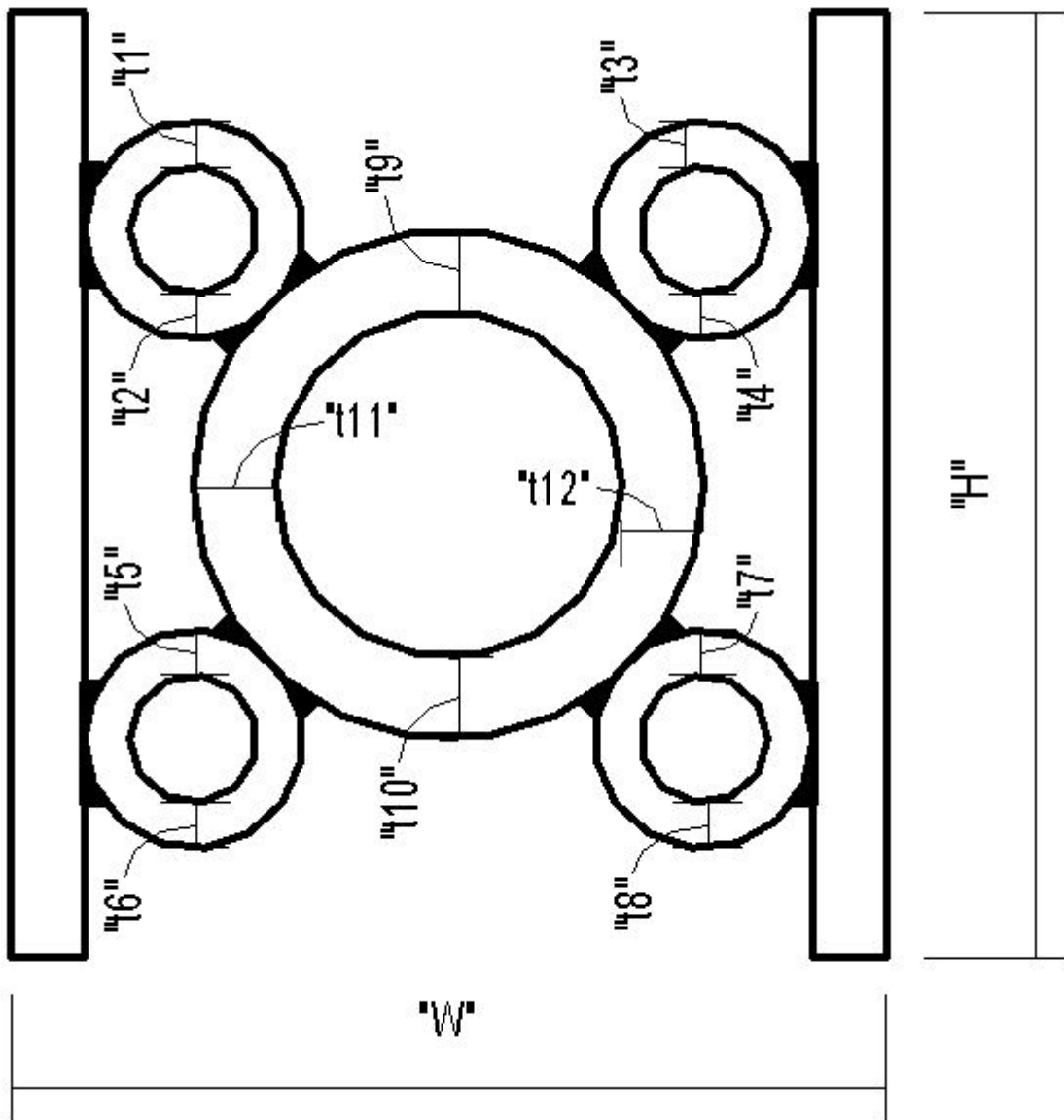


Figure B- 15: Index view of specimen's measurements for TS shape

Measurement	TS1-1	TS1-2	TS2-1	TS2-2	TS3-1	TS3-2	Actual (in)
H (in)	3.25	3.25	3.25	3.25	3.25	3.25	3.25
W (in)	3	3	3	3	3	3	3
t1 (in)	0.153	0.151	0.154	0.166	0.178	0.159	0.15625
t2 (in)	0.168	0.158	0.156	0.175	0.161	0.158	0.15625
t3 (in)	0.158	0.171	0.171	0.158	0.188	0.160	0.15625
t4 (in)	0.175	0.160	0.171	0.157	0.168	0.165	0.15625
t5 (in)	0.191	0.159	0.176	0.171	0.158	0.153	0.15625
t6 (in)	0.172	0.164	0.161	0.152	0.170	0.169	0.15625
t7 (in)	0.168	0.169	0.166	0.178	0.168	0.164	0.15625

t8 (in)	0.175	0.165	0.168	0.170	0.162	0.160	0.15625
t9 (in)	0.260	0.388	0.282	0.273	0.382	0.277	0.28125
t10 (in)	0.292	0.379	0.282	0.284	0.379	0.284	0.28125
t11 (in)	0.266	0.377	0.292	0.273	0.363	0.264	0.28125
t12 (in)	0.264	0.369	0.274	0.282	0.372	0.269	0.28125

CURRICULUM VITAE

Mohammed Aljuboori, P.E.

Academic Qualifications

University of Wisconsin-Milwaukee PhD in Civil Engineering Research: Energy Dissipating Connector for Precast Shear Walls In High-seismic Areas	Wisconsin, USA 2014-2019
University of Wisconsin-Milwaukee M.Sc. in Civil Engineering/ Structural Research: Development and Verification of an Intelligent Sensor System for Roadway and Bridge Surface Condition Assessments	Wisconsin, USA 2012-2014
Baghdad University B.Sc. in Civil Engineering	Baghdad, Iraq 2001 – 2003

Professional Certification /Training

- SPRAT Rope Access certification 2018
- ACI concrete Field Technician Grade I /US 2012
- Quality Assurance Quality Control Certificate/Iraq 2007
- Construction Quality Management Course /Iraq 2007
- OSHA Safety Standard/Iraq 2006
- Construction Quality Management Course /Iraq 2006
- Awarded the Chancellor’s Graduate student award for five semesters. 2012-2016

Skills and Areas of expertise

- Skilled in Computers software: RAMConcept, RAMStructures, RAMConnections, RAMElements, RAMBeam, RAMColumns, Tedds (TEKLA) AutoCAD, SAP2000, StressCheck, ETABS, RISA2D, OpenSEES, CSI Bridge, QConBridge, and some familiarity with Revit.
- Good Knowledge in ACI 318, AISC Construction Manual, LRFD specifications, ASCE07, and IBC.
- 16-month of work experience at Haditha Dam – Iraq
- Experience in Analysis and Design of structures, steel and reinforced concrete, Posttensioned concrete, Cold-Formed steel, wood design, Construction, Implementing, Supervision, Surveying.
- Construction Project Planning & Management for GOI projects (Provincial Level).
- Communication and coordination between GOI Ministries Director General and Coalition Forces including experience as USACE/Iraqi Governments Ministerial Liaison.
- Experience in construction management for large structures and facilities. I possess 8+ years of experience of working with with US firms or US funded projects in Iraq, followed by 4 years of experience in The United States.
- Commercial awareness & business acumen. Experience of working in multi-vendor environments.
- Ability to manage multiple projects simultaneously and under pressure.
- Directing technical process and resolve technical issues, managing multi teams and delegating tasks.

- Team work oriented, Detail oriented, Positive attitude, Data Entry, Coordination, & Time management.
- Design Stage Project Coordination and Sub-Contractors Management, Construction site works scheduling and coordination, and Design consultant.
- Good experience in running meetings, mentoring long-term projects and always staying ahead of the schedule.
- Languages: Arabic (Native) and English (Fluent).
- Citizenship: Dual, Iraqi-American

Professional Experience

**US Army Corps of Engineers,
Philadelphia, PA Structural designer/ Inspector
05/2018 - Present**

- Design and analysis of Bridges and Hydraulic Steel structures
- Inspection of existing Bridges and Hydraulic steel structures
- Design and analysis of new and existing buildings with various of types or construction
- Certified rope access climber by SPRAT

**Pierce Engineers,
Milwaukee, WI Project Manager Assistant / Structural designer/ Consultant
09/2014 – 05/2018**

- Correspondence communication among project contractors, consultant, and client and running meetings.
- Structural design of multi structural applications and buildings using different aspects of structural design for gravity and lateral loads.
- Worked on three Posttensioned Concrete projects: Kimpton hotel, parking structure of Brookfield corners mall in Wisconsin and 7-stories parking structure managed by Hammes Company
- Design and analysis for multistory buildings, lateral and gravity design.
- Developing some design spreadsheets using VBA.

**University of Wisconsin-Milwaukee,
Milwaukee, WI
CQC Geotechnical Manager,
08/2012 – 01/2013**

- Mentored the Geotechnical Quality Control Plan for some college sites.
- Attended the partnering meetings, QC Plan Meetings, Coordination and Mutual Understanding Meeting, conducts the QC meetings.
- Managed and coordinated three phases of control and documentation performed by the QC Specialists, laboratory personnel and other inspection and testing personnel required by the Contract.
- Preparing reports about all tests and experiments that were conducted
- Other duties as assigned.

**CME Associates, INC.
Syracuse, NY**

East

Project Construction Manager

Apr

2012-Aug 2012

- Collaborated with engineers, architects and other stakeholders to determine the specifications of the project.
- Obtained permits and licenses from appropriate authorities.
- Determined needed resources (manpower, equipment and materials) from start to finish with attention to budgetary limitations.
- Planned all construction operations and schedule intermediate phases to ensure deadlines will be met.
- Acquired equipment and material and monitor stocks to timely handle inadequacies.
- Ensured adherence to all health and safety standards and report issues.

WACOL/467 EPBS, Facility Engineer Team, USACE, COB Basrah and COB Adder

Baghdad, Iraq

Project Coordinator

Sep

2009-Jan2011

- Under the direction of the project manager, my responsibility was coordinating the deployment of multi-disciplined engineering team to work side by side with US Military Engineers (Facility Engineer Team).
- Managed the project schedule, cost, resources, and risk plans.
- Worked directly with DoD personnel to coordinate teams' assignments, mobilization and demobilization.
- Obtaining LOAs for project resources and equipment from both the US Base and GOI authorities.
- Coordinate and test the engineering equipment supplied by the vendors.

Danoub Group /US DoD funded projects

Baghdad, Iraq

Program Manager and Project Construction Manager

Jul

2010-Dec2010

- Follow up on Danoub's US funded projects.
- Coordinate meetings between Danoub Group and local officials.
- Managing construction phases and activities and related resources, this included scheduling the work and provide instructions and guidance to the project teams.
- Responsible for safe delivery of outcomes aligned with project schedule and cost.
- Managed Project Teams from project initiation through to Project completion. Act as a liaison with project clients and end users.
- Managed the Project costs and create monthly reports, including profit and loss reports.
- Maintained customer relationship to achieve long-term retention & satisfaction.
- Promoted QHSE compliance at every opportunity.
- Identified project risks and developed mitigation plans with subject matter experts.

WACOL/RCM/ITAO/USACE-GRD

Baghdad, Iraq

Project Manager Assistant/ MoE Liaison

Oct

2008-Oct 2010

- Under contract# W91GDW-08-Q-4033 (Oct 2008 – June 2009), I worked with WACOL/RCM as Project Coordinator and a Liaison with local officials of Iraq Ministry of Electricity. The objective

of this contract was to provide professional services to conduct a Site Security Assessment of the Ministry of Electricity (MoE)'s 36 most critical electric power infrastructure assets, as prioritized by Iraqi Transition Assistance Office (ITAO), US Army Corps of Engineers (USACE) Gulf Region Division (GRD), and MoE. In addition to coordinate the site assessment and gap analysis works, I was deployed as a member of the team to conduct presentation to the Deputy of the Minister of Electricity to advice of the methods and technology the ministry can employ to protect their critical assets in a lower intensity violent environment. Most relatively, I had the chance to visit or coordinate with the officials at the power stations at Mosul Dam (Mosul), Darbamdikhan Dam (Sulaymania), Haditha Dam (Al-Anbar), and Samara Dam (Slahaddin).

- While under contract # W917BG-10-P-0006 MoE/MoWR (May 2010 – Oct 2010) USACE Gulf Region Division-Central District, I was assigned as Assistant Project Manager with WACOL/RCM. The project objective was to provide protection performance work development services and prepare documents for Design – Building projects to bring the Iraqi Ministry of Electricity (MoE) into compliance with baseline physical security standards for critical infrastructure and headquarter facilities. Part of my responsibilities was to coordinate and meet with government officials at 36 MoE facilities including the Headquarters of both Ministry of Electricity and Ministry of Water Resource. Produced stage plans, highlight reports, documents translations, risk logs, requests for change etc., and provided strategic direction during the implementation stages.

InterSOS Humanitarian Org. /Project Funded by UNHCR

Baghdad/ Iraq

Project Manager/ Program Manager

Jul

2009-Dec 2009

- Responsible for the program to shelter the returnees who were displaced from their homes to other cities because of the cultic war.
- Responsible for selecting these beneficiaries, conducting assessments to estimate the cost of rehabilitating their houses, monitoring the implementation stage and commissioning.
- Coordinate the meetings between UNHCR-the donor- and InterSOS Organization.
- Preparing technical reports for each site visit.
- Manage the contracts with stakeholders from the Iraqi government.

Bennett & Fouch Association/ US Army Corps of Engineers (USACE)

Al-

Anbar /Iraq

Coordinator/Project Manager

Mar

2008-Jun 2009

- Project manager at Haditha Dam repairing project including turbine and gate maintenance works. The project included a new construction of Haditha camp (more than 600 workers in a site of an area of 1,563,243ft²)
- Coordination between the clients-Toltest Co- and my employer.
- Supervisor on QC daily Reports, redesign some incompatible designs, supervise the implementing of the Layout of project buildings, sewage system, water system, plumbing works, roads, water, and fuel pads, receiving the materials, and locate the missed Bench marks.
- Prepared and updated project schedule. Setting work process and target milestones for each phase based on the project plan.
- Monitored critical activities based on the project schedule and advise the project management.
- Performed other duties and responsibilities as assigned from time to time.

CAPE Environmental INC / US DoD funded projects

Basra /Iraq

Coordinator/Project Construction

May

2007-Feb 2008

- Supervision on more than 350 workers in a site of 1,291,670ft² area.
- Responsible for delivering projects against agreed scope, budget, schedule & customer expectations. Doing this whilst supervising, directing & motivating teams of multi-discipline contractors & employees.
- Determined the scheduling of different phases of a project based on established deadlines
- Negotiated contracts with architects, vendors, contractors and other workers.
- Escalated promptly any issues that may impact operations and planning with client to resolve them.
- Monitoring staff & team performance

AL-Muthana and Baghdad airport

Baghdad /Iraq

Construction Superintendent

May

2003-May 2007

- Worked as an intern before graduation and a supervisor assistant and supervisor in the airport where the main responsibility was monitoring concrete pours.
- Mentoring the work stages and ensure that they follow ACI requirements and aspect.
- My responsibility included auditing the construction material, coordinating the work with subcontractors and proceed the paperwork with government officials.

Researches

1) Energy Dissipating Connector for Precast Shear Walls in High-Seismic Areas.

- Partial fulfillment of requirements for PhD in engineering

2) Development and Verification of an Intelligent Sensor System for Roadway and Bridge Surface Condition Assessments.

- Sensing black ice formation on highways and developing a mechanism to send alerts to several receivers using different types of methods.

3) Using the Structures Dynamics Approaches in modeling vibrated panels by using SAP2000.

- I was able to predict the natural frequencies of the panel if one or more of its fasteners are loose.

4) Design of Clinic Building:

- Structural analysis and design for a four-story building.

5) Design of pedestrian bridge made of Aluminum 2024-T3:

- The project includes two phases:
 - a) Structural design and analysis of a 9ft length X 3ft width pedestrian bridge, with a lightest weight, also should meet the minimum life cycles requirements = 106 cycles.
 - b) Apply the fracture mechanics analysis and estimating the potential fatigue that might be caused by a 0.05in crack in the critical member.